ULTRAFAST CHARGE INJECTION DYNAMICS IN QUANTUM DOT SENSITIZED METAL OXIDES

BY

CONNER PATRICK DYKSTRA

DISSERTATION

Submitted in partial fulfillment of the requirements
for the degree of Doctor of Philosophy in Chemistry
in the Graduate College of the
University of Illinois Urbana-Champaign, 2023

Urbana, Illinois

Doctoral Committee:

Associate Professor Josh Vura-Weis Chair
Assistant Professor Renske van der Veen Co-Chair
Professor Catherine Murphy
Professor Moonsub Shim

Abstract

This thesis unravels the complex interactions between CdSe quantum dots (QDs) and ZnO nanorods during and after charge transfer using multi-modal time-resolved optical and X-ray techniques. CdSe - ZnO is a foundational system in photovoltaics, however the inability to study charge injection from the ZnO point of view has left open questions about the interaction between carriers post-charge injection.

Direct photoexcitation of ZnO was studied with a novel implementation of picosecond resolved X-ray absorption spectroscopy (XAS) by exploiting the oriented nature of the nanorods. ZnO has a wurtzite crystal structure, which is anisotropic and allows for the application of X-ray linear dichroism (XLD) to extract orbital dependent dynamics. The thermal impact of laser excitation was subtracted with a careful calibration in the extended X-ray absorption fine structure (EXAFS) region of the spectrum. The resulting nonthermal X-ray transient absorption (XTA) spectrum and transient XLD reveals a reduction in the absorption cross-section as a result of nonlocal core-hole screening. This effect had not previously been reported in XTA spectra. Upon excitation with low laser fluence, which limits the thermal impact from photoexcitation, the first instance of phase-space filling (PSF) in the hard X-ray regime was measured. This signal offers the possibility for the measurement of carrier- and material-specific dynamics since the holes and electrons have spectrally separated signals. Next, we sought to estimate the expected signal in an XTA experiment on the heterostructured CdSe - ZnO system, in which charges are transferred from the QD moiety to the ZnO.

PSF in the X-ray regime was correlated with a corresponding optical PSF signal at the ZnO band edge. Ultraviolet (UV) probe optical transient absorption (OTA) with direct

excitation of ZnO was used to estimate the optical PSF amplitude in ZnO that matches the necessary carrier concentration to measure PSF in the X-ray regime. CdSe - ZnO was then measured with optical excitation of the CdSe to test the feasibility of an optical pump - X-ray probe charge injection experiment. It was found that the efficiency of charge injection and resulting carrier concentration is insufficient under ideal circumstances to measure X-ray PSF within a reasonable averaging timeframe at synchrotron facilities. These experiments demonstrate the power of an alternative approach using purely optical techniques.

UV probe OTA is a powerful technique that directly interrogates the dynamics within wide band gap metal oxides. The direct band gap of ZnO is located at 3.3 eV, with an excitonic transition located at 365 nm. This transition gives strong signals far to the blue of the CdSe band gap. Applying dual UV/visible probe OTA directly correlates the kinetics of CdSe and ZnO. The implementation of a holistic kinetic model shows that charge injection is split into two time regimes one of which derives from heterogeneous ZnO states, likely due to facet-specific band bending. This work also addresses a longstanding issue within sensitized QD systems, which is how electrons and QD-bound holes interact after charge transfer. The holistic kinetic model reveals that there is a very short-lived intermediate state (<1 ps) that decreases with smaller QD sizes. The identity of this state is likely a localized surface state that arises from band bending in ZnO caused by adsorbed organic species, which contrasts with previous interpretations of a Coulombically bound interfacial exciton.

We have demonstrated the power, and limitations, of a novel time-resolved X-ray technique and its applicability to metal oxide materials and interfacial charge transfer in heterostructured materials. Two novel effects, hard X-ray PSF and nonlocal core-hole screening, were uncovered. While powerful, We showed that the achievable signal-to-noise ratio (SNR) at synchrotron based optical pump - X-ray probe experiments are not sufficient for charge injection studies in QD-sensitized nanomaterials. These results were followed up with optical measurements to show that charge injection in ZnO nanorods is strongly dependent on the surface chemistry of ZnO, in addition to the well-known dependence on CdSe chemistry. The assignment of the

intermediate state after charge injection to ZnO surface states offers a clear view on how ZnO based devices can be optimized. The UV-probe OTA approach demonstrated in this work offers opportunities for investigating the parameter space for QDHs, such as the dependence of charge injection on ZnO morphology, pump energy, and core-shell structures. Large scale X-ray facilities that offer high time resolution coupled with large X-ray fluxes can also be powerful avenues.

Acknowledgments

First and foremost, I thank my PHd adviser Renske van der Veen for her guidance and support throughout my PHd. I also thank the rest of my committee, Catherine Murphy, Moonsub Shim, and especially Josh Vura-Weis who served as a second advisor for the last few years of my work. I thank my constant collaborator Thomas Rossi for his insight and discussions. I thank all members of the van der Veen group past and present. In particular I thank Cecilia Gentle and Tyler Haddock for sharing long days and nights at beamtimes and fostering an open atmosphere. I thank Rachel Wallick and Jack Burke for sticking it out with me. I thank the rest of the group, Allan Sykes, Eric Thornburg, Oliver Lin, Frank Alcorn, and Omid Zandi for their friendship. I thank the rest of my cohort for sharing the grad school experience with me.

I thank my synthetic collaborator Michael Enright for his help and support. I thank our collaborators at Argonne National Lab, Dr. Don Walko, Dr. Gilles Doumy, and Dr. Anne Marie March and the members of the AMO physics group for their help during time-resolved beamtimes. I thank the Vura-Weis group for welcoming me into the group. I thank the staff scientists of the Materials Research Lab for sharing their expertise with me.

For companionship and sharing the struggles of graduate school, I thank my friends and family. I thank Oleg Davydovich for outlasting a pandemic with me, Matt Kromer for helping me escape urban trappings, and Will Andresen for wine nights. I thank Ashwathi Iyer for her constant support and belief in my abilities. Lastly I thank my family, including all my brothers Simon, Mackenzie, and Oliver for being pillars in my life. I thank my mother and father and bonus mother, without whom I never would have made it here.

Table of contents

Chapter 1

Introduction

1.1 Motivation

Meeting the worlds growing energy demands requires a diverse set of technologies to provide sufficient and consistent energy across seasons. Sustainable energy technologies have seen intense development with the looming threat of climate change and ecosystem destruction, with solar cells at the forefront. However the power conversion efficiency (PCE) of single junction devices is limited to 33.7 % due to intrinsic carrier losses, known as the Shockley-Queisser limit (SQL).[1] Surpassing this is a critical goalpost that nanomaterials may be able to reach.

Quantum dots (QDs) have emerged as strong candidates for high PCE solar cells because of their tunable absorption onsets and exotic carrier interactions that potentially enable efficiencies above the SQL.[3] QDs can be processed in unique ways to form hierarchical structures, known as Quantum Dot Heterostructures (QDHs). Shown in figure 1.1 are example photovoltaic architectures employing QDs, which belong to the class of 3rd-generation photovoltaics. CdSe QDs were the first monodisperse QDs synthesized with a simple hot injection technique,[4] and have been incorporated in many pioneering devices.[5] The CdSe band gap can be tuned from 2 to 2.8 eV, which is desirable for applications in LEDs and solar technology.[6] In addition, QDs have unique potential in high photon energy regimes due to multi-exciton generation, demonstrated in figure 1.1b, which has made characterizing carrier cooling, Auger recombination, and impact ionization rates a priority.[7]–[11] Many

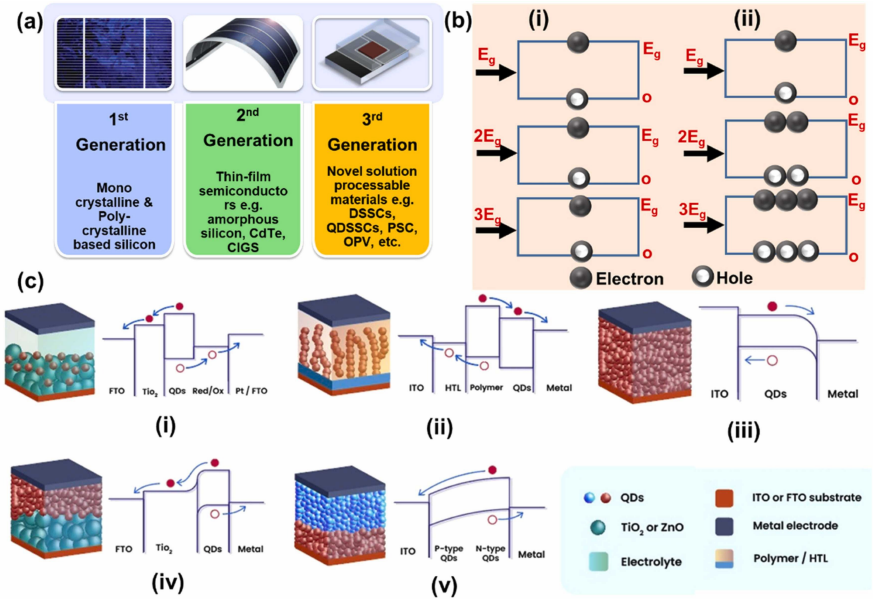

Figure 1.1: a) Classification of photovoltaic generations. b) Multi-exciton generation in QDs. c) Device architecture employing QDS. i) QDs deposited on TiO_2 with solution phase redox. ii) Photoactive polymer attached to hole transport layer (HTL), and QDs as electron transport layer (ETL). iii) Photoactive QDs to directly transport electrons and holes to carrier acceptors. iv) Photoactive QDs with TiO_2 as ETL. v) Photoactive p/n type QDs separate carriers before injection to carrier acceptors. Reproduced from reference [2]

different QDHs have been conceptualized and tested, shown in figure 1.1c. The highest performing QDH solar cell has only reached 18.1% conversion efficiency, still far below the SQL.[12] QDHs have not yet reached peak performance due to parasitic carrier trapping and recombination pathways, and an inability to fully exploit their unique capabilities.[13] One of the most debated factors holding QDHs back is the nature of the interface between QDs and the MO. This thesis will propose and test new investigative pathways for QDHs, and closely examine the interfacial barriers to efficient charge separation.

1.2 Organization of Thesis

This thesis is organized to introduce foundational concepts, technological appeal, and state of the field in chapter 2. From there chapter 3 discusses the the characterization of the CdSe - ZnO system, and methods the applied throughout this thesis. Chapter 4 then applies transient

X-ray spectroscopy to investigate the electron acceptor of the charge transfer system, the ZnO. Chapter 5 transitions to a study of the feasibility of applying transient X-ray spectroscopy to the QD sensitized ZnO system, while laying out the benchmarks needed for a successful experiment. Chapter 6 continues with an in-depth application of dual-probe optical transient spectroscopy to glean new insights into the nature of charge injection and the interfacial effects between ZnO and CdSe. We conclude with chapter 7, which lays out the contributions of this thesis to the area and a roadmap for the future.

Chapter 2

Charge Transfer in Quantum Dot Heterostructures

This chapter introduces the motivating concepts for this work. The unique photophysical aspects of quantum dots are discussed first in 2.1, followed by the current understanding of charge injection in QD sensitized metal oxides in 2.2. Finally, the dynamics at the interface of QD heterostructures are discussed in 2.3. This chapter is capped with a discussion of the need for new approaches to understanding these topics, in 2.4.

2.1 Photoexcitation of Quantum Dots

Semiconductor QDs belong to a class of materials that have quantized excitations due to having a confined excitonic wavefunction. As the natural extent of a bound electron-hole pair is limited by the physical extent of the nanocrystal (near the Bohr excitonic radius), a confinement energy is imposed that breaks the momentum symmetry, making the crystal momentum quantum number no longer good.[14] Instead, the excitonic wavefunction takes the form of hydrogenic orbitals, and must be described by an angular momentum quantum number.[15] This confinement effect quantizes the transition energies and induces a dependence of the optical transition energy on the nanocrystal diameter. The transition energetics can be further perturbed by varying the shape, from spherical to polyhedra, and dimensionality, from 0D dots to 1D wires and 2D plates.[16]

The discretized transitions allows for exotic carriers effects that can enhance the overall efficiency of photovoltaic devices. The phonon bottleneck can slow the energy dissipation of

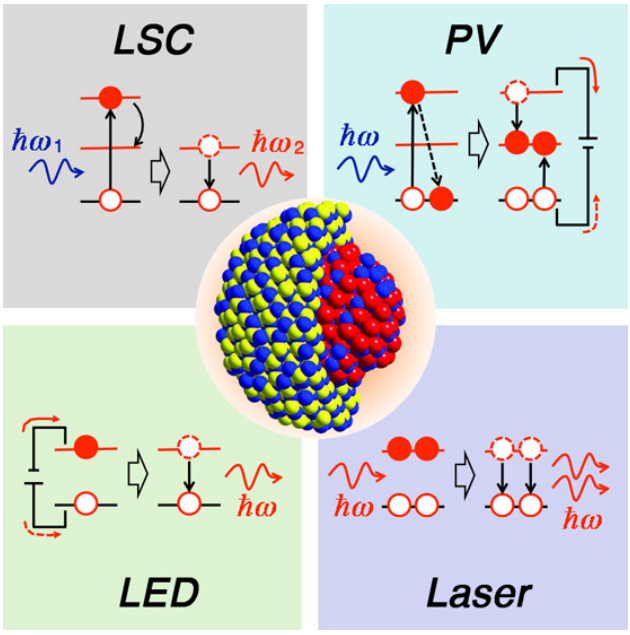

Figure 2.1: Applications of semiconductor nanocrystals as luminescent solar concentrators (LSC), photovoltaics (PV), light emitting diodes (LED), and for lasing applications. Reproduced from reference [17].

highly excited carriers, and hot electron transfer can lower the timescale for electron transfer to the physical limits.[18] Impact ionization turn a single high energy photon into multiple free carriers.[19] Harnessing these properties opens up many technological avenues. Shown in figure 2.1 are a few of the potential applications of QDs. Absorption followed by emission can be used as luminescent solar concentrators (LSC), or carrier transport of photoexcited charges can be directly used in photovoltaics. Incoherent radiative recombination from excited carriers can be employed in efficient LEDs, and coherent recombination can likewise be employed in lasing applications.

2.2 Charge Transfer in Quantum Dot Heterostructures

This work studies charge transfer in CdSe QDs coupled to ZnO nanorods. This system is shown schematically in figure 2.2. This architecture employs a type II band gap alignment between the CdSe and ZnO where electron injection is energetically favorable after photoexcitation of the CdSe, with a bifunctional linker to bind the two moieties together.[20] The system

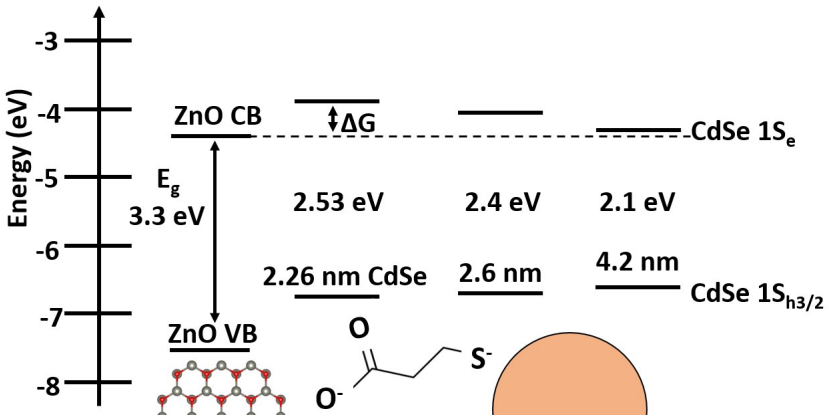

Figure 2.2: A highlevel view of the system under investigation. 3 different sizes of zinc blende CdSe quantum dots were molecularly tethered with 3-mercaptopropionic acid to wurtzite ZnO nanorods. The band gap of ZnO is 3.3 eV, while the band gap of CdSe is between 2.1 and 2.55 eV, as determined from the UV-Vis spectrum in solution. The approximate energy level positions are drawn from references [21], [23]. The approximate relationship of each quantum dot size to the driving force is also shown.

employed here includes three different QD sizes. The QDs are tethered to ZnO nanorods with 3-mercaptopropionic acid (MPA). The 4.2 nm QDs have a low lying electron state that is nearly isoenergetic to the ZnO conduction band, and are expected to yield slow charge injection kinetics.[21] Traditionally a metal oxide (MO), such as ZnO or TiO_2 is used for the electron acceptor. ZnO has a direct band gap, high electron mobility, and easy and cheap manufacturing into a wide range of structures, making it a popular choice for photovoltaic applications.[22]

Charge transfer in quantum dot sensitized metal oxides is often interpreted through the standard Marcus Theory framework, which extends transition state theory to the specific case of two coupled diabetic potential energy surfaces.[24]–[26] It has found wide-ranging applications in systems including molecular donor - molecular acceptor, nanocrystal - molecule, and nanocrystal - semiconductor systems,[20], [27]–[31] and is shown in equation 2.1:

$$k_{ET} = \int_{-\infty}^{\infty} dE \rho(E) |H_{DA}(E)|^2 \frac{1}{\sqrt{4\pi\lambda k_B T}} \exp\left(-\frac{(\lambda + \Delta G_0 + E)^2}{4\lambda k_B T}\right) \tag{2.1}$$

Marcus theory, as it applies to quantum dot - metal oxide heterostructures, relates the rate

of electron transfer to the density of acceptor states in the metal oxide $\rho(E)$, the reorganization energy of the environment λ, the driving force ΔG_0, and the electronic coupling between the donor and acceptor $|H_{DA}(E)|^2$. The reorganization energy describes the environment's response to charge injection. In QDHs the reorganization energy is small, or negligible due to the mesoscopic scale of the involved parties. For 2 nm CdSe quantum dots with a 1 nm thick alkanethiol shell, the total reorganization energy is around 34 meV, which includes inner and outer sphere components.[32], [33] The rate of charge transfer is dominated by the energy difference and electronic coupling between the QD excitonic state and the ZnO CB. ΔG_0 includes a range of energetic effects that qualify the total difference in energy, including the binding energy from the exciton in the QD, shifts in the ZnO CB due to electronic coupling, and differences in dielectric environments as the electron moves from the QD to the ZnO.[34], [35] It has been suggested that the normal Marcus behavior for electron transfer from quantum dots indicates charge transfer into a low DOS region of the metal oxide, meaning the metal oxide acceptor state can be treated as molecular-like. If charge injection took place into a quasi-continuum of states then there would be little influence of the driving force on the rate of charge transfer.[36] In the system studied here, donor and acceptor states are separated by an insulating energy barrier due to the organic linker that physically connects the two materials. The separation puts the CdSe - MPA - ZnO system in the nonadiabatic regime due to the weak electronic coupling.[15] This is typically considered as a tunneling barrier affecting the coupling term, where the rate of charge transfer decays exponentially as the distance between donor and acceptor increases. In this work, the organic linker is consistent between samples to isolate the influence of the quantum dot size and ZnO surface chemistry.

Alternative models for charge transfer that have been applied include the Newns-Anderson model of chemisorption,[37] or approaches using the spin-boson Hamiltonian that parallels transition state theory.[38], [39] The Newns-Anderson model was adapted from the Anderson model for the delocalization/localization interaction. When applied to the adsorption of

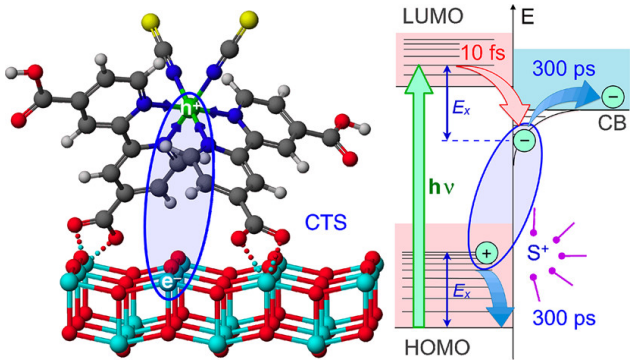

Figure 2.3: Illustration of the charge transfer state formed immediately after charge transfer from N719 dye into anatase TiO_2. Reproduced from reference [44].

quantum dots on metal oxides, a broadening of the discrete quantum dot energy levels that are resonant with MO states is expected, while the broad bands of the MO are unchanged. This becomes less important when the electronic coupling is weak, as is the case in quantum dots attached with a molecular linker.[15] Solving the spin-boson Hamiltonian attempts to characterize electron transfer, both adiabatic and nonadiabatic, within a dissipative environment.[40], [41] This approach takes into account the interaction of the donor - acceptor framework with the bath of vibrational transitions. This approach has found utility in systems with strong solvent interactions, such as biomolecules.[42], [43]

2.3 At the Interface Between Quantum Dots and Metal Oxides

The interface in QDHs acts as a barrier to charge separation due to the (typically insulating) organic layer that connects the QD and MO, which also introduces subbandgap states that can trap electrons and holes.[45] Identifying and amplifying the properties that promote charge separation is a critical goal for photovoltaic development, along with limiting the factors that trap carriers and enhance recombination.

Within the fields of organic semiconductors and hybrid organic - inorganic systems, it is accepted that charge transfer proceeds through an intermediate charge transfer state (CTS), as shown in figure 2.3.[46]–[48] The CTS is a bound state, described as an interfacial exciton,

between the positively charged moiety (QD/dye/organic semiconductor) and the electron at the surface of the ZnO. The hole is localized on the molecule, while the electron delocalizes over a few unit cells at the surface of the MO. The energetics of this state within a dye - ZnO system have been studied with electroluminescence and Stark spectroscopy, where the CTS luminescence varies in energy with the driving force of the dye and applied electric field.[49], [50] The CTS has been used to explain the slower electron transfer from dyes in ZnO compared with TiO_2, which is justified by the lower electrostatic screening in ZnO allowing for a stronger interaction between separated carriers.[51]–[53]

The dissociation rate of the CTS is commonly approximated with the Braun - Onsager model, which is given in equations 2.2 and 2.3 from reference [35]:

$$k_d(0) = \frac{q}{\epsilon_r \epsilon_0}(\mu_e + \mu_h) A * \exp\left(-\frac{E_b}{k_b T}\right) \tag{2.2}$$

$$E_b = W(\infty) = \frac{q^2}{4\pi\epsilon_r\epsilon_0} * \left[\frac{1}{R_{QD} + h} - \frac{1}{R_{QD} + h + \infty}\right] \tag{2.3}$$

Where $k_d(0)$ is the dissociation rate of the CT state when the electric field is 0. q, ϵ_r, and ϵ_0 are the elementary charge, dielectric constant of the medium, and the vacuum permittivity constant respectively. μ_e and μ_h are the carrier mobilities of the electron and hole, respectively. E_b is the binding energy of the exciton, defined as the work needed to separate the electron and hole to infinity, $W(\infty)$ equation 2.3. R_{QD} is the radius of the QD and h is the length of the linker molecule. The first term in equation 2.2 details the transport limited recombination rate, or Langevin recombination, which is the dominant recombination mechanism in low mobility materials, such as in organic semiconductors. Recent work has been done to recast the Braun - Onsager model for hybrid organic - inorganic systems,[54], [55] and apply it to systems like dye - sensitized ZnO.[56] The main difference in a hybrid system is the length scales of the carriers, where in the organic system one carrier is localized to a few molecules (Frenkel character) while the carrier within the inorganic material is delocalized over many lattice sites (Wannier - Mott character). As has been noted recently

though, the Braun - Onsager model is only applicable at low dissociation efficiencies and applied electric fields.[47], [57] Additionally, the interfacial dipole formed from charge transfer may induce a quantum confinement energy that reduces the binding energy of a CT state, and increase the dissociation rate, even in the absence of an external or static electric field.[47], [58], [59]

The existence of this state in QD-MO systems has been endorsed in references [34], [35], where terahertz spectroscopy was employed to study the carrier conductivity in ZnO and found that there is a delay of ∼20 - 60 ps between the initial charge separation and when the carriers in ZnO reach maximum conductivity. This delay was interpreted as evidence of the CTS, and is analyzed with the Braun - Onsager model where the Coulombic attraction between hole and electron is dependent on dielectric environment (approximated with the Maxwell - Bruggeman EMA) and the quantum dot size. The expected inverse relationship between quantum dot size and the lifetime of the CTS, due to the separation between charges, has not been verified. As has been noted recently though, the Braun - Onsager model is only applicable at low dissociation efficiencies and applied electric fields.[47], [57] The interfacial dipole formed after charge transfer may also induce a quantum confinement energy that reduces the binding energy of a CT state, and increase the dissociation rate even in the absence of an external or static electric field.[47], [58], [59]

The assignment of a CTS is predicated on there being a single charge injection pathway, where the CdSe injects charge within ∼10 picoseconds (as determined with OTA) followed by a slowly rising signal in ZnO (as determined with THz spectroscopy). Evidence against this assumption is presented in chapter 6.

Band bending is a well-known phenomenon where the energetics of the conduction or valence band is perturbed by dopants and surface donors, defects, strain, and applied potentials. It is a common topic in condensed systems, and to a lesser extent in nanomaterials, and to an even lesser extent in photochemistry.[60] The spatial extent of band bending in nanoparticles was developed by Albery and Bartlett in 1984.[61] Due to their small size,

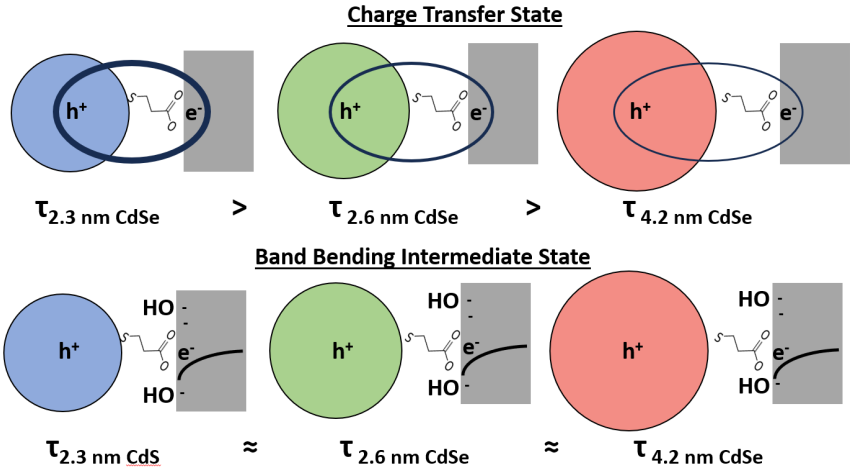

Figure 2.4: A pictorial depiction of the expected trend in the lifetime of the intermediate state with the size of quantum dots. If a charge transfer state does form, and because all other factors are equivalent, the lifetime should be shortest for the 4.2 nm CdSe QDs and increase with smaller QDs. If instead the carriers are localized due to band bending effects, the lifetime should be almost independent of the QD size.

nanoparticles are significantly impacted by the overall dielectric character. In ZnO and TiO_2 nanoparticles of similar size (16 and 14 nm, respectively), it was found that photogenerated charges had significantly higher lifetimes in ZnO, which can be partially attributed to ZnO's lower dielectric constant allowing for greater band bending across the nanoparticle given similar dopant concentrations.[22], [62]

Recently a pair of articles by the group of Gessner showed strong band bending at the $[1\,1\,\bar{2}\,0]$ ZnO surface due to hydroxylation.[63], [64] This band bending persisted for a depth of 6 nm before reaching flat band conditions. The hydroxylation could be removed by annealing at 400 C under ultra-high vacuum for 1 hour.[64] This band bending played a significant role in the electron dynamics after charge injection, where the injected charge was localized near the surface, and increased the magnitude of band bending.[63] The stability of adsorbates, and thus the band bending potential, with regards to pressure and temperature is variable with the crystal plane identity.[65] This could give heterogeneous band bending across a whole sample, where surface energetics will depend on the degree and identity of the adsorbates, along with the particular crystal facet.

The CTS assignment assumes a strong Coulombic interaction after charge transfer, which will vary widely with the range of QD sizes employed here. As depicted in figure 2.4, if the Coulombic interaction is the dominant interaction, then the lifetime of the intermediate state should increase as the QD size decreases. The surface chemistry is identical between samples, but a complicating factor is the excess electron energy. As the QD size decreases, the energetic difference between the QD excitonic state and the ZnO conduction band increases, referred to as the driving force. In organic photovoltaics a larger driving force has been shown to correlate with a decreased CTS lifetime because the hot interfacial exciton has excess energy to dissociate with.[66], [67] A similar effect may come into play here.

A competing model proposed here relies on the surface chemistry of ZnO. We propose here that band bending at the ZnO surface could explain an optically dark intermediate state. Recently a pair of articles showed strong band bending at the $[1\,1\,\bar{2}\,0]$ ZnO surface from adsorbed hydroxy species.[63], [64] After charge injection from N3, the magnitude of band bending was increased which helped localize the injected electrons near the surface.[63] As depicted in figure 2.4, if the intermediate state in QDHs is due to electrons localized near the surface from intrinsic band bending of ZnO, then the lifetime will be independent of the QD size. These competing models will be tested both with the QD size dependence and with a simple processing of the ZnO with is expected to reduce band bending at the surface, but should not affect the Coulombic interaction after charge transfer.

2.4 Ultrafast Spectroscopic Avenues

2.4.1 X-ray Transient Absorption Spectroscopy

There have been many studies of quantum dot (QD) sensitized metal oxides with model systems including CdSe/CdS/PbSe/PbS on TiO_2 or ZnO.[34], [68]–[70] However, there is significant disagreement in the ultrafast community over the timescales and yields of charge separation for very similar systems.[20], [34], [71], [72] The applied techniques usually include

optical transient absorption, terahertz spectroscopy, and a mix of nonlinear optical techniques. These suffer from intrinsic drawbacks: the signal of the electron and hole are convoluted together, and there is no differentiation between the donor and acceptor materials.

Ultrafast XTA has an inherent advantage in this regard because it detects transitions between core electrons and unoccupied valence or continuum orbitals. So called K-edge spectroscopy is element specific and can differentiate between the acceptor and donor materials. Conventional techniques have difficulty characterizing the dynamics of the electron and hole individually. XTA is unique in that the response of each material is separated by the elemental edges, and that carrier trapping can be distinguished from phase space filling by the energetic separation of structural and electronic signals.[73], [74] This is defined by the X-ray absorption near edge structure (XANES) and the EXAFS. The XANES contains transitions close to the ionization edge, which is a mix of bound transitions to delocalized and continuum states along with multiple scattering.[75] The EXAFS region gives geometric information by periodic modulations of the absorption cross-section by the ejected photoelectron scattering off nearby atoms.[76], [77] The XANES and EXAFS regions thus give distinct information on the material dynamics. The combination of XANES and EXAFS allows interrogation of structural distortions that occur at defect sites, like carrier trapping and polaron formation.[74], [78], [79] This could make it very powerful for characterizing a localized CTS.

Determining the suitability of a given system for an XTA experiment saves critical resources. Chapter 4 applies this powerful technique to bare ZnO nanorods, while the question of suitability is directly addressed in chapter 5.

2.4.2 Transient UV and Visible Probe Absorption Spectroscopy

Despite the importance of studying the QDH interface, it is uniquely difficult to directly interrogate. Time resolved X-ray photoelectron spectroscopy is very useful in hybrid organic-semiconductor structures, but is challenging with the mixed organic-inorganic coating on the ZnO.[64] Infrared spectroscopy can be difficult to interpret when the free carrier transitions

in ZnO significantly overlap with interband hole transitions in CdSe.[80]–[82] The most applied techniques are a mix of optical transient absorption (OTA), THz spectroscopy, and photoluminescence (PL) spectroscopy. OTA and PL has been applied to show that there is a strong dependence of the charge injection rate on QD size, and that the effects of photo-oxidation can be mitigated with core-shell QDs and judiciously chosen ligands.[83]–[85] THz spectroscopy has been widely applied to gain insight into the character of mobile carriers in ZnO.[20], [53] The most difficult question to answer is what is the magnitude of the interaction between electrons and holes post charge transfer?

An analogue to QD sensitized ZnO is dye sensitized ZnO, where there is significant evidence for the formation of a CT state in the moments after carrier injection, which impedes charge separation.[86]–[89] THz studies have found evidence for the formation of the CT state in QDHs, but the timescale and magnitude of the electron-hole interaction is still an open question. Dye-based CTS thermally dissociates on the ∼300 ps timescale, but the QDH CTS dissociates in $\sim 20-60$ picoseconds.[34], [35], [63] The timescale of dissociation for QDHs has been analyzed with the Braun-Onsager model to estimate a relatively large binding energy of 120 meV due to the strength of the Coulombic attraction between electrons and holes, which is dependent on the morphology and dielectric character of the system.[35], [53] Recent results bring this interpretation into question though.

In chapters 5 and 6, simultaneous UV and visible probe ultrafast transient absorption measurements were employed to answer the question of whether the intermediate state can truly be attributed to a CTS, and determine the factors affecting its lifetime. These studies include an additional sample with a varied processing of the ZnO to separate out how the ZnO surface chemistry affects the charge injection and intermediate state. UV probe transient absorption is an underutilized technique that probes the band gap dynamics of metal oxides directly, and is well suited to studying quantum dot sensitized metal oxides.[90] Electron injection results in state filling of the ZnO conduction band minimum, which bleaches the excitonic transition (3.4 eV).[90] Since CdSe has a band gap between 2 and 2.5 eV, the band

gap dynamics of the two materials are easily separated due to being spectrally distinct. UV probe spectroscopy at the band gap of ZnO does not have overlapping contributions from CdSe, as long as the difference in their band gaps is sufficiently large. Chapter 5 presents the results of this approach for a single QD size, while chapter 6 investigates the dependence of the intermediate state lifetime on the QD diameter.

Chapter 3

Methods and Characterization

This chapter presents the various synthetic methodologies and characterization techniques employed throughout this work. Section 3.1 details the synthetic recipes for the hydrothermal growth of ZnO nanorods, hot injection growth of CdSe nanocrystals, and the phase transfer and resulting sensitization of ZnO. Sections 3.2 and and 3.3 shows the full characterization of the bare ZnO and CdSe sensitized material, followed by the computational approach used to simulate X-ray absorption spectra in section 3.4. Section 3.5 presents the time resolved methodologies. Finally, section 3.6 gives the procedures applied to interpret the optical data presented in chapters 4 through 6.

3.1 Synthesis

3.1.1 ZnO Nanorods

The synthesis of an array of oriented ZnO nanorods begins with a seed layer of ZnO is deposited on two side polished 001-cut quartz purchased from MTI inc. (10 x 10 x 0.5 mm). The quartz substrate is first cleaned by sonication in acetone for 15 minutes, then sonication in ethanol for 15 minutes. 600 μ L of a 375 mM ethanolic solution of zinc acetate and ethanol amine was spin coated onto the cleaned quartz substrates at 3000 rpm over 45 seconds, which were then annealed in a clean tube furnace under argon. During annealing, the sample was first heated to 150 °C with a 10 °C/min ramp rate and held for 10 minutes, then heated to 400 °C and annealed for 20 minutes. The reaction vessel was cleaned with 1 M hydrochloric

acid, then washed with saturated sodium bicarbonate. This step is important to remove any ZnO crystals left behind from previous syntheses which can cause unwanted nucleation and irregular growth. The ZnO nanorods were grown in an aqueous 15 mM solution of Zn nitrate and hexmethylenetetramine (HMTA) at 90 C, for 45 minutes - 4 hours for 400 nm to 2 μm long nanorods, respectively. If desired, the nanorods were annealed after growth at 400 °C for 1 hour.

3.1.2 CdSe Quantum Dots

CdSe nanocrystals were synthesized similar to previously reported procedures.1-3 Cadmium oxide (CdO, 99.9%) and selenium (Se, 100 mesh, 99.999%), were obtained from Sigma Aldrich and used as received. Oleic acid (OA, 90%) and 1-octadecene (1-ODE, 90%) were obtained from Sigma Aldrich and used after purification by distillation. In a 50-mL, 3-neck flask, 300 mg CdO, 2 mL OA, and 20 mL 1-ODE were degassed under vacuum while stirring for 10 min. Nitrogen was introduced and the mixture was heated to 250 °C until the solution turned clear, signifying the formation of cadmium oleate. Upon turning clear, the temperature was reduced to 120 °C and 100 mg of Se powder was added via a solid addition funnel, and the solution was heated to 240 °C, leading the color to evolve from clear to yellow to orange indicating the nucleation and growth of CdSe quantum dots until the quantum dots reached the desired size. For 2.9 nm and 3.1 nm diameter quantum dots, solutions were removed from heat promptly upon reaching 240 °C or heated at 240 °C for 90 minutes respectively. Once the quantum dots reached the appropriate size, the heat was removed, and the reaction was quenched in a room-temperature oil bath. The CdSe quantum dots were purified in an N_2 filled glovebox by three cycles of precipitation and redissolution with a centrifuge at 7,000 rpm for 10 min using pentane as the solvent and ethanol as the antisolvent. [91]–[94]

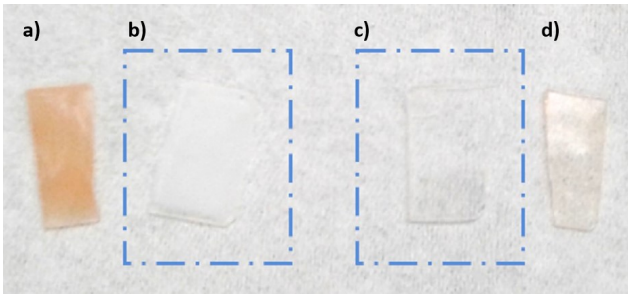

Figure 3.1: a) 4 hour growth nanorods sensitized with 2.7 nm CdSe. b) An image of ZnO nanorods after 4 hour growth and c) 45 minute growth. d) 45 minute grown ZnO sensitized with 2.7 nm CdSe.

3.1.3 Chemical Conjugation of CdSe and ZnO

The process of chemically linking QDs includes exchanging the native organic ligands with ligands that can coordinate to both QDs and a metal oxide. The moiety used to coordinate to the metal oxide is typically an oxygenic acid such as carboxylic acid, sulfonic acid, or phosphonic acid.[95], [96] MPA is a short chain molecule with a carboxylic acid for the metal oxide and a thiol to coordinate to the QD. This molecule is attractive for its simplicity and availability. The short length is ideal for maximizing electronic coupling, and therefore promoting charge injection. The thiol is also a very suitable coordinator for sulfur or selenium composed QDs. However swapping ligands on QDs and binding them to the surface of metal oxides is a defect inducing process. Deposition of QDs on the surface of a metal oxide can aggregate them, which can produce spurious signals from electronic coupling between QDs that must be carefully accounted for.[71] The use of Lewis acid ligands (or Z-type) can passivate surface defects though,[97]–[99] which limits surface trapping.

Exchanging the native organic ligands was done with a biphasic mixture of 100 μL MPA dissolved in water and 60 nmols of CdSe QDs dispersed in hexane. The mixture was shaken and lightly heated for 10 - 15 minutes, or until phase transfer had completed. The mixture was washed three times with hexane, then the QDs were aggregated with excess acetonitrile and centrifuged. After discarding the supernatant, the purified QDs were redispersed in 2-3 mLs of methanol or ethanol. Conjugation of the QDs with the ZnO was done by first heating

the ZnO in a vacuum oven at 70 C, then immediately immersing the ZnO in the QD solution. The mixture was kept at 50 C overnight, then the ZnO was washed with ethanol and stored under nitrogen in the dark.

Example samples are shown in 3.1a - d, for two growths of ZnO. The bare ZnO is cloudy white in the case of 4 hour growth seen in 3.1b, and clear in the case of 45 minute growth seen in 3.1c. Sensitized samples take on a light red color as shown in 3.1a and d.

Another chemical linker was also tested in addition to MPA which is sodium 1,2-dimercaptopropanesulfonate (DMPS), which is a sulfonate anchor group with a dithiol moiety that has been shown to improve the photostability of PbS QDs.[85] The sulfonate linker was seen to bind very strongly to TiO_2, and improved the stability of PdSe QDs (discussed in appendix B). The chemical conjugation between CdSe and ZnO followed the same biphasic exchange, purification, and conjugation as MPA. Opposite expectations though, time resolved experiments showed that the stability of this linker was less than MPA, which is discussed in chapter 5.

3.2 Electron Microscopy

3.2.1 Scanning Electron Microscopy

Scanning electron microscopy (SEM) was conducted on the Hitachi 4800 SEM, with a working distance of between 8.1 to 5.7 mm in ultra high resolution mode. The pictures shown in figure 3.2 employed mixed upper and lower detectors, or just the upper secondary electron detector for low working distance images. The accelerating voltage was 2 kV for high resolution, and 5 kV for wide view images. To avoid artifacts from charging samples were sputter coated with 5 nm of Pt. High resolution SEM images could not be obtained on the sensitized sample without sputter coating, which removes the ability to resolve QDs.

Figure 3.2 shows high and low magnification SEM images of the ZnO nanorods grown for 45 minutes,, which was studied in the optical transient absorption studies. These images

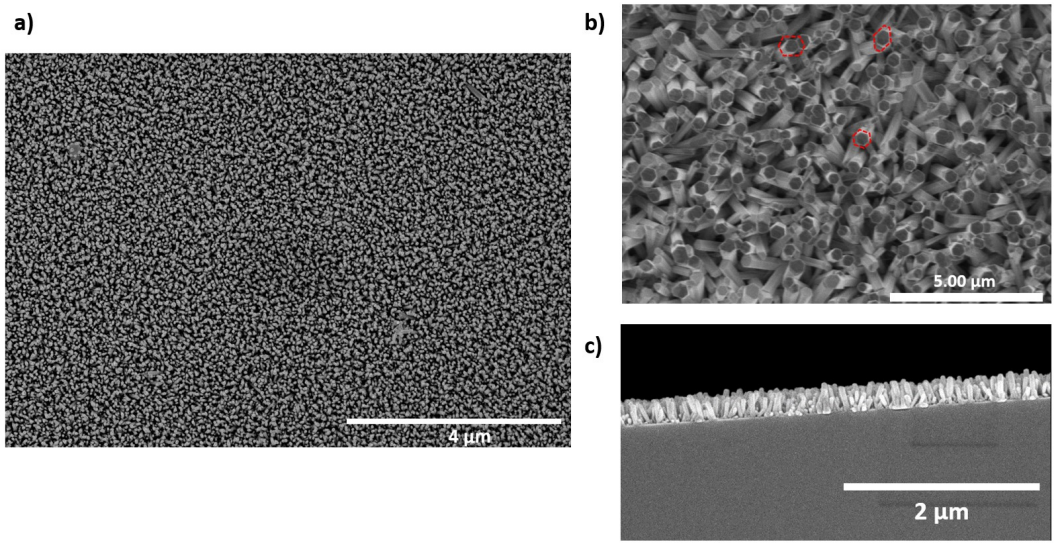

Figure 3.2: a) Widefield view of the ZnO nanorod samples with 45 minute growth time, at 12k magnification. b) Closeup view of the ZnO nanorods

were used to estimate the average nanorod density, length, and width. These values were estimated at 0.5 $\pm$0.1 μm long and 60 $\pm$10 nm in diameter wide. The nanorod density is 158 nanorods/μm^2. These values are used to estimate the surface area, and subsequently the quantum dot coverage, as described in section 3.3. Figure 3.2b highlights in red different hexagonal facets of the nanorods. The irregularity of these cross-sections could indicate that the nanorods have non-standard facets. It has been shown with Field Effect Scanning Electron Microscopy that hydrothermally grown, c-axis oriented nanorods form predominantly with side crystal planes of $[1\,0\,\bar{1}\,0]$ orientation.[100] However, both the $[1\,1\,\bar{2}\,0]$ and $[1\,0\,\bar{1}\,0]$ facets are fast growth facets and could give crystalline oriented nanorods, with similar surface energies.[101] The average tilt of the nanorods is $\sim 15^{\circ}$.

3.2.2 Transmission Electron Microscopy

Transmission electron microscopy (TEM) images were collected on a JEOL 2100 Cryo TEM with an accelerating voltage of 200 kV. The samples were prepared by scrubbing a bare or sensitized ZnO sample with tweezers, then applying a holey carbon supported on copper TEM grid.

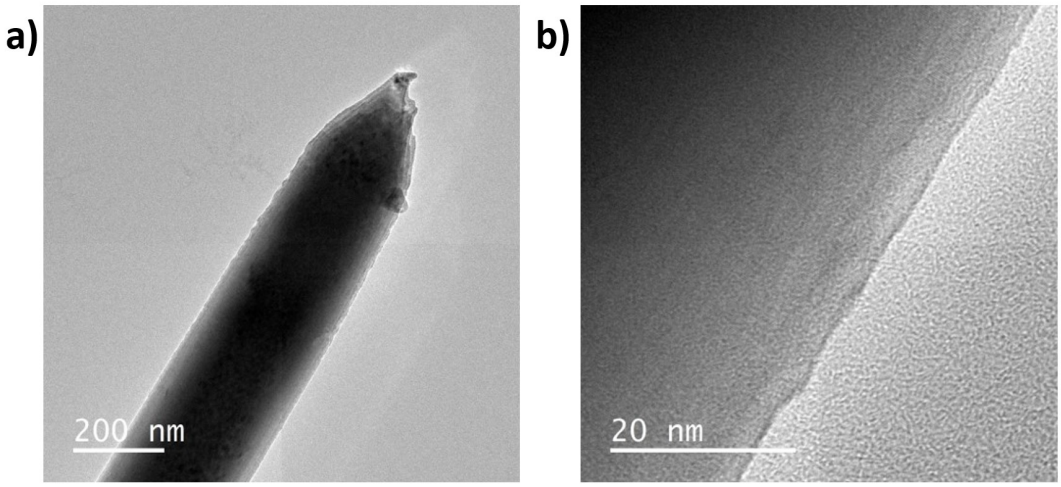

Figure 3.3: TEM images of broken ZnO nanorods deposited on a TEM grid at a) low magnification and b) high magnification.

Figure 3.3a and 3.3b show high resolution images of ZnO nanorods grown for 4 hours. SEM images from figure 3.2 show that the top of these rods have flat hexagonal faces, which is the terminating [0 0 0 1] facet. The tip seen in figure 3.3a is the portion of the nanorod grown from the seed layer connected to the quartz. Furrows can be seen running the length of the ZnO nanorod, which reflects the natural surface roughness of the $[1\,0\,\bar{1}\,0]$ facet.[65]

Figure 3.4 shows high resolution images of the CdSe sensitized ZnO nanorods. The ZnO in these images were grown for 1 hour, and were sensitized with 3.8 nm CdSe. Individual QDs are seen in red in 3.4b.

3.3 Spectroscopic Characterization

3.3.1 UV-Visible Absorption Spectroscopy

UV-Vis characterization was conducted on a Varian Cary 5G spectrometer. The spectra are taken with a blank measurement to eliminate matrix effects from contaminating the spectrum. Matching solvents and thickness were done in the case of solution phase measurements, or plain quartz in the case of ZnO solid state measurements. The traditional Beer-Lambert law

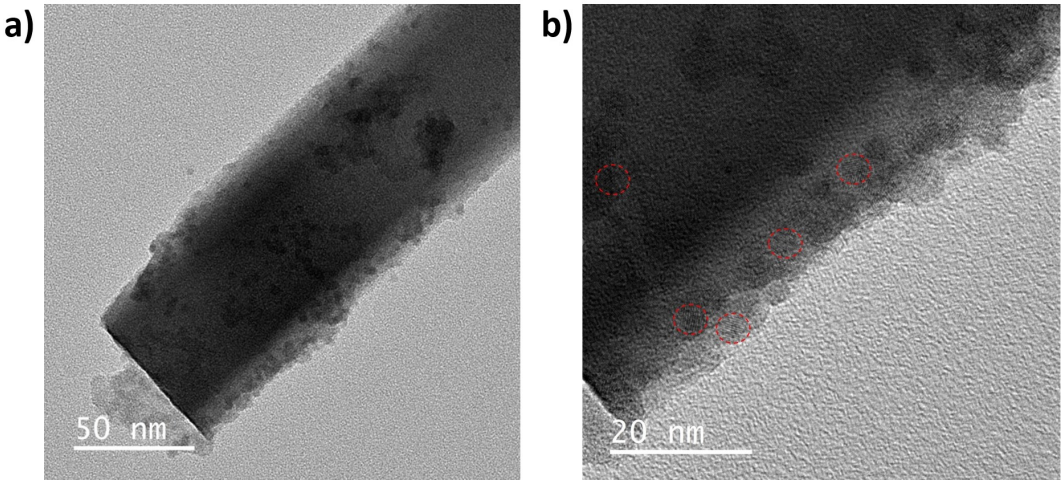

Figure 3.4: TEM images of broken ZnO nanorods, after sensitization with 3.9 nm CdSe QDs at a) low magnification and b) high magnification. Highlighted in red are individual QDs.

is given below:

$$\begin{aligned} I &= I_0 * e^{-l\epsilon c} \\ I/I_0 &= T = e^{-l\epsilon c} \\ OD &= ln(I/I_0) = -l\epsilon c \end{aligned} \tag{3.1}$$

QDs are unique in that their absorption at the excitonic transitions is dependent on the QD concentration, but transitions high above the band gap are dependent on the QD volume.[102] The absorption at the first excitonic transition is used to estimate the QD concentration, with the extinction coefficient estimated with equation 3.2. The size of each quantum dot sample was estimated with the position of the first excitonic transition according to equation 3.3:[102]

$$\epsilon = 155507 + 6.67054 * 10^{13} * e^{(-\lambda/0.10551)} \tag{3.2}$$

$$D(nm) = 59.60816 - 0.54736 * \lambda + 1.8873e^{-3} * \lambda^2 - 2.85743e^{-6} * \lambda^3 + 1.62974e^{-9}\lambda^4 \tag{3.3}$$

Where ϵ is the extinction coefficient, D is the diameter of the QDs in nanometers, and λ is the wavelength of the first excitonic transition. Figure 3.5a shows the dependence of the diameter and molar absorptivity on the position of the first excitonic transition. Figure

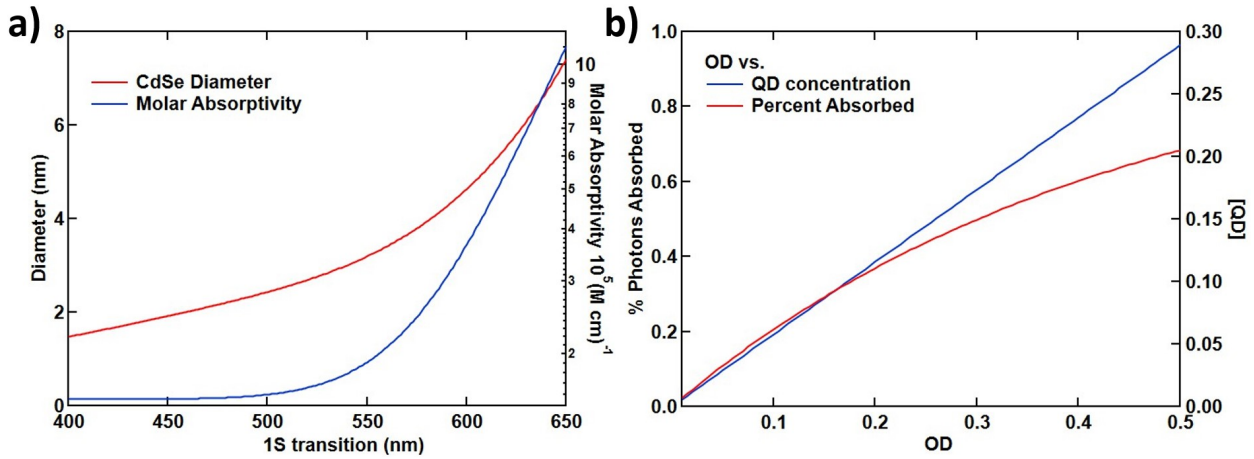

Figure 3.5: a) Change of CdSe molar absorptivity and diameter with position of 1st excitonic transition. b) Transmission and QD concentration change with OD. This relationship is linear for [QD] vs. OD.

3.5b shows the corresponding percent of photons absorbed and calculated concentration of the QDs on the OD of the solution. The OD varies linearly with the QD concentration, but this has a logarithmic relationship with the percent of photons absorbed. This will impact calculations of the average excitonic state, as described in section 3.5.1.

The band gap of ZnO was estimated with a Tauc plot by plotting the absorption spectrum as the square of the cross-section times the energy of the photon vs. the photon energy.[103], [104] The linear portion of the spectrum can then be fitted and extrapolated to intersect with the x-axis. The x-intercept gives the approximate band gap. This is shown in figure 3.6, with the band gap estimated to be 3.26 eV before annealing, and 3.22 eV after annealing. Band bending of the conduction band at the surface can reach a high enough magnitude to dip below the Fermi level, the removal of donors at the surface may red shift the optical band gap as the valence band renormalizes.

The results of sensitization with different QD sizes is shown in figure 3.7. Also shown is the spectra of the native oleic acid coated 2.6 nm CdSe compared to the MPA coated, phase-transferred CdSe. The CdSe shows no change in absorption spectrum during the ligand exchange and phase transfer aside from a slight solvatochromatic shift due to a change in the dielectric constant from toluene with an oleic acid coating, to methanol with

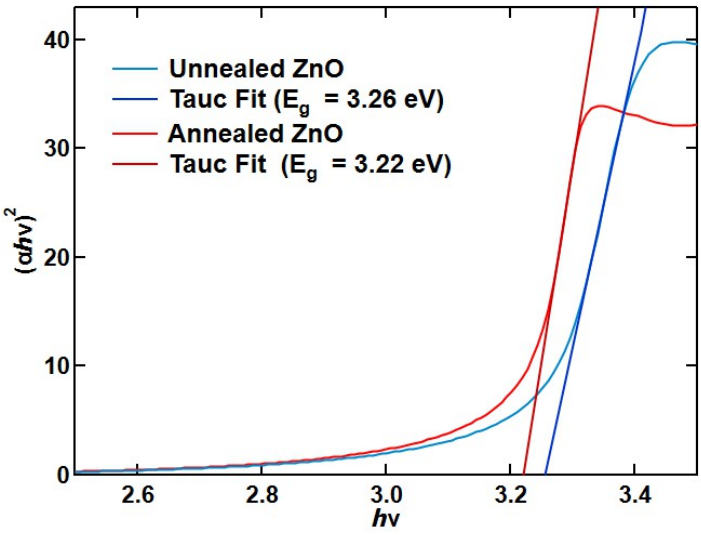

Figure 3.6: The Tauc plot for ZnO before (blue) and after annealing (red).

a mercaptopropionic acid coating. The solvatochromism is likely due to the impact of the altered dielectric function on the solvent image charge after exciton formation.[105] The size of the QDs is estimated with position of the first excitonic peak in toluene with equation 3.3. The sensitized ZnO features a sharp absorption onset at the band gap, along with an extended tail below the band gap, which is due to subbandgap states formed from crystalline disorder.[106], [107] The absorption difference between the unsensitized and sensitized ZnO at the CdSe excitonic peak was used to calculate the concentration of CdSe adsorbed to the ZnO, after aligning the baselines far below the peak absorption onset. A difference in baseline absorption can be attributed to adsorption induced disorder at the surface of ZnO.[108]–[110] With a survey of the ZnO nanorod dimensions, the QD coverage is estimated with equation 3.4:

$$\begin{aligned} Actual\ QDs\ nm^{-2} &= \frac{\Delta A * N_A}{\epsilon_{CdSe} * \rho_{ZnO} * SA_{ZnO}} \\ Ideal\ QDs\ nm^{-2} &= \frac{0.835}{D^2_{CdSe}} \\ \%Monolayer &= \frac{Actual}{Ideal} * 100 \end{aligned} \tag{3.4}$$

The actual density of QDs per square nm uses the absorption difference at the first

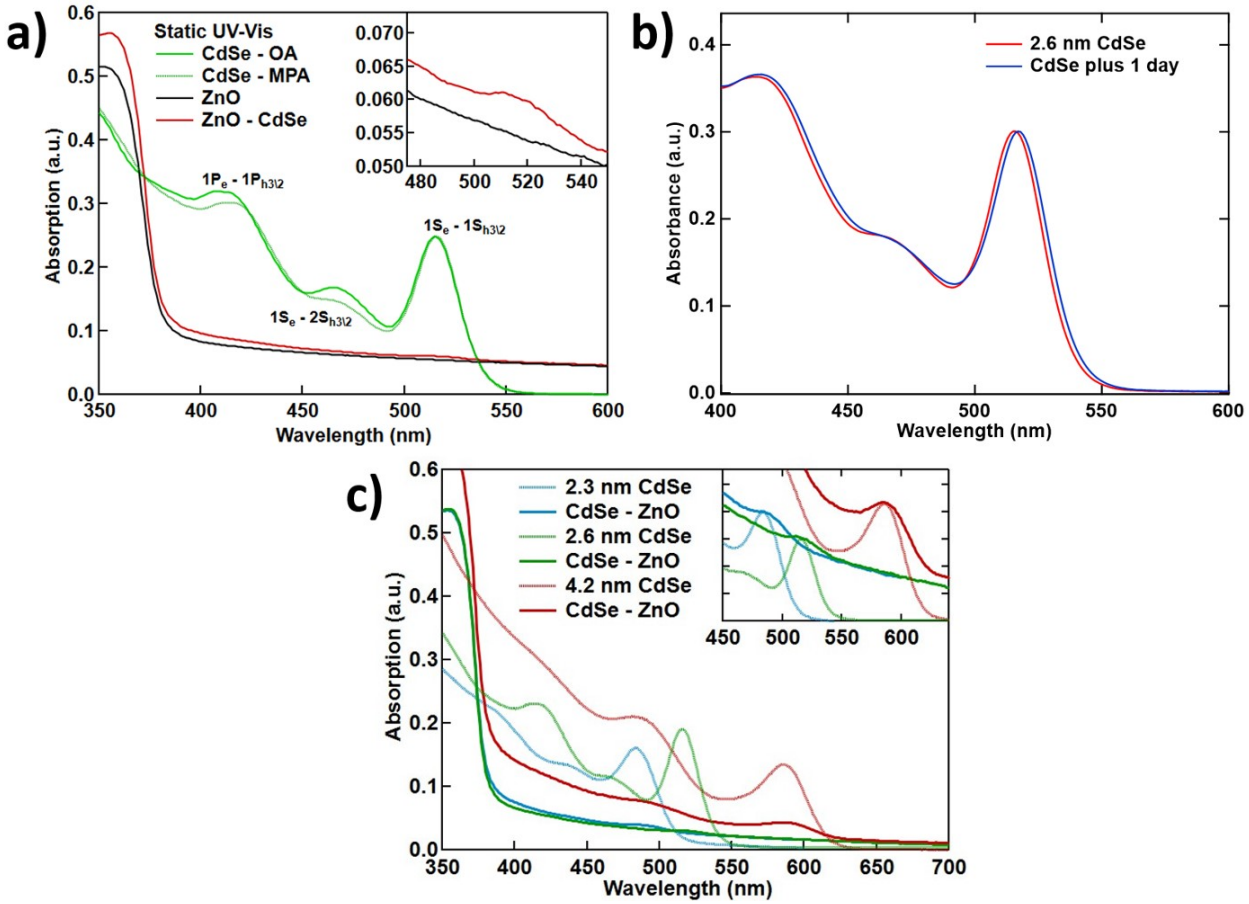

Figure 3.7: a) UV-Vis spectrum of 2.6 nm CdSe in hexane, with Oleic acid linker (solid green) and with MPA in methanol (dotted green). Labels denote the excitonic transitions. ZnO before sensitization (black) and after sensitization (red). The inset highlights the magnitude of the absorption change at the CdSe excitonic transition. b) CdSe in methanol is plotted (dotted) vs sensitized ZnO (solid) for each sample. 2.3 nm CdSe is plotted in blue, 2.6 nm in green, and 4.2 nm in red. The inset spotlights the alignment of the sensitized CdSe absorption against the solution phase transitions.

excitonic peak (ΔA) divided by the molar extinction coefficient (ϵ_{CdSe}) and multiplied by Avogadro's number. This value is then divided by the total surface area by taking the nanorod density per square micrometer (ρ_{ZnO}) multiplied by the average surface area of a nanorod (SA_{ZnO}). The ideal value is obtained by dividing a prefactor by the given quantum dot diameter squared (D^2_{CdSe}). The prefactor includes the necessary factors for the calculation of surface area required for close packed spheres. Thus, the percent monolayer is obtained by taking the actual QDs per square nanometer divided by the ideal times 100.

Aggregation of QDs is not expected to be an issue due to the stability of the quantum

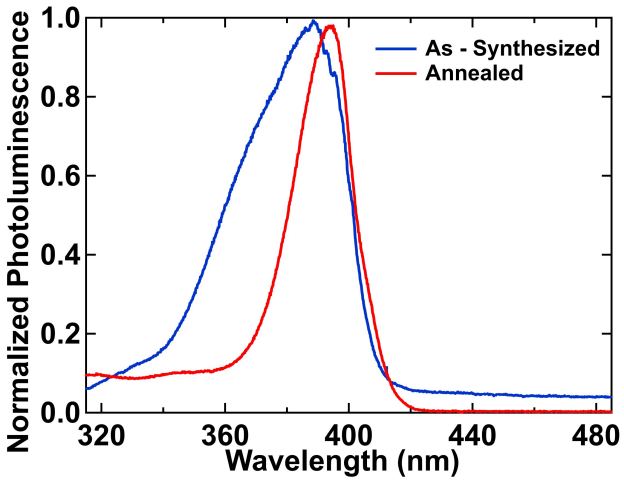

Figure 3.8: Photoluminescence of annealed (blue) and unannealed (red) ZnO. The shift of the emission peak matches the narrowing of the UV-Vis excitonic transition.

dot sensitizing solution confirmed with UV-Vis before and after sensitization, and the limited deposition of QDs on the surface of the ZnO.

3.3.2 Photoluminescence

Photoluminescence spectra were collected with a Horiba Jobin Yvon FluoroMax-3 fluorometer (excitation wavelength 532 nm), and decay curves were obtained by time-correlated single-photon counting (excitation wavelength: 532 nm, 120 ps pulse width, 3.13 MHz repetition rate, 200 μJ/cm^2).

Shown in figure 3.8 are static photoluminescence spectra of ZnO before and after annealing. The unannealed ZnO shows a broad emission peak at 385 nm. The annealed ZnO mirrors the shift in absorption shown in figure 3.6, where the emission peak shifts to the red. The annealed ZnO also shows a significantly narrower FWHM, indicating an increased crystallinity of the ZnO.

3.3.3 X-ray Absorption Spectroscopy

The ZnO XAS measurements were done at the Advanced Photon Source (APS), Argonne National Labs, at the 7-IDD beamline. The mode was 24 bunch filling with 109 mA ring

current, with a single Avalanche Photodiode Detector (APD) with Boxcar integration in total fluorescence yield mode. The X-ray spot was focused with a pair of Kirkpatrick-Baez mirrors to a 50 x 50 μm box-shaped spot. Normal incidence measurements oriented the c-axis of the ZnO perpendicular to the incident X-ray electric field. Diagonal incidence spectroscopy orients the nanorod c-axis at 45 degrees to the incident X-rays. The incident X-ray intensity is detected with an ion chamber filled with argon.

The APS produces X-rays by bringing electron bunches nearly to the speed of light and accelerating the electrons either by bending their trajectory, via bending magnet beamlines, or by inducing oscillating Lorentzian motion, with insertion devices that utilize periodic magnet arrays.

The X-ray cross-section is element dependent. The energy dependent absorption signal is defined by the Beer-Lambert law in the X-ray regime:

$$\begin{aligned} I &= I_0 e^{-\mu x} \\ \mu(E) &= \frac{ln(I_0/I)}{x} \end{aligned} \tag{3.5}$$

Where I_0 is the X-ray intensity before the sample, I is the intensity after the sample, μ is the absorption cross-section, and x is the thickness of the sample. The spectrum is detected via X-ray fluorescence of the sample. After excitation of the 1s core electron, a core hole is created. This hole is rapidly filled by a 2p electron, emitting Kα radiation which is then detected with an APD. The measured fluorescence intensity is quantified by:

$$I_f = I_0(\epsilon\Delta\Omega/4\pi) * \frac{\mu_x(E)[1 - e^{-(\mu_{tot}(E)/sin\theta + \mu_{tot}(E_f)/sin\phi)t}]}{\mu_{tot}(E)/sin\theta + \mu_{tot}(E_f)/sin\phi} \tag{3.6}$$

Which is a function of the solid angle of the detector, $\Delta\Omega$, as well as the path length of the incoming and emitted X-rays, $sin\theta$ and $sin\phi$ respectively. $\mu_{tot}(E)$ and $\mu_x(E)$ are the absorption cross-sections of the total sample and the target atom respectively at the incident X-ray energy, E, and fluoresced X-ray energy, E_f. ϵ is the radiative decay probability, and

t is the sample thickness. The spectrum can be significantly distorted by self-absorption for thick samples, $\mu t >> 1$, causing damping of the XAS features.[111]–[113] Equation 3.6 reduces significantly in the optically thin limit when $\mu t << 1$:

$$I_f \approx I_0 \epsilon \Delta\Omega / 4\pi * \mu_x(E) t \tag{3.7}$$

The fluorescence detected spectrum is then normalized by the edge jump, which converts the spectrum into the single atom spectrum.

3.3.4 X-ray Linear Dichroism

ZnO has a wurtzite crystal structure, which is anisotropic due to the elongated Zn - O bond along the c-axis. The linear dichroism of ZnO nanorods was interrogated with polarized X-rays, although polarization is not a necessity for linear dichroism. The evolution of the absorption cross-section with orientation is given below:[114]

$$\sigma^D(\hat{\epsilon}) = \sigma^D(0,0) - \frac{1}{\sqrt{2}}(3 * cos^2(\theta) - 1)\sigma^D(2,0) \tag{3.8}$$

Where $\sigma^D(\hat{\epsilon})$ is the dipole cross-section for a given orientation $\hat{\epsilon}$ of the X-ray electric field with respect to the ZnO crystal axis, at angle θ. $\sigma^D(0,0)$ is the isotropic tensor component, and $\sigma^D(2,0)$ is the dipolar tensor component.

3.3.4.1 XANES Analysis

The XAS data was processed using the X-ray Larch package, which includes fitting and subtraction of background above and below the white line, normalization of the edge jump, and flattening of the spectra.[115] The static XAS spectrum collected at incidence angles between 0 and 88°s is shown in figure 3.9. Monochromator glitches were removed at 9844 and 9846 eV, but weaker glitches remain as indicated with arrows in figure 3.9b. The ionization energy ($E0$) is set to 9662 eV for data processing. The pre-edge was background subtracted by

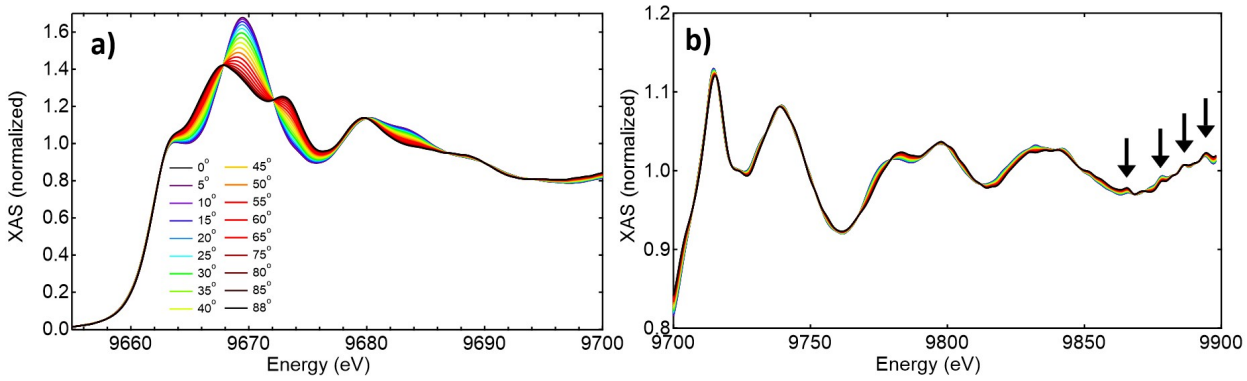

Figure 3.9: The X-ray linear dichroism is shown in the a) XANES and b) EXAFS regions from 0 to 88 °s.

fitting a linear function between -59 and -29 eV (relative to E0). The post-edge normalization energy range is set between 40.0 and 233.2 eV where a quadratic function is used to fit the post-edge baseline. Edge jump normalization is obtained by fitting the edge with a first order Victoreen function.

The XLD spectra are shown in figure 3.9. The XANES region shows two prominent isobestic points at 9667.8 eV and 9672.1 eV, along with a set at higher energies. The variation in the spectrum with angle reflects the high preferential orientation of the ZnO. The EXAFS region has lower sensitivity to the orientation of the nanorods since the photoelectron scattering is less sensitive to the bond geometry. However, the quality of orientation can still be extracted from the EXAFS region.

3.3.4.2 EXAFS Fitting

The EXAFS spectrum is defined by slowly oscillating signals >20 eV above the absorption edge. These oscillations are created from ejected photoelectrons scattering off nearby atoms interference with the absorption of X-rays at the absorbing atom. This interference is strongly dependent on the location and number of neighbor atoms, as well as on their Z number and local geometry. In this work the EXAFS fitting of the ZnO spectra was done simultaneously with the normal and diagonal incidence data. The scattering pathways were calculated with FEFF8, while the X-ray Larch python package was used to do the EXAFS fitting.[116], [117]

EXAFS analysis begins by extracting the momentum space signal from the XAS spectrum:

$$\chi(E) = \frac{\mu(E) - \mu_0(E)}{\mu_0(E)} \tag{3.9}$$

Where $\mu_0(E)$ is the smoothly varying background signal. $\chi(E)$ is then transformed into $\chi(k)$ by relating the energy to the momentum of the photoelectron via:

$$k = \sqrt{\frac{2m_e}{\hbar^2}(E - E_0)} \tag{3.10}$$

Where m_e is the mass of the electron, and E_0 is the edge of the XAS spectrum, traditionally defined as the max of the first derivative of the absorption spectrum. The EXAFS spectrum can then be analyzed in the context of a sum of scattering pathways:

$$\chi(k) = \Sigma_j \frac{N_j f_j(k) \exp^{-2R_j/\lambda(k)} \exp^{-2k^2\sigma_j^2}}{kR_j^2} sin\left[2kR_j + \delta_j(k)\right] \tag{3.11}$$

Where $f_j(k)$ is the scattering amplitude of the neighboring atom, j, and $\delta_j(k)$ is the phase shift of the scattered wave. Both of these factors are strongly dependent on the atomic mass of the scattering atom. $\lambda(k)$ is the mean free path of the photoelectron. These three factors can be calculated, and by fitting the spectrum to a summation of scattered paths we can extract the scattering length R_j, the coordination number of first (and sometimes second) shell atoms N_j, and the mean-square disorder of scattering atoms, σ_j^2, also known as the Debye-Waller (DW) factor. The dichroic nature in the EXAFS regime can be taken into account in the fitting by:

$$N_{app} = N\left(1 + \frac{I_{ord}}{2}(3cos^2\theta_1 - 1)(3cos^2\theta_2)\right) \tag{3.12}$$

Where N_{app} is the apparent coordination number, and θ_1 and θ_2 are the angles between the X-ray electric field and the crystal polar axis, and the X-ray field and single scattering pathway

Fitted EXAFS parameters	
S_0^2	0.831 (0.018)
ΔR: $Zn - O_{apical}$ (Å)	1.966 (0.002)
ΔR: $Zn - O_{equatorial}$ (Å)	1.958 (0.002)
ΔR: $Zn - Zn$ (Å)	3.191 (0.002)
I_{ord}	0.41 (0.07)
E_0 (eV)	-1.68 (0.17)
σ_O^2 (Å^2)	0.0043 (0.0005)
σ_{Zn}^2 (Å^2)	0.0066 (0.0005)

Table 3.1: Fitted EXAFS parameters for the XLD spectra of ZnO nanorods.

respectively. I_{ord} is a parameter describing the degree of nanorod orientation, with 1 being a perfectly oriented array and 0 being randomly distributed. Assuming a normal distribution, I_{ord} is related to the Half Width Half Max of the angular orientation distribution.[118], [119] Every spectra from 0 - 88°was fit simultaneously. The resulting fitted parameters are shown in table 3.1 The value of I_{ord} is 0.41 $\pm$ 0.07, which represents an angular distribution of 37 $\pm$ 1 °.

3.3.4.3 XAS Thermal Calibration

Transient XAS measurements require a high energy pulsed laser excitation, which often induces a thermal load on the sample that cannot be avoided. To address this, XAS temperature dependent spectra was collected at two angles, normal and diagonal incidence. The temperature dependent XAS spectra were analyzed in two ways: the first is by calculating a thermal transient signal, and the second is by fitting the EXAFS region to equation 3.12 to extract the impact of a heat jump on the crystal lattice. The calculation of the thermal transient signal is done by subtracting the ground state room temperature spectrum found in figure 3.9 from heated samples, which ranged from 10 °C to 300 °C.

Figure 3.10a and b shows the temperature dependent static spectra in the XANES and EXAFS region. The thermal difference spectra are shown in c-d. The largest amplitude changes occur at the white line and in the EXAFS region. The bond length changes and DW factors could be accurately extracted by simultaneously fitting the normal and diagonal

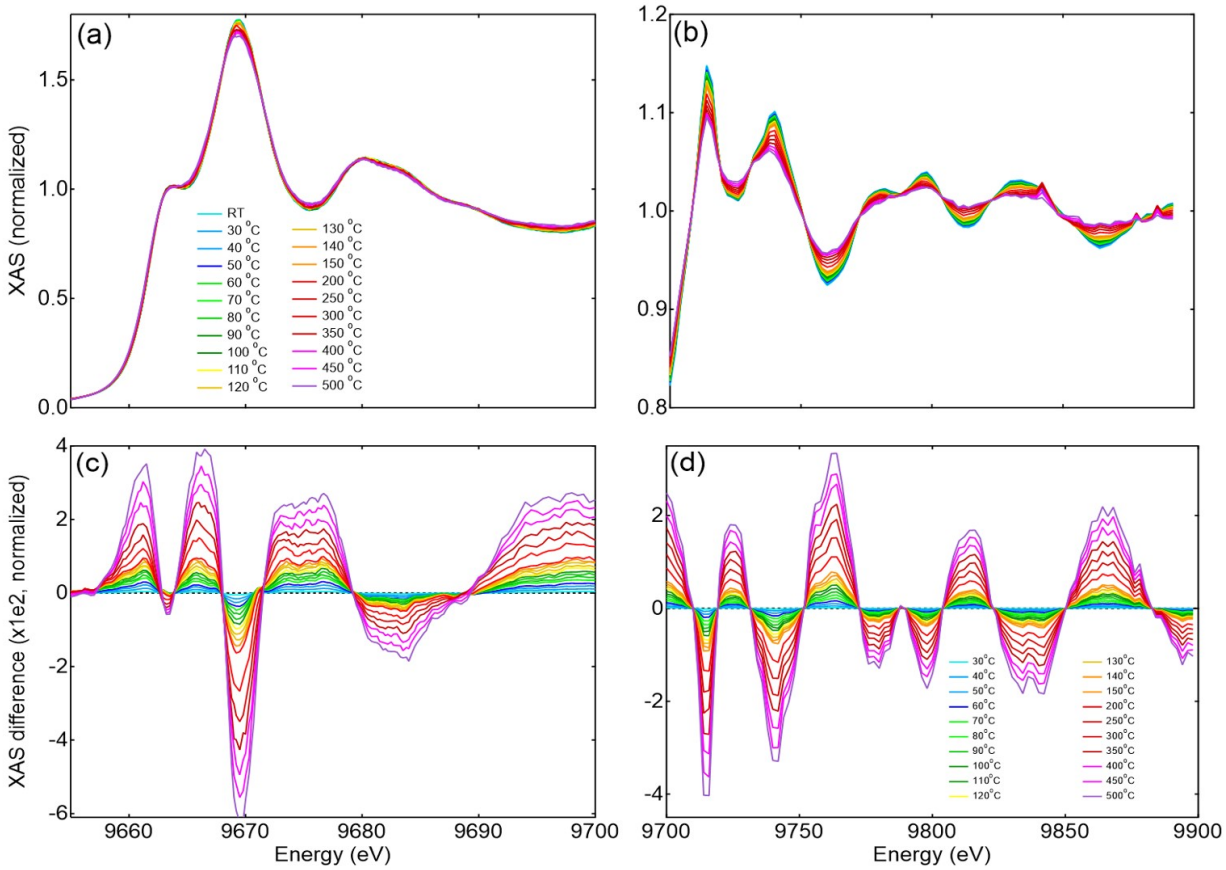

Figure 3.10: Temperature dependent X-ray absorption spectra at normal incidence in a) the XANES region and b) the EXAFS region. The thermal difference spectra calculated as with room temperature as the ground state in the c) XANES and d) EXAFS.

spectra at each temperature. However, there is a negligible change in the Zn-O bond length with temperature potentially due to intrinsic strain in the ZnO nanorods from their epitaxial connection to quartz. Thus, the dominant factor at high temperatures is an increase of the isotropic DW factor, which is reflected in severely damped EXAFS oscillations with no observable phase shift. The extracted DW factors for zinc and oxygen are shown in figure 3.11, where good agreement is found for the Zinc DW factor but large divergence of the Oxygen DW factor compared to literature measurements.

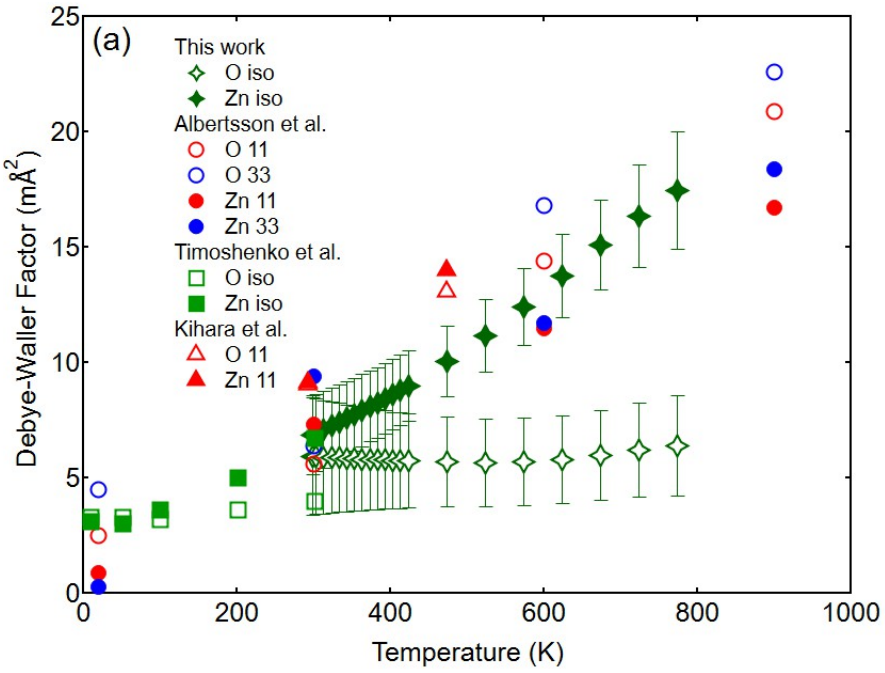

Figure 3.11: Variation of the isotropic DW factor for Zinc and Oxygen atoms vs. temperature for ZnO. Plotted against literature references [120]–[122]

3.3.5 X-ray Diffraction

X-ray diffraction measurements were taken on a Bruker D8 ADVANCE diffractometer with a Mo-Kα radiation source and a 2D Eiger2 R 500 K detector. The diffraction pattern is shown in figure 3.12 for oriented and unoriented samples. The oriented sample shows a single strong peak at ~ 34 °, which is assigned to the (002) reflection of the wurtzite nanorods. The (100) and (101) reflections are strongly damped as a result of the preferential orientation. Each peak has a double structure, which is due to the $K_{\alpha 1}$ and $K_{\alpha 2}$ radiation.

3.3.6 X-ray Photoelectron Spectroscopy

XPS measurements were performed with a Kratos Axis Ultra X-ray photoelectron spectrometer with monochromatic 210 W Al $K\alpha$ excitation (14 kV, 15 mA). The spectra were processed with the Casa XPS software. The carbon 1s photoemission peak at a binding energy reveals a low concentration of adsorbed organic molecules. This shows that the organic compounds

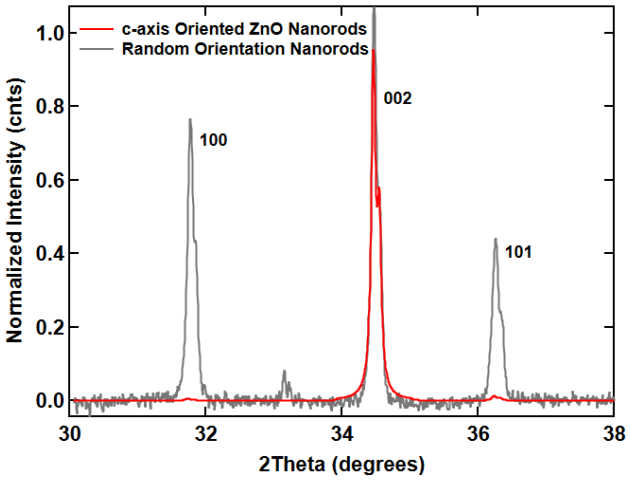

Figure 3.12: X-ray diffraction of oriented ZnO nanorods (red) and randomly oriented nanorods (black).

used as surfactant molecules or in the metal oxide precursors during the synthesis remain at the nanorod surface in some low concentration. The two peaks in the O 1s photoemission are usually assigned to surface oxygens (hydroxyls) and bulk-like oxygens with comparable intensities due to the surface sensitivity of XPS. Oxygen defects within the bulk provide a third peak at higher binding energies, which is observed in the low growth time samples.

Annealing the ZnO at high temperature improves the crystallinity of the nanorods, and has been shown to remove adsorbed surface contaminants. Since these nanorods are well oriented with their c-axis oriented normal to the crystal substrate, the [0 0 0 1] facet is the dominant facet observed by XPS, with other facets also seen at an oblique angle. Contrary to a and m-plane ZnO, contaminants adsorbed on the Zn-terminated [0 0 0 1] surface are stable up to 700 °C. The carbon 1s peak intensity decreases substantially after annealing, which is confirmed by the elemental ratios. Before annealing the atomic ratios are 39.5% carbon, 44% oxygen, and 16.5% zinc. After annealing the amount of oxygen increases to account for 50.1%, and zinc increases to account for 23.8%, while carbon decreased to 26.1%. Annealing has thus not completely removed the organic contaminants.

The C 1s photoelectron peak was used to calibrate the energy of the O 1s and Zn 3d measurements, which are shown in figure 3.13a and 3.13b respectively. At the oxygen 1s peak,

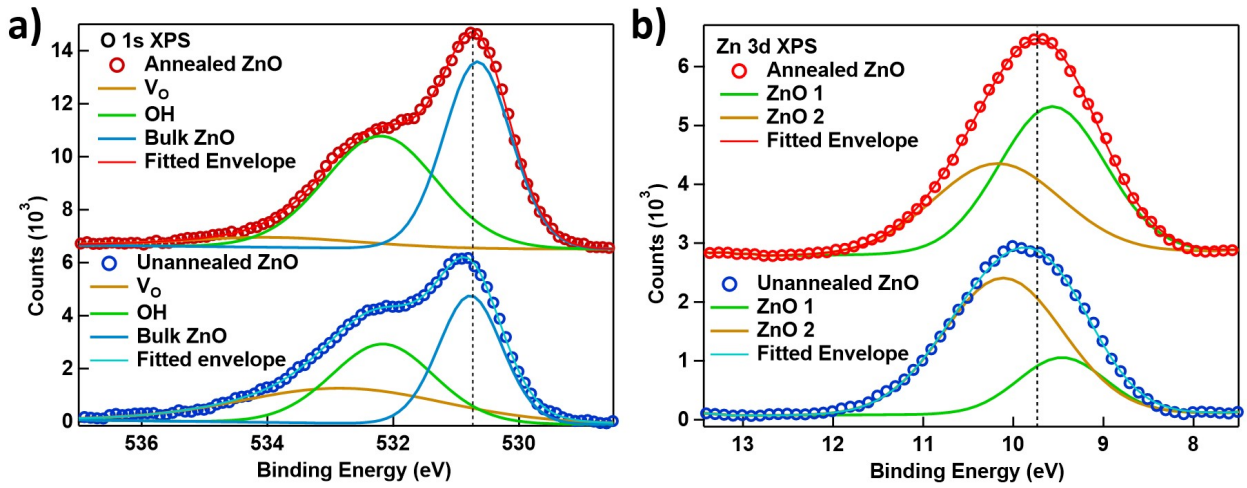

Figure 3.13: XPS data in ZnO nanorods grown for 45 minutes at the a) oxygen 1s edge, before and after annealing (blue and red), and with fittings to three gaussian peaks to account for oxygen vacancies (orange), hydroxide surface species (green), and bulk oxygen (teal). b) XPS data at the zinc 3d edge, before and after annealing (blue and red), and fitted to two Gaussian peaks. Annealed Spectra are offset vertically for clarity.

the signal can be fit to a sum of three Gaussian functions, which are attributed to oxygen defects, adsorbed hydroxides, and lattice bound oxygen.[123] Oxygen defects are not always observed in these samples when grown for longer times. However, when grown for 45 minutes the nanorods are susceptible to a higher defect concentration on the surface. The contribution of defect states and hydroxides decreases after annealing, matching the reduction in organic contaminants. The Zn 3d peak could be adequately fit with a sum of two Gaussian functions, which likely represents the different exposed facets. A single, skewed Gaussian could not account for the shape of the signal. A simple linear background subtraction was applied at the Zn 3d edge, and a U 2 Tougaard background was applied at the O 1s edge.[124] The peak position and contribution of each fitted component is shown in table 3.2 for the Zn 3d measurements, and table 3.3 for the O 1s measurements.

The Zn 3d character shows a shift of ∼120 meV to lower binding energies after annealing. As has been interpreted in references [63], [64], the difference at the 3d position is attributed to a reduction in the downward band bending of the valence and conduction bands near the surface. This is a lower magnitude difference than seen in previous papers on single

Fitted Zn 3d XPS parameters				
Material	$E1_{center}$ (FWHM)	E1 Area	$E2_{center}$ (FWHM)	E2 Area
Unannealed ZnO	9.46 eV (1.13 eV)	230.8	10.11 eV (1.56 eV)	766.5
Annealed ZnO	9.56 eV (1.39 eV)	734.3	10.18 eV (1.66 eV)	540.8

Table 3.2: Fitted XPS parameters for the Zn 3d for both annealed and unannealed samples.

Fitted O 1s XPS parameters						
Material	$E1_{center}$ (FWHM)	E1 Area	$E2_{center}$ (FWHM)	E2 Area	$E3_{center}$ (FWHM)	E3 area
Unannealed ZnO	530.8 eV (1.2 eV)	2084.4 eV	532.2 eV (1.9 eV)	2084.4	532.8 eV (3.9 eV)	1845 eV
Annealed ZnO	530.7 eV (1.3 eV)	3215.5 eV	532.2 eV (2.1 eV)	3212.5	533.9 eV (3.4 eV)	451.8 eV

Table 3.3: Fitted XPS parameters for O 1s for both annealed and unannealed samples.

crystal ZnO for this treatment.[63], [64] This can be attributed partially to the higher thermal stability of adsorbants on the exposed [0 0 0 1] facet. In addition the annealing was done under flowing argon rather than UHV.

3.4 Finite Difference Method for X-ray Near Edge Structure

XAS at the Zn K-edge is computed in real-space with the finite difference method (FDM) in the XANES and the full multiple scattering (FMS) in the EXAFS as implemented in FDMNES in the dipole approximation.[125] Table 3.4 gives the crystal parameters used for the calculations. The calculations are self-consistent with the Hedin-Lundqvist exchange correlation potential.[126]

Figure 3.14 shows the evolution of the calculated XANES with the cluster size. A converged cluster size is achieved for 8.10 Å in radius (183 atoms). The convergence was monitored by comparison with the static spectra, the position of the Fermi Level, and the Kohn-Sham energies for the zinc and oxygen atoms. The ground state electronic structure

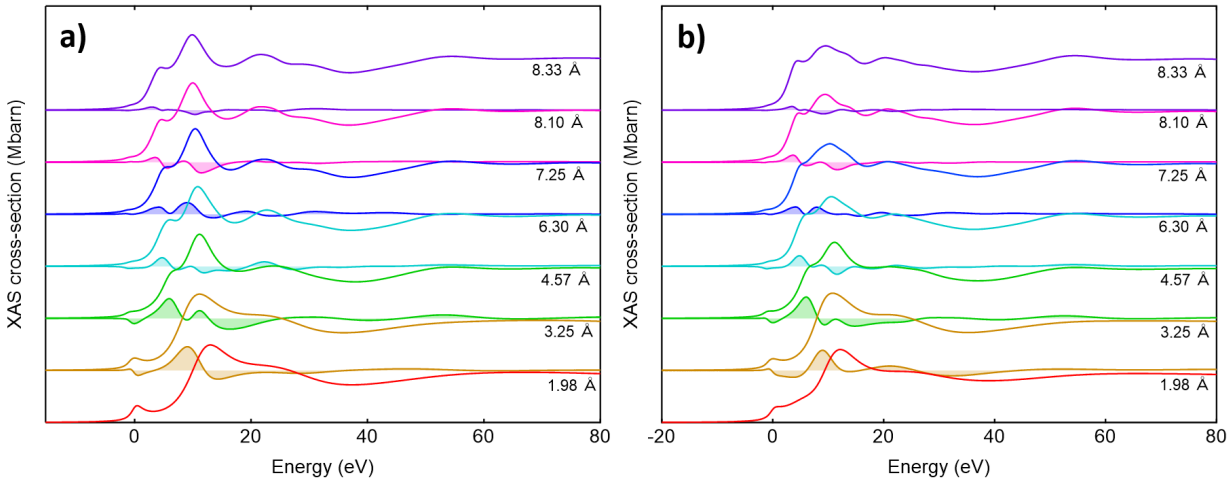

Figure 3.14: Radial convergence of FDMNES spectra at a) normal and b) diagonal incidence. Distances represent the radius of the real space DFT cluster with the absorbing atom at the center.

of Zn and O are used as the starting point for the DFT calculations. A partially screened core-hole (0.8) is required to improve the experimental agreement close to the edge. The keyword "Energpho" is used to convert from an energy axis relative to the Fermi level to an energy scale compatible with the photon energy by addition of the absorbing atom 1s electron ionization potential (9659 eV). The calculated XAS is convoluted with an energy-dependent arctan function implemented in FDMNES to account for the core-hole lifetime broadening according to:

$$\Gamma = \Gamma_0 + \Gamma_m \left(\frac{1}{2} + \frac{1}{\pi} \left(\frac{\pi}{3} \frac{\Gamma_m}{E_l} (e - \frac{1}{e^2}) \right) \right) \tag{3.13}$$

with $e = (E - E_f)/Ec$ and E_f being the Fermi energy. The parameters used for best

FDMNES Crystallographic Parameters	
Space Group	P63mc (186)
a	3.253 Å
c	5.194 Å
α	90 °
γ	120 °

Table 3.4: Crystallographic parameters used for ab initio simulations of the XANES and EXAFS spectra.

agreement with the static spectra are G_0 = 1.67 eV FWHM (bare Zn core-hole lifetime), G_m = 4.5 eV, E_c = 16 eV, and E_l = 13 eV. Calculations without core-hole in the final state of the transition matrix elements are performed with the "NonExc" keyword. Default calculations include a core-hole in the 1s orbital of the absorbing atom in the final state.

3.5 Time-Resolved Spectroscopy

3.5.1 Quantum Dot Excitonic Population

The number of photoexcited excitons per quantum dot is calculated according to equation 3.14, which is used to determine relevant fluence ranges for each sample:

$$< N >= \frac{\phi(1 - 10^{-OD_{pump}})}{[QD] * V_{interaction} * N_{Avogadro}} \tag{3.14}$$

where <N> is the average exciton population per QD, ϕ is the photon flux in photons/pulse, OD_{pump} is the OD of the sample at the pump wavelength, $[QD]$ is the QD concentration, and $V_{interaction}$ is the interaction volume of the pump laser with the sample, and $N_{Avogadro}$ is Avogadro's number. The photon flux is determined by converting the peak power per pulse to photons per pulse. $V_{interaction}$ is calculated by taking the spot size of the laser (measured on single experiment basis) and multiplying by the ZnO nanorod length, estimated at 0.4 μm from SEM images. From <N>, the distribution of excitonic states can be calculated with Poisson statistics according to equation 3.15:

$$\begin{aligned} N_i &= \frac{< N >^i * e^{-<N>}}{i!} \\ N_2 &= 1 - \sum_{n=0}^{i} N_i \\ N_{i>2} &= 0 \end{aligned} \tag{3.15}$$

N_i is the fraction of QDs with a given i excitonic state, and N_2 is the doubly excited state.

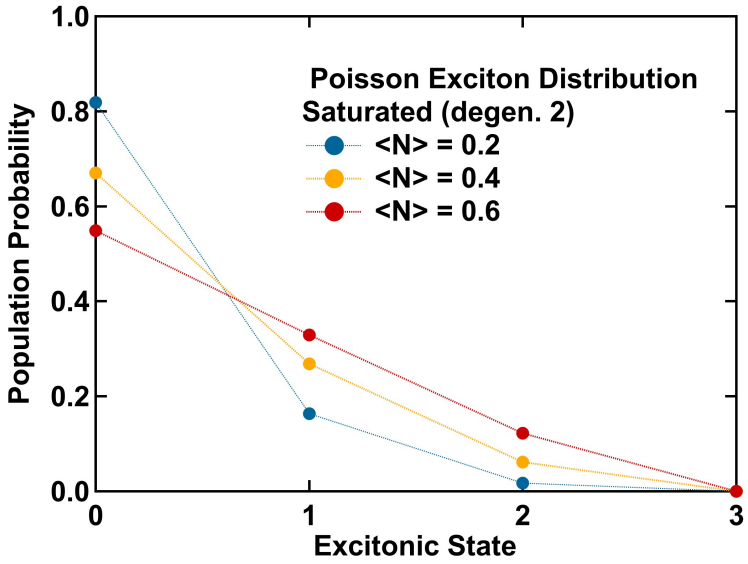

Figure 3.15: Population of excitonic states 0 - 3 for the saturated Poisson distribution.

The band edge degeneracy can be taken into account by requiring the sum of populations from N=0 to N=2 to equal 1, ($\sum_{n=0}^{2} N_i = 1$).[127] For excitations less than 1 photon per quantum dot the majority of QDs are unexcited, as shown in figure 3.15. Even at low excitations though, an appreciable number of multi-excitonic states can be expected. XAS feasibility experiments target a high <N> up to 1, while optical probe charge injection experiments target an <N> of 0.2, which gives 1.75% of QDs being doubly excited, with 16.4% of QDs being singly excited. QDs with biexcitonic states then compose approximately 10% of the excited QD states, which can account for as much as 20% of the total signal at the band gap. Since the spectrum changes rapidly due to charge transfer, it is not possible to disentangle the multiexcitonic dynamics. <N> of 0.2 is the lowest excitation achievable considering experimental constraints (e.g. QD concentration, laser power stability, and signal amplitude).

Figure 3.16 shows the dependence of <N> on QD concentration, OD, and fluence. This relationship is not always self-evident due to the linear relationship between concentration and OD, but the logarithmic relationship between OD and transmission. Figure 3.16a shows how a higher quantum dot concentration requires a higher fluence for the same target excitation. Figure 3.16b shows an alternative view where for a given fluence, varying the quantum dot

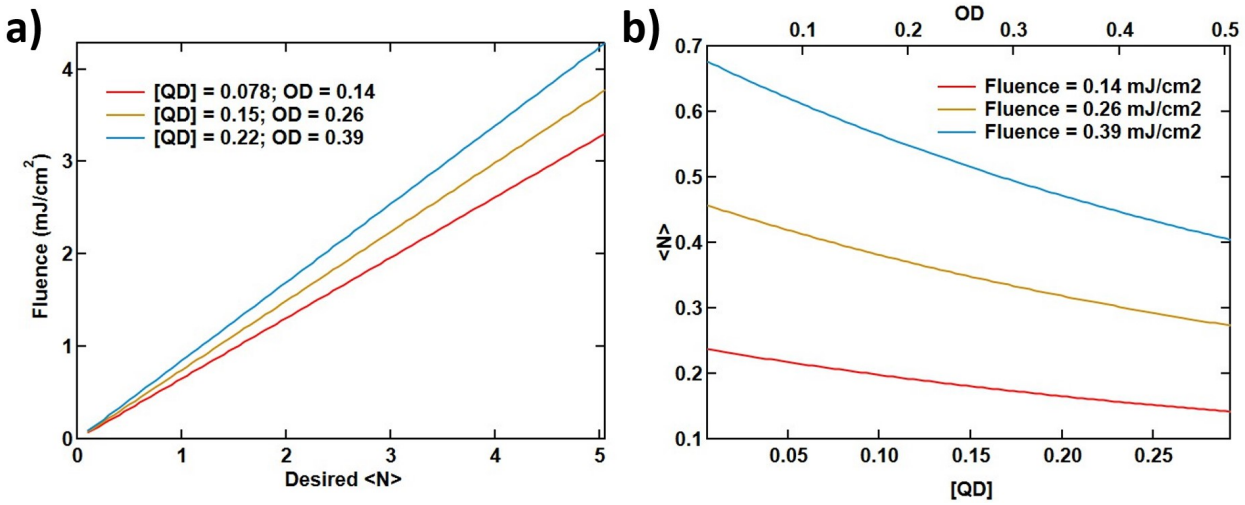

Figure 3.16: Dependence of <N>on QD concentration and fluence for different parameters. a) Necessary fluence needed for a desired <N>, for different [QD] and subsequent ODs. b) For given fluences, how <N>varies with [QD].

concentration results in nonlinear decrease of the average excitation.

3.5.2 Picosecond-Resolved X-ray spectroscopy

For X-ray transient absorption experiments, the X-ray penetration depth above the Zn K-edge is $\sim 8.5\mu$ms, which allows the use of thick samples to increase the signal.[128] The penetration depth during optical absorption experiments is much lower, and requires nanorods on the order of 500 nm in order to allow sufficient probe photons through. Transient X-ray absorption was conducted concurrently with static XAS at the APS. A Duetto laser operating at 1.3 MHz delivered up to 10 μJ per pulse at 355 nm, with 10 ps duration. The full experimental setup is described in reference [129], and illustrated in figure 3.17c.The time resolved XAS signal, detected in fluoresecence, is given by:

$$\Delta I_f = (I_{f,ON} - I_{f,OFF})/I_0 \tag{3.16}$$

Where $I_{f,ON}$ is the detected fluoresecence intensity of the laser on pulse, and $I_{f,OFF}$ is the laser off pulse. The absorbed fluence was between 1 and 7 mJ/cm^2 (calculated with $1/e^2$

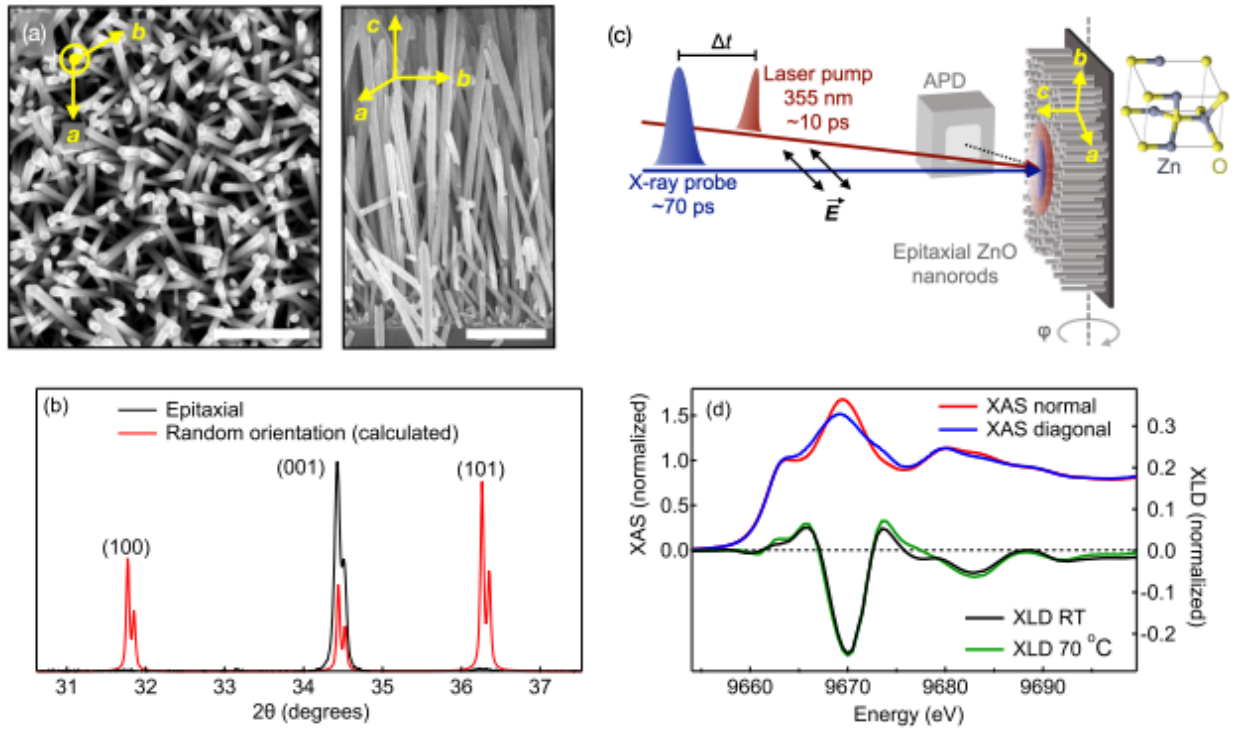

Figure 3.17: Combined experimental setup for transient XAS. a) SEM images of 2 μm long ZnO nanorods. b) XRD graph of oriented nanorods (black) plotted against a randomly oriented calculation (red). c) Polarization of time resolved setup between the X-rays and Laser, along with position of APD. Also included is the axis around which ZnO is rotated to obtain XLD spectra. d) Static XAS at normal (red) and diagonal (blue) incidence, plotted against the XLD spectra at room temperature (black) and 70 °C (green). Reproduced from reference [73].

diameter). The excited carrier concentration was calculated with equation 3.17 and estimated 100 ps after excitation, and shown in table 3.5.[73] The scans were averaged from a few hours to a full day, depending on the amplitude of the structural and electronic distortions created by photoexcitation.

$$n_{CarrierDensity} = \frac{(1-R) * F * f}{h\nu\lambda e} \tag{3.17}$$

Where R is the reflectivity (estimated at 0.24), F is the fluence in mJ/cm^2 calculated with the $1/e^2$ definition of spot size, f is the filling factor which accounts for the reduced coverage of ZnO on the substrate surface (estimated at 0.1 from SEM images), and $h\nu$ is the photon energy. λ is the penetration depth of the 355 nm laser, which is $\approx 111nm$. Since the ZnO

Table 1		
Fluence @ 355 nm	Carrier Concentration	Mott Density [22], [130], [131]
0.2 mJ/cm2	8.8e17 cm^{-3}	1.51e18 cm^{-3}
3.0 mJ/cm2	1.5e19	5.95e18
7.3 mJ/cm2	3.6e19	3.7e19

Table 3.5: Fluence vs carrier concentration from the April 2020 beamtime at the Advanced Photon Source, Argonne National Labs, calculated with equation 3.17. The reflectivity is estimated at 0.24 for a 2 μm thick sample of ZnO nanorods, oriented with c-axis perpendicular to incoming light.

nanorods are much longer than the penetration depth (1 - 2 μm), all the incoming radiation is assumed to be absorbed. The shortest recombination time constant estimated from the literature is 100 ps, which means the carrier concentration has fallen by 1/e (36%) over that time period.[132] These values are important in the context of chapter 5 Table 3.5 includes a few estimations of the Mott density. The Mott density is the threshold carrier concentration at which Coulombic screening is large enough to prevent the formation of excitons. This has important implications for a charge injection study because, as a general observation, it is near impossible to surpass the Mott density through charge injection unless the system is electrically driven. This is due to the fact that as carriers are injected, the chemical potential is driven higher,[130] and unless the driving force is very large the conduction band potential of ZnO will be greater than the photoexcited carrier potential in CdSe. Typically this is not a concern as the density of states in the CB is large enough that moderate amounts of charge injection have limited feedback on further charge injection. In addition, charge injection usually occurs through a tunnelling type mechanism, which is limited by the driving force and needs to take into account surface defect states to properly estimate.[5], [133], [134] As seen in table 3.5, the carrier concentration at which phase space filling was observed is just below the most conservative estimate of the Mott density, indicating that it is possible to reach this level of signal through charge injection.

The transient XLD signal employed in chapter 4 can be formalized with:

$$\Delta XTA = XTA_V - XTA_\perp = [XAS_V(T', s_V) - XAS_V] - [XAS_\perp(T', s_\perp) - XAS_\perp] \quad (3.18)$$

Where V and $\perp$ indicate diagonal and normal incidence respectively. For equivalent excitations the thermal impact will be equivalent, and denoted with T'. We assume here that the effect of screening on the XAS signal is anisotropic, and depends on the angle of incidence, and is given with s_V and $s_\perp$.

$$\begin{aligned} XLD &= XAS_V - XAS_\perp \\ \Delta XTA &= -XLD + XAS_V(T', s_V) - XAS_\perp(T', s_\perp) \end{aligned} \quad (3.19)$$

Where XLD is the static dichroism signal. The transient signal at normal and diagonal incidence ($XAS_\perp/XAS_V$) is then a difference of the inverse XLD signal. The XAS is split into the two contributions:

$$\Delta XTA = -XLD + XAS_V(T') - XAS_\perp(T') + XAS_V(s_V) - XAS_\perp(s_\perp) \quad (3.20)$$

As described in section 3.3.4.3, the transient thermal effects are provided by termperature based XAS measurements. From this, we find that the XLD is independent of temperature up to 70 °C. Then $XAS_V(T') - XAS_\perp(T')$ is approximately equal to the static XLD and leaves only the difference in screening:

$$\Delta XTA = XAS_V(s_V) - XAS_\perp(s_\perp) = \alpha XLD = \alpha(XAS_V - XAS_\perp) \quad (3.21)$$

with $\alpha < 0$. The proportionality constant indicates that the screening effect scales with the amplitude of ground state XAS. For instance, the white line at normal incidence has a greater absorption crossection indicating that the screening bleach is more pronounced at normal incidence than at diagonal incidence and gives $\alpha(XAS_V - XAS_\perp) > 0$. The opposite

is true for the features on either side of this feature at diagonal incidence, where the stronger absorption at diagonal incidence leads to a bleached feature instead.

3.5.3 Femtosecond-Resolved Optical Spectroscopy

Optical transient absorption experiments were done at the Materials Research Laboratory (MRL) at the University of Illinois Champaign - Urbana, Urbana. A regenerative Ti:Sapphire Spitfire laser was used to produce 2.4 W, 130 fs long pulses at 800 nm. These pulses were directed into NIR-UVIS Twins OPA. Half the pump laser is directed out of the OPA, which is then used to generate a white light continuum for the probe. The probe 800 nm light is directed from the OPA into a BBO (Thorlabs) to produce 400 nm light, which is then focused into a 1 mm thick CaF2 window to produce a spectrum of 400 - 250 nm light, or the BBO can be bypassed and the 800 nm light can be directly focused into the CaF2 to produce a spectrum from 750 - 350 nm. The 800 nm pump pulse was polarized at magic angle for all experiments, and accompanied with a broad band polarizer after the sample to account for the differential dispersion of the optics along the beampath.[135], [136] The OPA - NIRUVIS twins generates a pump pulse at 300 or 535 nm, with fluences between 0.005 and 10 mJ/cm^2. The pump pulses are directed through a chopper operating at 500 Hz, and focused onto the sample position. Spatial overlap and spot size estimation of the pump and probe beams is done with a Gentec Beamage 3.0 high speed profiler. The probe spot size is typically 15 μm x 15 μm, and the pump spot size is 100 μm x 60 μm. A large pump spot is used to allow the fluence to be estimated by the peak fluence, which is a more consistent definition and defined as twice the fluence calculated with $1/e^2$ spot size diameter. The two-photon absorption (2PA) absorption feature of ZnO was used to determine temporal overlap, using a high pump fluence and late delay times. The group velocity dispersion (GVD) induced by the variable velocity of probe wavelengths through the sample was corrected by fitting a third order polynomial to the wavelength dependent time - zero, as determined from the pump induced cross-phase modulation of a high fluence scan on bare quartz. Time zero is

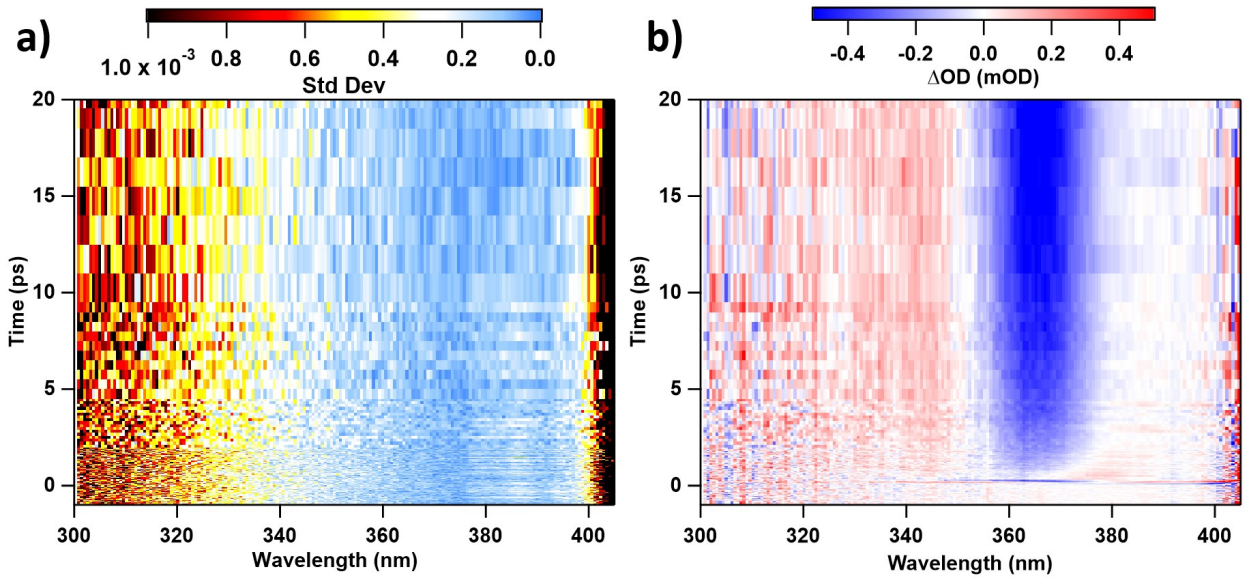

Figure 3.18: a) The standard deviation of each point in a typical UV-probe measurement of 2.6 nm CdSe - ZnO sample, and b) the matching 2D OTA spectrum. The sample was pumped at 515 nm with 20 μJ/cm^2, and had a signal strength of approximately 500 μ OD at 365 nm, after 100 picoseconds. The homogeneity of the standard deviation at all time points and wavelengths shows the stability of the signal over multiple scans.

then aligned across all wavelengths. Background signals are removed by subtracting the average of 10 pre-time zero data points from the post time-zero spectrum, both before and after GVD correction. The instrument response function (IRF) determines the minimum timescale where features can be accurately assessed. It is a Gaussian convolution of the transient signal, which is typically evaluated with a measurement of cross-phase modulation, which is dependent on the temporal overlap of the pump and probe pulses. The IRF is in the range 120 - 150 fs.

For each set of OTA measurements the map of the standard deviations was calculated. This map provides a good estimate of the stability of sample measurements over time, and whether corrections need to be applied to account for power drifts, or whether sample degradation is taking place. An example map of the standard deviations is shown in figure 3.18a, where the standard deviation is equivalent before and after t0 and through the whole spectral window. The charge injection signal is shown in 3.18b where the signal amplitude reached a maximum of approximately 0.5 mOD.

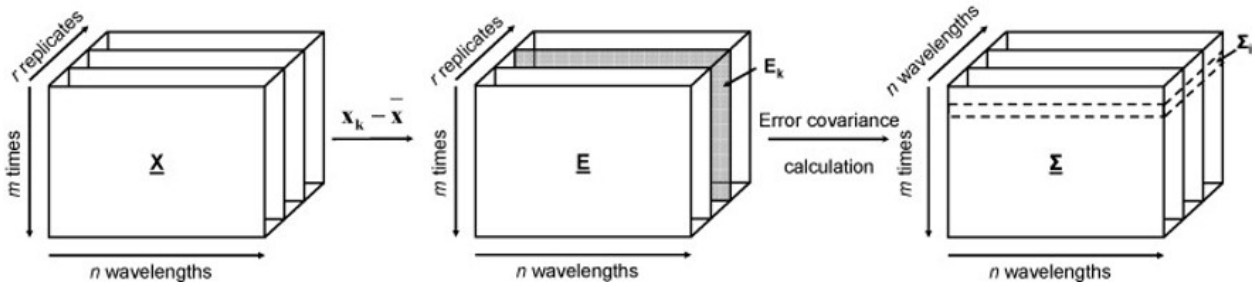

Figure 3.19: Construction of the covariance cube along wavelength and time axes. Reproduced from reference [137].

Covariance within a set of measurements is a very useful tool for understanding the source of instrumental error. Estimating the covariance across the wavelength and time axes of the OTA instrument requires building a 3-dimensional data cube out of a set of replicate transient absorption measurements. This process is illustrated in figure 3.19.[137]

The set of time-resolved measurements, with k replicates, is first concatenated into a wavelength by time by k data cube, $\underline{\mathbf{X}}$, which has the 2-dimensional mean $\overline{\mathbf{X}}$. The 3-dimensional error cube can then be calculated:

$$\mathbf{E}_k = \mathbf{X}_k - \overline{\mathbf{X}} \tag{3.22}$$

The measurement error structure along the wavelength axis can then be estimated for the *ith* spectrum in time to produce a symmetric wavelength by wavelength covariance matrix:

$$\Sigma_i = \frac{1}{r-1} * \Sigma_{k=1}^{r} (\mathbf{x}_k - \overline{\mathbf{x}})^T (\mathbf{x}_k - \overline{\mathbf{x}}) \tag{3.23}$$

This can be repeated for each time point to produce a time x wavelength x wavelength cube ($\underline{\mathbf{\Sigma}}$) where each wavelength-by-wavelength slice contains the covariances at that time point. This can be repeated for each individual wavelength as well to produce a wavelength x time x time covariance error cube. Examples of these data structures are shown in figure 3.20.

The wavelength covariance matrix in figure 3.20a shows that at 0.5 ps, there is a strong

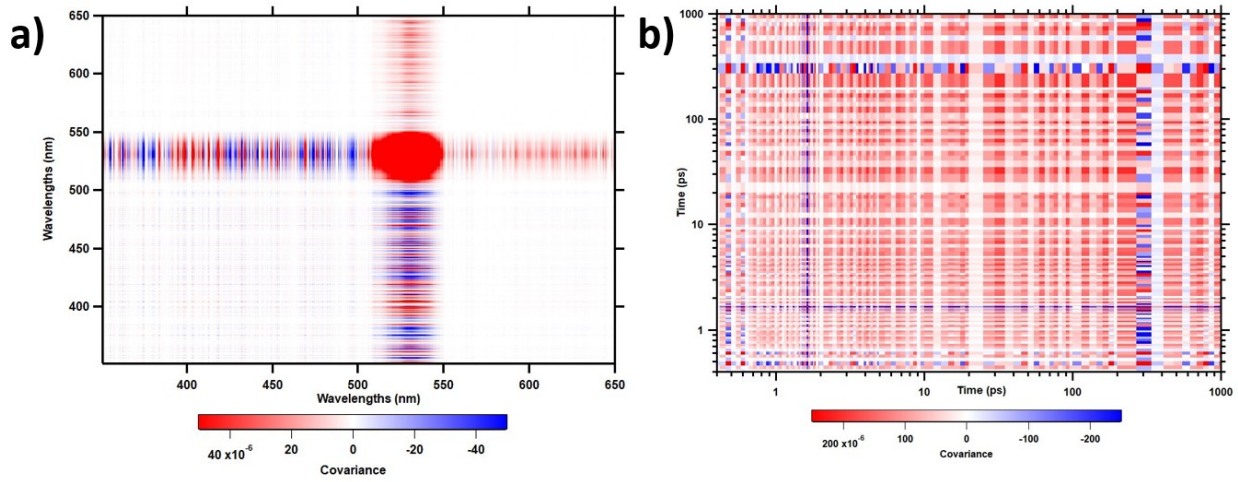

Figure 3.20: a) The wavelength covariance matrix at 0.5 ps for an OTA measurement on pure CdSe, with a fluence at 532 nm of 1mJ/cm^2. b) The temporal covariance matrix at 525 nm.

covariance with along all wavelengths with the error at 532 nm. This is the wavelength of the pump, so at any given time the variation in pump power will affect the signal stability at all wavelengths. The temporal covariance matrix in figure 3.20b shows that for a given wavelength, there is a covariance for periodic time points in an oscillating manor. The root cause of this is the stability of the white light continuum. The CaF_2 crystal is being translated back and forth across the pump beam, spending approximately 1 data averaging period in the center in between turning points. Because the 800 nm pump is very intense, the CaF_2 accumulates burn spots predominantly at these turning points. This matrix shows that this translation is introducing periodic noise that can be correlated between time points.

After photoexcitation, the transient spectrum can be written as a function of time and wavelength:[138]

$$\Delta A(\lambda, t) = \Sigma_{n=1}^{q} S_n(\lambda) e^{-t/\tau_n} \tag{3.24}$$

Which is a summation over q excitonic states, each of which decays exponentially. $S_n(\lambda)$ is a wavelength dependent prefactor, while τ is the decay of the excitonic state. This can be

rearranged to reflect the relationship of a given S to the TA spectra:

$$\begin{aligned} S_1(\lambda) &= (\Sigma_{i=1}^{\infty} p_i)\, \Delta A_1(\lambda) \\ S_n(\lambda) &= (\Sigma_{i=1}^{\infty} p_i)\, [\Delta A_n(\lambda) - \Delta A_{n-1}(\lambda)] \end{aligned} \tag{3.25}$$

Equation 3.25 expresses the spectrum amplitude in terms of a sum from each excitonic state. A transient spectrum can then be decomposed into kinetic traces at each wavelength and be globally fit by a sum of exponential components. Signals can be expressed as in equation 3.26:

$$\begin{aligned} S_1(\lambda) &= \gamma_1(\lambda)(1 - e^{-Cp}) \\ S_2(\lambda) &= \gamma_2(\lambda)(1 - e^{-Cp} - Cpe^{-Cp}) \end{aligned} \tag{3.26}$$

Where γ is a parameter representing the maximum amplitude, and C represents the relation between the excitation power and QD excitation as $< N >= Cp$. The terms in parantheses is an expansion of the excitonic populations given by the Poisson equation. Combined with a fluence dependent measurements, as shown in figure 3.21a, shows the time constant for each multiexcitonic state as a function of power, extracted from the global fits.

The first component represents radiative or non-radiative recombination, which takes place on the longest timescale. The second component represents biexciton recombination, which is relatively constant until excitonic states higher than 2 is reached. The third constant represents Auger recombination of 3 and higher excitons. These global fits represent the Decay Associated Difference Spectra (DADS) as a function of power. The extracted amplitude for each time constant can then be fit to the excitonic populations according to equation 3.26. Figure 3.21b shows the amplitude of the first two components versus fluence and gives the associated fits. The estimated average excitonic state is also given using the fit to the radiative recombination exponential component. The fit to the second component representing the biexponential component has significant error in the determination of $< N >$

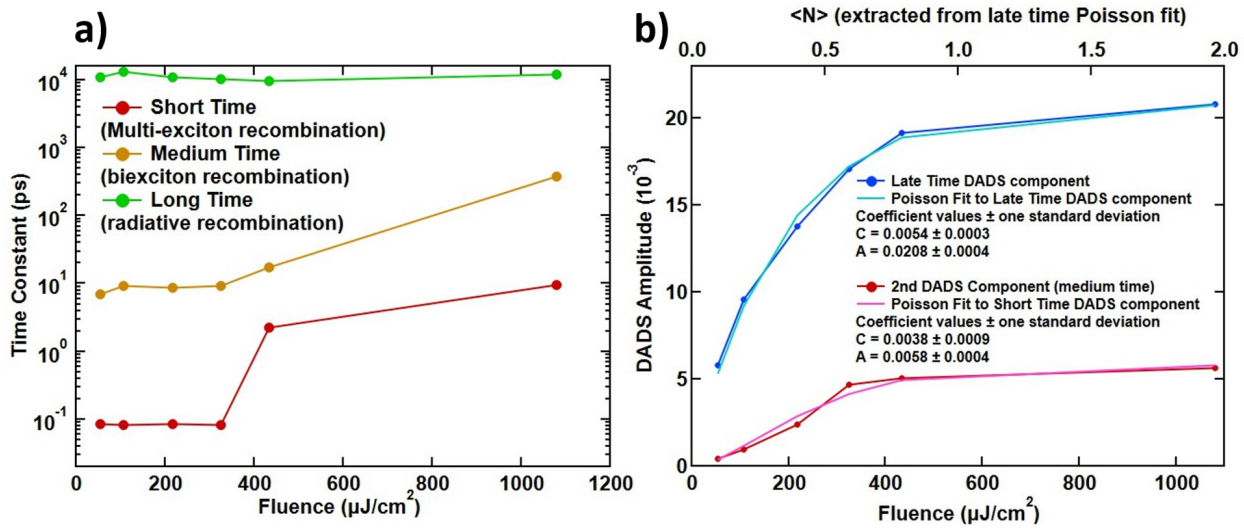

Figure 3.21: a) Time constants of recombination and biexciton lifetimes vs. fluence, extracted with global fitting. b) Fit of the amplitude of the first two components to the dependence of the signal on excitonic population.

because of the dependence on the optical thickness of the sample, where for any given fluence there will always be some biexciton population being created.

The physical underpinning of the optical transient absorption signals at the band gap in ZnO and CdSe is the same, being due to phase space filling (PSF, or Pauli blocking) of the band gap transition.[90] The spectral separation of these signals makes dual UV/visible probe OTA insightful to the carrier population dynamics. The ZnO signal is due solely to PSF from injected conduction band electrons because the band gap energetics at the CdSe/ZnO interface only permit the transfer of electrons. In CdSe the band edge transient is predominantly a measure of the electron population rather than holes because the 1st excitonic transition has a low electron degeneracy of 2 compared to the 6 of holes, and holes are rapidly trapped without a well passivated (ex. core - shell QDs) surface.[127], [139], [140] This is important since it means that back-electron transfer from ZnO that results in recombination with a hole, or hole transfer from CdSe to ZnO, cannot be accurately measured with CdSe band gap measurements.

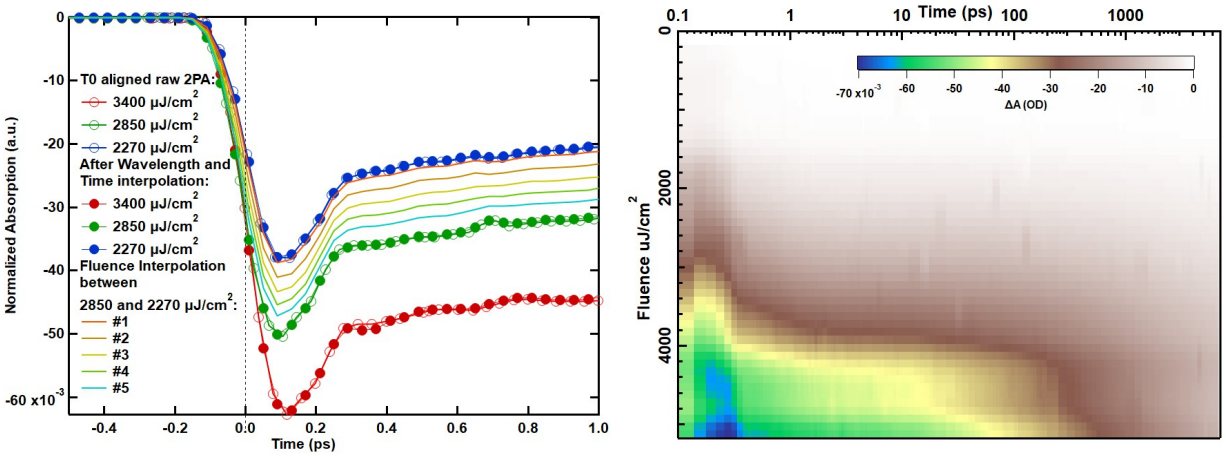

Figure 3.22: The left figure is a demonstration of the interpolation procedures for taking data from the raw 2PA data into a form that can be splined between fluences. The open circle red, green, and blue lines display t0 aligned kinetic traces at 365 nm after excitation with 3400, 2850, and 2270 $\mu J/cm^2$ 532 nm light, respectively. The close circle red, green, and blue traces are the same fluences after linear interpolation along the wavelength and time axes to produce data points that are consistently located. The solid lines show the results of interpolation between 2850 and 2270 $\mu J/cm^2$. At right is a complete slice of the splined two photon absorption data at 365 nm, plotted as fluence vs time.

3.6 Fitting, Splines, and Statistical Measures

3.6.1 Splined Two-Photon Absorption

Subtracting out 2PA components from charge injection datasets is important for evaluating the magnitude of charge injection in high fluence measurements. This is employed in interpreting the XTA feasibility results shown in chapter 5. Fluence dependent 2PA data must be assembled and interpolated to give a smoothly varying dataset. Before being compiled, each dataset was GVD corrected using the CPM artifact of a high fluence scan on a bare quartz slide, then background subtracted at all wavelengths. Using the signal at 365 nm, each dataset was aligned in time so that the middle of the rising edge of the bleach lies at 0 ps. As shown in figure 3.22a, the datasets were linearly interpolated onto matching time and wavelength axes. The wavelength axis of the 2D measurements was interpolated from the third order polynomial response of the monochromator grating onto a linear wavelength axis

with steps of 0.5 nm. The time axis of each measurement has steps of 5, 0.04, 0.15, 0.5, 1.5, 5, 10, 50, 200 ps between time delays of -50, -2, 0.5, 1.5, 5, 20, 100, 200, 1000, and 7000 ps. At this point there are 16 datasets with identical number of points, t0's, wavelength steps, and time steps. The 16 datasets were measured with fluences between 229 and 5600 $\mu J/cm^2$. They are then combined into a single three-dimensional data matrix and bilinearly splined to give 50 datasets across the same range of fluences. A slice of these datasets at 365 nm is shown at in figure 3.22b. Charge injection takes place over multiple ps, but 2PA is IRF limited, so the initial IRF limited bleach at 365 nm in charge injection experiments was matched in amplitude to the peak bleach of the splined 2PA dataset. The 2PA dataset was then subtracted from the charge injection dataset to give pure charge injection kinetics and amplitude. This works at low fluences, but at high fluences charge injection takes place on a shorter time scale, giving overlapping contributions between charge injection and 2PA. The correct 2PA dataset to subtract was then matched not only to the IRF limited bleach at 365 nm, but also to a low wavelength bleach at 340 nm.

3.6.2 Fitting OTA Kinetic Traces

Estimation of the time dependent kinetic behavior is one of the main purposes of time resolved spectroscopy. It can be approached in many different ways though. A sum of exponentials fitting is the most popular strategy employed due to its simplicity and ease of interpretation, which is defined in equation 3.27:

$$S(t) = \Sigma_{i=0}^{n} A_i * e^{-k_i t} \tag{3.27}$$

Where $S(t)$ is the observed time dependent transient signal. A_i is the amplitude of the exponential component i, with time constant k_i. The sum of exponential fittings employed the Nonlinear Least Squares method to minimize χ^2 with the lmfit python package. Kinetic data was weighted with the standard deviation at each point. For the OTA data of 2.6 nm and

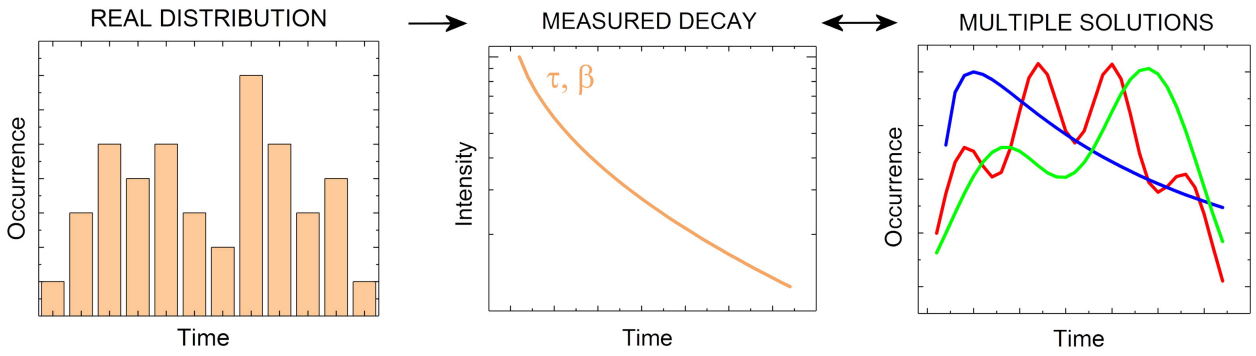

Figure 3.23: An illustration of the effect of a distribution of decay rates on the measured experimental kinetics. a) An example distribution of rates. b) The experimentally measured decay curve, as a function of decay rate and stretching factor. c) Different extracted distributions of decay rates. Reproduced from reference [142].

2.26 nm CdSe - ZnO samples, the UV datasets showed a slow decay of the charge injection signal over multiple nanoseconds. To correctly fit the overall shape, a single exponential decay was included alongside exponential rises. Since these processes are separated by multiple orders of magnitude, they do not interfere with the value of each other's time constant. The standard deviation of the fit was then calculated as the variation in the parameter needed to change χ^2 by 1. To make an objective decision on the correct sum of exponentials model to use, the full set of kinetic traces for each material were fit sequentially to a greater number of exponentials while computing the Akaike and Bayesian Information Criterion (AIC and BIC, respectively),[141] as defined below.

A sum of exponential fittings may not correctly account for the shape of the charge injection signal. Inhomogeneity may arise from a distribution of QD sizes, or a distribution of binding motifs.[143] A distribution of time constant rates may be required when ~ 3 or more exponentials are needed to match the shape of the experimental kinetic decay. The most common way to account for, or test for a distribution of rates, is the stretched exponential or Kohlrausch rate law:[142]

$$S = A * e^{(-kt)^{\beta}} \tag{3.28}$$

Where β is a stretch factor determining the deviation from monoexponential kinetics. While popular, a difficulty with this approach is that multiple different ensembles of decay

rates may give very similar experimental kinetics, making the extraction of a physical distribution very difficult.[142] This is shown schematically in figure 3.23. An alternative approach is to derived from a decay rate distribution, which is then integrated over to give the experimental decay. This is shown below:

$$H(k) = \frac{1}{k\sqrt{2\pi}\sigma} e^{-\frac{(ln\ k - \mu)^2}{2\sigma^2}} \tag{3.29}$$

$$S = \int_0^\infty H(k) e^{-kt} dk \tag{3.30}$$

Equation 3.29 describes a distribution of decay rates, where the logarithm of the distribution is normally distributed, known as the log norm function. $\mu = ln\ k_{mf}$ where k_{mf} is the mode of the distribution, and $\sigma = \frac{1}{\sqrt{2}} \sinh^{-1} \Delta k / 2k_{mf}$ where Δk is the width of the distribution. The signal can then be extracted as described with equation 3.30.[144] A lognorm decay rate matches stretched exponential kinetic behavior while being derived from a physically meaningful distribution.

3.6.3 Data Hierarchy

The OTA data discussed in chapters 5 and 6 is organized into a three-level hierarchy, as shown in figure 3.24. The lowest level is the spot level, which are the individual measurements taken in either the UV or the visible probe region. Each spot was acquired in a spatially distinct point on the sample, with no spot being repeated between the UV probe and visible probe measurements. Each spot was measured between 3 and 6 times to be sufficiently averaged. Enough spots were measured to give a statistically relevant measure of the true kinetics of either the CdSe or ZnO. These spots are aggregated into a probe-region-specific dataset representing the ZnO (UV probe data) or CdSe (visible probe data), termed a half-dataset. Two half-datasets are then combined into a material level dataset that represents the complete dynamics in the QD - ZnO system. Prior to being assembled into a material dataset, each

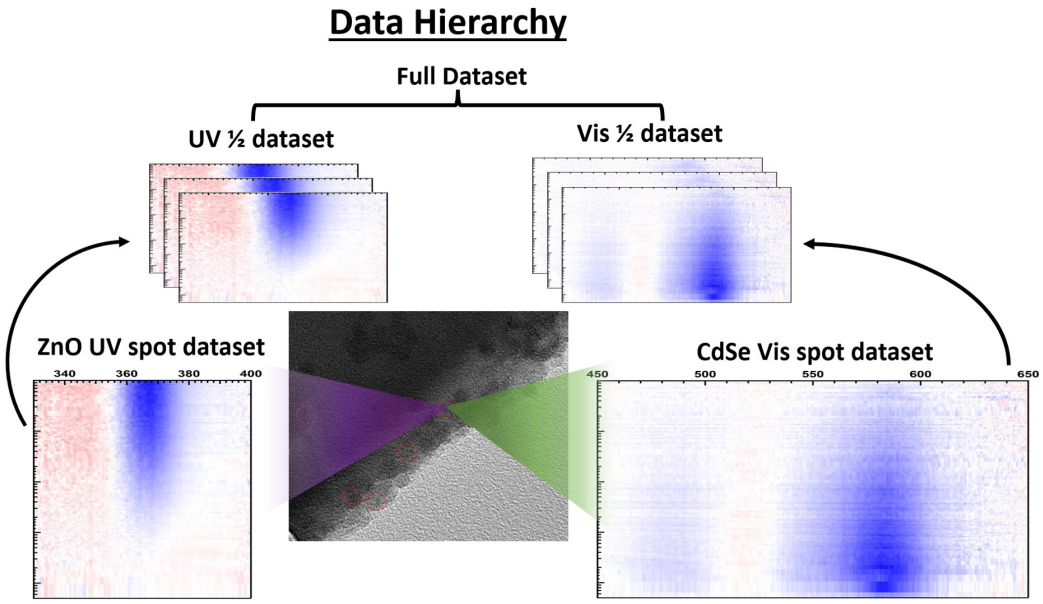

Figure 3.24: The organization of OTA data is separated into three levels: the spatially and probe-region distinct spot-datasets, the probe-region specific half-datasets which encompasses all spot datasets, and the sample specific all-encompassing full dataset. Each spot dataset will be averaged until a reasonable signal-to-noise is achieved. Each half-dataset will contain a minimum of 5 spot datasets, which represents the ZnO or CdSe dynamics within that sample. Finally, the full dataset will contain two half-datasets and represents the system dynamics, as can be observed with optical spectroscopy, as a whole.

half-dataset was normalized to the maximum intensity.

3.6.4 Akaike and Bayesian Information Criterion

A few statistical measures were relied on to decide between different kinetic models. Of these the reduced χ^2 is the most common. The intent of these measures is to penalize a fit based on the number of parameters needed to reduce the sum of squared errors. This procedure is shown in figure 3.25 for the 2.62 nm CdSe - ZnO sample UV half-dataset, using the measures defined below:

$$\chi^2_{red} = SSE/(n-p) \tag{3.31}$$

$$SSE = \sum_{i=1}^{n} (y - y_i)^2 \tag{3.32}$$

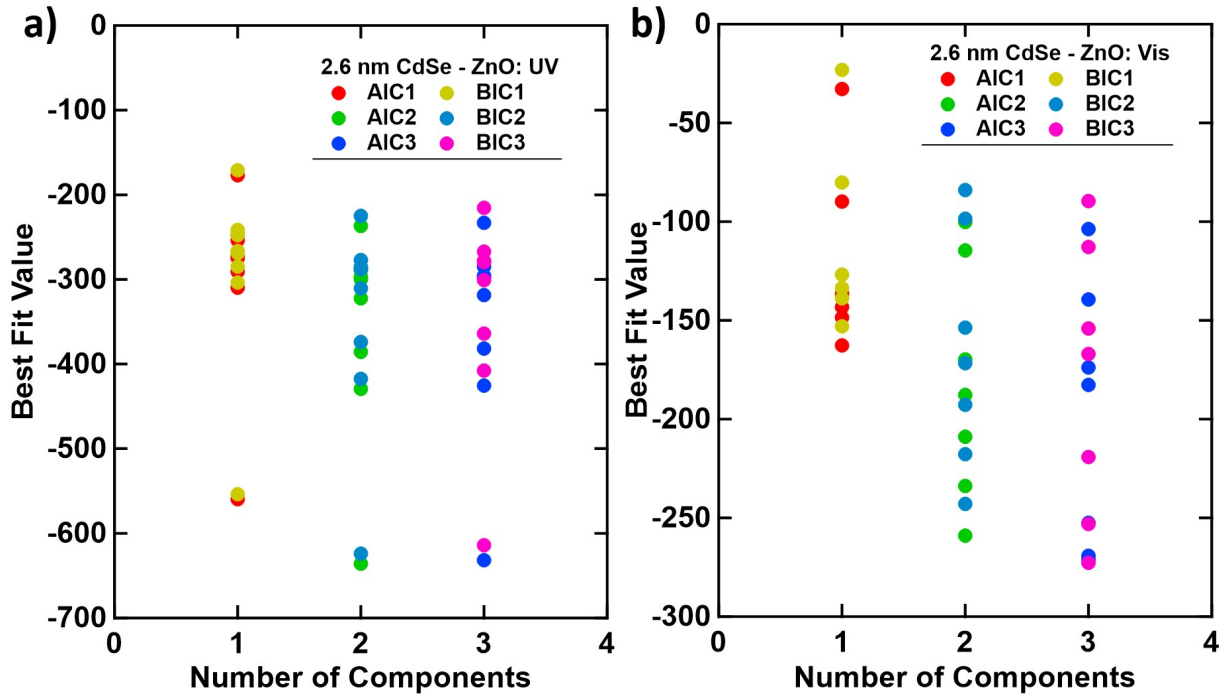

Figure 3.25: The combined Akaike and Bayesian Information Criterion values for the 2.6 nm CdSe - ZnO in the a) UV (at 365 nm) and b) visible (at 515 nm). Calculated with equations 3.31 through 3.32. The complete UV/Vis half-dataset is represented, which encompasses all averaged spot datasets. The number of components is specifically the number of exponentially falling/rising functions used to fit each dataset.

$$AIC = n * \ln\left(\frac{SSE}{n}\right) + \frac{2 * (p+2) * (p+1)}{(n-p-3)} \tag{3.33}$$

$$BIC = n * \ln\left(\frac{SSE}{n}\right) + (p+2) * \ln(n) \tag{3.34}$$

Each set of AIC/BIC values (orange and red, green and light blue, dark blue and pink) represents how well a given model fits the data. A lower AIC/BIC indicates the model fits the data better for the cost of including more parameters. The number of components is specifically the number of, in this case, rising exponentials used to fit the kinetic trace. Going from 1 to 2 components then, the AIC/BIC values decrease significantly for all spot-datasets. However, going from 2 to 3 components produces a slight increase in the AIC/BIC values for most of the datasets. 2 rising exponential components is then the ideal fit function for this half-dataset. Visible datasets which measure the CdSe are fitted with decaying exponential

functions. Each additional exponential requires the inclusion of two more parameters: an amplitude and a time constant. The inclusion of an extra component is then justified by reaching the minimum AIC/BIC. A sum of exponentials model is chosen for the half-dataset as a whole, without separating out individual spot datasets. Outlier spot-datasets were determined from the deviation of time constants from the weighted mean of the half-dataset. The AIC and BIC measures are most useful within similar classes of models, and is not necessarily reliable when comparing models with different functional forms.

3.6.5 Global Fitting

3.6.5.1 Charge Transfer State

Equation 3.35 shows the formal definition used to fit the experimental kinetics. Each term is defined as seen in figure 6.10a in the main text.

$$\begin{aligned} dN_{QD} &= -k_{ET} * N_{QD} + k_2 * N_{CTS} \\ dN_{CTS} &= k_{ET} * N_{QD} - k_2 * N_{CTS} - k_{diss} * N_{CTS} \\ dN_{ZnO} &= k_{diss} * N_{CTS} - k_{trap} * N_{ZnO} \end{aligned} \tag{3.35}$$

N_{QD}, N_{CTS}, and N_{ZnO} are the electron population of the QDs, CTS, and ZnO respectively, where $N_{QD} = 1$ at t_0. k_{ET} is the rate constant for charge transfer from CdSe into the CT state, and k_{diss} is the rate constant for charge separation at the interface of CdSe and ZnO. k_2 is the rate of back electron transfer from the charge transfer state. This process is expected to be unobservable, as the optical spectrum of CdSe is insensitive to the hole population. k_{trap} is the rate of electron trapping, or back electron transfer, in ZnO. The standard differential equations in 3.35 were solved analytically and used to fit the relevant UV and visible datasets.

k_{diss} and the CTS lifetime is a function of the Coulombic attraction between carriers, and thus of the dielectric environment. In dye-sensitized ZnO the positively charged dye and surface electron are separated by fewer than 5 Å, and the LUMO of the dye is in direct

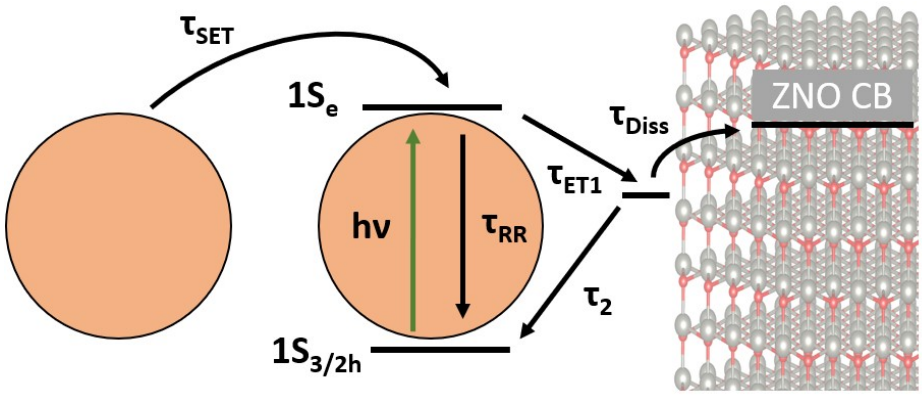

Figure 3.26: Graphic illustration of the Heterogenous Injection model as it was implemented during the global fit results shown below, and described by equation 3.36.

contact with the surface and is partially hybridized with the ZnO lattice.[49] Within the CdSe-ZnO system, the Coulombic attraction is thought to increase between the carriers as they are separated due to the lower dielectric constant of ZnO compared to CdSe.[34], [35]

3.6.5.2 Heterogeneous Injection

Heterogenous Injection (HI) is defined as charge transfer from indirectly attached QDs. These quantum dots are not chemically bound to the surface, and thus have a weaker electronic coupling. Rather, these QDs can transfer a charge to a directly attached QD, or transfer a charge through physical but not chemically bound contact. This model is illustrated in figure 3.26 and defined simply with a three state parallel decay model:

$$\begin{aligned} dN_{QD1} &= -k_{ET} * N_{QD1} \\ dN_{QD2} &= -k_{SET} * N_{QD2} \\ dN_{ZnO} &= k_{ET} * N_{QD1} + k_{SET2} * N_{QD} - k_{trap} * N_{ZnO} \end{aligned} \tag{3.36}$$

Where N_{QD} and N_{ZnO} are the electron populations in the quantum dots and ZnO respectively. k_{ET} and k_{SET} are the time constants for the direct and indirect quantum dots respectively. This model has been applied alongside the CTS model as the other likely explanation for the rising ZnO signal in terahertz spectroscopy.[34], [83] Within this

interpretation, the injection from indirectly attached quantum dots could range from 20 to 100 ps. Charge transfer from indirect quantum dots proceeds first through an adjacent quantum dot, and then into the metal oxide. Since electron transfer from the directly attached quantum dot should be much faster than carrier diffusion between quantum dots, the overall rate can be approximated as the rate of charge transfer between quantum dots. Injection from indirect quantum dots could be accentuated with exciton delocalizing ligands.[145], [146] Carrier diffusion between quantum dots is complicated by charge transfer taking place either into a neutral unexcited quantum dot, a neutral excited quantum dot, or a charged quantum dot post-electron transfer.

3.6.5.3 Band Bending

With this assumption a mixture of band bending effects govern the charge injection dynamics, allowing for injection pathways of varying character. One mechanism may include downward band bending, where the driving force is larger but could form a potential well that localizes carriers at the surface.[63], [64] Another mechanism may be less substantial downward band bending, or even upward band bending, which would give a lower driving force but prevent surface localization. This is graphically illustrated by figure 6.10b and formalized in equation 3.37.

$$\begin{aligned} dN_{QD1} &= -k_1 * N_{QD1} \\ dN_{QD2} &= -k_2 * N_{QD2} \\ dN_{Vbb} &= k_1 * N_{QD1} - k_{diss} * N_{Vbb} \\ dN_{ZnO} &= k_{diss} * N_{Vbb} + k_2 * N_{QD2} - k_{trap} * N_{ZnO} \end{aligned} \tag{3.37}$$

N_{QD1} and N_{QD2} are the populations of excited QD-bound electrons that are attached to ZnO surfaces of different character. The former population will experience a larger driving force, and thus undergo injection quickly, but may experience a potential at the surface that will force localization close to the surface. N_{QD2} represents the population of quantum

dots that are not coupled to a strong downward surface potential, but may be electronically coupled to states with a lesser magnitude of downward bending, or even upward bending. The time constants k_1 and k_2 represent the charge transfer rates into the ZnO potential well and low-magnitude bending respectively. k_{diss} represents the rate of dissociation out of the potential well. Any intermediate state for the k_2 pathway is likely to be unobservable due to overlapping kinetics. For example, if k_1 and k_2 are well separated in time, this would mean that k_2 is transferring electrons into a higher energy level with a fast dissociation into the bulk DOS. If k_{diss} was fast, then dissociation after k_2 would be much much faster. If k_{diss} is slow, then the timescales of k_1 plus dissociation would overlap with k_2 plus dissociation, and they would become inseparable. Within this framework, charge transfer into a low-magnitude band bending state plus any dissociation out of that state is approximated with a single time constant. It should be noted that the amplitude of either charge injection pathway is dependent on the crystal facet the quantum dot is bound to, and should thus depend on the thermodynamics of coordinating to competing sites. If the energetics of coordination do not discriminate between the two cases, then the two pathways should have roughly stochastic yields, despite the high-magnitude band bending being the most energetically favorable pathway. Given this, the relative stability of carboxylic acid binding between the facets, which could predispose one pathway over another, is expected to be a minor factor.[100], [109]

The formulations provided in equations 3.35 and 3.36 have significant functional overlap with 3.37, and in certain cases could overlap enough to be indistinguishable. The band bending and CTS models can be distinguished from their dependence on the quantum dot size, where the interaction term of the CTS model scales with the inverse of the quantum dot size while the band bending model should be roughly independent of the quantum dot size. However, the heterogeneous injection pathway is not exclusive to either model, and may be applied alongside both. The contribution of heterogeneous injection will only be relevant with a high quantum dot concentration where more than a monolayer is deposited,

and where photoexcitation is predominantly in indirectly attached QDs. This is not the case in the samples studied here.

Acknowledgements

I thank Thomas Rossi for assisting with the ZnO nanorod synthesis, and for conceptualizing the transient X-ray linear dichroism experiment. I additionally thank Thomas and Tyler Haddock for their help with collecting OTA data. I thank Michael Enright for synthesizing the CdSe quantum dots. I thank Cecilia Gentle for her help collecting TEM images and with ideas for the EXAFS analysis. I thank the MRL staff - especially Julio Soares - for their help with training and instrumentation.

Chapter 4

Non-Local Carrier Screening and Phase Space Filling in ZnO

4.1 Introduction

This chapter details the implementation and application of transient X-ray linear dichroism to ZnO nanorods. XTA on its own is a powerful technique that can interrogate local effects, such as polaron formation,[147]–[151] carrier trapping,[74], [79], [152], [153] lattice expansion,[154] and change of valence states.[155]–[158] Combining this with linear dichroism allows the dynamics of photoexcitation to be interrogated with orbital specificity.[114], [159] This is especially powerful for charge-injection experiments due to the ability to sensitively characterize trap states.[160], [161] Few techniques have the ability to discern the timescale and structure of trapped carriers with material specificity. The $[1\,0\,\bar{1}\,0]$ face has the most surface area in oriented ZnO nanorods, so charge injection would proceed predominantly through this facet, with carriers subsequently trapped at that interface.[162] Transient XLD offers the powerful ability to measure the timescale of carrier injection, the subsequent trapping at surface defect, and the structure of such a state. This is coupled with the elusive capability to track the fate of holes in charged QDs after charge injection.

A barrier to such powerful capabilities is the thermal impact of laser excitation and the

intrinsic low signal in XTA. The thermal impact from laser excitation has been shown to be quite significant, but is often neglected.[154], [163] In quantum dots intense excitation has been seen to induce transient melting and recrystallization.[9], [164] Section 4.2 details the usage of the temperature dependent XAS spectra to carefully calibrate the temperature jump after excitation, and the result from subtracting this contribution from the XTA spectrum. Section 4.3 interprets the resulting non-thermal XTA spectrum as nonlocal screening of the core hole, leading to a broad reduction in transition cross section. This is supported with ab initio calculations in 4.4. Finally, the first measurement of phase space filling at the K-edge is presented in section 4.5.

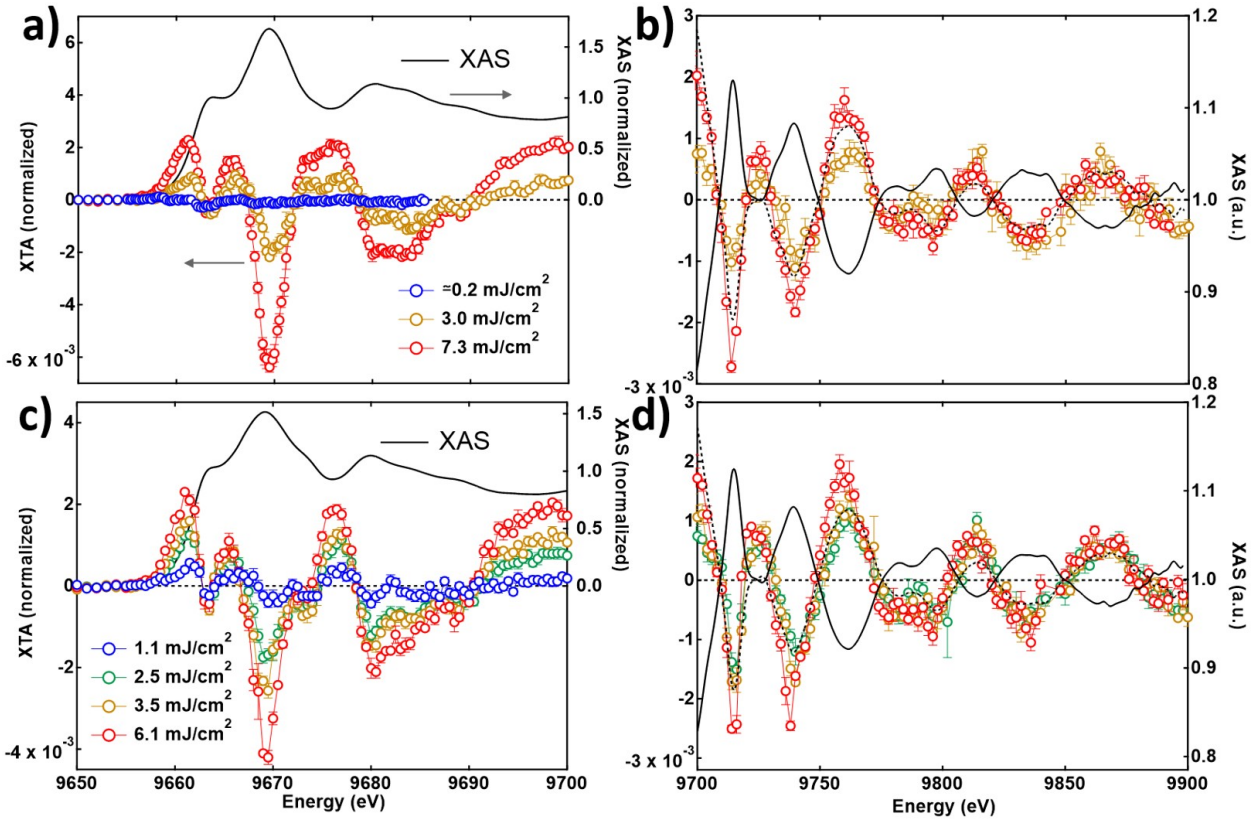

Figure 4.1: XTA spectra at the Zn K-edge in the XANES at a) normal incidence after excitation with $\sim$ 0.2, 3.0, and 7.3 mJ/cm^2 (blue, orange, red traces respectively), and c) diagonal incidence with 1.1, 2.5, 3.5, and 6.1 mJ/cm^2 (blue, green, orange, and red traces respectively). The EXAFS region is shown for b) normal incidence and d) diagonal incidence for the same range of fluences. In b) and d) are dotted lines indicating the sign flipped background subtracted EXAFS spectra. Adapted from reference [73].

4.2 Thermal Calibration and Heat Jump in Transient Experiments

The ZnO transient XANES spectrum is shown at normal and diagonal incidence, in the XANES and EXAFS regions, in figure 4.1a-d for fluences ranging from $< 1 \text{mJ/cm}^2$ to 7.3mJ/cm^2. The spectrum has a strong bleach at the white line, (9670 eV), with strong positive wings in the preedge (9661 eV), just before the white line (9665.5 eV), and just after the white line ($\sim$ 9676 eV). The dominant effect in the transient EXAFS is a damping of the features, with no change in frequency of the oscillations. This is shown clearly by the dotted lines of 4.1b and d, which is the inverted and background subtracted EXAFS signal. These features match the thermal difference spectra very closely, which can be seen in figure 4.2. As described in section 3.3.4.3 the dominant effect from a warm lattice is a damping of the EXAFS oscillations due to an increased DW factor, which minimal or no changes in bond lengths.

Since the transient EXAFS matches the thermal difference features so closely, it can be used to accurately calibrate the heat jump induced by laser excitation and allows the subtraction of the thermal signal in the XANES spectrum. The EXAFS region does not show significant linear dichroism, so either diagonal or normal incidence data can be used to calibrate the heat jump for identical fluences. The thermal calibration was done with static measurements of ZnO at a range of temperatures from room temperature to 500 °C in steps of 10 °C, similar to literature procedures with CuO.[163] As shown in figure 4.2b, excitation with 6.1 mJ/cm^2 at diagonal incidence produces an EXAFS signal with an amplitude that matches a heat jump of 60 °C, measured 100 ps after excitation. similarly, excitation with 7.3 mJ/cm^2 at normal incidence gives a heat jump of 70 °C. These assignments are corroborated with full-multiple scattering calculations with the DW model, as shown in figure 4.2b and d, where a simple increase of the DW factor (which represents the incoherent vibrational motion) accounts for the majority of the transient signal in the EXAFS.[165], [166] Figure 4.2a and c then show the transient XANES spectra for these fluences alongside the assigned

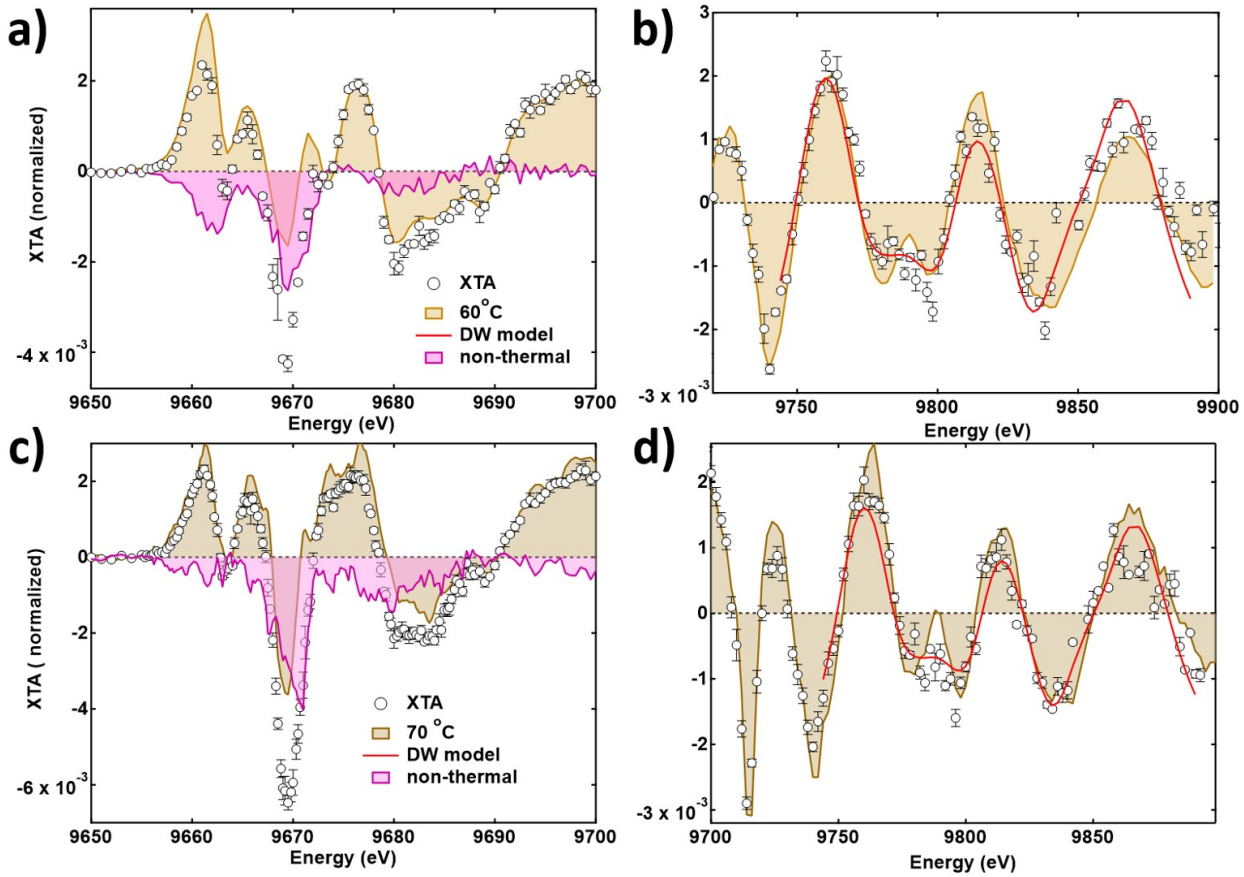

Figure 4.2: XTA spectra at diagonal (a,b) and normal (c,d) incidence (black circles) in the XANES (a, c) and EXAFS (b, d) for fluences of 6.1 mJ/cm^2 (a, b) and 7.3 mJ/cm^2 (c, d). The best matched thermal difference spectrum (green and blue shaded curves) along with FMS calculations (red lines). The FMS curves are obtained with a DW factor increase of 0.54 mÅ^2 (b) and 0.44 mÅ^2 (d). The non-thermal transient XANES contributions are obtained from the difference from the XTA and matched thermal difference spectra (pink shading). Adapted from reference [73].

thermal and nonthermal components. Ab initio simulations of thermal effects in the XANES are very challenging due to the promotion of forbidden transitions and complexity of multiple scattering pathways.[167] Thermal simulations were attempted with the FDMNES code by considering a normal distribution of atomic positions according to the DW factor and reconstructing the averaged XANES spectra. However, this did not give good agreement with the experimental thermal difference spectra. The lack of frequency modulations in the EXAFS implies that no significant bond length changes occur in the vicinity of the Zn atoms after photoexcitation. Hence the formation of hole polarons[168] and trapped holes[169] in

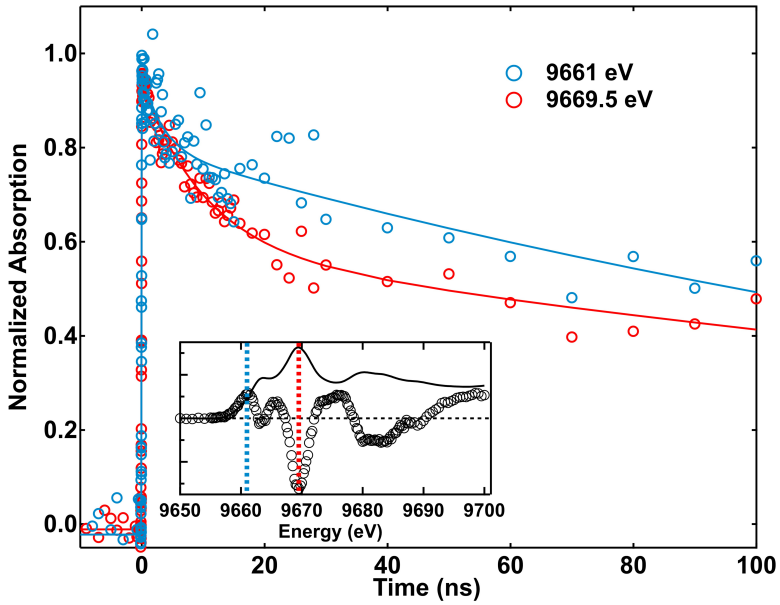

Figure 4.3: Normalized time traces at 9661 eV (blue circles) and 9669.5 eV (red circles) at normal incidence with a fluence of 7.3mJ/cm^2. Biexponential fittings are shown with continuous lines. Inset shows the energy position of the time traces on the XTA at the same incidence angle and fluence. Adapted from reference [73].

the epitaxial ZnO nanorods studied here can be excluded. The thermal component accounts for most of the positive amplitude in the XANES region, the resulting nonthermal signal is predominantly negative across the whole XANES region.

Figure 4.3 shows the kinetics at two energies for normal incidence and 7.3mJ/cm^2 excitation. At both 9661 eV and 9669.5 eV a prompt rise is seen. The feature at 9661 eV is dominated by thermal effects, while the feature at 9669.5 eV has contributions from both thermal and electronic effects. At the carrier densities employed here, which are near or above the Mott density,[22], [131] carrier diffusion after photoexcitation will be enhanced and result in homogeneous carrier distribution over the length of the nanorods within $\sim$ 100 ps.[170] There is a mismatch between the laser and X-ray penetration depth though that could lead to observation of inhomogeneous thermal effects. The 355 nm pump pulse has a penetration depth of $\sim$ 110 nm, while the penetration depth of X-rays above the Zn K-edge is $\sim$ 8.5μs.[128] For a lattice at 70 °C, the lattice should take approximately 370 ns to equilibrate along the length of the nanorod given a thermal diffusivity of $1.07\dot{1}0^{-5}$m^{2}s^{-1}.[171], [172]

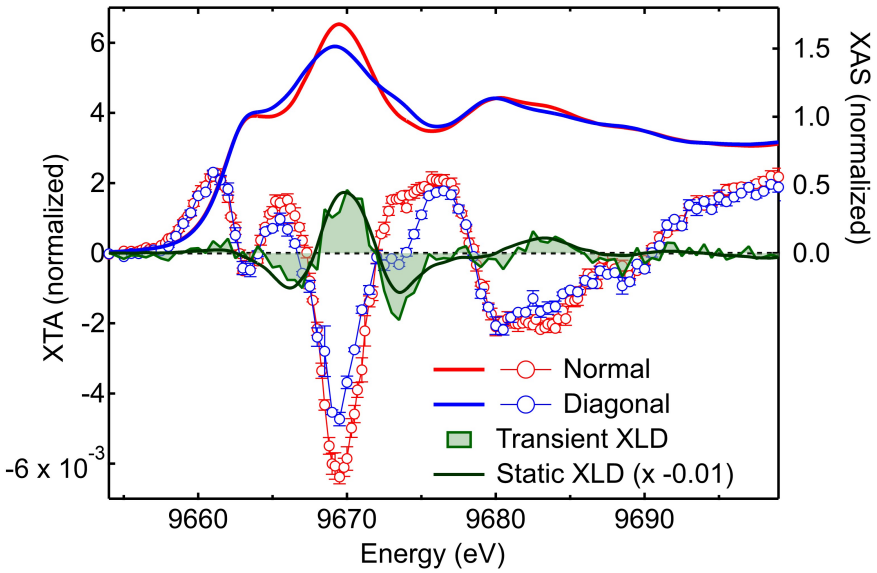

Figure 4.4: Transient XANES spectrum at normal (red circles) and diagonal (blue circles) incidence at ∼100 ps after photoexcitation at 355 nm with an excitation density of ∼3×10^{19} cm^{-3} (left axis). The resulting transient XLD spectrum (diagonal-normal) is shown in shaded green (left axis). The inverted static XLD spectrum (scaled by 0.01) is shown with a solid black curve. The XAS at normal (solid red) and diagonal (solid blue) incidence are shown for reference (right axis). Adapted from reference [73].

However, the hot lattice is caused by excited carriers depositing excess energy into lattice phonon modes. Since the carriers are homogeneously distributed quickly the thermal effects measured here are expected to equilibrate more quickly than the thermal diffusion would allow. The lack of a delayed rise of the signal at 9661 eV, which is mostly a thermal signal, supports this conclusion. The biexponential fits shown in figure 4.3 have time constants of 3 ± 3ns and 210 ± 70ns at 9661 eV, and 10 ± 3ns and 300 ± 170ns at 9669.5 eV. The fast component for these energies is estimated to be carrier recombination based on time resolved photoluminescence measurements, and the long time component to heat dissipation out of the system.

4.3 Non-local Carrier Screening

The non-thermal portion of the transient spectrum in 4.2a and c shows that the positive features in the XANES can be attributed to thermal effects. These results are corroborated by the transient XLD spectra, which is the difference between the transient XAS at normal and diagonal incidence. The static XLD does not vary strongly with temperature below 70 °C, meaning the increased temperature has an isotropic effect on the lattice. Then the laser-induced heating effectively cancels out in the transient XLD spectrum. As shown in figure 4.4, the transient XLD matches the scaled and inverted static XLD. The derivation of the transient XLD signal is given in section 3.3.4. The subtraction of the thermally calibrated spectra and the transient XLD support the interpretation that the dominant electronic signal is a broad reduction in the overall absorption cross-section.

Without the subtraction of the thermal component, the XTA features can be easily attributed to a red shift or broadening of the white line. Trapped holes and electrons are commonly interpreted as causing a shift in the ionization potential of the Zn K-edge. Even though the EXAFS region shows no sign of trapped carriers, we can rule out competing interpretations of the XANES region by calculating difference spectra with the experimental XAS spectra by applying a rigid blue or red shift, as shown in figure 4.5. Spectral blue shifts show poor agreement with the experimental spectra at normal and diagonal incidence, and can be ruled out. Spectral red shifts show rough qualitative agreement at a few features, but are consistently offset in energy. Since there is no way to account for this, a spectral red shift can also be ruled out. The absence of support for trapped charges is consistent between the EXAFS and XANES region.

The absence of significant structural distortion seen in the EXAFS analysis, and lack of chemical shift in the XANES, rules out effects that are strongly localized near Zn atoms. The nonthermal transient spectrum in the XLD and XANES is then interpreted as resulting from excited free, delocalized carriers rather than trapped carriers. The non-thermal transient

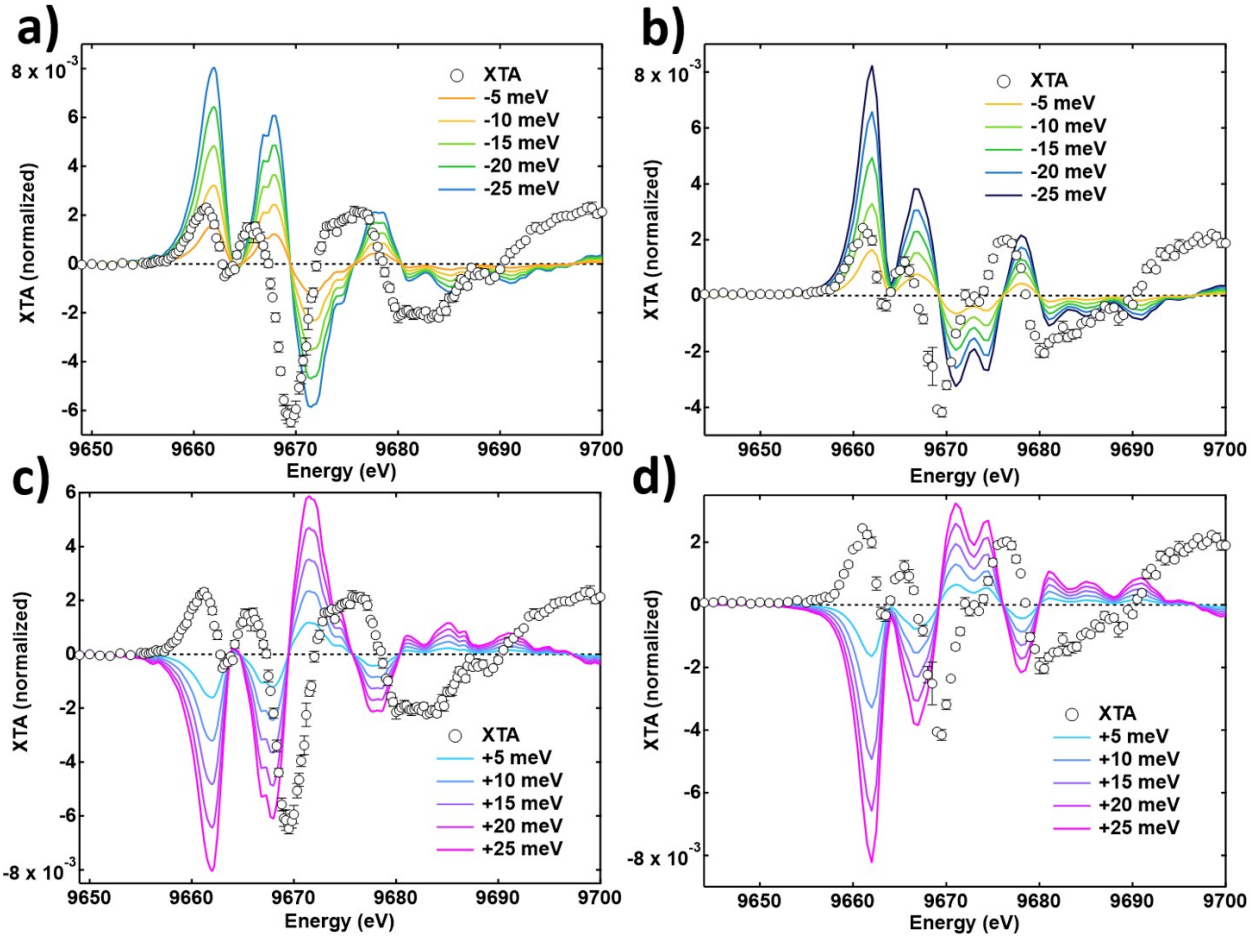

Figure 4.5: Simulated XTA upon rigid red (a,b) or blue (c,d) shifts of the experimental static XAS at normal (a,c) and diagonal (b,d) incidence. Adapted from reference [73].

resembles the spectral changes in the Zn XANES spectrum under constant irradiation, as shown in figure 4.6 (adapted from reference [173]), or of other sensitized ZnO nanomteri-als.[173]–[176] Under continuous irradiation thermal effects equilibrate with the environment, and do not contribute to differences with the "dark" signal. The shaded area in figure 4.6 then shows the qualitative match between a constant excited carrier population and the nonthermal XTA. Both thermal and nonthermal contributions to the XTA signal scale linearly with the excitation fluence. Since it is expected that photoexcitation results in trapped holes, as previously reported for ZnO nanoparticles,[74] and the spectra of sensitized materials is dominated by electrons, we interpret the nonthermal XTA spectrum as being dominated by free conduction band electrons. The depletion of XANES intensity by an excited delocalized

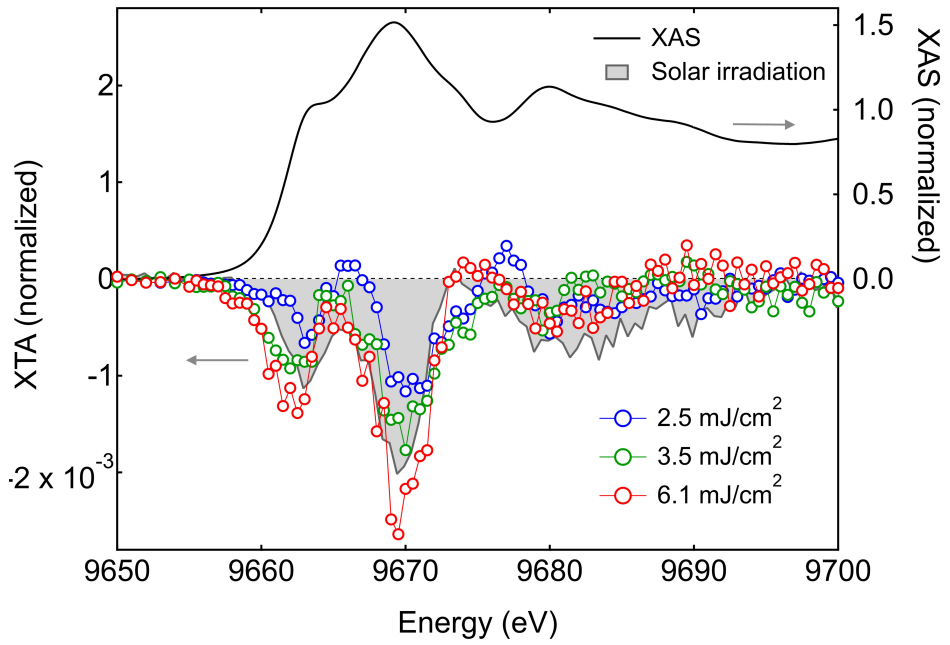

Figure 4.6: Nonthermal XTA spectra at diagonal incidence (colored circles, left axis). The static XAS is provided with a black line for reference (right axis). The difference XAS of ZnO nanorods under solar illumination with respect to a dark spectrum is provided for comparison (gray-shaded curve, scaled arbitrarily, adapted from Chen et al.[173]).

population of carriers is explained by Coulombic screening of the core hole.[177], [178] The excitation of a 1s electron leaves behind a 1s core hole, which will induce an electronic contraction of the valence orbitals. The photoexcited carrier population can then screen the interaction of this core hole with the valence orbitals, causing a renormalization of the transition cross-section. This assignment is supported with ab initio calculations in the following section.

4.4 Ab Initio XAS Calculations.

To support our interpretation of core-hole screening, ab initio calculations were performed as described in section 3.4 with and without a core-hole. Accurately incorporating the screened interaction of the core-hole and X-ray excited electron is very difficult and requires taking into account the multi-body excitonic effects, which can be done with the Bethe-Salpeter equation

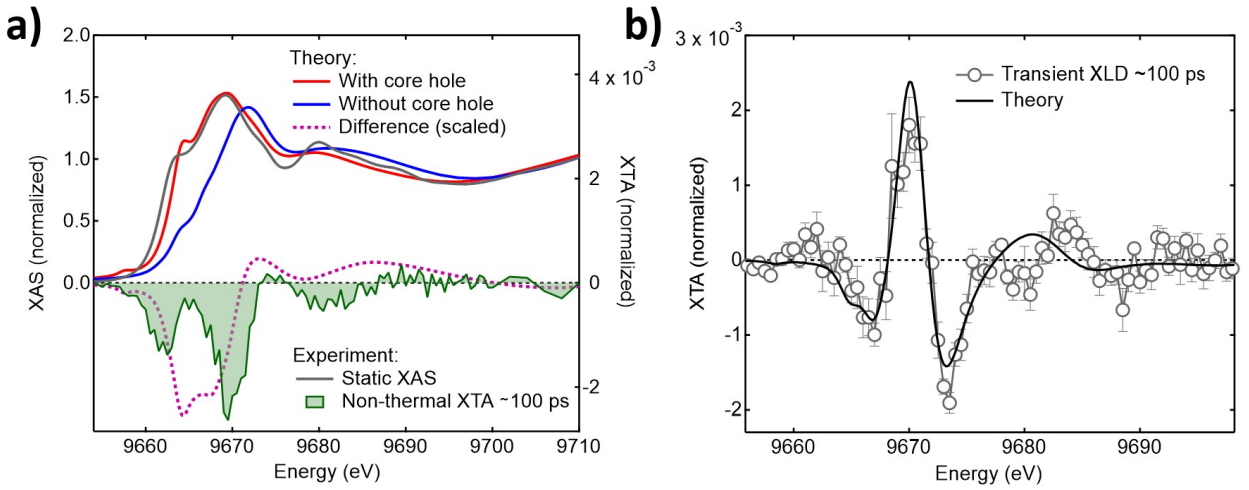

Figure 4.7: a) Ab initio calculations of the XAS spectra at normal incidence is shown with (red) and without (blue) a core-hole, alongside the static spectra XAS (gray). The red trace without a core-hole represents a fully screened core-hole. The difference between the two calculated spectra is compared (dotted line) with the experimental difference spectrum at 100 ps (shaded green). b) Comparison of theoretical (solid black) and experimental transient XLD, at 100 ps (open circles). Adapted from reference [73].

as implemented in, for example, the exciting code.[177], [179]–[181] Figure 4.7a shows the XANES spectra using the real-space DFT based FDMNES code.[182]. The presence of the core hole red shifts the XANES close to the ionization threshold.[183] The difference between the two spectra (without minus with core-hole, matching the transient effects) qualitatively matches the experimental non-thermal spectrum, with a broad bleach centered at and just below the white line. This indicates that enhanced screening of the core-hole predominantly reduces the XAS cross-section, with a minor contribution from a chemical shift. The agreement is only qualitative due to mismatches in the static spectrum, and the partial transient nature of screening by photoexcited carriers.[184], [185] These differences should be independent of the polarization. Figure 4.7b also shows the theoretical XLD spectrum, which has excellent agreement with the experimental transient XLD. The agreement is facilitated by systematic errors at normal and diagonal incidence, for example from many body effects, effectively canceling out. This demonstrates the utility of transient XLD in being able to substantiate observations without the need for extensive, high level calculations.

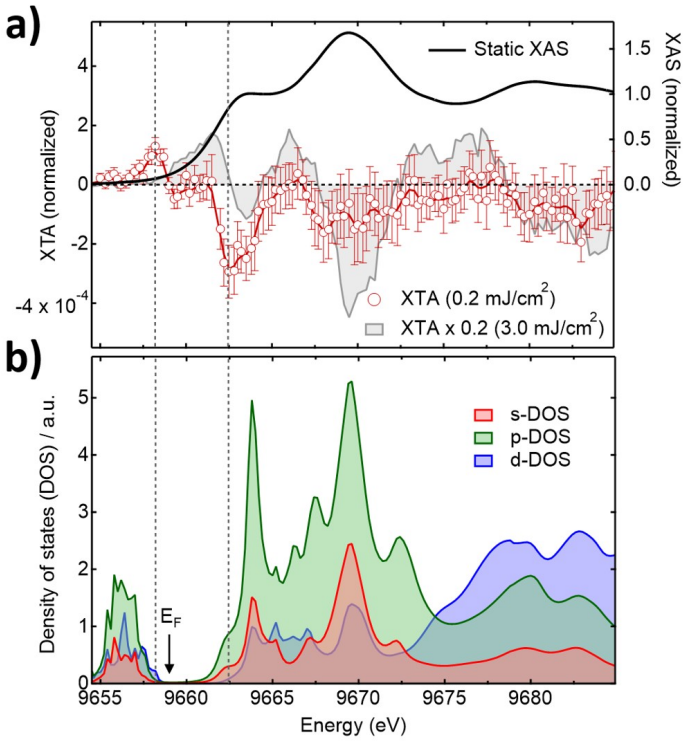

Figure 4.8: (a) XTA spectra at normal incidence, ∼100 ps, low laser fluence (∼0.2 mJ/cm^2, red circles) and higher laser fluence (3.0 mJ/cm^2, scaled by 0.2, gray-shaded curve, both left axis). The solid red line is a trendline. The experimental static XAS is shown with a black curve for reference (right axis). (b) Calculated Zn s-projected (shaded red), p-projected (shaded green), and d-projected (shaded blue) DOS with core hole calculated with the FDMNES code. Vertical dashed lines are centered at the PSF features in the low-fluence XTA. The Fermi energy is indicated in (b) by an arrow. Adapted from reference [73].

4.5 Phase Space Filling in Transient X-ray Spectroscopy

Excitation densities above 5e^{18}cm^{-3} show predominantly effects from the heat jump and non-local core-hole screening. Below this carrier density and with low laser fluence (<1mJ/cm^{-2}) both thermal and core-hole effects are reduced, allowing the observation of transient PSF to become visible as seen in figure 4.8a at normal incidence and lower fluence. This is seen as an increased absorption signal just below the Fermi level (E_F) due to the presence of holes at 9658 keV, matched by decreased absorption above the Fermi level due to phototexcited electrons at 9663 eV. Transient XPSF has been previously observed at L-[186], [187] and M-edges[160], [188]–[190]. The absence of signals that were attributed to thermal effects and

core-hole screening are evident by comparing the gray shaded area in 4.8a. There is still a moderate negative contribution at the white line and above the electron PSF signal (9662.5 eV), showing there is still a contribution to the signal from core-hole screening. This shows that the PSF siganl is highly dependent on the carrier concentration relative to the Mott density. The lack of a noticeable PSF signal in the high fluence regime could be because the the strong positive signal at 9661 eV subsumes the signal.

As seen by the vertical dashed lines in figure 4.8b, the position of these features matches the band edges in the l-projected density of states (DOS) as calculated with the FDMNES code.[44] in the presence of an unscreened core-hole. The agreement is very striking since the interaction of the core-hole with the valence states is not included in these calculations. The cost of calculating the DOS is less for the K-edge than at the L- or M- edges since the excitonic interaction needs to be included to match the experimental PSF signals.[188], [191], [192] In ZnO, the s- and d- states are hybridized with with the p- states due to the tetrahedral geometry of the Zn atoms. Thus the low energy positive feature is attributed to photogenerated holes in the valence band which gains intensity through hybridization of Zn d- and p- states, while the high energy bleach (9662.5 eV) is partially attributed to PSF of excited electrons in the conduction band occupying states with p-symmetry. The features above 9662.5 eV cannot be attributed to PSF since the occupation of those states would require very high carrier concentrations and hot population. They are attributed instead to transient core-hole screening.

4.6 Conclusion and Outlook

This chapter presents the results of transient X-ray linear dichroism on oriented ZnO nanorods. These results used transient XLD to subtract out the isotropic thermal effects from laser excitation, remove systematic errors in ab initio calculations, and support the observation of a reduction in absorption intensity that scales with the transition intensity. This technique

offers utility beyond what's been shown here. Transient XLD can extract information on the transient, orbital specific effects after photoexcitation. On the timescale investigated here, there was no discernable difference between the photodynamics of the a/b and c crystal axes. However on timescales below 10 ps there is transient optical dichroism, as revealed by ultrafast ellipsometry.[107], [193] Anisotropic core hole screening has also been reported.[178] This motivates a transient XLD experiment at high brilliance facilities capable of femtosecond resolution, such as an X-ray free electron laser.[194], [195] Further, materials like anatase TiO_2 that have anisotropic crystal structures and excitons oriented along crystal axes are perfect candidates for this technique.[90]

The careful calibration and subtraction of thermal effects reveals a novel electronic effect that has not been reported previously, but is expected to play a significant role in other XTA measurements at high carrier concentrations. The significance of this signal will depend on the material though. For instance, strongly correlated conduction band carriers are may affect the strength of core-hole screening.[196] The identification and assignment of the XTA features was supported with ab initio XAS calculations. Finally, the first observation of PSF in the hard X-ray regime was reported. This measurement was only made possible when high carrier concentrations did not overwhelm the modest electronic signal from PSF, and thermal effects were essentially negligible.

The PSF signal has the most import for a charge injection study. The carrier concentration in ZnO will likely be substantially lower from charge injection and thermal effects will be less prominent at the Zn edge since it is not being directly excited. Chapter 5 pairs these X-ray results with OTA to discern the limiting factors for an XTA QDH charge transfer study.

Acknowledgements.

I thank Thomas Rossi for help with the data collection, workup, and interpretation. I thank the AMO Physics Group at Argonne National Labs for their expertise running time-resolved

beamtimes. I also thank the group of students who have consistently helped run these experiments including Cecilia Gentle, Tyler Haddock, Rachel Wallick, Jack Burke. I also thank the Materials Research Lab for providing the facilities and instruments for synthesizing samples and characterizations.

Chapter 5

Feasibility of Transient X-ray Absorption on Quantum Dot Sensitized ZnO

5.1 Introduction

This chapter presents the opportunities and constraints in applying XTA to a charge injection study with QDHs. XTA, as an element specific core-hole spectroscopy, is sensitive to electro-structural distortions on a per-atom basis, making it a powerful tool for characterizing trap states.[74], [78] A transient X-ray PSF signal that has been normalized by the static spectrum (figure 4.6) represents an electronic change per atom, which depends on the number of carriers in the conduction and valence band against the projected DOS. The carrier signature from PSF can benchmark the timescale of charge injection. These powerful experiments have numerous constraints though, including low time resolution, tight experimental time windows, lower SNR than optical techniques, and high excitation powers. Establishing the conditions necessary for a successful XTA measurement will save critical resources.

Optical and X-ray techniques are complementary, where OTA is sensitive to changes in electronic transitions and insensitive to optically dark states, such as trapping at defects or spin forbidden transitions.[197]–[200] The X-ray PSF signal can be related to an optical PSF signal in ZnO because photoexcited carriers at the conduction band minimum or valence band maximum block the excitonic transition.[90], [201], [202] Thus the magnitude of the optical signal from OTA can be directly correlated with the expected PSF magnitude in XTA with

proper control experiments. The difficulty of normalizing OTA per-atom is circumvented by measuring identical samples and under identical conditions to the results of chapter 4. This would not be possible for an indirect band gap material like TiO_2, where charge injection induces Coulombic screening of the excitonic transition and does not have a significant PSF.[90]

Multiple factors come into play in synchrotron experiments including the timescale of processes, sensitivity to the desired signal, and sample integrity. Section 5.2 presents these considerations, which is followed by a discussion of the relevant optical processes in section 5.3. The experimental constraints are presented from the sample perspective in section 5.4, followed by the correlation of optical data with XTA data from 4.5 in section 5.5. Finally, section 5.6 presents the holistic view of the system and suitability for transient XAS.

5.2 X-ray to Optical Regimes

The first consideration when designing an XTA experiment is whether the timescale of the phenomenon matches the synchrotron capabilities. As discussed in section 3.5.2, the APS has a time resolution of ∼80 ps.[129] While it is possible to extract information on processes earlier than this limit,[203] in this case the low time resolution will likely work in favor of charge injection since back electron transfer will occur on the 100's of ns timescale.[20], [34], [71], [83] Optical experiments have much finer time resolution, on the order of ∼130 fs, which allows us to say with certainty whether the charge injection phenomena will be isolated, or overlap with extraneous effects. Of particular interest is the timescale of two-photon absorption (2PA). 2PA becomes relevant when high fluences induce simultaneous absorption of two photons. The wurtzite crystal structure of ZnO has no inversion symmetry, and thus a non-zero third order susceptibility, which enhances 2PA.[204], [205]

The laser fluence needed to achieve the threshold XTA signal in a charge injection experiment, where phase space filling can be measured within 1 day, will have complications

from 2PA and thermal effects. 2PA will directly excite the ZnO through absorption of two photons at 532 nm, which creates a second PSF signal that obscures charge injection, both in OTA and XTA experiments. In order to obtain an accurate measure of the magnitude of charge injection, the 2PA signal must be subtracted out. This will be done by measuring a thorough fluence dependent measurement as presented in sections 5.3 and 5.5. Thermal effects can dominate XTA spectra at high fluences and overwhelm smaller, electronic effects.[9], [73], [74], [154], [206] It is necessary then to achieve threshold signal levels through charge injection with an upper bound on the laser fluence we use. It is unknown if, with highly excited quantum dots, thermal energy will be transferred from quantum dots to the ZnO with enough efficiency to complicate a Zn K-edge XTA measurement, but it undoubtedly will complicate a measurement at the Se K-edge of the CdSe quantum dots. One consideration is that charge injection may occur solely from thermalized band edge carriers. In that scenario the signal from charge injection will saturate once all QDs are excited, which would place an upper bound on the useful fluence. Once all quantum dots are excited the theoretical charge injection limit would be reached.

A last consideration in a multi-day, high fluence charge injection XTA study is the quantum dot sample integrity. Oxidation, photooxidation, and photocorrosion can strip quantum dots of their surface ligands and etch away the surface.[99] These effects can disturb the electronic structure of a quantum dot by modulating the confinement energy and ligand field effects, and compromise the attachment to ZnO as well as make charge injection energetically unfavorable. This has been approached a number of ways, including through environmental controls like preparing samples under inert atmosphere. Synthetic methods employ core-shell architectures with type II, quasi type II, or inverted type I band alignments,[127], [207] or less often around photo-oxidation resistant ligands.[208] The stability of these samples under XTA conditions is examined in section 5.4.

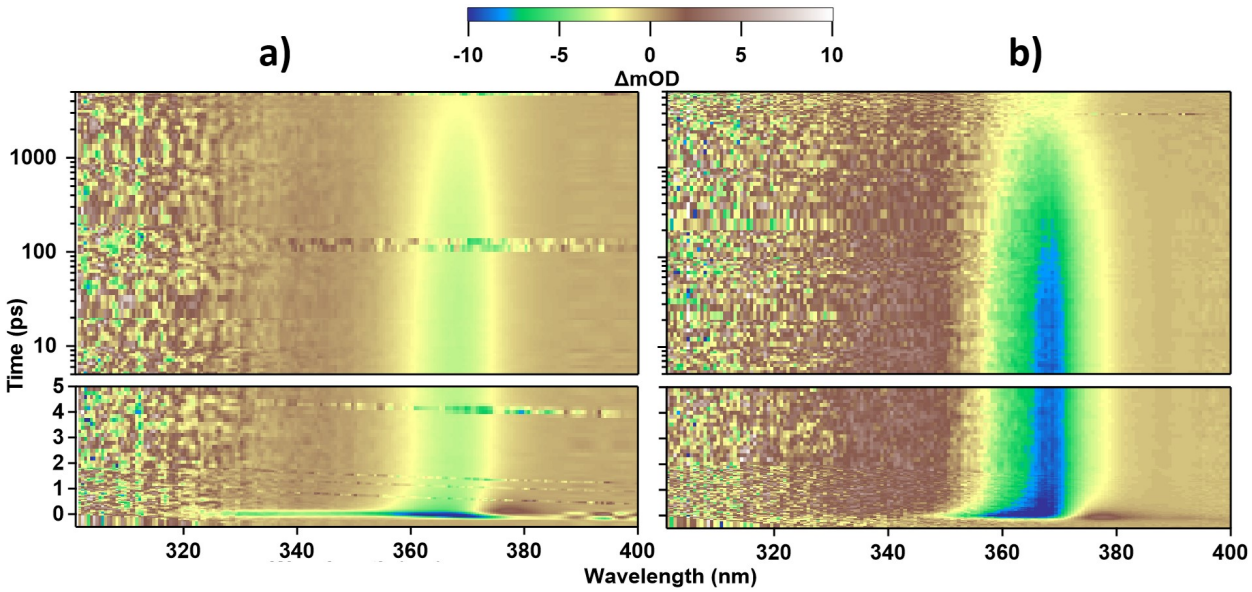

Figure 5.1: a) 2D plots of ZnO excited 960 $\mu J/cm^2$ of 532 nm light and b) with 5.5 $\mu J/cm^2$ of 300 nm light. The bleach of the exciton is centered at 365 nm. The decay is biexponential with direct excitation (100 ps, >5 ns), and 4 exponential with two-photon absorption (0.1 ps, 0.5 ps, 250 ps, >5 ns) partially due to the strong SPM feature .

5.3 Direct and Two-Photon Excitation of ZnO

The first objective is to relate the optical PSF amplitude to the approximate carrier concentration. Direct excitation of ZnO with 300 nm light excites carriers at the Γ point of the Brillouin zone into the conduction band. An exciton with a binding energy of 60 meV forms after the carriers cool down to the band edge.[209] As a direct band gap material phase space filling is the dominant effect from direct excitation and charge injection, with minor contributions from coulombic screening.[90] PSF manifests as a bleach of the ground state transition at 365 nm, as seen in figure 5.1 that scales with the carrier concentration. The relationship is linear at moderate carrier concentrations, but will be subsumed at high carrier concentrations close to the Mott density by carrier screening and the dissolution of excitons.

2PA in ZnO will complicate XTA measurements at high fluence since it will give overlapping signals with charge injection. In addition it will depend on the peak intensity of the pumping laser and the orientation of the nanorods, both of which are relevant experimental

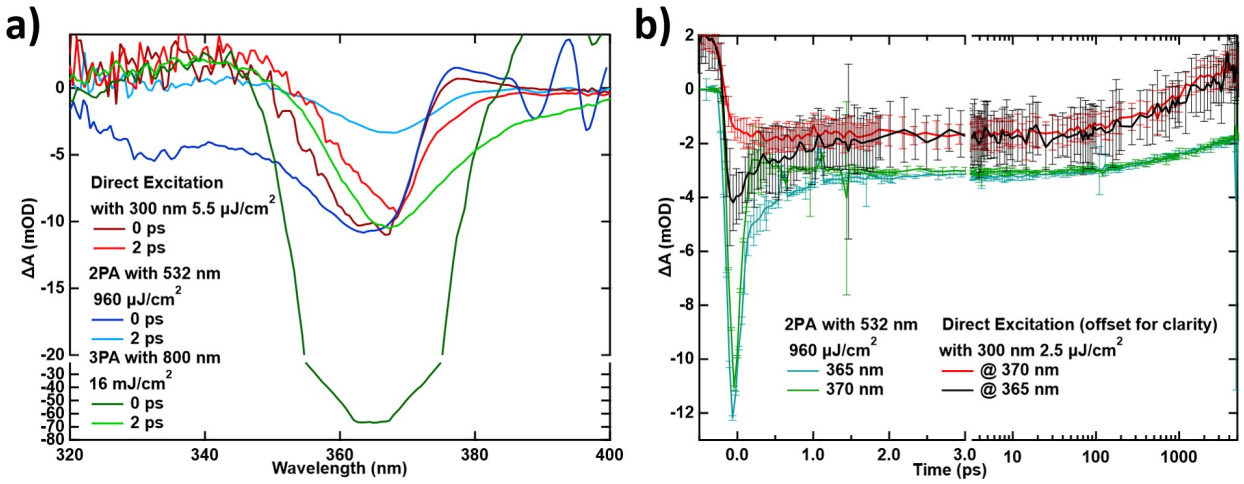

Figure 5.2: A comparison of spectral and kinetic characteristics between direct and two-photon excitation is shown. At left is a spectral comparison of the same datasets taken at 0 ps, 2 ps, and 1 ns for the 2PA (black, red, yellow) and direct (dark blue, light blue, green) excitations. At right are kinetic traces at 360, 365, and 370 nm of samples with identical peak amplitudes. In dark blue, light blue, and green are kinetics traces for 2PA with 960 μJ/cm^2 excitation of 532 nm. There is an IRF limited decay on the order of 100 fs, followed by a >7 ns decay. The black, red, and yellow traces are kinetic traces after direct excitation with 5.5 μJ/cm^2 of 300 nm. There is a rising bleach over 0.4 ps at 370 nm due to the fading band gap renormalization effect as carriers cool to the band edge. The kinetic traces at 360 and 365 do not show the same decay over 0.1 ps as in 2PA, instead showing a decay on the order of 1 ps for possible reasons that are discussed in the text.

parameters.[205], [210]–[213] However, the longer pump pulse (∼10 ps) used in XTA experiments at beamline 7ID-D of the APS[129] - compared to the 130 fs pulse length used in OTA experiments - will produce approximately 80 times less 2PA for identical fluences due to the reduced peak power.

Figure 5.1 shows a 2PA measurement with fluence of 600 $\mu J/cm^2$ with 532 nm light. Near time zero, an excited state absorption (ESA) feature can be seen at 380 nm due to the excited carrier population causing band gap renormalization (BGR). This is balanced out at late times by the Burstein - Moss effect and enhanced the carrier dependent screening of the exciton interaction.[130], [204], [214] A broad positive ESA to the blue of the band gap can be seen in both graphs of figure 5.1, which is the Drude free-carrier response inducing a change in the index of refraction.[130], [215]

A comparison of the spectral features at 0 and 2 ps is shown in figure 5.2 between single-,

two-, and three- photon absorption processes. At 0 ps, the single and two photon experiments show very similar features with a strong bleach at 362 nm due to PSF of the band edge excitonic transition, with an ESA at 378 nm due to band gap renormalization. At later times the band edge bleach shifts to 365 nm as seen at 2 ps. Both 2PA and 3PA traces have a high amplitude bleach at 0 ps that decays between 0 and 2 ps to give similar amplitudes at 2 ps. This signal near t0 scales with the intensity of the pump pulse. This indicates the high intensity bleach in 2PA and 3PA measurements result from self-phase modulation (SPM) rather than being an ultrafast carrier process. The conditions employed to measure X-ray PSF was 0.3 mJ/cm^2 at 355 nm, which gives a bleach of -68 mOD after 100 ps. Two carriers are excited per 350 nm photon and both contribute to the optical PSF signal, but X-ray PSF measures electrons and holes separately and will only measure electrons in a charge injection experiment. The threshold signal level that makes an XTA PSF experiment possible is then half the optical signal, ~ -34 mOD at 100 ps. Below this level, it is anticipated that the time needed to collect data will be too burdensome.

There are slight differences in relaxation kinetics between direct excitation and 2PA, shown in figure 5.2b. 2PA will generate highly excited carriers, which do not contribute to PSF effects and screens the excitonic transition less effectively. The increased penetration depth of 2PA also leads to a homogeneous carrier distribution, whereas direct excitation has a much lower penetration depth and should give an excited carrier population concentrated near the top of the nanorods. The inhomogeneous carrier distribution will saturate surface trap states quickly, then disperse throughout the nanorod before further trapping can occur. Given a carrier diffusivity of 0.05 - 0.5 cm^{2}s^{-1} along the c-axis of wurtzite and at similar carrier concentrations,[216] it could take $\approx$10 - 100 ps for a homogeneous carrier distribution to be reached. This limits the trapping rate and prolongs the excited population lifetime. The time zero signal is much broader in 2PA than in direct excitation, which could be due to rapidly cooling carriers. The selection rules in 2PA allows for a wider momentum range for photoexcited carriers compared to direct excitation.[217] These states cool with varying rates

due to the mix of cooling processes (inter/intra valley scattering) and produce an energetically broad bleach near time zero while the carriers are cooling. A thorough comparison of carrier cooling and trapping in direct and two-photon absorption is beyond the scope of this report.

There are differences in the 2PA kinetics at high fluences, which may be relevant in an XTA experiment. At fluences below 4000 μJ/cm^2, >60% of the IRF limited bleach decays within 3 ps. This is attributed to the strong SPM signal and cooling of the initial hot carrier population at surface defects.[130], [162], [209], [218] Above this level the IRF limited bleach decays less at early times, but there is a pronounced decay on the time scale of 100's of ps and 7 - 8 ns that increases from <5%, with 1 mJ/cm^2, to 20%, with 4 mJ/cm^2. These two timescales can be attributed to recombination at the surface and in the bulk for the 100 ps and multi-ns components respectively.[219] The shift in relative amplitude from short to long timescales could be due to a saturation of surface defect states at high fluences, followed by defect mediated recombination and subsequent trapping at the now vacant trap states. Before being used to interpret charge injection results, the 2PA datasets were compiled as described in section 3.6.1.

5.4 Sample Integrity and Homogeneity

To assess the optimal sample conditions for XTA, a few experiments were done with variable QD sizes and organic linkers with the goal being to characterize the timescales of charge injection, the stability over multiple measurements, and the variation with fluence.

Figure 5.3a shows the results of charge injection at the ZnO band gap with low fluence for 3 QDHs exploring the size and organic linker parameter space. In the figure, three different systems are compared at the peak of the ZnO excitonic bleach: 3.9 nm QDs molecularly attached with either MPA or DMPS, and 2.9 nm QDs linked with DMPS. The traces are not normalized, and show the magnitude of charge injection in the three systems with similar levels of excitation. Charge injection occurs gradually over 50 ps for the DMPS samples, and

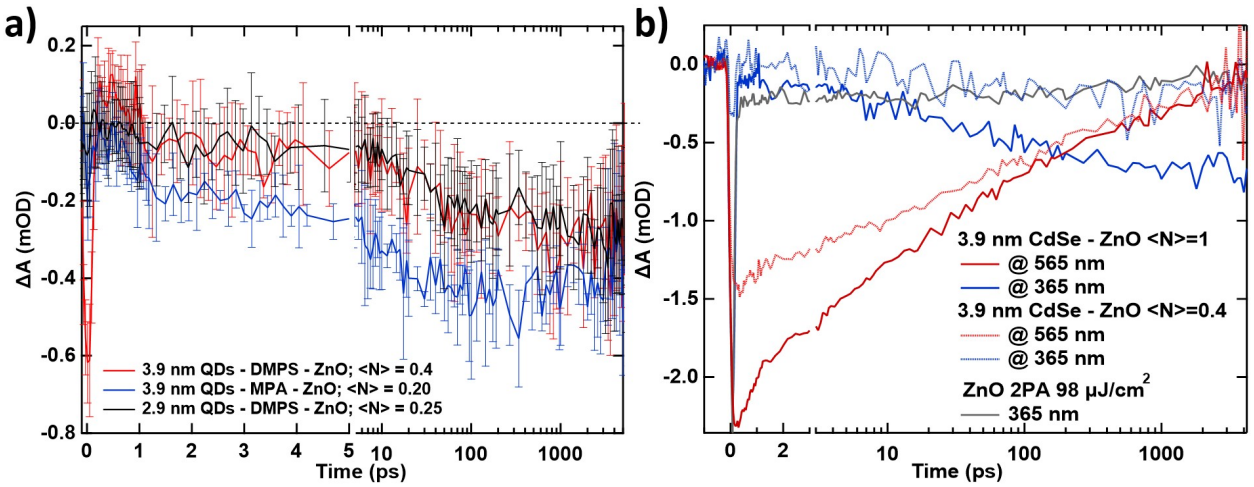

Figure 5.3: a) Comparison of the charge injection kinetics across samples. At left the kinetics of 3 systems are compared at 365 nm: 3.9 nm QDs conjugated to ZnO with either MPA (blue) or DMPS (red) along with 2.9 nm QDs conjugated to ZnO with DMPS (black). The systems were excited with 532 nm light and an average exciton of between 0.2 and 0.4. b) Fluence dependent kinetics of charge injection for 3.9 nm CdSe - MPA - ZnO for <N> of 1 (dark red/dark blue for visible/UV), and for <N>of 0.4 (light red/light blue for visible/UV). Also shown is the approximate 2PA contribution (gray).

occurring faster and with greater yield for the MPA CdSe, likely due to the improved electronic coupling. The slow rise in the ZnO bleach has been observed in previous experiments with QD - ZnO and dye - ZnO systems with time resolved terahertz and infrared spectroscopy. This is typically attributed to the formation of an interfacial charge-transfer (CT) exciton. The CT exciton is estimated to have a binding energy of 150 meV and dissociates in 40 - 200 ps.[34], [52], [220] This will be returned to in chapter 6.

The matching kinetics and yield of the DMPS samples, regardless of QD size, shows that DMPS stunts charge injection. These samples do not have similar quantum dot coverage. This discrepancy is largest between the 2.9 nm QD sample and all other samples. For example, while the 2.9 nm QDs - DMPS - ZnO sample has <N>= 0.25, this describes the expected fraction of quantum dots that have multiexcitons rather than the absolute excited QD population. That sample had many more excited QDs than either other sample. In addition, the two DMPS samples have nearly identical charge injection levels, despite similar levels of excited quantum dot population. The sample conjugated with MPA thus has much

greater charge injection than either other sample despite having fewer excited quantum dots and lower driving force. These results indicate that MPA leads to greater charge injection, most likely due to the shorter QD to metal oxide distance in MPA vs. DMPS, which motivates using MPA over NaDMPS.

Figure 5.3b shows the dependence of charge injection on the excitation power for the 3.9 nm - DMPS - ZnO system. Since these QDs are being excited above the band gap, an excitation of <N>= 1 produces a distribution where 37% of QDs are singly excited, 18% of QDs are doubly excited, and 8% of QDs are excited with 3 or more excitons. At the QD band gap, 23 % of the signal decays within 1.7 ps, which reflects the Auger recombination of multiexcitons. There is no corresponding rise in the ZnO signal, and the kinetics of the <N>of 0.4 sample is identical to the high fluence sample, where only 6% of the QD population is more than singly excited. A consideration outlined in 5.2 is that charge transfer may only take place from fully thermalized carriers, which is justified when considering that the timescale of charge injection is mostly insensitive to the concentration of multi-excitons. If charge injection occurred through hot states it would be expected that the UV signal would rise as recombination occurred. Following this, maximizing the driving force between ZnO and CdSe with small QDs is likely to yield the most charge injection.

Experiments with a photoxidation-resistant ligand seemed to lower charge injection, as seen in figure 5.3a from the comparison of MPA and DMPS organic linkers. In terms of stability, counterintuitively MPA gives more stable QDs during charge injection as seen in figure 5.4a and b. The contours trace a -0.5 ΔmOD surface in the quantum dot kinetics. The samples shown are 3.9 nm QDs attached to ZnO either with MPA (5.4a) or NaDMPS (5.4b). The contour area reflects the magnitude of the signal, and the change in the contour area from scan to scan reflects a change in the bleach response due to photodegradation. With similar concentration and excitation conditions, the quantum dots attached with MPA show a greater magnitude of bleach and less degradation from scan to scan. NaDMPS was used because it has been shown to prolong stability in solution, but the result in a charge

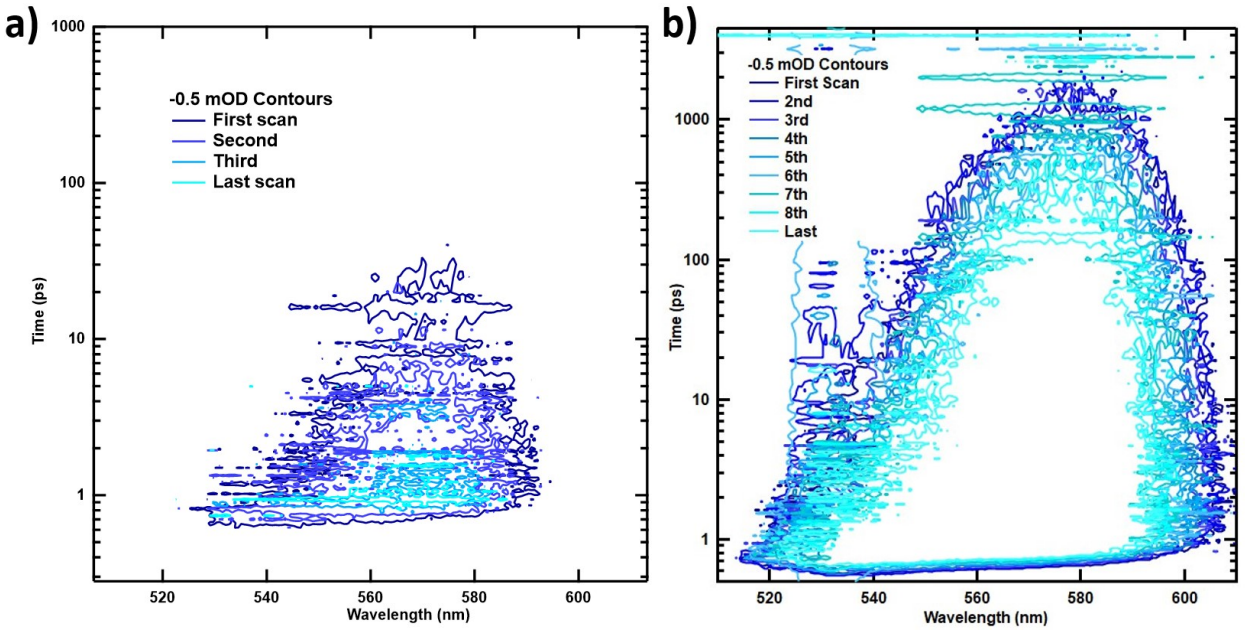

Figure 5.4: Contour plots showing the spectral change over time of two ZnO - QD samples with 3.9 nm CdSe QDs and excited with identical fluences, using the chemical linker a) DMPS and b) MPA. Both samples were detected in the visible, where the peak of the exciton is 580 nm.

transfer system was a less robust system, contrary to expectations. There have been mixed results on the utility of dithiols in preventing photooxidation, which has been attributed to the difference in steric hindrance between a 1,2- and a 1,3- disulfide bond.[85], [99] In the charge transfer system studied here, DMPS did not improve the stability.

During OTA studies quantum dot integrity can be directly assessed by changes in exciton peak positions, new kinetic decay channels, and reduced charge injection amplitude in the UV.[83] Under XTA conditions it is to observe the effects of photoxidation due to the presence of 2PA and thermal effects from the laser as well as the long measurement times. Presumably if a clear charge injection signature can be observed in ZnO then it will also be possible to monitor photoxidation indirectly. In the interest of limiting photoxidation during OTA studies, the sample was moved every 30 minutes and kept under flowing nitrogen. It was possible to continuously move the sample, but sample inhomogeneity increases the noise level significantly. Samples showed 30 to 50% variation in charge injection over the sample surface, which likely reflects uneven QD deposition. Constant sample motion is also not

available during experiments at the APS due to sample stage jitter and movement backlash. In addition, it would be desirable to conduct X-ray transient linear dichroism spectroscopy, which would require rotating the sample and maintaining a center of rotation. A static sample position then provides critical information on the expected sample stability during an XTA measurement.

5.5 Charge Injection from CdSe

To have the best chance at measuring X-ray PSF in QDHs, charge injection needs to be maximized. Achieving sufficient charge injection, regardless of the neatness of the QDH interface, is the priority. There are multiple factors that determine the yield of charge. The organic ligand length, the band gap offset between QD and metal oxide, the percent of excited QDs, and their excitonic state. MPA is typically used as the connecting ligand between QDs and MOs due to its short length ensuring good electronic coupling. The second harmonic available for pumping at the APS is 532 nm, which constrains the size of QDs that can be used. QDs smaller than 2.82 nm will have too large of a band gap for excitation. Using larger QDs will bring higher excitonic transitions into the pumping wavelength range, which allows for higher excitation densities than pumping at the band edge due to the low degeneracy (2). However, larger QDs will have a lower driving force (see section 2.2) than smaller QDs which would give a slower charge injection rate and thus more competition from auger and carrier recombination processes.

Figure 5.5 is a compilation of the peak charge injection signal from across a few series of measurements. The first few measurements, shown in blue, had by far the weakest signal of a few hundreds of μOD. The levels of charge injection reached from the second (red) and third (orange) generation measurements was larger and consistently -2 to -3 mOD, but still low. The green dots show a single sample that far exceeded expectations, reaching as far as -14 mOD.

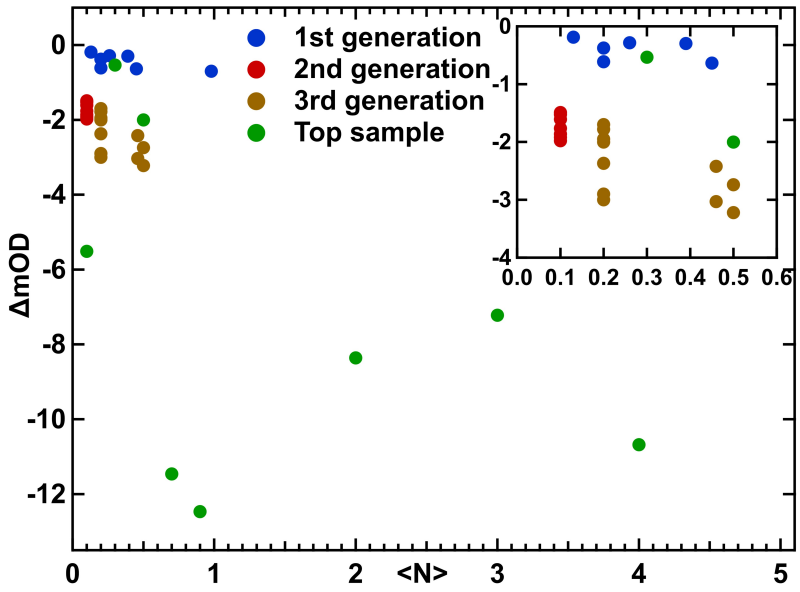

Figure 5.5: The figure at right compares the peak charge injection amplitude across all samples, divided up into batches of samples and measurements. In blue are the first samples created and measured, followed by red and brown as the 2nd and 3rd batches respectively. In green is the sample with the largest charge injection signal measured.

Figure 5.6 shows the 2D map of 2.9 nm CdSe - MPA - ZnO sample excited with a fluence of 596 $\mu J/cm^2$ before (a) and after (b) 2PA subtraction. There is a slight ESA at 380 nm that is not completely removed after 2PA subtraction. This feature can be attributed to the CdSe quantum dots, which has an ESA feature located here. This signal is broad enough to overlap with the excitonic bleach in ZnO, but is weak and does not interfere with the interpretation of the peak bleach amplitude from charge injection. The subtraction of 2PA is

The contribution of 2PA to the kinetic traces at various fluences is shown in figure 5.7a. At low fluences, the magnitude of 2PA is low and reaches a minimum after 2 ps. High fluence measurements have significant 2PA amplitude at later times that may not be completely subtracted out. Figure 5.7b shows the kinetics and amplitude of the charge injection dataset with the greatest charge injection, after subtracting out the 2PA signal. At low fluence (<N> <1) the ZnO bleach rises over the first 10 ps, and levels off at 100 ps followed by a slight decay of the signal over multiple nanoseconds. At high fluence (<N> >1, right) charge injection is almost IRF limited followed by a substantial decay over the experimental

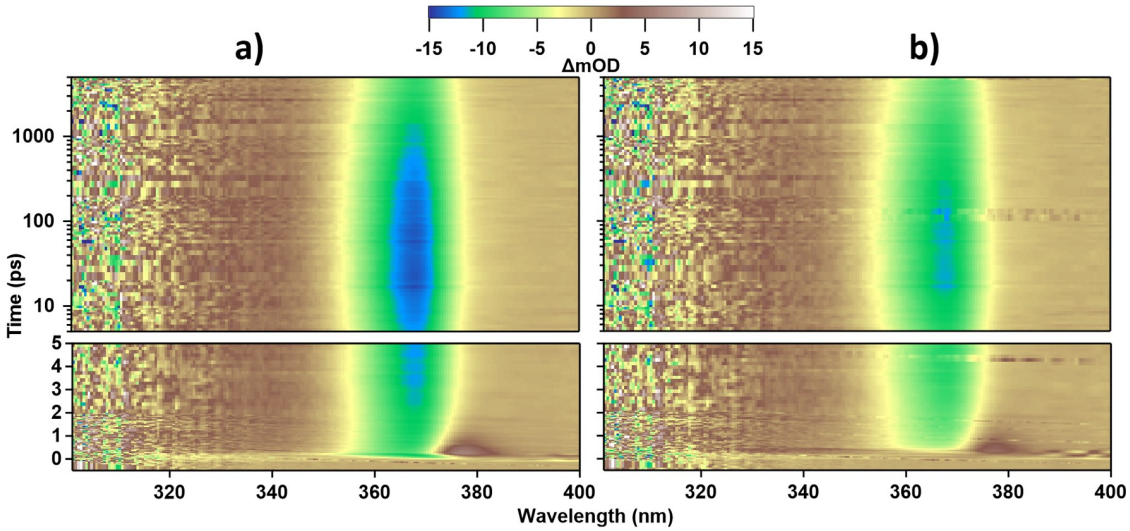

Figure 5.6: 2D plots of 2.9 nm CdSe - MPA - ZnO excited with 596 $\mu J/cm^2$ of 532 nm light (left). At right is the data after subtracting out the 2PA absorption component. The 2PA that was subtracted from the CdSe-ZnO was matched to the IRF limited rise, without creating a high energy ESA.

time window. The decay of the UV signal seen in figure 5.7b in all datasets on the ∼100 ps timescale may be attributed to back electron transfer,[34], [68]–[70] it is more likely to be due to carrier trapping as there is no decay of the visible signal seen here. This decay is much more substantial at high fluence as seen in figure 5.7b, which is unusual in that it suggests enhanced back electron transfer or carrier recombination/trapping from the high, 2PA induced carrier concentration. However there is not a literature precedent for such high fluence charge injection measurements.

The results shown in figure 5.7b offer critical insights. Low excitation conditions (<N> <1), shown in figure 5.3a, had injection time scales of 10's to 100's of ps that was consistent at higher excitations. The 2PA subtracted datasets show different kinetic regimes at high and low excitation conditions though. Fluences high enough to saturate the band edge exciton state show much quicker injection kinetics, indicating that the CdSe biexciton state could be involved in charge transfer through an auger-assisted type mechanism.[221], [222] This behavior is undesirable for a synchrotron experiment, and could complicate faster resolution experiment such as an X-ray free electron laser (XFEL). Charge injection that takes place

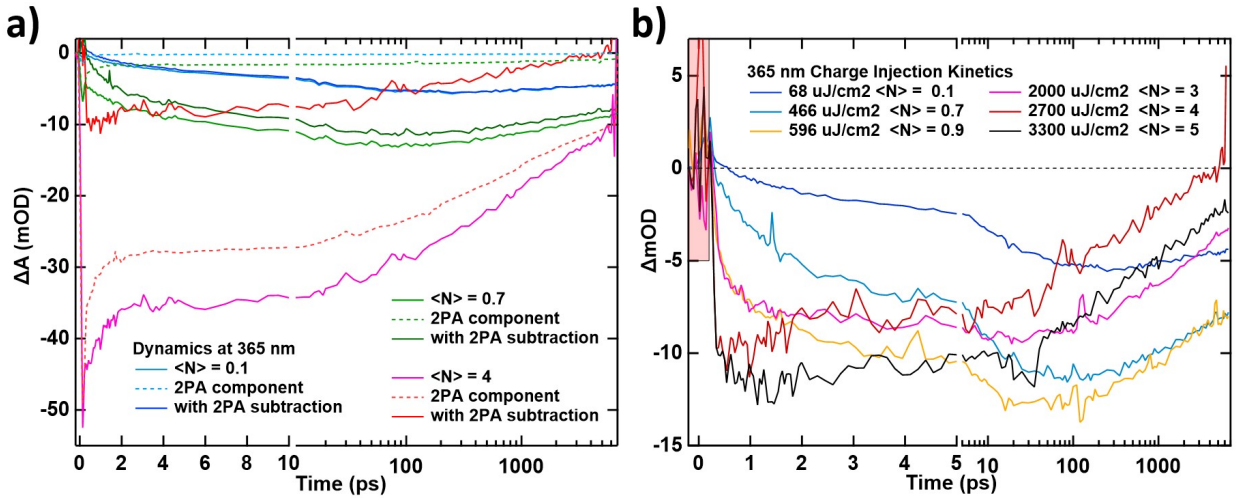

Figure 5.7: a) A comparison for three fluences (<N > = 0.1, 0.7, 4) of the raw charge injection signal (pink, light green, light blue), the 2PA contribution (dotted red, green, blue), and the resulting 2PA subtracted data (red, dark green, dark blue). b) The kinetics at the peak of the ZnO exciton for the best charge injection sample, after subtracting out the 2PA contribution, over a range of fluences. The red box indicates the region where the 2PA signal was gauged against the SPM.

over 100's of ps with limited decay over nanoseconds is ideal for the limited time resolution of a synchrotron and would allow charge injection to outlast the 2PA signal. Having a large discrepancy in the time scales of charge injection and 2PA would allow the two contributions to be disentangled simply by measuring data at different times. At any fluence that induces both 2PA and charge injection, 2PA decays when charge injection is reaching its maximum. The remaining amplitude decays on the time scale of 10 ns as expected of carrier recombination in ZnO as shown in figure 5.7b.[162] Charge injection is expected to reach a maximum after 100 ps and then level off, with a slow decay due to carrier recombination, back electron transfer, and trapping. Features of an XTA spectrum that decay from early to late times could be attributed to 2PA, while features that grow from early to late times could be attributed to charge injection, and measuring 10's of nanoseconds after excitation would have a very low contribution from 2PA. Separating 2PA from charge injection in an XTA measurement then would not necessarily require an extensive 2PA dataset. Having the two processes take place over similar time scales, as in the <N> = 4 and 5 data in figure 5.7b, convolutes the two and

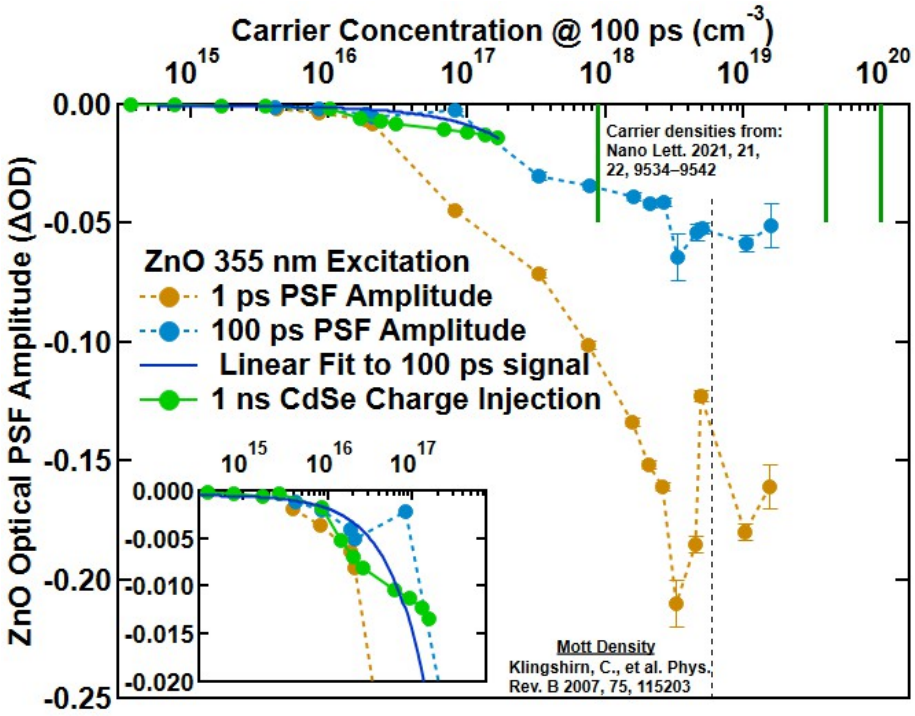

Figure 5.8: Using the equation 3.17, the carrier concentration of a ZnO nanorod sample was estimated at 100 ps from excitation with 320 nm light, and plotted against carrier concentration. The amplitude is plotted 1 ps after excitation (orange trace) and after 100 ps (blue trace). The estimated carrier concentrations from the APS are shown on the top axis as green bars, along with an estimate of the Mott density in ZnO (dotted lines) taken from reference [131]. Two ZnO-CdSe samples are also shown with the peak amplitude from charge injection plotted with various fluences and the peak charge injection signal reached.

would require a complete 2PA fluence dataset, as demonstrated in these OTA experiments. The advantage of a synchrotron is that 2PA is expected to be 80 times less prominent at an XTA beamline, as mentioned in section 5.3. The impact of 2PA will be more substantial at an XFEL where the short laser pulses (<100 fs) create high peak powers, which would produce more 2PA.

A greater issue than 2PA are the signs of saturation in the charge injection kinetics. While this was predicted to be present, the charge injection yield per quantum dot is low for most samples. In figure 5.7b the signal at <N>=0.9 rises from -12 mOD to -14 mOD at <N>= 5, which is an increase of 16% in charge injection yield while the total fraction of excited quantum dots rises by almost 33 %. This is an indication that the majority of QDs that

inject carriers only inject a single carrier. This is evidenced by the fact that the percentage of QDs with a biexciton rises from 16.4 % at <N>= 0.9 to 97 % at <N>= 5 again without a corresponding increase in charge injection amplitude. On the other hand, as seen in figure 5.7a, 2PA rises steadily. As the fluence increases the percentage of the signal at 1 ns due to 2PA rises from $\approx 0\%$ to almost 60 %. This is partially due to the increase in 2PA, but also to the decay of injected carriers at high fluences. This can be seen in figure 5.7b at high fluence where the signal from charge injection decays nearly to 0 after 6 nanoseconds while the 2PA signal persists, compared to low fluence where the charge injection signal outlasts the experimental time window.

Figure 5.8 is a comparison between direct excitation and charge injection (with 2PA subtraction) amplitudes at excitation fluences comparable to the X-ray PSF measurement. The amplitude of the bleach of the ZnO transition after excitation with 300 nm is shown at 1 ps and at 100 ps against the carrier concentration at 100 ps. The carrier concentration was calculated at each fluence with equation 3.17. Shown in green are the bleach amplitudes from a typical conjugated sample and from the best charge injection sample, respectively. The 100 ps bleach from direct excitation was linearly fit, shown as a solid blue line, and required to pass through 0. The slope of the linear fit was $-4.7e^{-19} \pm 0.2e{-}19$. This linear fit was used to align the bleach amplitude from charge injection with carrier concentration. Also shown are markers indicating the Mott density and the carrier concentration used during the X-ray PSF measurements. As discussed in 5.3, a signal level of -68 mOD was recorded at 100 ps after direct excitation with 0.2 mJ/cm^2 of 300 nm light, which defines twice the signal amplitude that needs to be reached from charge injection to match the carrier concentration at the APS, given by the intersection of the green bar at $10e^{18}cm^{-3}$ and the blue data. As seen in figure 5.5, typical samples reached a charge injection amplitude of -3 mOD, and the peak magnitude reached from a sensitized system was -14 mOD (green), 41% (-34 mOD / -14 mOD) of the X-ray PSF signal. The standard deviation improves with the square root of the integration time, so the required time to average the X-ray PSF signal from charge injection

would be ∼6.3 days to achieve the necessary level of SNR (∼ 4.6). As discussed in section 5.4, this sample was highly inhomogeneous and irreproducible. Most samples gave less deviation across the sample, but the strongest signal only gave high charge injection across narrow regions of the sample. The low charge injection signal taken with the unfavorable kinetics at high fluence make this system unfeasible for an XTA experiment.

5.6 Conclusions and Outlook

Using comparative measurements between OTA and XTA on similar systems, synchrotron-based XTA charge injection experiments on quantum dots chemically coupled to ZnO has been found to be unfeasible due to the limited charge injection and sample inhomogeneity that would give unreliable and long data integration times. Excitation with 0.2 mJ/cm^2 at 300 nm, similar to conditions at the APS synchrotron, produced a bleach at 365 nm of -68 mOD in 1 μm long ZnO nanorods. This matches the conditions under which phase space filling was measured over the course of a single day at the APS, and determines the threshold OTA signal needed from charge injection. The best sample that has been produced achieved a signal level of -14 mOD, which would require ∼ 6 days of integration time to reach an SNR of ∼ 4.6. This magnitude of signal was not reproducible, and all samples suffered from a degree of inhomogeneity. At high fluences the kinetics of charge injection and 2PA were very similar, which convolutes the two signals and would require much more data to separate out the two effects during an XTA measurement. 2PA is a complicating feature in high fluence OTA measurements, but is expected to be reduced in amplitude by around 60 times due to the lower peak power from the long laser pulses at the APS. However this does not overcome the fundamentally low signal from charge injection. XTA has slower feedback than OTA due to it is highly monochromatized detection scheme, which means that problems during a beamtime would be difficult to address in a timely manner.

Across a range of experimental conjugation procedures with high-quality CdSe quantum

dots, the best samples produced still fall short of being viable samples for an XTA beamtime. However, this method sets the groundwork for a future charge injection beamtime and allows us to gauge what is a necessary level of signal for this system, or other systems that inject charge, such as dye-sensitized ZnO. Adding a shell to CdSe is unlikely to improve charge transfer except for quasi-type II or inverted type-I, but using a linking ligand that improves electronic coupling (such as exciton delocalizing ligands, or few atom inorganic ligands) may improve charge transfer enough to surpass the threshold signal level.[145], [207], [223] However, this work has demonstrated the power of dual UV-Vis probe OTA and opened avenues for investigation. Phenomenon that are difficult to directly characterize, or that require complex data fitting schemes, can be studied with this technique for relatively few tradeoffs. Phenomena this technique can be readily applied to are comparative studies of the timescale of extraction for multiple electrons through multi-exciton generation or hot electron transfer, or evaluating the quantum yield of QDHs on the ultrafast timescale.

Acknowledgements

I thank Michael Enright for supplying the CdSe used in this data. I thank Tyler Haddock and Thomas Rossi for a superior OTA setup.

Chapter 6

Dual Probe Optical Transient Absorption on CdSe - ZnO

6.1 Introduction

Chapter 5 applied UV-visible probe OTA for a comparative study to the XTA results of chapter 4. XTA provides the utility of investigating material specific structural and electronic changes, which provides insight into lattice distortions and trap states as well as giving direct, accurate timescales for charge injection. Dual probe OTA can provide the material specificity with the spectral separation between QD and ZnO band gap transitions. While electrons in ZnO and holes in CdSe are trapped in optically dark states,[130], [224], [225] the electronic transitions probed in OTA does allow for a sensitive measure of the charge injection time scale. The holistic dynamics of the photoexcitated carrier population can also be correlated between the two materials. Section 6.2 interprets the dynamics after QD band gap excitation for a single size of QD-ZnO heterostructure. Analysis of that system reveals biexponential injection kinetics that is attributed to heterogeneity of the ZnO surface chemistry. That is followed by section 6.3, which investigates the QD size dependence of an optically dark, intermediate state. Global fitting is applied to propose a holistic kinetic model that addresses both the heterogeneity of charge injection and the size dependence of the intermediate state.

6.2 Evidence for Split QD Populations

Broadband UV/visible probe transient absorption spectroscopy is employed to track the dynamics of electron injection from CdSe QDs into ZnO nanorods. This optical technique is useful in that the ZnO band gap ($\sim$ 3.3 eV) is spectrally distinct from the CdSe QDs ($\sim 2.6 - 2.1$ eV).[90] The spectral separation between CdSe and ZnO transient signals allows selective probing of both materials within a single technique. This makes it a powerful tool for correlating the rate of carriers entering the ZnO bulk density of states with the injection and trapping dynamics in CdSe. We show that charge transfer proceeds through a short-lived intermediate state into heterogeneous acceptor states, and distinguish two timescales for charge injection. This conclusion is supported by an analysis correlating the amplitude and time scales of both the CdSe and ZnO transient signals. A strategy of wide-scale sampling is employed to ensure robust and statistically relevant results from QDHs.

6.2.1 Spectral Analysis

The static UV-Vis spectra of the QDs before and after ligand exchange, and the subsequent sensitization of ZnO with MPA-coated CdSe, are shown in figure 3.7. After exchanging the native oleic acid ligand with MPA, the CdSe shows no change in absorption spectrum aside from a slight solvatochromatic shift due to a change in the dielectric constant from toluene with an oleic acid coating, to methanol coated with MPA as shown in figure 3.7a. The CdSe QDs have a first excitonic transition, labeled $1S_e - 1S_{h3/2}$, located at 515 nm.[102] Neat ZnO features a sharp absorption onset at 360 nm near the band gap of 380 nm (3.26 eV), along with an extended tail below the band gap, which is due to subbandgap states formed from crystalline disorder and to Mie scattering from the densely packed nanorods.[106], [107], [226]

An SEM image of the ZnO nanorods is shown in figure 3.2. The nanorods have an average length of about 500 nm and diameter of about 60 nm. The nanorod density is $\sim$ 158 nanorods/μm^2. QD-sensitized ZnO features a weak absorption bump at the CdSe

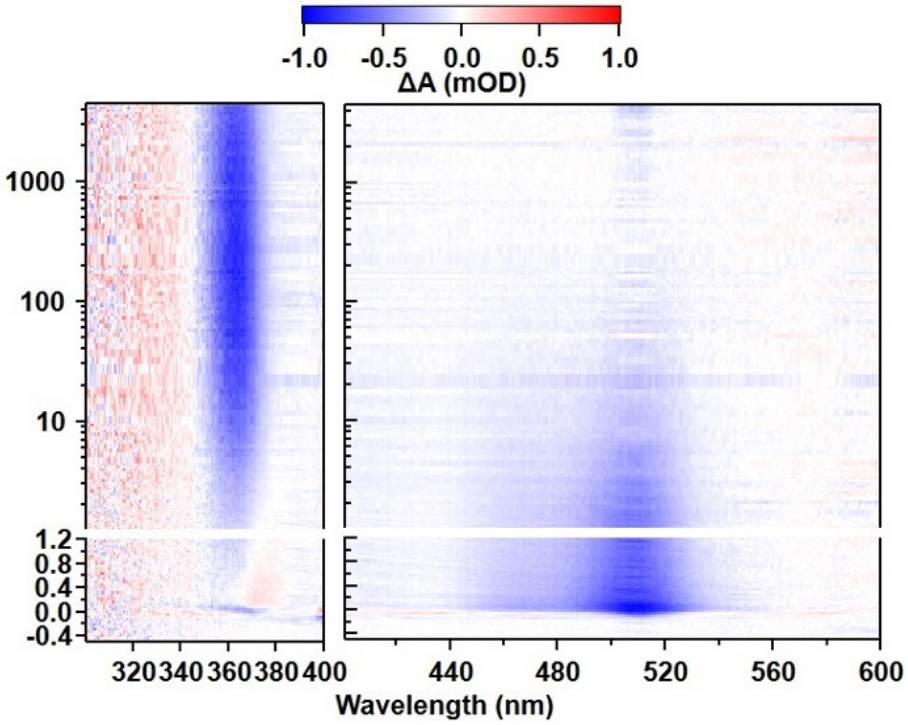

Figure 6.1: A combined 2 dimensional dataset for a typical measurement in the UV (left) and visible (right). The bleach of the CdSe band edge appears immediately and quickly decays, while the bleach of the ZnO appears within 1 picosecond and grows in amplitude over a 100 picoseconds.

1st excitonic transition. The absorption difference between the unsensitized and sensitized ZnO at the CdSe excitonic peak was used to calculate the concentration of CdSe adsorbed to the ZnO, after aligning the baselines far below the peak absorption onset. A difference in baseline absorption can be attributed to adsorption induced disorder at the surface and increased scattering crossection.[90], [108]–[110] The QD coverage is estimated at 17% of a monolayer. Aggregation of QDs is safely excluded due to the stability of the QD sensitizing solution, confirmed with UV-Vis spectra before and after sensitization, and the sub-monolayer deposition of QDs. This can also be seen in the SEM images, in 3.2c, where the roughening of the ZnO surface from a full monolayer is not observed.[34]

An example transient absorption dataset is shown in figure 6.1 with a color-coded 2D map. Spectral traces taken at 1, 2, and 100 ps are shown in figure 6.2. The UV and visible measurements shown in figure 6.1 are taken from different spots on the sample, and represent

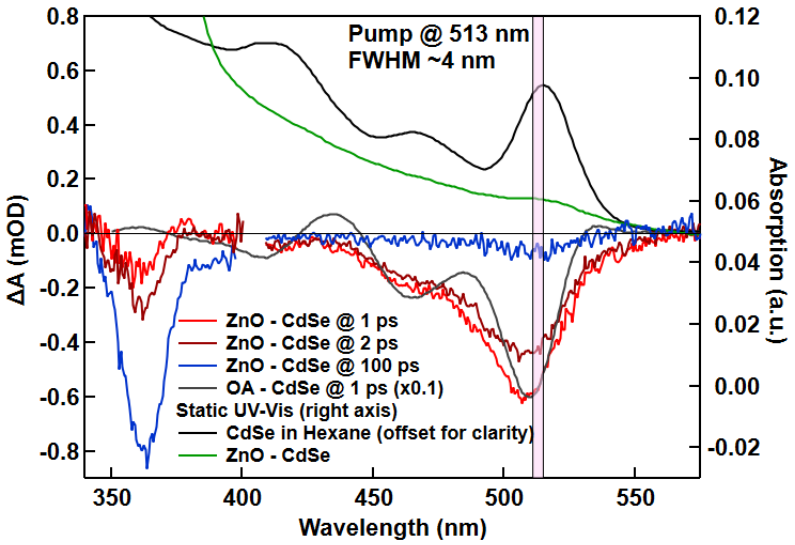

Figure 6.2: The transient signal from solution phase CdSe (gray) at 1 ps, CdSe - ZnO at 1 ps (light red), 2 ps (dark red), and at 100 ps (blue) is shown. The pink box shows the center and FWHM of the pump spectrum, located at 513 nm with 4 nm FWHM, and 71 μJ/cm^2. Also shown is the static UV-Vis spectrum of solution phase 2.6 nm CdSe (black, right axis, offset for clarity) along with the CdSe - ZnO after sensitization (green, right axis).

single measurements out of multiple. Prominent bleaches are seen at 365 nm and 510 nm, which are due to ZnO and CdSe respectively. As described in section 3.5.3 both of these signals are due to PSF. At 1 ps the CdSe - ZnO matches the solution phase CdSe closely, as shown in figure 6.2, before significant charge transfer has occurred. The solution phase CdSe features a sharply defined bleach at the peak of of the first excitonic transition at 510 nm, with a small excited state absorption at 535 nm due to the dynamic Stark effect.[138], [227] The sensitization process results in a slight Ostwald ripening, as seen with the static UV-Vis of the solution phase CdSe after 1 day, in figure 3.7b.[228] Sensitization has broadened the CdSe excitonic transition due to electronic coupling with the ZnO bulk-like and surface states, which combined with the slight Ostwald ripening likely obscurs the stark effect.[20] The second excitonic transition, $1S_e - 2S_{h3/2}$, shares the lowest electron state with the first transition, $1S_e$, and is bleached from PSF with identical kinetics to the first transition. After 100 ps charge injection has nearly finished, with almost no intensity in the visible region for the CdSe - ZnO while the UV signal has significantly more amplitude.

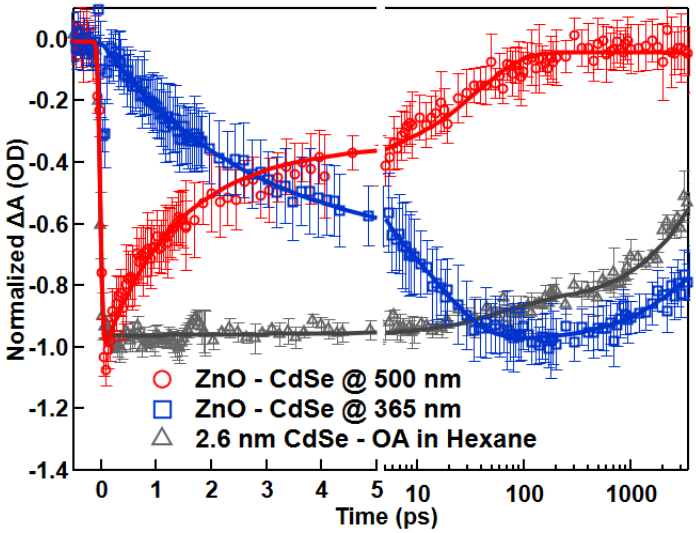

Figure 6.3: Representative transient kinetics for the sensitized sample are shown at 500 nm and at 365 nm (red circles and blue squares, respectively). The kinetics for CdSe solution phase measurements are also shown (gray triangles). Solid lines are the kinetic fits to the data. All samples had target <N> of 0.2.

The negative feature at 365 nm grows in amplitude over 10's of ps, as shown in figure 6.3. This bleach is due to injected electrons occupying the ZnO conduction band minimum and preventing absorption into the excitonic state. Below 350 nm is a broad excited state absorption feature, which is due to a change in the refractive index of ZnO due to free carriers.[130]

6.2.2 Kinetic Analysis

Figure 6.3 shows the comparative kinetics between solution phase CdSe (gray circles), and sensitized samples in the UV (blue circles) and visible (red circles). A representative kinetic trace of ZnO was taken at 365 nm and binned over ±1 nm, while a representative CdSe kinetic trace was extracted at 500 nm and binned over ±1 nm. Included in figure 6.3 are the multiexponential kinetic fits for each dataset. For CdSe QDs in solution, a two exponential decay function is required to fit the kinetics (gray curve in figure 6.3). The first component occurs on a time scale of 60 ± 11 ps and accounts for 11 ± 7% of the intensity. The second component occurs on the 7.9 ± 0.2 ns time scale and accounts for 89 ± 1%. The first

2.6 nm CdSe - ZnO				
Material	τ_1	τ_2	τ_{RR}	τ_{BET}
CdSe	0.9 ± 0.2 ps (55 ± 6%)	15 ± 3 ps (40 ± 5%)	1e6 *ps* (5%)	—
ZnO	2.4 ± 0.6 ps (52 ± 10%)	16 ± 6 ps (48 ± 10%)	—	4 ± 1 ns (37 ± 5%)

Table 6.1: Time constants obtained via sum-of-exponentials fitting to the measured kinetic traces at 365 nm for ZnO, and at 500 nm for 2.6 nm CdSe. In parentheses are the amplitudes of each exponential component, where τ_1 and τ_2 are the first two rising/decaying time constants for ZnO/CdSe respectively. τ_{RR} is the amplitude of the CdSe that decays outside the temporal window. τ_{BET} is the fitted decay of the ZnO signal, loosely assigned to back electron transfer.

component is due to a low degree of biexciton generation and recombination despite the low fluence, and the second component is due to radiative and nonradiative recombination.[8], [138], [229]

The visible signal of the sensitized sample decays much quicker than the solution phase CdSe, and includes a bleach in the UV that increases over time. The kinetics of the ZnO and CdSe signals (UV and visible respectively) were fit with a sum of exponentials. These fits are shown alongside the kinetic traces in figure 6.3 (continuous curves), and the resulting averaged time constants and amplitudes are recorded in table 6.1. The CdSe kinetics were fit with two decaying exponentials and a long-lasting component that decays outside the temporal window of the measurement. The ZnO kinetics were fit with two rising exponentials and a single decaying exponential. The amplitude of τ_1 in both materials is slightly above 50%, while the amplitude of τ_2 is between 40 and 50%. τ_1 in CdSe is 0.900 ±0.2 ps, and in ZnO is 2.4 ±0.6 ps, which are separated by 1.5 ps. This difference is attributed to an optically dark intermediate state, which will be discussed later.[35] τ_2 are equivalent within the confidence interval between CdSe and ZnO at 15 ±3 ps and 16 ±6 ps respectively. The physical phenomenon being measured is identical between ZnO and CdSe, so the amplitude of each exponential component is a good measure of the movement of the electronic population. The absolute amplitude of each component should not be compared to each other because the magnitude of the PSF effect of a single electron will be different between the two materials.

τ_1 has the same relative amplitude for CdSe as ZnO at $55 \pm 5\%$ and $52 \pm 10\%$ respectively. The same is true for τ_2, at $40 \pm 5\%$ and $48 \pm 10\%$ for CdSe and ZnO. If charge injection proceeded on a single timescale, say τ_1, then we would expect a single rising component for ZnO that had 100% amplitude, regardless of the relative amplitude of τ_1 in CdSe. That the relative amplitude in ZnO is split between τ_1 and τ_2 in a way that matches the CdSe, with very similar timescales, may mean charge injection from CdSe into ZnO follows two distinct pathways. This conclusion will be justified in the following paragraphs.

Multi-exponential decays of CdSe transient signals are commonly observed in QDHs. It is usually attributed to charge transfer, back electron transfer, and trapping at surface states which may overlap in time.[20], [34], [83] Here, the multi-exponential decay of the CdSe bleach is directly correlated to the multi-exponential rise of the ZnO bleach via amplitudes. There is a remaining 5% amplitude that decays on a much longer timescale, which is assigned to the recombination of remaining non-injecting QDs or PSF from untrapped holes.[139] The decay of the ZnO signal occurs on 4 ± 1 ns and accounts for 37 $\pm$5% of the electron population. This timescale is consistent with previous THz measurements, which has been attributed to positively charged quantum dots limiting the mobility of injected electrons and promoting back-electron transfer.[34], [35] It is not clear in this instance whether the decay is due to trapping at bulk or surface defects in ZnO, or back electron transfer into CdSe since the remaining amplitude in the CdSe signal is too low to discern the dynamics of the QD holes. Back electron transfer has been estimated to take place on a longer timescale ($\sim 100' sns$), so this could favor carrier trapping, with the remaining bleach amplitude remaining far outside the temporal window.[20], [34], [71], [83]

Multiexponential rise times in ZnO upon injection have been seen in dye sensitized ZnO nanoparticles by time resolved terahertz and IR spectroscopy, with similar timescales and amplitudes as in this study.[52], [230]–[232] Those dynamics have been attributed to the interaction of the cationic dye and injected electrons forming a bound charge-transfer state that dissociates on the 10's of ps timescale. Previous results with transient absorption and

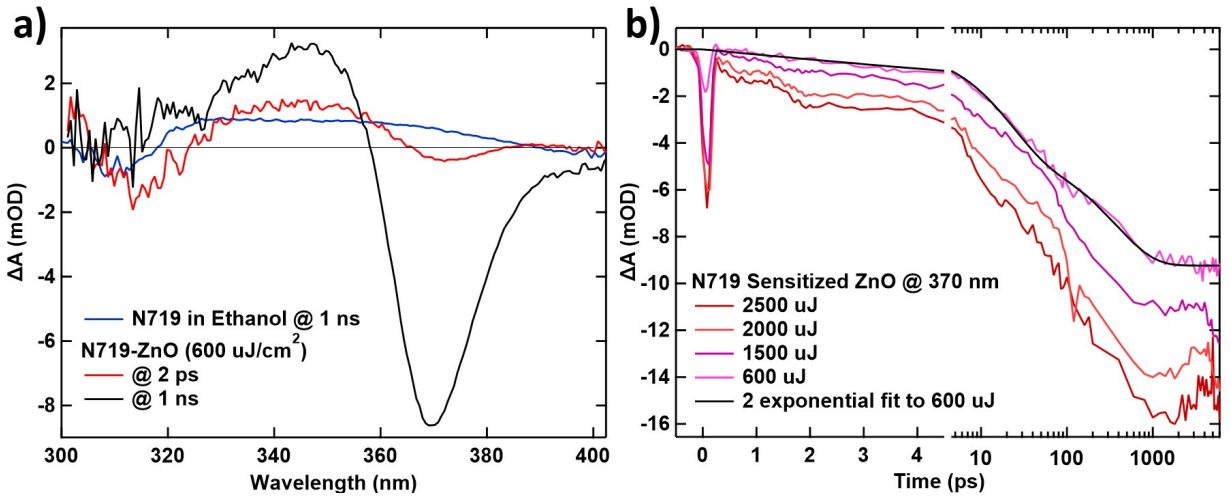

Figure 6.4: a) Spectral slices at 2 ps (red trace) and 1 ns (blue trace) for N719 sensitized ZnO nanorods after excitation at 532 nm with 600 600μJ/cm^2, along with a representative spectral trace from N719 in ethanol at 1 ns (blue trace). b) shows kinetics at 370 nm in N719 sensitized ZnO after excitation with fluences from 600 - 2500 $\mu J/cm^2$ (light red to dark red), along with a biexponential fit to the 600 $\mu J/cm^2$ (blue trace).

terahertz spectroscopy on CdSe sensitized ZnO nanorods have attributed the fastest CdSe decay (1 - 3 ps) to electron transfer into a charge transfer state, followed by dissociation out of this state to give a prolonged growth of free carrier conductivity in ZnO over 20 to 60 ps.[34], [35] A bound interfacial state should not contribute to a bleach of the band edge transition in ZnO due to the electron not occupying the bulk DOS, and the CTS is likely formed from subbandgap surface states in ZnO.[52], [53], [233] A dipole allowed transition into this state should have an energy equal to the difference between the hole in the QD and electron in the ZnO, and would be far below the ZnO band gap.[49], [65], [230], [234] The insensitivity of the UV probe to a bound interfacial state can be verified with dye-sensitized ZnO measurements, which does not show a signal from the rapidly populated (<300 fs) intermediate state, shown in figure 6.4.[53], [63], [90], [235]

Dye sensitized ZnO was measured for a comparison to literature and CdSe sensitized samples. 532 nm pump excites the ^{1}MLCT of N719, which relaxes to the ^{3}MLCT state which persists for 20 ns.[236] The spectral comparison is shown in figure 6.4a between N719 sensitized ZnO and N719 dye in ethanol. The N719 dye shows broad ESA from 400 nm

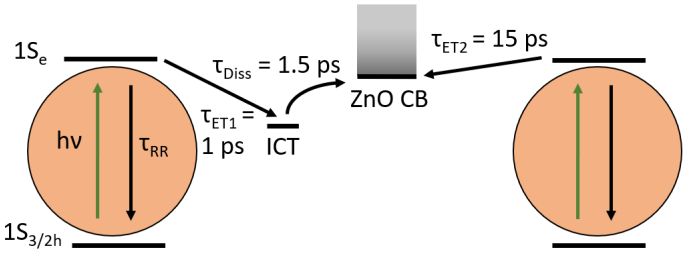

Figure 6.5: Based on the argument that the UV probe is not sensitive to an intermediate surface state, and considering the correlation of time constants and amplitudes, the picture proposed in this article is depicted. Charge injection takes place through two uncorrelated states with different driving forces, followed by dispersion into the bulk DOS.

to 320 nm, followed by a bleach at 310 nm of the ligand-centered state.[90] The sensitized ZnO shows a strong bleach at 370 nm due to phase space filling of photoinjected electrons, coupled with an induced absorption at 350 nm due to an increased refractive index of the free conduction band carriers, which also contributes to the bleach to the red of band edge exciton due to an decreased refractive index below the band edge.[107]

Figure 6.4b shows kinetic traces at 370 nm for 4 excitation fluences. The rising signal requires a biexponential function to be satisfactorily fit. The time constants are 22 $\pm$ 2 ps and 380 $\pm$ 50 ps, with amplitudes of 49 and 51 % respectively, similar to literature. [52], [63], [90] N719 transfers an electron from the photoexcited MLCT into the intermediate ICT state within 600 fs, followed by dissociation into the bulk DOS.[52], [63], [90], [231] The absence of a subpicosecond bleach indicates the CTS is optically dark, or has an optical transition outside the UV spectral window. The injection yield is linear with fluence, along with an increased baseline due to two-photon injection.

Because the UV probe is not sensitive to the occupation of an intermediate state, the two exponential processes in the ZnO could be interpreted either as picosecond charge transfer from CdSe into a single intermediate state with dissociation occurring on a fast and a long timescale, or the more likely scenario of charge transfer from distinct QD-ZnO states with different driving forces, as illustrated in figure 6.5. The first option does not provide a satisfactory explanation for the second CdSe decay. The closely matched timescales and

amplitudes in the kinetic fits make it more likely that the measured kinetics are due to electron transfer from two different states with independent driving forces. The lifetime of the intermediate state can be roughly estimated by the observed difference between electrons leaving the CdSe and arriving in the ZnO bulk DOS. For the first decay and rise of the transient signals in CdSe and ZnO, this lifetime is estimated at 1.5 ps. This is shorter than previous estimates of 20 - 60 ps, as measured for an identical system.[34], [35] Comparing the second transient decay and rise of the CdSe and ZnO respectively, we do not observe a measurable intermediate state lifetime. This is justified by a reduced ability to resolve the relatively short intermediate state lifetime in longer timescale processes.

The amplitude ratio between the two charge transfer pathways shows that there is an equal chance of either pathway being available to a given QD, but not both. If the fastest charge injection pathway was available to all QDs, charge injection would proceed through that pathway with an efficiency governed by the ratio between the two timescales. With the injection timescales measured here, $\frac{0.9}{15+0.9} \sim 94\%$ of charge injection would proceed through the fast pathway (0.9 ps) if it was available for all QDs. A root cause for this split population is discussed below.

As shown in figure 6.2, the band gap excitation selects for a relatively narrow range of QD sizes that can not explain significant amplitude of charge injection at late times. Heterogenous charge transfer (HCT) is a mechanism where indirectly attached QDs (i.e. not in direct contact with the surface) transfer charge through directly attached QDs into ZnO.[34] Similar to previous arguments with much higher QD coverage, the low QD coverage make this mechanism unlikely in this work. Since the QD coverage is estimated at 17% of a monolayer and approximately 1 in 5 QDs are excited, the statistical likelihood of having half of all charge transfer taking place from indirectly attached QDs is small. Critically the long 15 ps rise of the ZnO transient signal is consistent with previous THz results on identical systems, but the short 2.4 ps rise is not.[20], [34] This could be due to the reduced ability to resolve timescales near the IRF in THz measurements, and indicates that sample quality in

this study is comparable to past studies with higher concentrations of adsorbed QDs.

Another consideration for heterogeneity is the binding motif of the MPA linker, where alternative coordinations could induce HCT. The ligand exchange and phase transfer is done stepwise, so sensitization is not likely to give QDs with alternative coordination. Additionally, the thiol moiety of MPA is much more likely to coordinate to the CdSe than the carboxylic acid.[99], [237] The lack of aggregation, seen in the stability of the UV-Vis spectrum before and afters sensitization, and that sensitization is done without excess ligand means there is not a significant concentration of free MPA under these conditions. The carboxylic acid termination of MPA coordinates to ZnO in its deprotonated form imposed by the pH. The last consideration is whether ligands are coordinated in a mono or bi-dendate fashion, but since each QD is likely adsorbed to the ZnO through multiple ligands this is unlikely to differentiate QDs. Therefore we can safely exclude HCT from causing two charge injection time scales.

We must also consider whether the second component of ZnO can be directly attributed to charge injection. An alternative explanation is that all electrons are injected on the 1 ps timescale as measured in the visible and the 15 ps decay of the CdSe corresponds to the decay of carriers which do not contribute to the injection. In this scenario, the increased bleaching in ZnO is due to carrier cooling of the injected electrons. If one assumes injected electrons do not immediately occupy the ZnO conduction band minimum, then they would not contribute to PSF effects, but a weak bleach at the band edge may be due to Coulombic screening of the band edge exciton.[90] There are multiple arguments against this though. As described in section 3.6.1, high pump fluences can notably produce two photon absorption (2PA) in ZnO to create a conduction band electron and valence band hole. Even at the low fluences applied here, the nanoscale dimensions of ZnO enhance the 2PA cross-section and allow for a small degree of 2PA excitation.[213]

Figure 6.6a shows the signal at the ZnO band edge after 2PA to give an amplitude similar to the charge injection amplitude. The high intensity bleach at 0.1 and 0.2 ps is due to

self phase modulation between pump and probe photons at the ZnO band gap.[81] Carrier cooling takes place within a picosecond from high lying states and is accompanied by spectral changes from band gap renormalization. There is no spectral evolution of the UV signal either in position or shape after the first few picoseconds to interfere with the timescales of charge injection measured here. Thus both rising components in sensitized ZnO should be attributed to charge injection. Figure 6.6b shows the subpicosceond dynamics after charge injection from 2.3 nm CdSe. The signal from 2PA decays rapidly within 1 ps, falling from ~ -0.5mOD to ~ -0.15 mOD within 300 fs, while the signal in 2.3 nm CdSe-ZnO shows no decay over the same timeframe, and in fact increases slightly in intensity. This indicates that the ZnO bleach increases by as much as -0.34 mOD over the first picosecond. Thus most of the amplitude within this timeframe can be attributed to charge injection from CdSe into ZnO. However, the actual kinetics of this increase are thoroughly obscured. While previous work attempted to subtract the 2PA signal to obtain the approximate magnitude of charge injection, this procedure is not guaranteed to preserve the sensitive kinetics of the optically dark state.

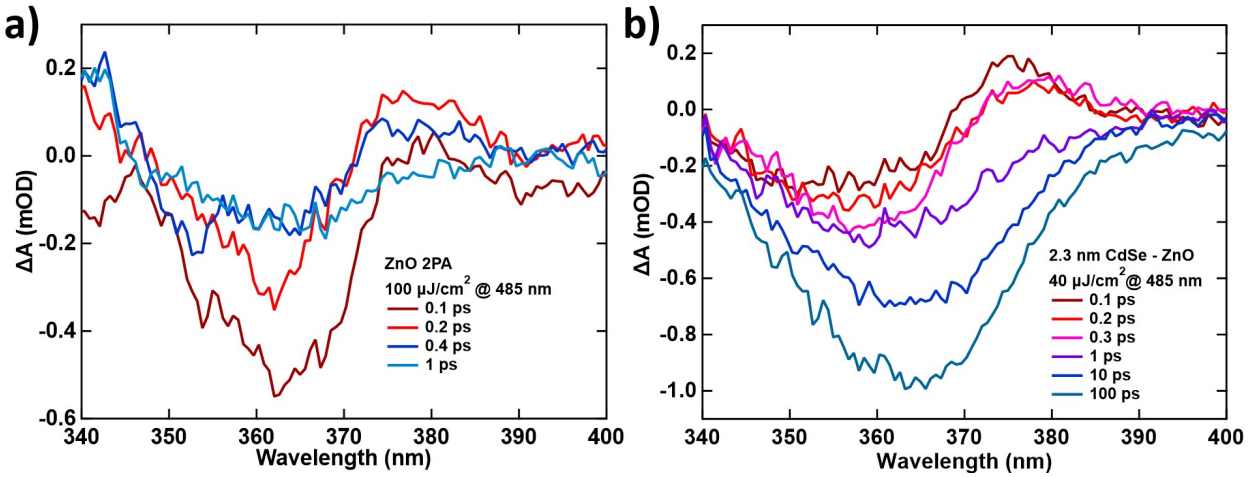

Figure 6.6: a) Spectral slices of two-photon absorption in ZnO after excitation with 100 μJ/cm^2 at 485 nm. Time points depicted are at 0.1 ps, 0.2 ps, 0.4 ps, and 1 ps (dark red, light red, light blue, and dark blue respectively). b) Spectral slices of 2.3 nm CdSe - ZnO in the UV after excitation with 485 nm pump, at a fluence of 40 μJ/cm^2 at 0.1 ps, 0.2 ps, and 0.3 ps, 1 ps, 10 ps, and 100 ps (dark red, light red, light blue, and dark blue respectively).

The arguments above are consistent with literature arguments, but where previous results found evidence for a long-lived intermediate state, our results point to a scenario with a short lived intermediate state where the injection dynamics are not split by heterogeneity of the QDs, but instead by heterogeneity of the ZnO. This has been proposed before for Z907-sensitized ZnO to explain multiexponential kinetics.[238] A likely cause could be band bending at the surface that splits the ZnO acceptor states. Band bending effects in ZnO can be very strong, as demonstrated by recent articles.[63], [64] The low static dielectric constant of ZnO relative to other metal oxides allows for strong band bending effects even in nanoparticles on the 10 nm scale, and has been credited for the kinetic differences in dye - sensitized systems.[22], [62] Distinct charge injection pathways could arise from variable band bending magnitude at the $[0\,0\,0\,1]$ facet and the $[1\,0\,\bar{1}\,0]$ facet, which can reach values of $\sim -580meV$ and $\sim -300meV$ respectively.[65] The difference in band bending between facets is derived from the distinct morphology of each plane and the corresponding stability of chemisorbed water and hydroxy species. This scenario would explain a wide separation in charge transfer timescales and allows for a roughly equivalent injection amplitude and yield between the two pathways.

6.3 Charge Transfer State

The following sections build on the previous results showing the separation of injection into two timescales. Four samples are studied to investigate the nature of the intermediate state introduced in the previous section, which includes three different QD sizes and a ZnO treatment. This intermediate state is thought to result from Coulombic attraction, however it is found to have a lifetime that decreases with decreasing QD size, which is anti-aligned with expectations if the Coulombic interaction was dominant. Additionally, annealing the ZnO was found to reduce the intermediate state lifetime to the point that it was not detectable. Instead of being Coulombically bound, an intrinsic surface potential from band bending in

ZnO could localize injected electrons in an optically dark surface state for up to a few ps. Finally, these results are compared to the current understanding of charge injection from CdSe quantum dots into ZnO.

6.3.1 Characterization

The static UV-Vis spectra ZnO after sensitization with different QD sizes is shown in figure 3.7, along with the spectra of the native oleic acid coated 2.6 nm CdSe compared to the MPA coated, phase-transferred CdSe. The QDs show no change in absorption spectrum during the ligand exchange and phase transfer aside from a slight solvatochromatic shift due to a change in the dielectric constant from toluene with an oleic acid coating, to methanol and coated with MPA.[105] The sensitized ZnO features a small peak at the CdSe excitonic transitions (590, 515, and 485 nm) and a sharp absorption onset at the ZnO band gap of 3.3 eV, along with an extended tail below the ZnO band gap from crystalline disorder forming subbandgap states.[106], [107] Despite this extended tail, there is no evidence of single photon absorption at the ZnO band gap in transient experiments. The absorption difference between the unsensitized and sensitized ZnO at the CdSe excitonic peak was used to calculate the concentration of CdSe adsorbed to the ZnO, after aligning the baselines far below the peak absorption onset. A difference in baseline absorption can be attributed to adsorption induced disorder at the surface of ZnO.[108]–[110] The ZnO nanorods are 400 nm long by 60 nm wide, with a density of 158 nanorods/μm^2 via an SEM survey. Using the estimated QD concentration, the QD coverage is estimated at 8.8, 18.5, and 42 % of a monolayer for the 2.3 nm, 2.6 nm, and 4.2 nm CdSe respectively. Aggregation of quantum dots is not expected to be an issue when the QD sensitizing solution maintains stability before and after sensitization, as confirmed with UV-Vis, and the submonolayer QD coverage.

Annealing ZnO induces multiple changes, which is described in full in chapter 3. Figure 6.7 shows the effect of annealing on the XPS spectrum at the O 1s and Zn 3d peaks. Since these nanorods are well oriented with their c-axis oriented normal to the crystal substrate,

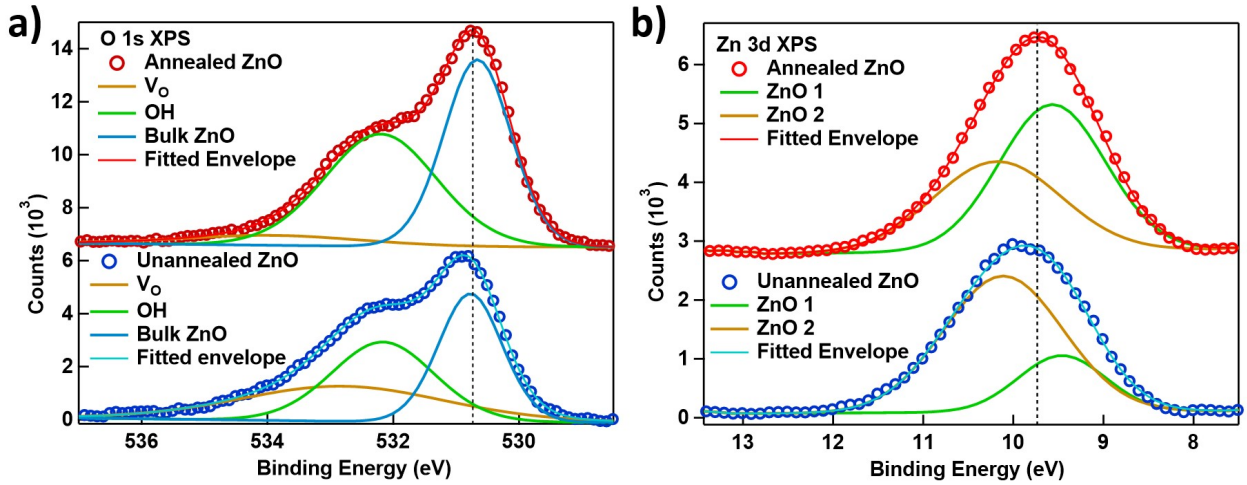

Figure 6.7: a) The XPS data at the oxygen 1s edge, before and after annealing (blue and red), and with fittings to three gaussian peaks to account for oxygen vacancies (orange), hydroxide surface species (green), and bulk oxygen (teal). b) The XPS data at the zinc 3d edge, before and after annealing (blue and red), and fitted to two gaussian peaks.

the [0 0 0 1] facet is the dominant facet observed by XPS, with other facets also seen from an oblique angle. Contrary to a and m-plane ZnO, contaminants adsorbed on the Zn-terminated [0 0 0 1] surface are stable up to 700 °C.[65] Annealing at the relatively low temperature of 400 °C will not completely remove the organic contaminants, which is confirmed with the elemental ratios. The carbon 1s peak intensity decreases substantially after annealing, which is confirmed by the elemental ratios. Before annealing the atomic ratios are 39.5% carbon, 44% oxygen, and 16.5% zinc. After annealing the amount of oxygen increases to account for 50.1%, and zinc increases to account for 23.8%, while carbon decreases to 26.1%.

The C 1s photoelectron peak was used to calibrate the energy of the O 1s and Zn 3d measurements, which are shown in figure 6.7a and 6.7b respectively. At the oxygen 1s peak, the signal can be fit to a sum of three Gaussian functions, which are attributed to oxygen defects, adsorbed hydroxides, and lattice bound oxygen.[123] Oxygen defects are not always observed in these samples when grown for longer times. The contribution of defect states and hydroxide species to the signal decreases after annealing, matching the reduction in organic contaminants. The Zn 3d peak could be adequately fit with a sum of two Gaussian functions, which could represent the different exposed facets. A single, skewed Gaussian

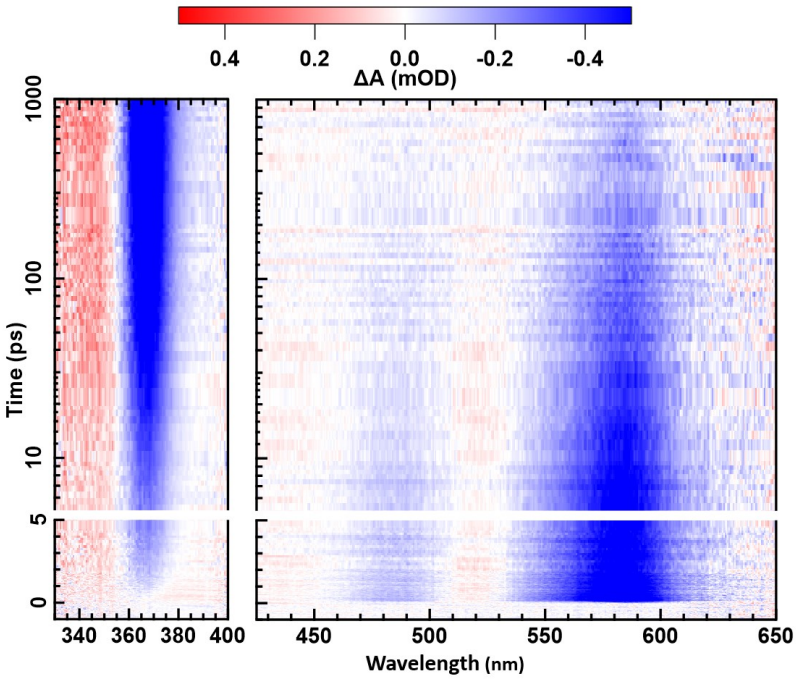

Figure 6.8: Shows a representative 2-dimensional transient spectrum for the 4.2 nm CdSe - ZnO sample (offset by 0.1 ps), excited at 590 nm with a fluence of 32 μJ/cm^2. On the left is the UV spectrum, from 330 - 400 nm, with a bleach signal located at 368 nm from charge injection into the ZnO. On the right is the visible spectrum from 450 nm to 650 nm, with a strong bleach of the band edge transition in CdSe, centered near 590 nm.

could not account for the shape of the signal. The peak position and contribution of each fitted component is shown in table 3.2 for the Zn 3d measurements, and table 3.3 for the O 1s measurements. The Zn 3d character shows a shift of ∼120 meV to lower binding energies after annealing, along with a narrowing of the FWHM by 70 meV. A corresponding shift of the O 1s peak by 150 meV to lower binding energies is also seen. As has been interpreted in references [63], [64], the reduced elemental carbon percentage and peak shifts and narrowing are attributed to a reduction in the downward band bending of the valence and conduction bands near the surface as a result of a removal of surface adsorbates. The photoluminescence and UV-Vis shows a narrower band edge transition compared to unannealed ZnO. XRD shows that the crystallinity improves and tensile strain is released along the c-axis of the nanorods. FTIR spectra also shows a decrease in the adsorbed hydroxide concentration, corroborating the XPS measurements.

6.3.2 Spectral and Kinetic Analysis

Figure 6.8 shows a typical transient absorption dataset for 4.2 nm CdSe quantum dots on ZnO, offset in time by 0.1 ps to allow for log-spaced time points. After excitation, the CdSe is bleached at the first excitonic transition near 590 nm, and at the second excitonic transition above 500 nm. These features come from photoexcited electrons occupying the lowest lying excitonic state, $1S_e$, which limits further excitation into that state. The degeneracy of the corresponding hole state is much higher, so the electron population is the dominant contribution to these bleaches.[140] As the CdSe bleach decays, the ZnO bleach at 365 nm grows in, reaching a maximum amplitude after about 500 ps. This bleach is due to transferred electrons occupying the conduction band minimum, blocking further excitation at the ZnO band gap. An excited state absorption (ESA) at higher energies can be seen with identical dynamics to the ZnO bleach, which is attributed to free carriers in the conduction band changing the refractive index of ZnO.[130] The data showed no degradation over the course of the measurements as evidenced by the map of the standard deviations, an example of which is in figure 3.18, being equivalent before t_0 and after the appearance of the ZnO signal, and within the spectral window.

Figure 6.9a shows a spectral trace at 1 ps for each size of CdSe for a single spot dataset, alongside the static UV-Vis spectrum for the conjugated samples. The transient bleach has maximum amplitude at the first excitonic transition for all three samples, with a matching transient bleach from the second excitonic transition. Each sample was excited at the CdSe band edge (485 nm, 515 nm, and 590 nm) with low fluence (20 μJ/cm^2 to 70 μJ/cm^2), so the kinetic and spectral characteristics are not complicated by carrier cooling or multiexcitonic effects.

Figure 6.9b shows a sample kinetic trace for a single spot dataset, from each sample and set of white light conditions. For the UV traces of ZnO, kinetic traces were binned over $\pm$1 nm at 365 nm. When the CdSe spectrum is dominated by electron state filling,[140] the kinetics

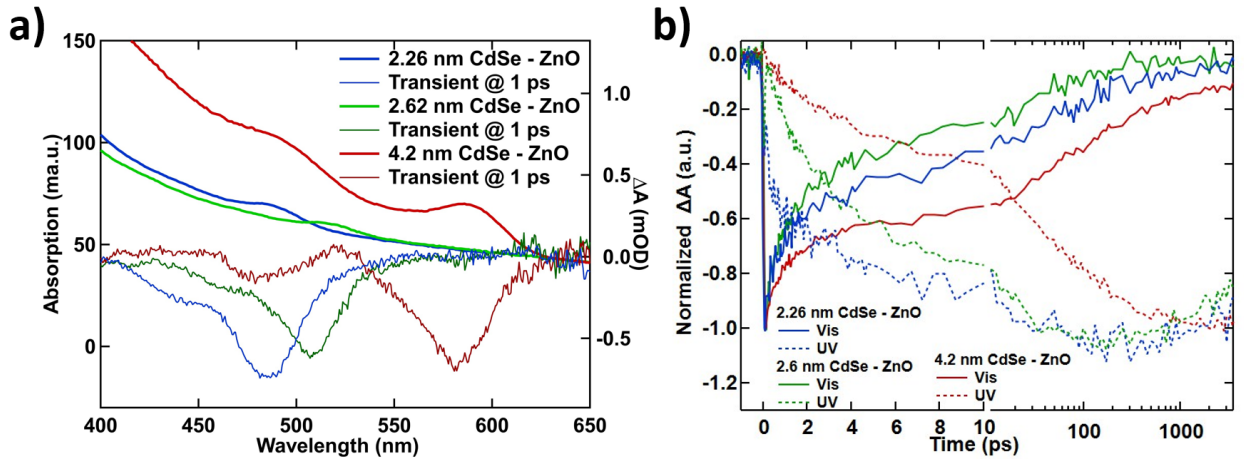

Figure 6.9: a) Representative unnormalized transient spectral traces for each sample at 1 ps alongside the static UV-Vis of the conjugated samples. The 4.2 nm CdSe - ZnO in red, the 2.6 nm CdSe - ZnO in green, and the 2.3 nm CdSe - ZnO in blue. Excitation wavelengths were 590 nm, 515 nm, and 485 nm for the 4.2 nm CdSe, 2.6 nm CdSe, and 2.3 nm CdSe respectively. All samples had target target <N> of 0.2. b) Example kinetic traces from single spot datasets for all sensitized, unannealed samples, both in the visible (solid traces) and UV (dotted traces). All traces in the UV were collected at 365 nm, and the visible traces were collected at 470 nm, 500 nm, and 590 nm, for the 2.3 nm CdSe (blue), 2.6 nm CdSe (green), and 4.2 nm CdSe (red). All traces were normalized to -1.

of the $1S_e - 2S_{h3/2}$ transition are equivalent to the $1S_e - 1S_{h3/2}$ transition. Thus the CdSe kinetic traces were taken on the blue side of the excitonic transition and binned over ± 1 nm. Charge injection proceeds on two timescales, as our previous article discusses. The sample with the smallest driving force, the 4.2 nm QD sample, shows significant charge injection within 10 picoseconds and continues to 1 nanosecond. This is attributed to heterogeneity of the ZnO acceptor states where two acceptor states lead to different driving forces and charge injection on widely separated timescales.

For the 2.6 nm and 4.2 nm samples, the kinetic traces cross very close to the 0.5 normalized δA point, as explored in the following discussion, this shows that the two materials trade amplitude evenly with only a very short lived intermediate state. A long lived intermediate state would have the kinetic traces cross at a lower amplitude. The outlier is the 2.3 nm CdSe sample, where the traces cross close to -0.6 normalized δA. This is attributed to a nominal amount of 2PA in ZnO in the 2.3 nm CdSe sensitized sample, even though the fluence was

near the lowest achievable.

Table 6.2 shows the value of the time constants obtained by averaging the fitted time constants from each spot dataset using a sum-of-exponentials model. There are a few identifiable trends from the unannealed samples:

1. A difference between τ_1 for CdSe and τ_1 for ZnO can be resolved that decreases with smaller QDs.

2. τ_1 for CdSe and ZnO are similar in amplitude, and τ_2 is nearly equivalent in amplitude and value between CdSe and ZnO for all samples.

3. The amplitude of charge injection is evenly split between τ_1 and τ_2 for the UV and is correlated to the amplitudes in the visible.

4. Both τ_1 and τ_2 shift to faster time scales from 4.2 nm QDs to 2.6 nm QDs, but is almost the same from 2.6 nm QDs to 2.3 nm QDs.

5. There is a decay of the UV signal, which occurs on a longer timescale than these measurements and cannot be accurately fit.

Trend 1 is the main subject of this study, to resolve the QD size dependence of the intermediate state lifetime. This will be returned to shortly. Trends 2 and 3 were analyzed in our previous article focusing on the 2.6 nm CdSe - ZnO dataset. The conclusions of that analysis will be continued here, where charge injection is found to proceed on two timescales with near equivalent amplitudes. The 4.2 nm QDs is the sample with the lowest driving force, but shows charge injection on 4 ps and 40 ps timescales. The two timescales are attributed to heterogeneity of the ZnO acceptor states where two states with different driving forces give charge injection on widely separated timescales, but similar yields. The physical reasoning is that different facets of ZnO have different band edge positions and reactivity which can, for example, impact photocatalytic properties in $BiVO_4$.[239]

Trend 4 can be attributed to the increased driving force from large to small QDs, vis-a-vis Marcus Theory. The leveling off of timescales from 2.6 nm to 2.3 nm CdSe is commonly attributed to the "Inverted Region" in Marcus theory where the reorganization energy and driving force become nearly equivalent and counteracting charge injection. Quantum dots have been seen to circumvent the inverted region through Auger-assisted electron transfer in QD - molecule systems,[222], [240] and hole transfer from ZnO to CdS QDs.[241] These experiments are not sufficient to distinguish whether the 2.3 nm QDs are entering the inverted region or subverting it.

These charge injection timescales differ from some experimental work on an identical system,[20], [34] but matches well some ab initio calculations.[242] The third time constant for CdSe was held constant at 100 ns due to being outside the temporal window of the setup. The long timescale is attributed to recombination in quantum dots that do not transfer charge, and accounts for 5 - 20% of the total amplitude.

Annealing the ZnO has a pronounced effect on both CdSe and ZnO time constants. For both materials, the kinetics shift to significantly later times for both time constants, with the first component shifting from 0.800/2.4 ps to 2.5/3.4 ps for CdSe and ZnO respectively. The second component shifts from 15 ps before annealing to approximately 50 ps after annealing. The first component has a decreased amplitude compared to the unannealed sample, decreasing to 35 - 40 %, but the amplitude of the second component increases to around 60%.

Returning to trend 1, a localized CT state should have a transition energy far below the bulk band gap transition, and is thus invisible to the UV probe transient absorption measurement. The CTS lifetime can be approximated as the time lag between the first CdSe decay and one or both ZnO components, referred to as $\Delta\tau$, and is calculated in table 6.3. $\Delta\tau_1$ is largest for the 4.2 nm CdSe at 2.8 ps, which decreases to 1.5 ps for 2.6 nm CdSe, and down to 1 ps when the ZnO is annealed. Finally, for the 2.3 nm quantum dots there is no detectable $\Delta\tau_1$, but this determination is complicated by two photon absorption (TPA) effects (section

2.3 nm CdSe - ZnO				
Material	τ_1	τ_2	τ_{RR}	τ_{BET}
CdSe	1 ± 0.2 ps (50 ± 4%)	25 ± 8 ps (37 ± 4%)	1e6 *ps* (13%)	—
ZnO	0.9 ± 0.1 ps (60 ± 5%)	14 ± 5 ps (40 ± 5%)	—	—
2.6 nm CdSe - ZnO				
CdSe	0.8 ± 0.2 ps (55 ± 6%)	15 ± 3 ps (40 ± 5%)	1e6 *ps* (5%)	—
ZnO	2.4 ± 0.6 ps (52 ± 10%)	16 ± 6 ps (48 ± 10%)	—	4 ± 1 ns (37 ± 5%)
2.6 nm CdSe - Annealed ZnO				
CdSe	2.5 ± 0.6 ps (35 ± 5%)	53 ± 10 ps (47 ± 5%)	1e6 *ps* (18%)	—
ZnO	3.4 ± 0.5 ps (41 ± 4%)	47 ± 6 ps (59 ± 3%)	—	100 ± 0 ns (200 ± 300%)
4.2 nm CdSe - ZnO				
CdSe	1.5 ± 0.3 ps (38 ± 3%)	70 ± 10 ps (38 ± 3%)	1e6 *ps* (24%)	—
ZnO	4.3 ± 0.5 ps (47 ± 4%)	77 ± 11 ps (53 ± 4%)	—	—

Table 6.2: Time constants obtained via sum-of-exponentials fitting to the measured kinetic traces at 365 nm for ZnO, and at 500 nm for 2.6 nm CdSe. In parentheses are the amplitudes of each exponential component.

3.6.1). If Coulombic forces are the dominant interaction, the differentiating factor between samples is the physical separation of electrons and holes, since all other factors are identical. Reducing the QD diameter by a factor of 2 should increase the binding energy of the CTS by almost 1.5 between the 4.2 and 2.3 nm CdSe, and thus increase the CTS lifetime from 2.8 to ∼4.2 ps.[35] $\Delta\tau_1$ for the 2.3 nm CdSe sample is near zero, but has uncertainty due to TPA. In the 2.6 nm CdSe $\Delta\tau_1$ decreases by 1.3 ps, which is anti-aligned with the expected trend. Annealing ZnO further decreases the intermediate state lifetime by 0.5 ps. The CdSe is coated in MPA which is not affected by annealing, so the decrease of the intermediate state lifetime should not be attributed to a change in the dielectric environment. These results make the CTS assignment unfavorable. $\Delta\tau_2$ for all samples is near 0 for all samples, which could be caused by an inability to resolve small differences in timescale for longer processes

Difference in Timescales		
Sample	$\Delta\tau_1$	$\Delta\tau_2$
2.3 nm CdSe - ZnO	$\sim$ 0 ps	$\sim$ 5 ps
2.6 nm CdSe - ZnO	1.5 ps	$\sim$ 0 ps
2.6 nm CdSe - Annealed ZnO	1 ps	$\sim$ 0 ps
4.2 nm CdSe - ZnO	2.8 ps	$\sim$ 0 ps

Table 6.3: Differences in time constants obtained through sum-of-exponentials fittings.

with subsequently larger error bars.

Alternative to the CT state, a mixture of band bending effects could govern the charge injection dynamics. One charge transfer pathway may include downward band bending that localizes carriers at the surface.[63], [64] Another pathway may have less substantial downward band bending, or even upward band bending, which would give a lower driving force (and thus slower charge injection) but prevent surface localization. Figure 6.10b graphically illustrates this scenario, and formalized in section 3.6.5.3.

6.3.3 Global Target Analysis

As discussed in section 6.3.2 and our previous article, charge injection proceeds through two pathways in order to sufficiently fit the charge injection results. Additionally, there is an optically dark intermediate state with a lifetime of up to a few picoseconds, which decreases with smaller quantum dot sizes. Any interpretation of this signal must also explain the effect annealing has on the timescales of both charge injection pathways and the intermediate state lifetime. Sum of exponentials fitting can only approximate the intermediate state lifetime. To extract the most accurate time constants and physical picture, holistic kinetic models were applied to the full datasets for each sample to fit all spot datasets in the UV and visible, simultaneously. The one exception is the 2.3 nm QD sample, which was not fit due to interference from TPA. The strength of this approach is that a close to complete accounting of the photoexcited electron population can be made. The absolute quantum yield cannot be accurately calculated here since electrons that are trapped before reaching the ZnO DOS will

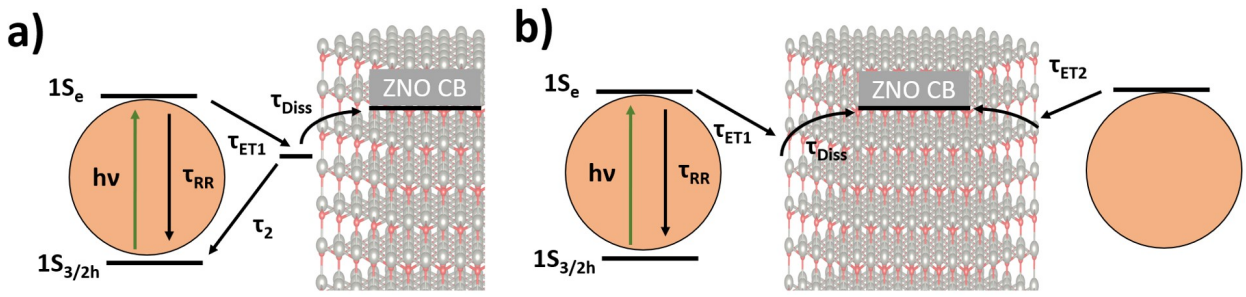

Figure 6.10: a) A graphic illustration of the CTS model as it was implemented during the global fitting, and described in 3.35. b) A graphic illustration of the band bending model as it was implemented during the global fit results shown below, and described in 3.37.

be unaccounted for. An approximate quantum yield can be calculated, which is discussed in appendix A.

The formal definitions of the kinetic models are given in section 3.6.5.1 through 3.6.5.3. The raw data and best fits are shown in figure 6.11 - 6.13. The models are blind to the physical interpretation, and only attempt to describe the data. Whichever model matches the data best will then be analyzed for the most appropriate physical model. The two models considered the most plausible are shown pictorially in figure 6.10a and 6.10b, referred to as the three and four state models respectively. Figure 6.10a considers a single QD population with a single charge injection rate, while figure 6.10b considers two distinct QD populations with two injection rates and an intermediate state only for the fast charge injection pathway. Alternative permutations give poor agreement with experimental data. The globally fitted time constants for the two best models and all samples are shown in table 6.4.

For both sizes of quantum dots and the annealed dataset, the four state model produces the smallest degree of systematic error and fits the biexponential nature of the ZnO signal well, as originally supposed in section 6.3.2. The 3 state global model produces significant systematic error, which can be seen in the residual traces in figures 6.11 - 6.13. Thus, the four state model is concluded to be the most descriptive model. The first CdSe charge transfer component is 0.59 ± 0.07 and 1.58 ± 0.09 ps, with a 0.4 ± 0.1 and 0.78 ± 0.09 ps delayed UV rise for the 2.6 nm and 4.2 nm CdSe respectively. The quick charge transfer time is again

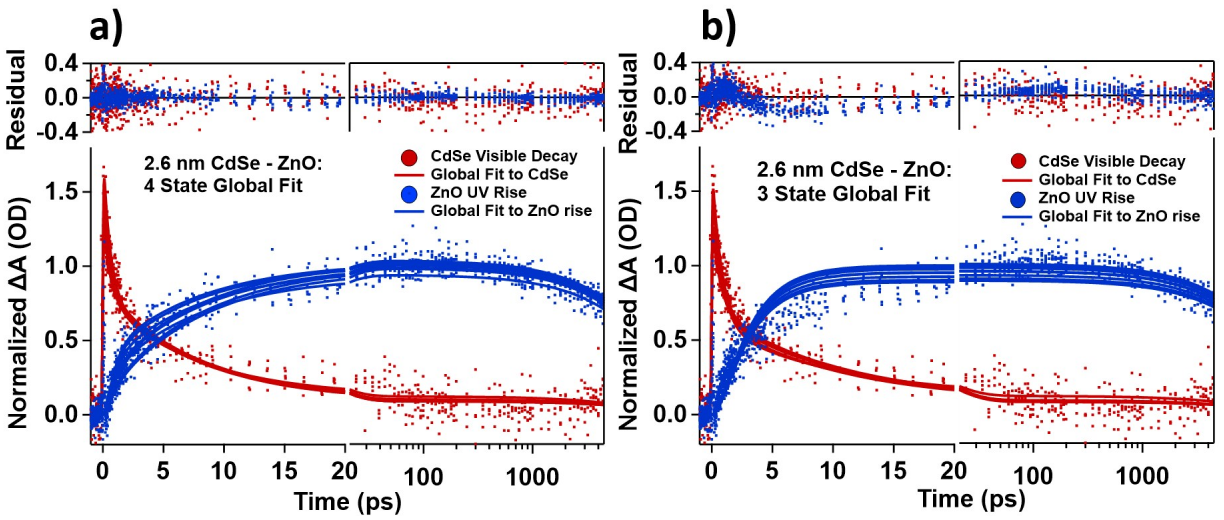

Figure 6.11: Global kinetic fits to UV (blue dots) and visible (red dots) datasets for 2.6 nm CdSe - ZnO. a) The global fits to the proposed 4 state model are shown as solid traces in the visible (red) and UV (blue). Also shown is the residual for each trace on the top of the graph for the UV (blue dots) and visible data (red dots). b) The global fits to the 3 state model, along with the residuals for each dataset and kinetic fit.

notable, being much faster than most prior estimates.[20], [34] Such fast processes have been interpreted as being trapping at surface states. This is not done here since there is a clear relation to the UV signal. The dissociation time constant is size dependent, which is twice as fast for the 2.6 nm CdSe as the 4.2 nm CdSe. The second charge transfer pathway occurs on 7.8 ± 0.6 and 58 ± 2 ps timescales, for the 2.6 nm and 4.2 nm CdSe respectively. The strong size dependence of the second charge injection pathway matches literature values for identical systems very closely.[20], [34] The global fitting also shows that annealing ZnO has removed the intermediate state between the CdSe and ZnO, as the lifetime of the intermediate state is reduced so much that it is unobservable. The time scale of electrons leaving the CdSe increases from 0.59±0.07 to 2.4 ± 0.1 ps. The second charge injection time scale has also been pushed from 7.8 ± 0.6 ps to 44 ± 2 ps. Thus the timescale of electron injection was strongly impacted by the surface chemistry of the ZnO, and the intermediate state has had its lifetime reduced to the point that it is unobservable.

The three state model does not include a second rising component in the ZnO signal, which leads to clear systematic errors. The second CdSe decaying component would be

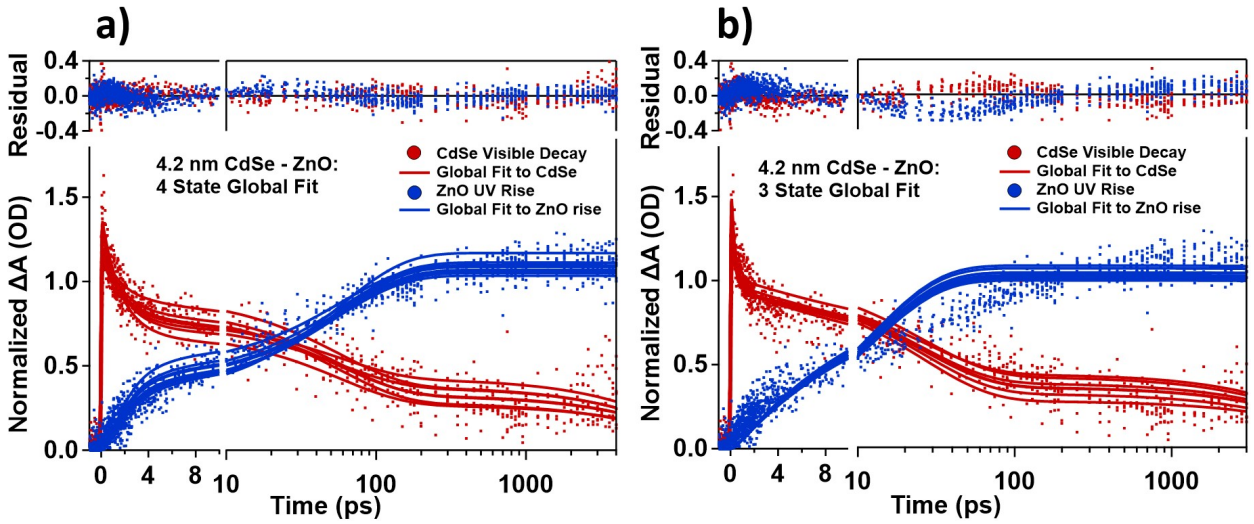

Figure 6.12: Global kinetic fits to UV (blue dots) and visible (red dots) datasets for 4.2 nm CdSe - ZnO. a) The global fits to the proposed 4 state model are shown as solid traces in the visible (red) and UV (blue). Also shown is the residual for each trace on the top of the graph for the UV (blue dots) and visible data (red dots). b) The global fits to the 3 state model, along with the residuals for each dataset and kinetic fit.

interpreted as electron trapping at the CdSe surface. The time scale for the electrons leaving the CdSe is 800 and 330 femtoseconds for the 2.6 nm and 4.2 nm CdSe, which is substantially faster than literature values of 4 - 10 ps and is slower for the smaller QD sizes.[34], [35], [83] The 330 fs process is so fast, the only process which could match this time scale is hot electron transfer, which is not allowed here because of the band edge excitation.[71] The sup-picosecond injection time constants are driven by the rise of the ZnO signal. Since the ZnO signal begins rising near time zero and continues for up to 100 ps, a significant population of electrons must occupy the interfacial state within a picosecond, followed by a slow dissociation out of the intermediate state. The timescale of dissociation is 2.5 ps and 12.3 ps for the 2.6 and 4.2 nm CdSe samples, which is a ∼fivefold reduction when going from large to small QDs. This model has large residual variance, and is less favorable than the four state model.

The model proposed here to explain these results is heterogeneous band bending. Two populations of surface states are allowed to exist by assuming facet dependent energetics. ZnO surfaces can experience significant downward band bending, or neutral or upward band

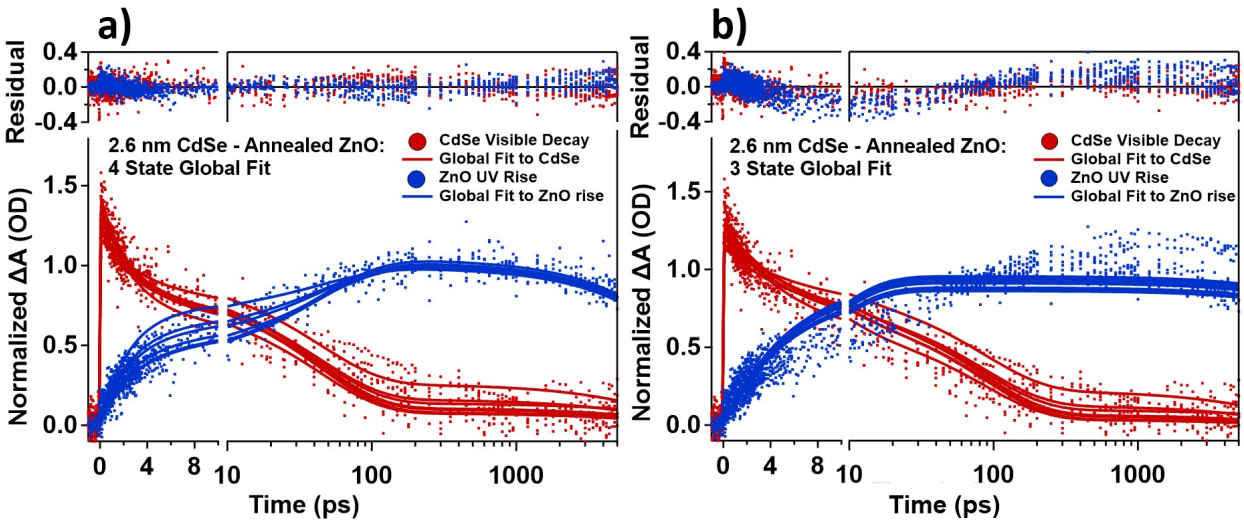

Figure 6.13: Global kinetic fits to UV (blue dots) and visible (red dots) datasets for 2.6 nm CdSe - Anealed ZnO. a) The global fits to the proposed 4 state model are shown as solid traces in the visible (red) and UV (blue). Also shown is the residual for each trace on the top of the graph for the UV (blue dots) and visible data (red dots). b) The global fits to the 3 state model, along with the residuals for each dataset and kinetic fit.

bending depending on the facet and adsorbed species.[100] Downward band bending gives a larger driving force, thus charge transfer would be much faster and potentially be strongly localized, inducing a measurable delay between charge transfer and the bleach of the band edge transition. Concurrently a neutral or upward band bending will have slower charge transfer behavior with a delay-less (or a small relative to the injection timescale) ground state bleach. The magnitude of downward band bending is expected to increase after charge injection and is thus dependent on the quantum yield of charge injection.[63] This makes it difficult to fully rationalize the decreasing intermediate state lifetime with decreasing QD size within this model. Potentially, the larger driving force in small QDs gives injected electrons excess kinetic energy that promotes injection into the bulk DOS.

Annealing the ZnO can be explained within this interpretation as band character at the surface being restored to near flat band conditions, or at least to reduced band bending. This would affect the driving force at the surface, and would affect the timescales of the two charge injection pathways independently. The removal of the intermediate state indicates that the reduced band bending is not sufficient to localize injected charges at the surface.

This also shows that there is no hybridized state between the CdSe and ZnO at the interface. Heterogeneous acceptor states could derive from the crystalline nanorod facets. Since the nanorods are c-oriented, the top of the nanorods is the [0 0 0 1] facet, which is Zn terminated. The band bending of the [0 0 0 1] facet is significantly more thermally stable than the [1 0 $\bar{1}$ 0] facet, which could explain why the timescales are more differentiated after annealing.[65] This would attribute the fastest injection pathway to charge transfer in the [1 0 $\bar{1}$ 0] facet and the slower charge injection to [0 0 0 1] facet. A second possibility is that charge injection is differentiated between the [1 0 $\bar{1}$ 0] and [1 1 $\bar{2}$ 0] facets. Typically hydrothermally grown nanorods are expected to have [1 0 $\bar{1}$ 0] facets, but the [1 1 $\bar{2}$ 0] facet is also a fast growth facet with only slightly lower surface stabilization, and could have significant yield in hydrothermal syntheses.[101]

The CTS model proposes an intermediate state that should have an increasing lifetime with smaller QD sizes. This behavior is not seen in the four state global fitting (or three state fitting). The intermediate state is 780 fs for 4.2 nm QDs and decreases to 400 fs with 2.6 nm QDs. Following estimations outlined in reference [35], these values correspond to a binding energy of $\sim 40meV$. This binding energy is on the order of k_bT, and can not be attributed to a bound state using this framework. A second consideration is that this interpretation lacks a proper explanation for the effect of annealing. If Coulombic attraction is the dominant force, which only depends on the quantum dot size and dielectric environment, then no factors at play can adequately explain the effect of annealing. Annealing removed adsorbed surface species, but will not affect the environment around the quantum dots at all, thus the dielectric environment of the charges will be minimally altered by annealing.

A last physical model under consideration is the heterogeneous injection model, which describes prolonged charge injection from indirectly attached quantum dots. A few experimental factors make this mechanism unlikely though. The strongest argument is the low quantum dot coverage. Having at least half of the injected charge carriers come from indirectly attached quantum dots (for each quantum dot size) would require at least one indirectly attached

4.2 nm CdSe - ZnO					
Model	τ_{CdSe}	τ_{diss}	τ_2	τ_{RR}	τ_{trap}
3 - State	0.33 ± 0.03 ps	12.3 ± 0.3 ps	26 ± 2 ps	100 ± 0 ns	—
4 - State	1.58 ± 0.09 ps	0.78 ± 0.09 ps	58 ± 2 ps	100 ± 0 ns	—
2.6 nm CdSe - ZnO					
3 - State	0.80 ± 0.08 ps	2.5 ± 0.2 ps	11 ± 1 ps	100 ± 0 ns	20 ± 2 ns
4 - State	0.59 ± 0.07 ps	0.4 ± 0.1 ps	7.8 ± 0.6 ps	100 ± 0 ns	16 ± 1 ns
2.6 nm CdSe - Annealed ZnO					
3 - State	5.6 ± 0.2 ps	0.00 ± 0.06 ps	86 ± 5 ps	100 ± 0 ns	100 ± 25 ns
4 - State	2.37 ± 0.12 ps	0.00 ± 0.05 ps	44 ± 2 ps	100 ± 0 ns	21 ± 1 ns

Table 6.4: Time constants obtained via global fitting to the measured kinetic traces at 365 nm for ZnO, and at 590 nm for 4.2 nm CdSe or 515 nm for 2.6 nm CdSe.

quantum dot for each directly attached quantum dot, which is strongly unlikely given the submonolayer QD coverage.

The short but measurable difference between the first CdSe decay and ZnO rise within the four state model is much faster than would be implied by the magnitude of band bending seen in references [63] and [64]. There are a few effects that could explain this result: the band character after MPA adsorption, electronic coupling with the CdSe quantum dots, and the phase space filling effect of electrons within the bent band region. Adsorbed MPA does not form shallow donor states, and so is not expected to induce the same magnitude of downward band bending as an adsorbed hydroxide layer.[64] Similarly, electronic coupling between the CdSe quantum dots and ZnO could further lessen the band bending and still giving a driving force difference between the two populations of quantum dots. However, the adsorption of quantum dots has not been seen to noticeably shift the ZnO valence or conduction bands.[21] The last possibility is that injected carriers are only dark to the optical probe while localized close to the surface within the largest magnitude potential, which they escape from quickly but remain loosely localized close to the surface as seen in reference [63].

Of the models tested here, a four state model with two distinct QD populations and a single short lived intermediate state describes the data best and minimizes systematic errors. Of the physical pictures considered, band bending at the ZnO surface matches the kinetic models and explains the presented trends. The energetics at different facets is enough to split charge injection into two regimes, which will be strongly affected by annealing ZnO. The band bending picture is flexible enough to account for both a split population of quantum dots and an intermediate state between the CdSe and ZnO signals. In addition, the band bending results are the most physically consistent. Annealing ZnO removes adsorbed surface species, which reduces band bending and shifts charge injection to later time scales. In addition the lifetime of the intermediate state was reduced to an undetectable degree, as reduced band bending results in a lower surface potential.

6.3.4 Comparison to Previous Results

The observation of two charge injection domains would be very difficult for prior experiments to observe. The early timescale component could be masked in terahertz spectroscopy by mobile holes. Additionally, this technique may not be able to sensitively distinguish between native potential fields at the surface originating from band bending and a transient photoinduced field at the interface. Interpretations so far have relied on applying the Maxwell Garnett effective medium model to estimate the dielectric constant, but this may not be an adequate assumption with the mixed organic/inorganic interface. At late times, this may still be an adequate measure. The absence of a charge transfer state may be attributed to a few physical effects. For one, the naked hole within the quantum dot will form a repulsive image charge with the organic matrix the QD is embedded in. This would add a self-energy term to the hole and will likely weaken the interaction between QD and ZnO.[243], [244] In addition, the electron accumulation layer from downward band bending makes the surface n-type, which leads to a weak counteracting Helmholtz layer in the adsorbed species.[60] This could act to screen the photoexcited charges from each other and prevent strong interactions.

Magnetotransport measurements have also found that the electrons in the accumulation layer have a reduced mobility compared to bulk electrons.[245] Lastly, THz spectroscopy may not be capable of deciphering whether electrons at the surface of ZnO are under the influence of an interfacial dipole moment, or an intrinsic surface potential.

It must also be asked whether the presence of strong surface potentials in ZnO still makes the Braun - Onsager model applicable. Recent work has been done to recast the model for hybrid organic - inorganic systems,[54], [55] and apply it to dye - sensitized ZnO.[56] As has been noted recently though, the Braun - Onsager model is only applicable at low dissociation efficiencies and applied electric fields.[47], [57] Additionally, the interfacial dipole formed from charge transfer may induce a quantum confinement energy that reduces the binding energy of a CT state and increase the dissociation rate even in the absence of an external or static electric field.[47], [58], [59] The presence of a strong potential at the interface may require a model that takes a more detailed accounting of such effects.[47]

The timescale of the second injection pathway in unannealed samples matches previous results, but the short timescale component has not been directly observed. Many QD sensitized metal oxide studies are done on nanoparticulate metal oxide systems, which offers a mix of poorly defined interface states. An optical UV probe charge injection study on sensitized single crystal films showing a clear single exponential rise in ZnO would conclusively show that charge injection proceeds through a facet dependent mechanism. These results give insight to the limiting factors in quantum dot sensitized solar cells. Even though the annealed ZnO pushed charge injection to longer time scales, it also showed greater quantum efficiency, indicating that annealing removed detrimental subbandgap trap states. This is shown in appendix A. Removing band bending at the surface should also increase the mobility of injected electrons.

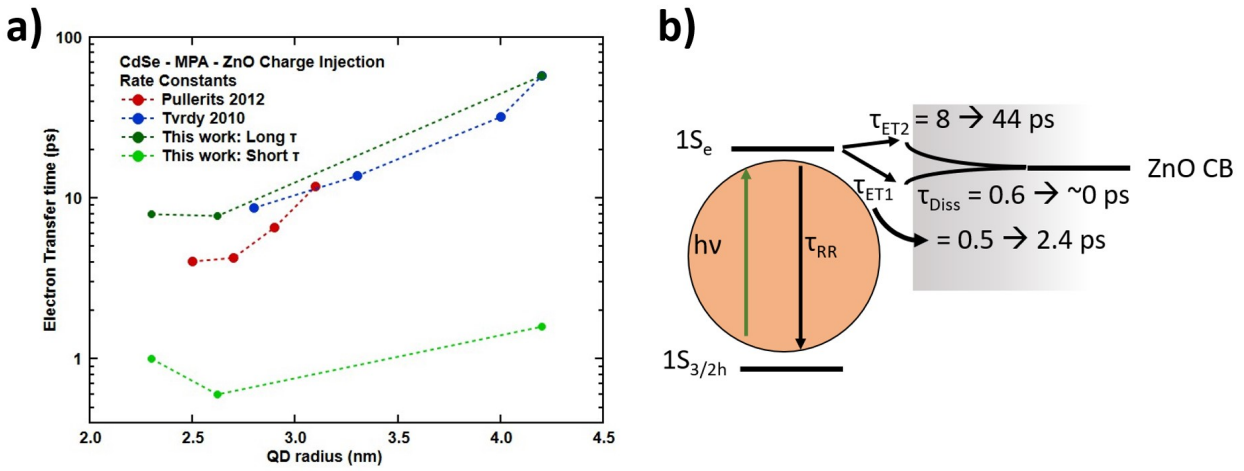

Figure 6.14: a) The results of global fitting to multiple time constants vs. literature values for this same system, with the exception of the 2.3 nm CdSe, where results were taken from the UV sum of exponentials fitting. Long and short time constants are represented by dark and light green, respectively. b) A pictorial representation of the proposed effect annealing ZnO has on charge injection.

6.4 Conclusion

A series of quantum dot sensitized ZnO samples were measured with dual-probe transient absorption spectroscopy in order to support or disprove current models of interfacial interactions in this system. Notably, all samples showed charge injection on significantly shorter timescales than has been observed or assigned in previous literature. This is shown in figure 6.14 which compares the time scale of charge injection between identical systems, and highlights the component of charge injection that is at least an order of magnitude faster than previous estimates. Simultaneously, charge injection on the 10's of ps timescale corroborates previous measurements. These results find little support for the presence of an interfacial exciton after charge transfer from CdSe QDs due to the small intermediate state lifetime, with an anti-aligned size dependent trend in the dissociation timescale. This was supported with global target analysis of the CdSe and ZnO transient absorption data, which had poor agreement with the CTS model. An alternative model proposes band bending as a source for both the intermediate "dark" state and the split charge injection timescales. In this scenario

the intermediate state has a size independent (or weakly dependent) lifetime, and the two timescales is explained as facet dependent band character. Coulombic attraction between carriers post-charge transfer is not the most likely interpretation.

These conclusions were found by comparing two distinct, material specific signatures across four samples with different sizes of CdSe quantum dots and ZnO treatment. Annealing was found to remove surface-adsorbed species on the ZnO, which affected the magnitude of band bending. The results of this are shown in figure 6.14, where the fastest time scale for charge injection increased from 600 fs to 2.4 ps, and the elimination of any observable intermediate state. Concurrently, the second charge injection pathway saw an increase from 8 ps to 44 ps. The overall effect from annealing was a complete removal of the intermediate state, pushing more charge injection towards later times, and an increased quantum yield from charge injection. These results are most adequately explained within the band bending picture, however it is not a perfect explanation. The defect concentration and doping characteristics of the ZnO at the surface are also expected to change after annealing, potentially affecting the electronic character of ZnO and corresponding charge transfer timelines.

Acknowledgements

I thank Michael Enright for supplying the CdSe used in this data. I thank Thomas Rossi for help in data interpretation. I thank Rick Haasch for collecting XPS data.

Chapter 7

Conclusions and Future Outlook

7.1 Conclusion

In this thesis, we have applied time-resolved optical and X-ray techniques to unravel charge dynamics in complex heterostructured nanomaterials. X-ray linear dichroism spectroscopy was demonstrated on oriented ZnO nanorods to uncover transient core-hole screening, a previously undescribed phenomenon in XTA.[73] Further, these experiments measured phase-space filling in the hard X-ray regime for the first time, setting the stage for a potential charge transfer experiment. Combining these results with UV-probe OTA measurements allowed us to define the limiting factors in completing an XTA charge injection study on QDHs. These efforts found that the efficiency of charge injection is too low to reach the threshold signal for an XTA study. Ultrafast spectroscopy of QDHs must contend with material and charge injection constraints. XTA has high potential for characterizing carrier trap states and injection timescales, but the low overall concentration of injected carriers makes these experiments difficult. The bar for a successful experiment can be lowered either by achieving a higher yield of charge injection through materials engineering, or by increasing the sensitivity of XTA setups. The former can likely be accomplished with core-shell quantum dots, with high yield conjugation procedures, or with ligands that enhance charge injection.[68], [69], [145], [246] The latter can be achieved at high brilliance, low emittance X-ray facilities, like an XFEL.[194], [195] However, the intense radiation from these sources will likely affect the integrity of the QDHs.

UV-probe OTA proved its own utility in discerning charge injection dynamics. Dual probe OTA allowed simultaneous measurements of the QD and ZnO band gaps. Charge injection was found to obey biexponential behavior in ZnO which was ascribed to a split population of QD-ZnO states. This data was supported with global target analysis, and used to interpret the nature of the optically dark intermediate state. The literature so far has interpreted this state to belong to a Coulombically bound interfacial exciton.[34], [35] However, the required QD size dependence could not be verified. Instead, the intermediate state is attributed to intrinsic surface potentials in ZnO from adsorbed species. This was supported with a simple annealing experiment to reduce the band bending, which found that the intermediate state was unobservable while pushing charge injection to longer timescales, consistent with the band bending interpretation. This work highlights the importance of optimizing charge injection from both material perspectives. The surface structure and chemistry of metal oxides is as important to the timescale and efficiency of charge injection as the surface chemistry of QDs. While the dominant paradigm is that faster charge injection timescales are more competitive with trapping and recombination pathways, this work challenges whether this is a worthwhile trade off when fast charge injection requires a defect or adsorbate rich n-type ZnO surface. Devices employing ZnO should instead aim for high quality interfaces where band bending will not lower the mobility of injected carriers, even if charge injection takes place over a longer timescale on average.[245]

7.2 Future Directions

The discovery of nonlocal core-hole screening in K-edges of metal oxide materials opens many opportunities to investigate the nature of this effect. The evolution of the screening with carrier density is still unknown. Phase space filling is an often-cited result of photoexcitation, but at excitation densities above the Mott threshold this signal was largely absent, leaving only a strong thermal signal and the nonlocal core-hole screening. The core-hole screening

feature can still be seen at excitation densities below the Mott density, but the absence of the photoinduced absorption below the edge at high excitations is puzzling. The absence of a clear PSF signal that scales similarly to the core-hole screening signal leads to the question of whether the two are anti-correlated, and potentially derive from bound and unbound carriers respectively.

Transient XLD was used to remove the isotropic, laser induced thermal effects and systematic ab initio errors. This technique can be used much more powerfully though. Information can be extracted on the transient, orbital specific effects after photoexcitation. Materials like anatase TiO_2 are perfect candidates for this technique due to the anisotropic crystal structure, and oriented excitonic states.[90] In ZnO there were no anisotropic thermal or electronic effects on the 100 ps timescale. However, on the 1 ps timescale there is transient optical dichroism.[107], [193] Anisotropic core hole screening has also been reported for $LiCoO_2$,[178] and recent results from Bethe-Salpeter calculations have supported the presence of anisotropic core-hole screening in ZnO from a hot carrier population. Additionally, these simulations indicate that a fraction of the white line bleach at the Zn K-edge is actually due to PSF. This motivates a transient XLD experiment at high brilliance facilities capable of femtosecond resolution, such as an X-ray free electron laser.[194], [195] Answering questions about the evolution of core-hole screening and PSF with fluence, and the ultrafast anisotropic dynamics could be done with a set of fluence dependent measurements with transient XLD.

The results of UV-probe OTA has shown that charge injection depends sensitively on the surface chemistry of both CdSe and ZnO, with potentially high impact from the ZnO facet that charge injection is proceeding through. Attributing the biexponential injection to facet specific energetics can be tested rigorously either with sensitive single crystal thin films, or by varying the aspect ratio of the ZnO nanorods in order to control the ratio of c-plane to m- or a-plane ZnO. UV-probe OTA offers many options beyond what is showcased in this thesis. Phenomenon that are typically difficult to investigate with IR, THz, or visible probe transient absorption can be investigated very substantively with the UV-probe. Potential avenues

include examining the rate and yield of hot-electron injection, multiexciton generation, and the dependence of charge injection on the materials processing of a variety of QDHs.

Finally, the optically dark intermediate state has been found to have a lifetime on the order of 1.5 - 2 ps for CdSe quantum dots, which is reduced to an unmeasurable lifetime when the ZnO is annealed. This conclusion could only be arrived at by averaging over the sample heterogeneity. Individual measurements gave variable lifetimes for the intermediate state, as well as better and worse agreement between the second charge injection timescales. The intermediate state lifetime is hypothesized to be independent of the CdSe size, but is dependent on the driving force and excess kinetic energy of injected electrons. The relatively slow timescale of charge injection in ZnO has been attributed to the long lifetime of this intermediate state, but this work contends with that picture. Rather, as has been interpreted previously, the low density of states at the conduction band minimum in ZnO could be the reason for slow charge injection.[247] Further testing the assignment of the intermediate state could be done with a core-shell system where the Coulombic interaction is reduced compared to the isolated QD core, but have the same driving force as the core alone. Optimizing charge injection in QDHs will benefit from optimizing the facet energetics and band bending character at the interface.

References

[1] W. Shockley and H. J. Queisser, "Detailed Balance Limit of Efficiency of p-n Junction Solar Cells," *Journal of Applied Physics*, vol. 32, no. 3, pp. 510–519, Mar. 1961, ISSN: 0021-8979. DOI: 10.1063/1.1736034. [Online]. Available: http://aip.scitation.org/doi/10.1063/1.1736034.

[2] A. S. Rasal, S. Yadav, A. A. Kashale, A. Altaee, and J.-Y. Chang, "Stability of quantum dot-sensitized solar cells: A review and prospects," *Nano Energy*, vol. 94, p. 106 854, Apr. 2022, ISSN: 22112855. DOI: 10.1016/j.nanoen.2021.106854. [Online]. Available: https://linkinghub.elsevier.com/retrieve/pii/S2211285521011034.

[3] D. Wang, F. Yin, Z. Du, D. Han, and J. Tang, "Recent progress in quantum dot-sensitized solar cells employing metal chalcogenides," *Journal of Materials Chemistry A*, vol. 7, pp. 26 205–26 226, 46 Nov. 2019, ISSN: 2050-7496. DOI: 10.1039/C9TA10557C. [Online]. Available: https://pubs.rsc.org/en/content/articlehtml/2019/ta/c9ta10557c.

[4] C. B. Murray, S. Sun, W. Gaschler, H. Doyle, T. A. Betley, and C. R. Kagan, "Colloidal synthesis of nanocrystals and nanocrystal superlattices," *IBM Journal of Research and Development*, vol. 45, pp. 47–56, 1 Jan. 2001, ISSN: 0018-8646. DOI: 10.1147/rd.451.0047. [Online]. Available: http://ieeexplore.ieee.org/document/5389082/.

[5] R. S. Selinsky, Q. Ding, M. S. Faber, J. C. Wright, and S. Jin, "Quantum dot nanoscale heterostructures for solar energy conversion," *Chem. Soc. Rev.*, vol. 42, pp. 2963–2985, 7 2013, ISSN: 0306-0012. DOI: 10.1039/C2CS35374A. [Online]. Available: http://xlink.rsc.org/?DOI=C2CS35374A.

[6] B. N. Pal, Y. Ghosh, S. Brovelli, *et al.*, "Giant cdse/cds core/shell nanocrystal quantum dots as efficient electroluminescent materials: Strong influence of shell thickness on light-emitting diode performance," *Nano Letters*, vol. 12, pp. 331–336, 1 Jan. 2012, ISSN: 1530-6984. DOI: 10.1021/nl203620f. [Online]. Available: https://pubs.acs.org/doi/10.1021/nl203620f.

[7] V. I. Klimov, A. A. Mikhailovsky, D. W. McBranch, C. A. Leatherdale, and M. G. Bawendi, "Quantization of Multiparticle Auger Rates in Semiconductor Quantum Dots," *Science*, vol. 287, no. 5455, pp. 1011–1013, 2000. DOI: 10.1126/science.287.5455.1011. [Online]. Available: http://science.sciencemag.org/content/287/5455/1011.

[8] V. I. Klimov, J. A. McGuire, R. D. Schaller, and V. I. Rupasov, "Scaling of multiexciton lifetimes in semiconductor nanocrystals," *Physical Review B*, vol. 77, no. 19, p. 195 324, May 2008, ISSN: 1098-0121. DOI: 10.1103/PhysRevB.77.195324. [Online]. Available: https://link.aps.org/doi/10.1103/PhysRevB.77.195324.

[9] M. S. Kirschner, D. C. Hannah, B. T. Diroll, *et al.*, "Transient melting and recrystallization of semiconductor nanocrystals under multiple electron–hole pair excitation," *Nano Letters*, vol. 17, pp. 5314–5320, 9 Sep. 2017, ISSN: 1530-6984. DOI: 10.1021/acs.nanolett.7b01705. [Online]. Available: https://pubs.acs.org/doi/10.1021/acs.nanolett.7b01705.

[10] A. J. Nozik, M. C. Beard, J. M. Luther, M. Law, R. J. Ellingson, and J. C. Johnson, "Semiconductor quantum dots and quantum dot arrays and applications of multiple exciton generation to third-generation photovoltaic solar cells," *Chemical Reviews*, vol. 110, pp. 6873–6890, 11 Nov. 2010, ISSN: 00092665. DOI: 10.1021/cr900289f. [Online]. Available: http://pubs.acs.org/doi/abs/10.1021/cr900289f.

[11] J. B. Sambur, T. Novet, and B. A. Parkinson, "Multiple exciton collection in a sensitized photovoltaic system," *Science*, vol. 330, pp. 63–66, 6000 Oct. 2010, ISSN:

1095-9203. DOI: 10.1126/science.1191462. [Online]. Available: http://science.sciencemag.org/content/330/6000/63.full.

[12] *Best research-cell efficiency chart — photovoltaic research — nrel*. [Online]. Available: https://www.nrel.gov/pv/cell-efficiency.html.

[13] G. S. Selopal, H. Zhao, Z. M. Wang, and F. Rosei, "Core/shell quantum dots solar cells," *Advanced Functional Materials*, vol. 30, p. 1 908 762, 13 Mar. 2020, ISSN: 1616-301X. DOI: 10.1002/adfm.201908762. [Online]. Available: https://onlinelibrary.wiley.com/doi/abs/10.1002/adfm.201908762.

[14] A. L. Efros and M. Rosen, "The electronic structure of semiconductor nanocrystals," *Annual Review of Materials Science*, vol. 30, pp. 475–521, 1 Aug. 2000, ISSN: 0084-6600. DOI: 10.1146/annurev.matsci.30.1.475. [Online]. Available: https://www.annualreviews.org/doi/10.1146/annurev.matsci.30.1.475.

[15] W. A. Tisdale and X. Y. Zhu, "Artificial atoms on semiconductor surfaces," *Proceedings of the National Academy of Sciences*, vol. 108, pp. 965–970, 3 Jan. 2010, ISSN: 0027-8424. DOI: 10.1073/pnas.1006665107. [Online]. Available: http://www.pnas.org/cgi/doi/10.1073/pnas.1006665107.

[16] J. A. Scher, J. M. Elward, and A. Chakraborty, "Shape matters: Effect of 1d, 2d, and 3d isovolumetric quantum confinement in semiconductor nanoparticles," *The Journal of Physical Chemistry C*, vol. 120, pp. 24 999–25 009, 43 Nov. 2016, ISSN: 1932-7447. DOI: 10.1021/acs.jpcc.6b06728. [Online]. Available: https://pubs.acs.org/doi/10.1021/acs.jpcc.6b06728.

[17] J. M. Pietryga, Y.-S. Park, J. Lim, *et al.*, "Spectroscopic and device aspects of nanocrystal quantum dots," *Chemical Reviews*, vol. 116, pp. 10 513–10 622, 18 Sep. 2016, ISSN: 0009-2665. DOI: 10.1021/acs.chemrev.6b00169. [Online]. Available: https://pubs.acs.org/doi/10.1021/acs.chemrev.6b00169.

[18] P. Singhal and H. N. Ghosh, "Hot charge carriers in quantum dots: Generation, relaxation, extraction, and applications," *ChemNanoMat*, vol. 5, cnma.201900025, 8 Apr. 2019, ISSN: 2199-692X. DOI: 10.1002/cnma.201900025. [Online]. Available: https://onlinelibrary.wiley.com/doi/abs/10.1002/cnma.201900025.

[19] P. Kambhampati, "Multiexcitons in semiconductor nanocrystals: A platform for optoelectronics at high carrier concentration," *The Journal of Physical Chemistry Letters*, vol. 3, pp. 1182–1190, 9 May 2012, ISSN: 1948-7185. DOI: 10.1021/jz300239j. [Online]. Available: https://pubs.acs.org/doi/10.1021/jz300239j.

[20] K. Tvrdy, P. A. Frantsuzov, and P. V. Kamat, "Photoinduced electron transfer from semiconductor quantum dots to metal oxide nanoparticles," *Proceedings of the National Academy of Sciences*, vol. 108, pp. 29–34, 1 Jan. 2011, ISSN: 0027-8424. DOI: 10.1073/pnas.1011972107. [Online]. Available: https://pnas.org/doi/full/10.1073/pnas.1011972107.

[21] B. Carlson, K. Leschkies, E. S. Aydil, and X.-Y. Zhu, "Valence band alignment at cadmium selenide quantum dot and zinc oxide (10-10) interfaces," *The Journal of Physical Chemistry C*, vol. 112, pp. 8419–8423, 22 Jun. 2008, ISSN: 1932-7447. DOI: 10.1021/jp7113434. [Online]. Available: https://pubs.acs.org/doi/10.1021/jp7113434.

[22] U. Ozgur, Y. I. Alivov, C. Liu, *et al.*, "A comprehensive review of zno materials and devices," *Journal of Applied Physics*, vol. 98, p. 041 301, 4 Aug. 2005, ISSN: 0021-8979. DOI: 10.1063/1.1992666. [Online]. Available: https://aip.scitation.org/doi/abs/10.1063/1.1992666.

[23] R. W. Meulenberg, J. R. Lee, A. Wolcott, J. Z. Zhang, L. J. Terminello, and T. V. Buuren, "Determination of the exciton binding energy in cdse quantum dots," *ACS Nano*, vol. 3, pp. 325–330, 2 Feb. 2009, ISSN: 19360851. DOI: 10.1021/NN8006916. [Online]. Available: https://pubs.acs.org/doi/full/10.1021/nn8006916.

[24] R. A. Marcus, "On the theory of electron-transfer reactions. vi. unified treatment for homogeneous and electrode reactions," *The Journal of Chemical Physics*, vol. 43, 2 1965, ISSN: 00219606. DOI: 10.1063/1.1696792.

[25] R. A. Marcus, "Chemical and electrochemical electron-transfer theory," *Annual Review of Physical Chemistry*, vol. 15, pp. 155–196, 1 Oct. 1964, ISSN: 0066-426X. DOI: 10.1146/annurev.pc.15.100164.001103. [Online]. Available: https://www.annualreviews.org/doi/10.1146/annurev.pc.15.100164.001103.

[26] R. A. Marcus, "Electron transfer reactions in chemistry. theory and experiment," *Reviews of Modern Physics*, vol. 65, 3 1993, ISSN: 00346861. DOI: 10.1103/RevModPhys.65.599.

[27] A. V. Akimov, A. J. Neukirch, and O. V. Prezhdo, "Theoretical insights into photoinduced charge transfer and catalysis at oxide interfaces," *Chemical Reviews*, vol. 113, pp. 4496–4565, 6 Jun. 2013, ISSN: 0009-2665. DOI: 10.1021/cr3004899. [Online]. Available: https://pubs.acs.org/doi/10.1021/cr3004899.

[28] J. K. Utterback, J. L. Ruzicka, H. R. Keller, L. M. Pellows, and G. Dukovic, "Electron transfer from semiconductor nanocrystals to redox enzymes," *Annual Review of Physical Chemistry*, vol. 71, pp. 335–359, 1 Apr. 2020, ISSN: 0066-426X. DOI: 10.1146/annurev-physchem-050317-014232. [Online]. Available: https://www.annualreviews.org/doi/10.1146/annurev-physchem-050317-014232.

[29] I. Robel, V. Subramanian, M. Kuno, and P. V. Kamat, "Quantum dot solar cells. harvesting light energy with cdse nanocrystals molecularly linked to mesoscopic TiO_2 films," *Journal of the American Chemical Society*, vol. 128, pp. 2385–2393, 7 Feb. 2006, ISSN: 0002-7863. DOI: 10.1021/ja056494n. [Online]. Available: https://pubs.acs.org/doi/10.1021/ja056494n.

[30] J. Huang, Z. Huang, Y. Yang, H. Zhu, and T. Lian, "Multiple exciton dissociation in cdse quantum dots by ultrafast electron transfer to adsorbed methylene blue,"

Journal of the American Chemical Society, vol. 132, pp. 4858–4864, 13 2010. DOI: 10.1021/ja100106z. [Online]. Available: http://pubs.acs.org/doi/full/10.1021/ja100106z.

[31] M. Sykora, M. A. Petruska, J. Alstrum-Acevedo, I. Bezel, T. J. Meyer, and V. I. Klimov, "Photoinduced charge transfer between cdse nanocrystal quantum dots and ru-polypyridine complexes," *Journal of the American Chemical Society*, vol. 128, pp. 9984–9985, 31 Aug. 2006, ISSN: 00027863. DOI: 10.1021/JA061556A. [Online]. Available: https://pubs.acs.org/doi/full/10.1021/ja061556a.

[32] D. M. Sagar, R. R. Cooney, S. L. Sewall, *et al.*, "Size dependent, state-resolved studies of exciton-phonon couplings in strongly confined semiconductor quantum dots," *Physical Review B*, vol. 77, p. 235 321, 23 Jun. 2008, ISSN: 1098-0121. DOI: 10.1103/PhysRevB.77.235321. [Online]. Available: https://link.aps.org/doi/10.1103/PhysRevB.77.235321.

[33] M. Iwamatsu, M. Fujiwara, N. Happo, and K. Horii, "Effects of dielectric discontinuity on the ground-state energy of charged si dots covered with a layer," *Journal of Physics: Condensed Matter*, vol. 9, pp. 9881–9892, 45 Nov. 1997, ISSN: 0953-8984. DOI: 10.1088/0953-8984/9/45/016. [Online]. Available: https://iopscience.iop.org/article/10.1088/0953-8984/9/45/016.

[34] K. Žídek, K. Zheng, C. S. Ponseca, *et al.*, "Electron Transfer in Quantum-Dot-Sensitized ZnO Nanowires: Ultrafast Time-Resolved Absorption and Terahertz Study," *Journal of the American Chemical Society*, vol. 134, no. 29, pp. 12 110–12 117, Jul. 2012, ISSN: 0002-7863. DOI: 10.1021/ja3029679. [Online]. Available: http://pubs.acs.org/doi/10.1021/ja3029679.

[35] S. B. N., H. Němec, K. Žídek, *et al.*, "Time-resolved terahertz spectroscopy reveals the influence of charged sensitizing quantum dots on the electron dynamics in zno," *Physical Chemistry Chemical Physics*, vol. 19, pp. 6006–6012, 8 Feb. 2017, ISSN: 1463-

9076. DOI: 10.1039/C6CP07509F. [Online]. Available: http://xlink.rsc.org/?DOI=C6CP07509F.

[36] K. E. Knowles, M. D. Peterson, M. R. McPhail, and E. A. Weiss, "Exciton dissociation within quantum dot-organic complexes: Mechanisms, use as a probe of interfacial structure, and applications," *Journal of Physical Chemistry C*, vol. 117, pp. 10 229–10 243, 20 May 2013, ISSN: 19327447. DOI: 10.1021/JP400699H/. [Online]. Available: https://pubs.acs.org/doi/full/10.1021/jp400699h.

[37] D. M. Newns, "Self-consistent model of hydrogen chemisorption," *Physical Review*, vol. 178, p. 1123, 3 Feb. 1969, ISSN: 0031899X. DOI: 10.1103/PhysRev.178.1123. [Online]. Available: https://journals.aps.org/pr/abstract/10.1103/PhysRev.178.1123.

[38] H. A. Kramers, "Brownian motion in a field of force and the diffusion model of chemical reactions," *Physica*, vol. 7, pp. 284–304, 4 Apr. 1940, ISSN: 0031-8914. DOI: 10.1016/S0031-8914(40)90098-2.

[39] E. Sim and N. Makri, "Path integral simulation of charge transfer dynamics in photosynthetic reaction centers," *Journal of Physical Chemistry B*, vol. 101, pp. 5446–5458, 27 Jul. 1997, ISSN: 15206106. DOI: 10.1021/JP970707G/. [Online]. Available: https://pubs.acs.org/doi/full/10.1021/jp970707g.

[40] N. Makri, E. Sim, D. E. Makarov, and M. Topaler, "Long-time quantum simulation of the primary charge separation in bacterial photosynthesis.," *Proceedings of the National Academy of Sciences*, vol. 93, pp. 3926–3931, 9 Apr. 1996, ISSN: 00278424. DOI: 10.1073/PNAS.93.9.3926. [Online]. Available: https://www.pnas.org/doi/abs/10.1073/pnas.93.9.3926.

[41] N. Makri and D. E. Makarov, "Tensor propagator for iterative quantum time evolution of reduced density matrices. i. theory," *The Journal of Chemical Physics*, vol. 102,

p. 4600, 11 Jun. 1998, ISSN: 0021-9606. DOI: 10.1063/1.469508. [Online]. Available: https://aip.scitation.org/doi/abs/10.1063/1.469508.

[42] G. R. Haynes and G. A. Voth, "Effect of nonlinear dissipation on quantum-activated rate processes in condensed phases," *Physical Review A*, vol. 46, p. 2143, 4 Aug. 1992, ISSN: 10502947. DOI: 10.1103/PhysRevA.46.2143. [Online]. Available: https://journals.aps.org/pra/abstract/10.1103/PhysRevA.46.2143.

[43] A. Garg, J. N. Onuchic, and V. Ambegaokar, "Effect of friction on electron transfer in biomolecules," *The Journal of Chemical Physics*, vol. 83, p. 4491, 9 Aug. 1998, ISSN: 0021-9606. DOI: 10.1063/1.449017. [Online]. Available: https://aip.scitation.org/doi/abs/10.1063/1.449017.

[44] J. C. Brauer, A. Marchioro, A. A. Paraecattil, A. A. Oskouei, and J. E. Moser, "Dynamics of interfacial charge transfer states and carriers separation in dye-sensitized solar cells: A time-resolved terahertz spectroscopy study," *Journal of Physical Chemistry C*, vol. 119, pp. 26 266–26 274, 47 Nov. 2015, ISSN: 19327455. DOI: 10.1021/ACS.JPCC.5B06911. [Online]. Available: https://pubs.acs.org/doi/full/10.1021/acs.jpcc.5b06911.

[45] V. Consonni, J. Briscoe, E. Kärber, X. Li, and T. Cossuet, "Zno nanowires for solar cells: A comprehensive review," *Nanotechnology*, vol. 30, p. 362 001, 36 Sep. 2019, ISSN: 0957-4484. DOI: 10.1088/1361-6528/ab1f2e. [Online]. Available: https://iopscience.iop.org/article/10.1088/1361-6528/ab1f2e.

[46] L. Shi, C. K. Lee, and A. P. Willard, "The enhancement of interfacial exciton dissociation by energetic disorder is a nonequilibrium effect," *ACS Central Science*, vol. 3, pp. 1262–1270, 12 Dec. 2017, ISSN: 23747951. DOI: 10.1021/ACSCENTSCI.7B00404. [Online]. Available: https://pubs.acs.org/doi/full/10.1021/acscentsci.7b00404.

[47] D. Liraz and N. Tessler, "Charge dissociation in organic solar cells—from onsager and frenkel to modern models," *Chemical Physics Reviews*, vol. 3, p. 031 305, 3 Sep. 2022. DOI: 10.1063/5.0099986. [Online]. Available: https://aip.scitation.org/doi/abs/10.1063/5.0099986.

[48] K. Vandewal, "Interfacial charge transfer states in condensed phase systems," *Annual Review of Physical Chemistry*, vol. 67, pp. 113–133, 1 May 2016, ISSN: 0066-426X. DOI: 10.1146/annurev-physchem-040215-112144. [Online]. Available: https://www.annualreviews.org/doi/10.1146/annurev-physchem-040215-112144.

[49] F. Piersimoni, R. Schlesinger, J. Benduhn, *et al.*, "Charge transfer absorption and emission at zno/organic interfaces," *Journal of Physical Chemistry Letters*, vol. 6, pp. 500–504, 3 Feb. 2015, ISSN: 19487185. DOI: 10.1021/JZ502657Z. [Online]. Available: https://pubs.acs.org/doi/full/10.1021/jz502657z.

[50] U. Hörmann, S. Zeiske, F. Piersimoni, *et al.*, "Stark effect of hybrid charge transfer states at planar zno/organic interfaces," *Physical Review B*, vol. 98, p. 155 312, 15 Oct. 2018, ISSN: 24699969. DOI: 10.1103/PHYSREVB.98.155312. [Online]. Available: https://journals.aps.org/prb/abstract/10.1103/PhysRevB.98.155312.

[51] A. Janotti and C. G. V. de Walle, "Fundamentals of zinc oxide as a semiconductor," *Reports on Progress in Physics*, vol. 72, p. 126 501, 12 Oct. 2009, ISSN: 0034-4885. DOI: 10.1088/0034-4885/72/12/126501. [Online]. Available: https://iopscience.iop.org/article/10.1088/0034-4885/72/12/126501.

[52] D. Stockwell, Y. Yang, J. Huang, C. Anfuso, Z. Huang, and T. Lian, "Comparison of electron transfer dynamics from coumarin 343 to tio2, sno2, and zno nanocrystalline thin films: Role of interface-bound charge-separated pairs," *Journal of Physical Chemistry C*, vol. 114, pp. 6560–6566, 14 Apr. 2010. DOI: 10.1021/JP912133R. [Online]. Available: https://pubs.acs.org/doi/full/10.1021/jp912133r.

[53] H. Němec, J. Rochford, O. Taratula, *et al.*, "Influence of the electron-cation interaction on electron mobility in dye-sensitized zno and tio2 nanocrystals: A study using ultrafast terahertz spectroscopy," *Physical Review Letters*, vol. 104, p. 197 401, 19 May 2010, ISSN: 00319007. DOI: 10.1103/PHYSREVLETT.104.197401/. [Online]. Available: https://journals.aps.org/prl/abstract/10.1103/PhysRevLett.104.197401.

[54] A. Panda, C. K. Renshaw, A. Oskooi, K. Lee, and S. R. Forrest, "Excited state and charge dynamics of hybrid organic/inorganic heterojunctions. ii. experiment," *Physical Review B - Condensed Matter and Materials Physics*, vol. 90, p. 045 303, 4 Jul. 2014, ISSN: 1550235X. DOI: 10.1103/PHYSREVB.90.045303/. [Online]. Available: https://journals.aps.org/prb/abstract/10.1103/PhysRevB.90.045303.

[55] C. K. Renshaw and S. R. Forrest, "Excited state and charge dynamics of hybrid organic/inorganic heterojunctions. i. theory," *Physical Review B - Condensed Matter and Materials Physics*, vol. 90, p. 045 302, 4 Jul. 2014, ISSN: 1550235X. DOI: 10.1103/PHYSREVB.90.045302/. [Online]. Available: https://journals.aps.org/prb/abstract/10.1103/PhysRevB.90.045302.

[56] A. Panda, K. Ding, X. Liu, and S. R. Forrest, "Free and trapped hybrid charge transfer excitons at a zno/small-molecule heterojunction," *Physical Review B*, vol. 94, p. 125 429, 12 Sep. 2016, ISSN: 24699969. DOI: 10.1103/PhysRevB.94.125429. [Online]. Available: https://journals.aps.org/prb/abstract/10.1103/PhysRevB.94.125429.

[57] M. Wojcik and M. Tachiya, "Accuracies of the empirical theories of the escape probability based on eigen model and braun model compared with the exact extension of onsager theory," *The Journal of Chemical Physics*, vol. 130, p. 104 107, 10 Mar. 2009, ISSN: 0021-9606. DOI: 10.1063/1.3082005. [Online]. Available: https://aip.scitation.org/doi/abs/10.1063/1.3082005.

[58] V. I. Arkhipov, P. Heremans, and H. Bässler, "Why is exciton dissociation so efficient at the interface between a conjugated polymer and an electron acceptor?" *Applied Physics*

Letters, vol. 82, p. 4605, 25 Jun. 2003, ISSN: 0003-6951. DOI: 10.1063/1.1586456. [Online]. Available: https://aip.scitation.org/doi/abs/10.1063/1.1586456.

[59] S. D. Baranovskii, M. Wiemer, A. V. Nenashev, F. Jansson, and F. Gebhard, "Calculating the efficiency of exciton dissociation at the interface between a conjugated polymer and an electron acceptor," *Journal of Physical Chemistry Letters*, vol. 3, pp. 1214–1221, 9 May 2012, ISSN: 19487185. DOI: 10.1021/JZ300123K/. [Online]. Available: https://pubs.acs.org/doi/full/10.1021/jz300123k.

[60] Z. Zhang and J. T. Yates, "Band bending in semiconductors: Chemical and physical consequences at surfaces and interfaces," *Chemical Reviews*, vol. 112, pp. 5520–5551, 10 Oct. 2012, ISSN: 00092665. DOI: 10.1021/CR3000626/. [Online]. Available: https://pubs.acs.org/doi/full/10.1021/cr3000626.

[61] W. J. Albery and P. N. Bartlett, "The transport and kinetics of photogenerated carriers in colloidal semiconductor electrode particles," *Journal of The Electrochemical Society*, vol. 131, pp. 315–325, 2 Feb. 1984, ISSN: 0013-4651. DOI: 10.1149/1.2115568/XML. [Online]. Available: https://iopscience.iop.org/article/10.1149/1.2115568.

[62] M. Quintana, T. Edvinsson, A. Hagfeldt, and G. Boschloo, "Comparison of dye-sensitized zno and TiO_2 solar cells: Studies of charge transport and carrier lifetime," *Journal of Physical Chemistry C*, vol. 111, pp. 1035–1041, 2 Jan. 2007, ISSN: 19327447. DOI: 10.1021/JP065948F/. [Online]. Available: https://pubs.acs.org/doi/full/10.1021/jp065948f.

[63] S. Neppl, J. Mahl, F. Roth, *et al.*, "Nanoscale confinement of photo-injected electrons at hybrid interfaces," *Journal of Physical Chemistry Letters*, vol. 12, pp. 11 951–11 959, 49 Dec. 2021, ISSN: 19487185. DOI: 10.1021/ACS.JPCLETT.1C02648. [Online]. Available: https://pubs.acs.org/doi/full/10.1021/acs.jpclett.1c02648.

[64] J. Mahl, O. Gessner, J. V. Barth, P. Feulner, and S. Neppl, "Strong potential gradients and electron confinement in zno nanoparticle films: Implications for charge-carrier

transport and photocatalysis," *ACS Applied Nano Materials*, vol. 4, pp. 12 213–12 221, 11 Nov. 2021, ISSN: 25740970. DOI: 10.1021/ACSANM.1C02730/. [Online]. Available: https://pubs.acs.org/doi/full/10.1021/acsanm.1c02730.

[65] R. Heinhold, S. P. Cooil, D. A. Evans, and M. W. Allen, "Stability of the surface electron accumulation layers on the nonpolar (1010) and (1120) faces of zno," *Journal of Physical Chemistry C*, vol. 118, pp. 24 575–24 582, 42 Oct. 2014, ISSN: 19327455. DOI: 10.1021/JP507820M/. [Online]. Available: https://pubs.acs.org/doi/full/10.1021/jp507820m.

[66] G. Grancini, M. Maiuri, D. Fazzi, *et al.*, "Hot exciton dissociation in polymer solar cells," *Nature Materials 2012 12:1*, vol. 12, pp. 29–33, 1 Dec. 2012, ISSN: 1476-4660. DOI: 10.1038/nmat3502. [Online]. Available: https://www.nature.com/articles/nmat3502.

[67] A. E. Jailaubekov, A. P. Willard, J. R. Tritsch, *et al.*, "Hot charge-transfer excitons set the time limit for charge separation at donor/acceptor interfaces in organic photovoltaics," *Nature Materials 2012 12:1*, vol. 12, pp. 66–73, 1 Dec. 2012, ISSN: 1476-4660. DOI: 10.1038/nmat3500. [Online]. Available: https://www.nature.com/articles/nmat3500.

[68] M. Abdellah, K. Žídek, K. Zheng, P. Chábera, M. E. Messing, and T. Pullerits, "Balancing electron transfer and surface passivation in gradient cdse/zns core-shell quantum dots attached to zno," *The Journal of Physical Chemistry Letters*, vol. 4, pp. 1760–1765, 11 Jun. 2013, ISSN: 1948-7185. DOI: 10.1021/jz4006459. [Online]. Available: https://pubs.acs.org/doi/10.1021/jz4006459.

[69] T. Hansen, K. Žídek, K. Zheng, *et al.*, "Orbital Topology Controlling Charge Injection in Quantum-Dot-Sensitized Solar Cells," *The Journal of Physical Chemistry Letters*, vol. 5, no. 7, pp. 1157–1162, Apr. 2014, ISSN: 1948-7185. DOI: 10.1021/jz5001193. [Online]. Available: http://pubs.acs.org/doi/10.1021/jz5001193.

[70] A. Honarfar, H. Mourad, W. Lin, *et al.*, "Photoexcitation Dynamics in Electrochemically Charged CdSe Quantum Dots: From Hot Carrier Cooling to Auger Recombination of Negative Trions," *ACS Applied Energy Materials*, vol. 3, no. 12, pp. 12 525–12 531, Dec. 2020, ISSN: 25740962. DOI: 10.1021/acsaem.0c02478. [Online]. Available: https://dx.doi.org/10.1021/acsaem.0c02478.

[71] E. Cánovas, H. Wang, M. Karakus, and M. Bonn, "Hot electron transfer from pbse quantum dots molecularly bridged to mesoporous tin and titanium oxide films," *Chemical Physics*, vol. 471, pp. 54–58, Jun. 2016, ISSN: 03010104. DOI: 10.1016/j.chemphys.2015.11.005. [Online]. Available: https://linkinghub.elsevier.com/retrieve/pii/S0301010415003456.

[72] K. P. Acharya, T. R. Alabi, N. Schmall, *et al.*, "Linker-free modification of tio2 nanorods with pbse nanocrystals," *Journal of Physical Chemistry C*, vol. 113, pp. 19 531–19 535, 45 2009, ISSN: 19327447. DOI: 10.1021/jp907321h.

[73] T. C. Rossi, C. P. Dykstra, T. N. Haddock, *et al.*, "Charge carrier screening in photoexcited epitaxial semiconductor nanorods revealed by transient x-ray absorption linear dichroism," *Nano Letters*, vol. 21, pp. 9534–9542, 22 Nov. 2021, ISSN: 15306992. DOI: 10.1021/ACS.NANOLETT.1C02865. [Online]. Available: https://pubs.acs.org/doi/abs/10.1021/acs.nanolett.1c02865.

[74] T. J. Penfold, J. Szlachetko, F. G. Santomauro, *et al.*, "Revealing hole trapping in zinc oxide nanoparticles by time-resolved x-ray spectroscopy," *Nature Communications*, vol. 9, 1 Dec. 2018, ISSN: 20411723. DOI: 10.1038/S41467-018-02870-4.

[75] A. Kuzmin and J. Chaboy, "Exafs and xanes analysis of oxides at the nanoscale," *IUCrJ*, vol. 1, pp. 571–589, 2014, ISSN: 20522525. DOI: 10.1107/S2052252514021101.

[76] C. M. Gentle, Y. Wang, T. N. Haddock, C. P. Dykstra, and R. M. van der Veen, "Internal atomic-scale structure determination and band alignment of ii–vi quantum

dot heterostructures," *The Journal of Physical Chemistry C*, vol. 124, pp. 3895–3904, 6 Feb. 2020, ISSN: 1932-7447. DOI: 10.1021/acs.jpcc.9b11443.

[77] T. Rossi, T. J. Penfold, M. H. Rittmann-Frank, *et al.*, "Characterizing the structure and defect concentration of zno nanoparticles in a colloidal solution," *Journal of Physical Chemistry C*, vol. 118, pp. 19 422–19 430, 33 Aug. 2014, ISSN: 19327455. DOI: 10.1021/JP505559U.

[78] M. H. Rittmann-Frank, C. J. Milne, J. Rittmann, M. Reinhard, T. J. Penfold, and M. Chergui, "Mapping of the photoinduced electron traps in TiO_2 by picosecond x-ray absorption spectroscopy," *Angewandte Chemie International Edition*, vol. 53, pp. 5858–5862, 23 Jun. 2014, ISSN: 1521-3773. DOI: 10.1002/anie.201310522. [Online]. Available: http://doi.wiley.com/10.1002/anie.201310522.

[79] Y. Obara, H. Ito, T. Ito, *et al.*, "Femtosecond time-resolved x-ray absorption spectroscopy of anatase tio2 nanoparticles using xfel," *Structural Dynamics*, vol. 4, 4 Jul. 2017, ISSN: 23297778. DOI: 10.1063/1.4989862.

[80] M. M. Taheri, K. C. Elbert, S. Yang, *et al.*, "Distinguishing electron and hole dynamics in functionalized cdse/cds core/shell quantum dots using complementary ultrafast spectroscopies and kinetic modeling," *Journal of Physical Chemistry C*, vol. 125, pp. 31–41, 1 Jan. 2021, ISSN: 19327455. DOI: 10.1021/acs.jpcc.0c07037. [Online]. Available: https://dx.doi.org/10.1021/acs.jpcc.0c07037.

[81] K. B. Ucer, R. A. Wall, K. C. Lipke, and R. T. Williams, "Picosecond transient absorption and excitonic luminescence at low temperature in undoped zno," *physica status solidi (b)*, vol. 245, pp. 2680–2683, 12 Dec. 2008, ISSN: 1521-3951. DOI: 10.1002/PSSB.200879895. [Online]. Available: https://onlinelibrary.wiley.com/doi/full/10.1002/pssb.200879895.

[82] J. B. Asbury, Y. Q. Wang, and T. Lian, "Multiple-exponential electron injection in ru(dcbpy)2(scn)2 sensitized zno nanocrystalline thin films," *Journal of Physical*

Chemistry B, vol. 103, pp. 6643–6647, 32 Aug. 1999, ISSN: 15206106. DOI: 10.1021/JP991625Q/. [Online]. Available: https://pubs.acs.org/doi/full/10.1021/jp991625q.

[83] K. Žídek, K. Zheng, M. Abdellah, P. Chábera, T. Pullerits, and M. Tachyia, "Simultaneous creation and recovery of trap states on quantum dots in a photoirradiated cdse–zno system," *Journal of Physical Chemistry C*, vol. 118, pp. 27 567–27 573, 47 Nov. 2014. DOI: 10.1021/JP509242R. [Online]. Available: https://pubs.acs.org/doi/full/10.1021/jp509242r.

[84] R. Adhikari, K. Basu, Y. Zhou, *et al.*, "Heterostructured quantum dot architectures for efficient and stable photoelectrochemical hydrogen production," *Journal of Materials Chemistry A*, vol. 6, pp. 6822–6829, 16 Apr. 2018, ISSN: 2050-7496. DOI: 10.1039/C7TA11378A. [Online]. Available: https://pubs.rsc.org/en/content/articlehtml/2018/ta/c7ta11378a.

[85] I. S. Moody, A. R. Stonas, and M. C. Lonergan, "Pbs nanocrystals functionalized with a short-chain, ionic, dithiol ligand," *Journal of Physical Chemistry C*, vol. 112, pp. 19 383–19 389, 49 Dec. 2008, ISSN: 19327447. DOI: 10.1021/jp807360q. [Online]. Available: http://pubs.acs.org/doi/10.1021/jp807360q.

[86] T. P. Chou, Q. Zhang, and G. Cao, "Effects of dye loading conditions on the energy conversion efficiency of zno and tio2 dye-sensitized solar cells," *The Journal of Physical Chemistry C*, vol. 111, pp. 18 804–18 811, 50 Dec. 2007, ISSN: 1932-7447. DOI: 10.1021/jp076724f. [Online]. Available: https://pubs.acs.org/doi/10.1021/jp076724f.

[87] M. Y. Guo, A. M. C. Ng, F. Liu, *et al.*, "Effect of native defects on photocatalytic properties of zno," *Journal of Physical Chemistry C*, vol. 115, pp. 11 095–11 101, 22 Jun. 2011, ISSN: 19327447. DOI: 10.1021/JP200926U/. [Online]. Available: https://pubs.acs.org/doi/full/10.1021/jp200926u.

[88] B. A. Gregg, "Excitonic solar cells," *The Journal of Physical Chemistry B*, vol. 107, pp. 4688–4698, 20 May 2003, ISSN: 1520-6106. DOI: 10.1021/jp022507x. [Online]. Available: https://pubs.acs.org/doi/10.1021/jp022507x.

[89] J. Fan, Y. Hao, C. Munuera, *et al.*, "Influence of the annealing atmosphere on the performance of zno nanowire dye-sensitized solar cells," *Journal of Physical Chemistry C*, vol. 117, pp. 16 349–16 356, 32 Aug. 2013, ISSN: 19327447. DOI: 10.1021/JP405557B. [Online]. Available: https://pubs.acs.org/doi/full/10.1021/jp405557b.

[90] E. Baldini, T. Palmieri, T. Rossi, *et al.*, "Interfacial Electron Injection Probed by a Substrate-Specific Excitonic Signature," *Journal of the American Chemical Society*, vol. 139, no. 33, pp. 11 584–11 589, Aug. 2017, ISSN: 0002-7863. DOI: 10.1021/jacs.7b06322. [Online]. Available: http://pubs.acs.org/doi/10.1021/jacs.7b06322.

[91] I. Chambrier, C. Banerjee, S. Remiro-Buenamañana, Y. Chao, A. N. Cammidge, and M. Bochmann, "Synthesis of porphyrin-cdse quantum dot assemblies: Controlling ligand binding by substituent effects," *Inorganic Chemistry*, vol. 54, pp. 7368–7380, 15 Aug. 2015, ISSN: 1520510X. DOI: 10.1021/ACS.INORGCHEM.5B00892. [Online]. Available: https://pubs.acs.org/doi/full/10.1021/acs.inorgchem.5b00892.

[92] J. Jasieniak, C. Bullen, J. V. Embden, and P. Mulvaney, "Phosphine-free synthesis of cdse nanocrystals," *Journal of Physical Chemistry B*, vol. 109, pp. 20 665–20 668, 44 Nov. 2005, ISSN: 15206106. DOI: 10.1021/JP054289O/. [Online]. Available: https://pubs.acs.org/doi/full/10.1021/jp054289o.

[93] D. A. Henckel, M. J. Enright, N. P. Eslami, D. M. Kroupa, D. R. Gamelin, and B. M. Cossairt, "Modeling equilibrium binding at quantum dot surfaces using cyclic voltammetry," *Nano Letters*, vol. 20, pp. 2620–2624, 4 Apr. 2020, ISSN: 15306992. DOI: 10.1021/ACS.NANOLETT.0C00162. [Online]. Available: https://pubs.acs.org/doi/full/10.1021/acs.nanolett.0c00162.

[94] M. J. Enright and B. M. Cossairt, "Synthesis of tailor-made colloidal semiconductor heterostructures," *Chemical Communications*, vol. 54, pp. 7109–7122, 52 Jun. 2018, ISSN: 1364-548X. DOI: 10.1039/C8CC03498B. [Online]. Available: https://pubs.rsc.org/en/content/articlehtml/2018/cc/c8cc03498b.

[95] J. Yang, J. Y. Lee, and J. Y. Ying, "Phase transfer and its applications in nanotechnology," *Chemical Society Reviews*, vol. 40, pp. 1672–1696, 3 2011, ISSN: 03060012. DOI: 10.1039/b916790k.

[96] D. A. Hines and P. V. Kamat, "Quantum dot surface chemistry: Ligand effects and electron transfer reactions," *The Journal of Physical Chemistry C*, vol. 117, pp. 14 418–14 426, 27 Jul. 2013, ISSN: 1932-7447. DOI: 10.1021/jp404031s. [Online]. Available: http://pubs.acs.org/doi/10.1021/jp404031s.

[97] N. Kirkwood, J. O. V. Monchen, R. W. Crisp, *et al.*, "Finding and fixing traps in ii–vi and iii–v colloidal quantum dots: The importance of z-type ligand passivation," *Journal of the American Chemical Society*, vol. 140, pp. 15 712–15 723, 46 Nov. 2018, ISSN: 0002-7863. DOI: 10.1021/jacs.8b07783. [Online]. Available: https://pubs.acs.org/doi/10.1021/jacs.8b07783.

[98] Q. Dai, Y. Zhang, Y. Wang, *et al.*, "Ligand effects on synthesis and post-synthetic stability of pbse nanocrystals," *The Journal of Physical Chemistry C*, vol. 114, pp. 16 160–16 167, 39 Oct. 2010, ISSN: 1932-7447. DOI: 10.1021/jp102660g. [Online]. Available: http://pubs.acs.org/doi/10.1021/jp102660g.

[99] J. Aldana, Y. A. Wang, and X. Peng, "Photochemical instability of cdse nanocrystals coated by hydrophilic thiols," *Journal of the American Chemical Society*, vol. 123, pp. 8844–8850, 36 2001, ISSN: 00027863. DOI: 10.1021/ja016424q. [Online]. Available: https://pubs.acs.org/doi/full/10.1021/ja016424q.

[100] D. Mora-Fonz, J. Buckeridge, A. J. Logsdail, *et al.*, "Morphological features and band bending at nonpolar surfaces of zno," *Journal of Physical Chemistry C*, vol. 119,

pp. 11 598–11 611, 21 May 2015, ISSN: 19327455. DOI: 10.1021/ACS.JPCC.5B01331/. [Online]. Available: https://pubs.acs.org/doi/full/10.1021/acs.jpcc.5b01331.

[101] C. Wöll, "The chemistry and physics of zinc oxide surfaces," *Progress in Surface Science*, vol. 82, pp. 55–120, 2-3 Jan. 2007, ISSN: 0079-6816. DOI: 10.1016/J.PROGSURF.2006.12.002.

[102] J. Jasieniak, L. Smith, J. van Embden, P. Mulvaney, and M. Califano, "Re-examination of the size-dependent absorption properties of cdse quantum dots," *The Journal of Physical Chemistry C*, vol. 113, pp. 19 468–19 474, 45 Nov. 2009, ISSN: 1932-7447. DOI: 10.1021/jp906827m. [Online]. Available: https://pubs.acs.org/doi/10.1021/jp906827m.

[103] B. D. Viezbicke, S. Patel, B. E. Davis, and D. P. Birnie, "Evaluation of the tauc method for optical absorption edge determination: Zno thin films as a model system," *physica status solidi (b)*, vol. 252, pp. 1700–1710, 8 Aug. 2015, ISSN: 1521-3951. DOI: 10.1002/PSSB.201552007. [Online]. Available: https://onlinelibrary.wiley.com/doi/full/10.1002/pssb.201552007.

[104] J. Tauc, R. Grigorovici, and A. Vancu, "Optical properties and electronic structure of amorphous germanium," *physica status solidi (b)*, vol. 15, pp. 627–637, 2 Jan. 1966, ISSN: 1521-3951. DOI: 10.1002/PSSB.19660150224. [Online]. Available: https://onlinelibrary.wiley.com/doi/full/10.1002/pssb.19660150224.

[105] C. A. Leatherdale and M. G. Bawendi, "Observation of solvatochromism in cdse colloidal quantum dots," *Physical Review B - Condensed Matter and Materials Physics*, vol. 63, p. 165 315, 16 Apr. 2001, ISSN: 1550235X. DOI: 10.1103/PhysRevB.63.165315. [Online]. Available: https://link.aps.org/doi/10.1103/PhysRevB.63.165315.

[106] F. Urbach, "The long-wavelength edge of photographic sensitivity and of the electronic absorption of solids," *Physical Review*, vol. 92, p. 1324, 5 Dec. 1953, ISSN: 0031899X.

DOI: 10.1103/PhysRev.92.1324. [Online]. Available: https://journals.aps.org/pr/abstract/10.1103/PhysRev.92.1324.

[107] O. Herrfurth, S. Richter, M. Rebarz, *et al.*, "Transient birefringence and dichroism in zno studied with fs-time-resolved spectroscopic ellipsometry," *Physical Review Research*, vol. 3, p. 013 246, 1 Mar. 2021, ISSN: 2643-1564. DOI: 10.1103/PhysRevResearch.3.013246. [Online]. Available: https://link.aps.org/doi/10.1103/PhysRevResearch.3.013246.

[108] T. Toyoda, W. Yindeesuk, K. Kamiyama, *et al.*, "The electronic structure and photoinduced electron transfer rate of cdse quantum dots on single crystal rutile TiO_2: Dependence on the crystal orientation of the substrate," *Journal of Physical Chemistry C*, vol. 120, pp. 2047–2057, 4 Feb. 2016, ISSN: 19327455. DOI: 10.1021/ACS.JPCC.5B09528/. [Online]. Available: https://pubs.acs.org/doi/full/10.1021/acs.jpcc.5b09528.

[109] T. Toyoda, W. Yindeesuk, K. Kamiyama, S. Hayase, and Q. Shen, "Adsorption and electronic structure of cdse quantum dots on single crystal zno: A basic study of quantum dot-sensitization system," *Journal of Physical Chemistry C*, vol. 120, pp. 16 367–16 376, 30 Aug. 2016, ISSN: 19327455. DOI: 10.1021/ACS.JPCC.6B04130. [Online]. Available: https://pubs.acs.org/doi/full/10.1021/acs.jpcc.6b04130.

[110] T. Toyoda, Q. Shen, N. Nakazawa, Y. Yoshihara, K. Kamiyama, and S. Hayase, "Exponential optical absorption edge in pbs quantum dot-ligand systems on single crystal rutile-TiO_2 revealed by photoacoustic and absorbance spectroscopies," *Materials Research Express*, vol. 9, p. 025 005, 2 Feb. 2022, ISSN: 2053-1591. DOI: 10.1088/2053-1591/AC4F86. [Online]. Available: https://iopscience.iop.org/article/10.1088/2053-1591/ac4f86.

[111] L. Tröger, D. Arvanitis, K. Baberschke, H. Michaelis, U. Grimm, and E. Zschech, "Full correction of the self-absorption in soft-fluorescence extended x-ray-absorption fine structure," *Physical Review B*, vol. 46, pp. 3283–3289, 6 Aug. 1992, ISSN: 0163-1829. DOI: 10.1103/PhysRevB.46.3283. [Online]. Available: https://link.aps.org/doi/10.1103/PhysRevB.46.3283.

[112] P. Pfalzer, J.-P. Urbach, M. Klemm, *et al.*, "Elimination of self-absorption in fluorescence hard-x-ray absorption spectra," *Physical Review B*, vol. 60, pp. 9335–9339, 13 Oct. 1999, ISSN: 0163-1829. DOI: 10.1103/PhysRevB.60.9335. [Online]. Available: https://link.aps.org/doi/10.1103/PhysRevB.60.9335.

[113] R. M. Trevorah, C. T. Chantler, and M. J. Schalken, "Solving self-absorption in fluorescence," *IUCrJ*, vol. 6, pp. 586–602, 4 Jul. 2019, ISSN: 20522525. DOI: 10.1107/S2052252519005128.

[114] C. Brouder, "Angular dependence of x-ray absorption spectra," *Journal of Physics: Condensed Matter*, vol. 2, pp. 701–738, 3 Jan. 1990, ISSN: 0953-8984. DOI: 10.1088/0953-8984/2/3/018. [Online]. Available: https://iopscience.iop.org/article/10.1088/0953-8984/2/3/018.

[115] M. Newville, "Larch: An analysis package for xafs and related spectroscopies," *Journal of Physics: Conference Series*, vol. 430, p. 012 007, 1 Apr. 2013, ISSN: 1742-6596. DOI: 10.1088/1742-6596/430/1/012007. [Online]. Available: https://iopscience.iop.org/article/10.1088/1742-6596/430/1/012007.

[116] M. Newville, "Ifeffit: Interactive xafs analysis and feff fitting," *Journal of Synchrotron Radiation*, vol. 8, pp. 322–324, 2 Mar. 2001, ISSN: 09090495. DOI: 10.1107/S0909049500016964.

[117] M. Newville, "Exafs analysis using feff and feffit," *Journal of Synchrotron Radiation*, vol. 8, pp. 96–100, 2 Mar. 2001, ISSN: 0909-0495. DOI: 10.1107/S0909049500016290. [Online]. Available: https://scripts.iucr.org/cgi-bin/paper?S0909049500016290.

[118] A. Manceau and M. L. Schlegel, "Texture effect on polarized exafs amplitude," *Physics and Chemistry of Minerals*, vol. 28, pp. 52–56, 1 2001, ISSN: 03421791. DOI: 10.1007/s002690000127. [Online]. Available: https://link.springer.com/article/10.1007/s002690000127.

[119] J. Dittmer and H. Dau, "Theory of the linear dichroism in the extended x-ray absorption fine structure (exafs) of partially vectorially ordered systems," *Journal of Physical Chemistry B*, vol. 102, pp. 8196–8200, 42 Oct. 1998, ISSN: 15206106. DOI: 10.1021/JP981049I/. [Online]. Available: https://pubs.acs.org/doi/full/10.1021/jp981049i.

[120] K. Kihara and G. Donnay, "Anharmonic thermal vibrations in zno," *Canadian Mineralogist*, 1985.

[121] J. Albertsson, S. C. Abrahams, and Å. Kvick, "Atomic displacement, anharmonic thermal vibration, expansivity and pyroelectric coefficient thermal dependences in zno," *Acta Crystallographica Section B Structural Science*, vol. 45, pp. 34–40, 1 Feb. 1989, ISSN: 0108-7681. DOI: 10.1107/S0108768188010109. [Online]. Available: https://scripts.iucr.org/cgi-bin/paper?S0108768188010109.

[122] J. Timoshenko, A. Anspoks, A. Kalinko, and A. Kuzmin, "Temperature dependence of the local structure and lattice dynamics of wurtzite-type zno," *Acta Materialia*, vol. 79, pp. 194–202, Oct. 2014, ISSN: 1359-6454. DOI: 10.1016/J.ACTAMAT.2014.07.029.

[123] J. Fang, H. Fan, Y. Ma, Z. Wang, and Q. Chang, "Surface defects control for zno nanorods synthesized by quenching and their anti-recombination in photocatalysis," *Applied Surface Science*, vol. 332, pp. 47–54, Mar. 2015, ISSN: 0169-4332. DOI: 10.1016/J.APSUSC.2015.01.139.

[124] M. H. Engelhard, D. R. Baer, A. Herrera-Gomez, and P. M. A. Sherwood, "Introductory guide to backgrounds in xps spectra and their impact on determining peak intensities," *Journal of Vacuum Science and Technology A: Vacuum, Surfaces, and Films*, vol. 38,

p. 063 203, 6 Sep. 2020, ISSN: 0734-2101. DOI: 10.1116/6.0000359. [Online]. Available: https://avs.scitation.org/doi/abs/10.1116/6.0000359.

[125] Y. Joly, "X-ray absorption near-edge structure calculations beyond the muffin-tin approximation," *Physical Review B*, vol. 63, p. 125 120, 12 Mar. 2001, ISSN: 1550235X. DOI: 10.1103/PhysRevB.63.125120. [Online]. Available: https://journals.aps.org/prb/abstract/10.1103/PhysRevB.63.125120.

[126] L. Hedin and B. I. Lundqvist, "Explicit local exchange-correlation potentials," *Journal of Physics C: Solid State Physics*, vol. 4, p. 2064, 14 Oct. 1971, ISSN: 0022-3719. DOI: 10.1088/0022-3719/4/14/022. [Online]. Available: https://iopscience.iop.org/article/10.1088/0022-3719/4/14/022.

[127] H. Zhu, N. Song, W. Rodríguez-Córdoba, and T. Lian, "Wave function engineering for efficient extraction of up to nineteen electrons from one cdse/cds quasi-type ii quantum dot," *Journal of the American Chemical Society*, vol. 134, pp. 4250–4257, 9 Mar. 2012. DOI: 10.1021/JA210312S. [Online]. Available: https://pubs.acs.org/doi/full/10.1021/ja210312s.

[128] B. L. Henke, E. M. Gullikson, and J. C. Davis, "X-ray interactions: Photoabsorption, scattering, transmission, and reflection at e = 50-30, 000 ev, z = 1-92," *Atomic Data and Nuclear Data Tables*, vol. 54, pp. 181–342, 2 1993, ISSN: 0092640X. DOI: 10.1006/ADND.1993.1013.

[129] A. M. March, A. Stickrath, G. Doumy, *et al.*, "Development of high-repetition-rate laser pump/x-ray probe methodologies for synchrotron facilities," *Review of Scientific Instruments*, vol. 82, 7 2011. DOI: 10.1063/1.3615245. [Online]. Available: http://aip.scitation.org/doi/10.1063/1.3615245.

[130] M. A. Versteegh, T. Kuis, H. T. Stoof, and J. I. Dijkhuis, "Ultrafast screening and carrier dynamics in ZnO: Theory and experiment," *Physical Review B - Condensed Matter and Materials Physics*, vol. 84, no. 3, p. 035 207, Jul. 2011, ISSN: 10980121.

DOI: 10.1103/PhysRevB.84.035207. arXiv: 1012.3600. [Online]. Available: https://journals.aps.org/prb/abstract/10.1103/PhysRevB.84.035207.

[131] C. Klingshirn, R. Hauschild, J. Fallert, and H. Kalt, "Room-temperature stimulated emission of zno: Alternatives to excitonic lasing," *Physical Review B*, vol. 75, p. 115 203, 11 Mar. 2007. DOI: 10.1103/PhysRevB.75.115203. [Online]. Available: https://journals.aps.org/prb/abstract/10.1103/PhysRevB.75.115203.

[132] G. Xiong, U. Pal, and J. G. Serrano, "Correlations among size, defects, and photoluminescence in zno nanoparticles," *Journal of Applied Physics*, vol. 101, p. 024 317, 2 Jan. 2007, ISSN: 0021-8979. DOI: 10.1063/1.2424538. [Online]. Available: https://aip.scitation.org/doi/abs/10.1063/1.2424538.

[133] Y. Kim, S. Cho, S. Jeong, *et al.*, "Competition between charge transport and energy barrier in injection-limited metal/quantum dot nanocrystal contacts," *Chemistry of Materials*, vol. 26, pp. 6393–6400, 22 Nov. 2014. DOI: 10.1021/CM502763Z. [Online]. Available: https://pubs.acs.org/doi/full/10.1021/cm502763z.

[134] D. M. Adams, L. Brus, C. E. D. Chidsey, *et al.*, "Charge transfer on the nanoscale: Current status," *The Journal of Physical Chemistry B*, vol. 107, pp. 6668–6697, 28 Jul. 2003, ISSN: 1520-6106. DOI: 10.1021/jp0268462. [Online]. Available: http://pubs.acs.org/doi/abs/10.1021/jp0268462.

[135] H.-S. Tan, I. R. Piletic, and M. D. Fayer, "Polarization selective spectroscopy experiments: Methodology and pitfalls," *Journal of the Optical Society of America B*, vol. 22, p. 2009, 9 Sep. 2005, ISSN: 0740-3224. DOI: 10.1364/JOSAB.22.002009. [Online]. Available: https://www.osapublishing.org/abstract.cfm?URI=josab-22-9-2009.

[136] S. Schott, A. Steinbacher, J. Buback, P. Nuernberger, and T. Brixner, "Generalized magic angle for time-resolved spectroscopy with laser pulses of arbitrary ellipticity," *Journal of Physics B: Atomic, Molecular and Optical Physics*, vol. 47, p. 124 014, 12 Jun.

2014, ISSN: 0953-4075. DOI: 10.1088/0953-4075/47/12/124014. [Online]. Available: https://iopscience.iop.org/article/10.1088/0953-4075/47/12/124014.

[137] L. Blanchet, J. Réhault, C. Ruckebusch, J. P. Huvenne, R. Tauler, and A. de Juan, "Chemometrics description of measurement error structure: Study of an ultrafast absorption spectroscopy experiment," *Analytica Chimica Acta*, vol. 642, pp. 19–26, 1-2 May 2009, ISSN: 00032670. DOI: 10.1016/j.aca.2008.11.039. [Online]. Available: https://linkinghub.elsevier.com/retrieve/pii/S0003267008019387.

[138] T. Labrador and G. Dukovic, "Simultaneous determination of spectral signatures and decay kinetics of excited state species in semiconductor nanocrystals probed by transient absorption spectroscopy," *The Journal of Physical Chemistry C*, vol. 124, pp. 8439–8447, 15 Apr. 2020. DOI: 10.1021/ACS.JPCC.0C01701. [Online]. Available: https://pubs.acs.org/doi/abs/10.1021/acs.jpcc.0c01701.

[139] G. Grimaldi, J. J. Geuchies, W. van der Stam, *et al.*, "Spectroscopic evidence for the contribution of holes to the bleach of cd-chalcogenide quantum dots," *Nano Letters*, vol. 19, pp. 3002–3010, 5 May 2019. DOI: 10.1021/ACS.NANOLETT.9B00164. [Online]. Available: https://pubs.acs.org/doi/full/10.1021/acs.nanolett.9b00164.

[140] D. P. Morgan and D. F. Kelley, "What Does the Transient Absorption Spectrum of CdSe Quantum Dots Measure?" *Journal of Physical Chemistry C*, vol. 124, no. 15, pp. 8448–8455, Apr. 2020, ISSN: 19327455. DOI: 10.1021/acs.jpcc.0c02566. [Online]. Available: https://dx.doi.org/10.1021/acs.jpcc.0c02566.

[141] R. Hyndman and G. Athanasopoulos, *Forecasting: Principles and Practice*, 3rd ed. Otexts, 2021. [Online]. Available: https://otexts.com/fpp3/.

[142] M. Greben, P. Khoroshyy, I. Sychugov, and J. Valenta, "Non-exponential decay kinetics: Correct assessment and description illustrated by slow luminescence of si nanostructures," *Applied Spectroscopy Reviews*, vol. 54, pp. 758–801, 9 Oct. 2019,

ISSN: 0570-4928. DOI: 10.1080/05704928.2018.1517263. [Online]. Available: https://www.tandfonline.com/doi/full/10.1080/05704928.2018.1517263.

[143] V. A. Belyakov, V. A. Burdov, R. Lockwood, and A. Meldrum, "Silicon nanocrystals: Fundamental theory and implications for stimulated emission," *Advances in Optical Technologies*, 2008, ISSN: 16876393. DOI: 10.1155/2008/279502.

[144] A. Nguyen, C. M. Gonzalez, R. Sinelnikov, *et al.*, "Detection of nitroaromatics in the solid, solution, and vapor phases using silicon quantum dot sensors," *Nanotechnology*, vol. 27, p. 105 501, 10 Feb. 2016, ISSN: 0957-4484. DOI: 10.1088/0957-4484/27/10/105501. [Online]. Available: https://iopscience.iop.org/article/10.1088/0957-4484/27/10/105501.

[145] M. S. Azzaro, A. Dodin, D. Y. Zhang, A. P. Willard, and S. T. Roberts, "Exciton-delocalizing ligands can speed up energy migration in nanocrystal solids," *Nano Letters*, vol. 18, 5 2018, ISSN: 15306992. DOI: 10.1021/acs.nanolett.8b01079.

[146] K. E. Knowles, M. T. Frederick, D. B. Tice, A. J. Morris-Cohen, and E. A. Weiss, "Colloidal quantum dots: Think outside the (particle-in-a-)box," *Journal of Physical Chemistry Letters*, vol. 3, pp. 18–26, 1 Jan. 2011. DOI: 10.1021/JZ2013775. [Online]. Available: https://pubs.acs.org/doi/full/10.1021/jz2013775.

[147] J. E. Katz, X. Zhang, K. Attenkofer, *et al.*, "Electron small polarons and their mobility in iron (oxyhydr)oxide nanoparticles," *Science*, vol. 337, pp. 1200–1203, 6099 Sep. 2012, ISSN: 10959203. DOI: 10.1126/SCIENCE.1223598.

[148] F. G. Santomauro, J. Grilj, L. Mewes, *et al.*, "Localized holes and delocalized electrons in photoexcited inorganic perovskites: Watching each atomic actor by picosecond x-ray absorption spectroscopy," *Structural Dynamics*, vol. 4, 4 Jul. 2017, ISSN: 23297778. DOI: 10.1063/1.4971999.

[149] K. Zheng, M. Abdellah, Q. Zhu, *et al.*, "Direct experimental evidence for photoinduced strong-coupling polarons in organolead halide perovskite nanoparticles," *Journal of*

Physical Chemistry Letters, vol. 7, pp. 4535–4539, 22 Nov. 2016, ISSN: 19487185. DOI: 10.1021/ACS.JPCLETT.6B02046.

[150] C. Liu, H. Tsai, W. Nie, D. J. Gosztola, and X. Zhang, "Direct spectroscopic observation of the hole polaron in lead halide perovskites," *Journal of Physical Chemistry Letters*, vol. 11, pp. 6256–6261, 15 Aug. 2020, ISSN: 19487185. DOI: 10.1021/ACS.JPCLETT.0C01708.

[151] O. Cannelli, N. Colonna, M. Puppin, *et al.*, "Quantifying photoinduced polaronic distortions in inorganic lead halide perovskite nanocrystals," *Journal of the American Chemical Society*, vol. 143, pp. 9048–9059, 24 Jun. 2021, ISSN: 15205126. DOI: 10.1021/JACS.1C02403.

[152] F. G. Santomauro, A. Lübcke, J. Rittmann, *et al.*, "Femtosecond x-ray absorption study of electron localization in photoexcited anatase tio 2," *Scientific Reports*, vol. 5, Oct. 2015, ISSN: 20452322. DOI: 10.1038/SREP14834.

[153] A. Koide, Y. Uemura, D. Kido, *et al.*, "Photoinduced anisotropic distortion as the electron trapping site of tungsten trioxide by ultrafast w l1-edge x-ray absorption spectroscopy with full potential multiple scattering calculations," *Physical Chemistry Chemical Physics*, vol. 22, pp. 2615–2621, 5 2020, ISSN: 14639076. DOI: 10.1039/C9CP01332F.

[154] D. Hayes, R. G. Hadt, J. D. Emery, *et al.*, "Electronic and nuclear contributions to time-resolved optical and x-ray absorption spectra of hematite and insights into photoelectrochemical performance," *Energy and Environmental Science*, vol. 9, pp. 3754–3769, 12 2016, ISSN: 1754-5692. DOI: 10.1039/C6EE02266A.

[155] J. E. Katz, B. Gilbert, X. Zhang, K. Attenkofer, R. W. Falcone, and G. A. Waychunas, "Observation of transient iron(ii) formation in dye-sensitized iron oxide nanoparticles by time-resolved x-ray spectroscopy," *Journal of Physical Chemistry Letters*, vol. 1, pp. 1372–1376, 9 May 2010, ISSN: 19487185. DOI: 10.1021/JZ100296R.

[156] Y. Uemura, D. Kido, Y. Wakisaka, *et al.*, "Dynamics of photoelectrons and structural changes of tungsten trioxide observed by femtosecond transient xafs," *Angewandte Chemie*, vol. 128, pp. 1386–1389, 4 Jan. 2016. DOI: 10.1002/ANGE.201509252.

[157] A. Hassan, X. Zhang, X. Liu, *et al.*, "Charge carriers modulate the bonding of semiconductor nanoparticle dopants as revealed by time-resolved x-ray spectroscopy," *ACS Nano*, vol. 11, pp. 10 070–10 076, 10 Oct. 2017, ISSN: 1936086X. DOI: 10.1021/ACSNANO.7B04414.

[158] A. Hassan, X. Zhang, C. Liu, and P. T. Snee, "Electronic structure and dynamics of copper-doped indium phosphide nanocrystals studied with time-resolved x-ray absorption and large-scale dft calculations," *Journal of Physical Chemistry C*, vol. 122, pp. 11 145–11 151, 20 May 2018, ISSN: 19327455. DOI: 10.1021/ACS.JPCC.8B02124.

[159] T. C. Rossi, D. Grolimund, M. Nachtegaal, *et al.*, "X-ray absorption linear dichroism at the ti k edge of anatase tio2 single crystals," *Physical Review B*, vol. 100, p. 245 207, 24 Dec. 2019, ISSN: 2469-9950. DOI: 10.1103/PhysRevB.100.245207. [Online]. Available: https://link.aps.org/doi/10.1103/PhysRevB.100.245207.

[160] J. Vura-Weis, C. M. Jiang, C. Liu, *et al.*, "Femtosecond m2,3-edge spectroscopy of transition-metal oxides: Photoinduced oxidation state change in α-fe2o3," *Journal of Physical Chemistry Letters*, vol. 4, pp. 3667–3671, 21 Nov. 2013, ISSN: 19487185. DOI: 10.1021/JZ401997D. [Online]. Available: https://pubs.acs.org/doi/abs/10.1021/jz401997d.

[161] M. Zürch, H. T. Chang, P. M. Kraus, *et al.*, "Ultrafast carrier thermalization and trapping in silicon-germanium alloy probed by extreme ultraviolet transient absorption spectroscopy," *Structural Dynamics*, vol. 4, 4 Jul. 2017, ISSN: 23297778. DOI: 10.1063/1.4985056.

[162] L. Foglia, S. Vempati, B. T. Bonkano, *et al.*, "Revealing the competing contributions of charge carriers, excitons, and defects to the non-equilibrium optical properties

of zno," *Structural Dynamics*, vol. 6, p. 034 501, 3 May 2019, ISSN: 2329-7778. DOI: 10.1063/1.5088767. [Online]. Available: http://aca.scitation.org/doi/10.1063/1.5088767.

[163] J. Mahl, S. Neppl, F. Roth, *et al.*, "Decomposing electronic and lattice contributions in optical pump-x-ray probe transient inner-shell absorption spectroscopy of cuo," *Faraday Discussions*, vol. 216, pp. 414–433, 2019, ISSN: 13645498. DOI: 10.1039/C8FD00236C.

[164] M. S. Kirschner, B. T. Diroll, A. Brumberg, *et al.*, "Optical signatures of transiently disordered semiconductor nanocrystals," *ACS Nano*, vol. 12, pp. 10 008–10 015, 10 Oct. 2018, ISSN: 1936-0851. DOI: 10.1021/acsnano.8b04435. [Online]. Available: https://pubs.acs.org/doi/10.1021/acsnano.8b04435.

[165] A. Anspoks, A. Kalinko, R. Kalendarev, and A. Kuzmin, "Local structure relaxation in nanocrystalline ni1 - xo thin films," *Thin Solid Films*, vol. 553, pp. 58–62, Feb. 2014, ISSN: 00406090. DOI: 10.1016/J.TSF.2013.08.132.

[166] I. Jonane, A. Anspoks, G. Aquilanti, and A. Kuzmin, "High-temperature x-ray absorption spectroscopy study of thermochromic copper molybdate," *Acta Materialia*, vol. 179, pp. 26–35, Oct. 2019, ISSN: 13596454. DOI: 10.1016/J.ACTAMAT.2019.06.034.

[167] D. Manuel, D. Cabaret, C. Brouder, P. Sainctavit, A. Bordage, and N. Trcera, "Experimental evidence of thermal fluctuations on the x-ray absorption near-edge structure at the aluminum ¡math display="inline"¿ ¡mi¿k¡/mi¿ ¡/math¿ edge," *Physical Review B*, vol. 85, p. 224 108, 22 Jun. 2012, ISSN: 1098-0121. DOI: 10.1103/PhysRevB.85.224108. [Online]. Available: https://link.aps.org/doi/10.1103/PhysRevB.85.224108.

[168] H. Sezen, H. Shang, F. Bebensee, *et al.*, "Evidence for photogenerated intermediate hole polarons in zno," *Nature Communications*, vol. 6, Apr. 2015, ISSN: 20411723. DOI: 10.1038/NCOMMS7901.

[169] A. Janotti and C. G. V. D. Walle, "Oxygen vacancies in zno," *Applied Physics Letters*, vol. 87, pp. 1–3, 12 Sep. 2005, ISSN: 00036951. DOI: 10.1063/1.2053360.

[170] J. C. Blake, J. Nieto-Pescador, Z. Li, and L. Gundlach, "Ultraviolet femtosecond kerr-gated wide-field fluorescence microscopy," *Optics Letters*, vol. 41, p. 2462, 11 Jun. 2016, ISSN: 0146-9592. DOI: 10.1364/OL.41.002462.

[171] M. W. Wolf and J. J. Martin, "Low temperature thermal conductivity of zinc oxide," *Physica Status Solidi (a)*, vol. 17, pp. 215–220, 1 May 1973, ISSN: 00318965. DOI: 10.1002/pssa.2210170124.

[172] D. R. Lide, *CRC handbook of chemistry and physics*. CRC press, 2004, vol. 85.

[173] H. M. Chen, C. K. Chen, C. C. Lin, *et al.*, "Multi-bandgap-sensitized zno nanorod photoelectrode arrays for water splitting: An x-ray absorption spectroscopy approach for the electronic evolution under solar illumination," *Journal of Physical Chemistry C*, vol. 115, pp. 21 971–21 980, 44 Nov. 2011, ISSN: 19327447. DOI: 10.1021/JP204291B.

[174] H. M. Chen, C. K. Chen, C. J. Chen, *et al.*, "Plasmon inducing effects for enhanced photoelectrochemical water splitting: X-ray absorption approach to electronic structures," *ACS Nano*, vol. 6, pp. 7362–7372, 8 Aug. 2012, ISSN: 19360851. DOI: 10.1021/NN3024877.

[175] H. M. Chen, C. K. Chen, M. L. Tseng, *et al.*, "Plasmonic zno/ag embedded structures as collecting layers for photogenerating electrons in solar hydrogen generation photoelectrodes," *Small*, vol. 9, pp. 2926–2936, 17 Sep. 2013, ISSN: 16136810. DOI: 10.1002/SMLL.201202547.

[176] Y. R. Lu, Y. F. Wang, H. W. Chang, *et al.*, "Effect of fe2o3 coating on zno nanowires in photoelectrochemical water splitting: A synchrotron x-ray spectroscopic and spectromicroscopic investigation," *Solar Energy Materials and Solar Cells*, vol. 209, Jun. 2020, ISSN: 09270248. DOI: 10.1016/J.SOLMAT.2020.110469.

[177] O. Šipr, A. Šimůnek, S. Bocharov, T. Kirchner, and G. Dräger, "Geometric and electronic structure effects in polarized v k -edge absorption near-edge structure spectra of v2o5," *Physical Review B*, vol. 60, pp. 14 115–14 127, 20 Nov. 1999, ISSN:

0163-1829. DOI: 10.1103/PhysRevB.60.14115. [Online]. Available: https://link.aps.org/doi/10.1103/PhysRevB.60.14115.

[178] A. Juhin, F. D. Groot, G. Vankó, M. Calandra, and C. Brouder, "Angular dependence of core hole screening in licoo2: A dft+u calculation of the oxygen and cobalt k -edge x-ray absorption spectra," *Physical Review B - Condensed Matter and Materials Physics*, vol. 81, 11 Mar. 2010, ISSN: 10980121. DOI: 10.1103/PHYSREVB.81.115115.

[179] R. Zeller, "Calculated core hole effects on the k x-ray spectra of bcc transition metals," *Zeitschrift für Physik B Condensed Matter*, vol. 72, pp. 79–85, 1 Mar. 1988, ISSN: 07223277. DOI: 10.1007/BF01313114.

[180] A. Gulans, S. Kontur, C. Meisenbichler, *et al.*, "Exciting: A full-potential all-electron package implementing density-functional theory and many-body perturbation theory," *Journal of Physics Condensed Matter*, vol. 26, 36 Sep. 2014, ISSN: 1361648X. DOI: 10.1088/0953-8984/26/36/363202.

[181] K. Gilmore, J. Vinson, E. L. Shirley, *et al.*, "Efficient implementation of core-excitation bethe-salpeter equation calculations," *Computer Physics Communications*, vol. 197, pp. 109–117, Dec. 2015, ISSN: 00104655. DOI: 10.1016/J.CPC.2015.08.014.

[182] O. Bunău and Y. Joly, "Self-consistent aspects of x-ray absorption calculations," *Journal of Physics Condensed Matter*, vol. 21, 34 2009, ISSN: 1361648X. DOI: 10.1088/0953-8984/21/34/345501.

[183] F. Jollet and C. Noguera, "Core hole effect on the xas si k edge shape in α-quartz," *physica status solidi (b)*, vol. 179, pp. 473–488, 2 1993, ISSN: 15213951. DOI: 10.1002/PSSB.2221790222.

[184] J. J. Rehr, "Excited state electronic structure and the theory of x-ray spectra," *Journal of Physics Condensed Matter*, vol. 15, 5 Feb. 2003, ISSN: 09538984. DOI: 10.1088/0953-8984/15/5/317.

[185] J. Vinson, J. J. Rehr, J. J. Kas, and E. L. Shirley, "Bethe-salpeter equation calculations of core excitation spectra," *Physical Review B - Condensed Matter and Materials Physics*, vol. 83, 11 Mar. 2011, ISSN: 10980121. DOI: 10.1103/PHYSREVB.83.115106.

[186] P. W. Hillyard, S. V. Kuchibhatla, T. E. Glover, *et al.*, "Atomic resolution mapping of the excited-state electronic structure of cu2 o with time-resolved x-ray absorption spectroscopy," *Physical Review B - Condensed Matter and Materials Physics*, vol. 80, 12 Sep. 2009, ISSN: 10980121. DOI: 10.1103/PHYSREVB.80.125210.

[187] S. Neppl, J. Mahl, A. S. Tremsin, *et al.*, "Towards efficient time-resolved x-ray absorption studies of electron dynamics at photocatalytic interfaces," *Faraday Discussions*, vol. 194, pp. 659–682, 0 Dec. 2016, ISSN: 1364-5498. DOI: 10.1039/C6FD00125D. [Online]. Available: https://pubs.rsc.org/en/content/articlehtml/2016/fd/c6fd00125d.

[188] M. F. Lin, M. A. Verkamp, J. Leveillee, *et al.*, "Carrier-specific femtosecond xuv transient absorption of pbi2 reveals ultrafast nonradiative recombination," *Journal of Physical Chemistry C*, vol. 121, pp. 27 886–27 893, 50 Dec. 2017, ISSN: 19327455. DOI: 10.1021/ACS.JPCC.7B11147.

[189] S. K. Cushing, A. Lee, I. J. Porter, *et al.*, "Differentiating photoexcited carrier and phonon dynamics in the δ, l, and σ valleys of si(100) with transient extreme ultraviolet spectroscopy," *Journal of Physical Chemistry C*, vol. 123, pp. 3343–3352, 6 Feb. 2019, ISSN: 19327455. DOI: 10.1021/ACS.JPCC.8B10887.

[190] S. K. Cushing, I. J. Porter, B. R. de Roulet, *et al.*, "Layer-resolved ultrafast extreme ultraviolet measurement of hole transport in a ni-tio2-si photoanode," *Science Advances*, vol. 6, 14 Apr. 2020, ISSN: 23752548. DOI: 10.1126/SCIADV.AAY6650.

[191] S. K. Cushing, C. J. Chen, C. L. Dong, *et al.*, "Tunable nonthermal distribution of hot electrons in a semiconductor injected from a plasmonic gold nanostructure," *ACS Nano*, vol. 12, pp. 7117–7126, 7 Jul. 2018, ISSN: 1936086X. DOI: 10.1021/ACSNANO.8B02939.

[192] H. Liu, I. M. Klein, J. M. Michelsen, and S. K. Cushing, "Element-specific electronic and structural dynamics using transient xuv and soft x-ray spectroscopy," *Chem*, vol. 7, pp. 2569–2584, 10 Oct. 2021, ISSN: 24519294. DOI: 10.1016/J.CHEMPR.2021.09.005.

[193] S. Richter, O. Herrfurth, S. Espinoza, *et al.*, "Ultrafast dynamics of hot charge carriers in an oxide semiconductor probed by femtosecond spectroscopic ellipsometry," *New Journal of Physics*, vol. 22, p. 083 066, 8 Aug. 2020, ISSN: 1367-2630. DOI: 10.1088/1367-2630/ABA7F3. [Online]. Available: https://iopscience.iop.org/article/10.1088/1367-2630/aba7f3.

[194] B. W. Mcneil and N. R. Thompson, "X-ray free-electron lasers," *Nature Photonics 2010 4:12*, vol. 4, pp. 814–821, 12 Nov. 2010, ISSN: 1749-4893. DOI: 10.1038/nphoton.2010.239. [Online]. Available: https://www.nature.com/articles/nphoton.2010.239.

[195] M. Chollet, R. Alonso-Mori, M. Cammarata, *et al.*, "The x-ray pump–probe instrument at the linac coherent light source," *Journal of Synchrotron Radiation*, vol. 22, pp. 503–507, 3 May 2015, ISSN: 1600-5775. DOI: 10.1107/S1600577515005135. [Online]. Available: http://scripts.iucr.org/cgi-bin/paper?S1600577515005135.

[196] V. N. Antonov, L. V. Bekenov, and A. N. Yaresko, "Electronic structure of strongly correlated systems," *Advances in Condensed Matter Physics*, vol. 2011, 2011, ISSN: 16878108. DOI: 10.1155/2011/298928.

[197] W. Hua, S. Mukamel, and Y. Luo, "Transient x-ray absorption spectral fingerprints of the s1 dark state in uracil," *The Journal of Physical Chemistry Letters*, vol. 10, pp. 7172–7178, 22 Nov. 2019, ISSN: 1948-7185. DOI: 10.1021/acs.jpclett.9b02692. [Online]. Available: https://pubs.acs.org/doi/10.1021/acs.jpclett.9b02692.

[198] B. R. Watson, B. Doughty, and T. R. Calhoun, "Energetics at the surface: Direct optical mapping of core and surface electronic structure in cdse quantum dots using broadband electronic sum frequency generation microspectroscopy," *Nano Letters*,

vol. 19, pp. 6157–6165, 9 Sep. 2019. DOI: 10.1021/ACS.NANOLETT.9B02201. [Online]. Available: https://pubs.acs.org/doi/full/10.1021/acs.nanolett.9b02201.

[199] A. D. Johnson, F. Cheng, Y. Tsai, and C.-K. Shih, "Giant enhancement of defect-bound exciton luminescence and suppression of band-edge luminescence in monolayer wse2–ag plasmonic hybrid structures," *Nano Letters*, vol. 17, pp. 4317–4322, 7 Jul. 2017. DOI: 10.1021/ACS.NANOLETT.7B01364. [Online]. Available: https://pubs.acs.org/doi/full/10.1021/acs.nanolett.7b01364.

[200] P. C. Sercel and A. L. Efros, "Band-edge exciton in cdse and other ii-vi and iii-v compound semiconductor nanocrystals - revisited," *Nano Letters*, vol. 18, pp. 4061–4068, 7 Jul. 2018, ISSN: 1530-6984. DOI: 10.1021/acs.nanolett.8b01980. [Online]. Available: https://pubs.acs.org/doi/10.1021/acs.nanolett.8b01980.

[201] M. Usuda, N. Hamada, T. Kotani, and M. van Schilfgaarde, "All-electron gw calculation based on the lapw method application to wurtzite zno," *Physical Review B*, vol. 66, p. 125 101, 12 Sep. 2002, ISSN: 0163-1829. DOI: 10.1103/PhysRevB.66.125101. [Online]. Available: https://link.aps.org/doi/10.1103/PhysRevB.66.125101.

[202] J. G. Lu, S. Fujita, T. Kawaharamura, *et al.*, "Carrier concentration dependence of band gap shift in n-type zno:al films," *Journal of Applied Physics*, vol. 101, p. 083 705, 8 Apr. 2007, ISSN: 0021-8979. DOI: 10.1063/1.2721374. [Online]. Available: https://aip.scitation.org/doi/abs/10.1063/1.2721374.

[203] A. M. March, G. Doumy, A. Andersen, *et al.*, "Elucidation of the photoaquation reaction mechanism in ferrous hexacyanide using synchrotron x-rays with sub-pulse-duration sensitivity," *The Journal of Chemical Physics*, vol. 151, p. 144 306, 14 Oct. 2019, ISSN: 0021-9606. DOI: 10.1063/1.5117318. [Online]. Available: https://pubs.aip.org/aip/jcp/article/1063386.

[204] J. H. Lin, H. J. Su, C. H. Lu, C. P. Chang, W. R. Liu, and W. F. Hsieh, "Pump polarization dependent ultrafast carrier dynamics and two-photon absorption in an

a-plane zno epitaxial film," *Applied Physics Letters*, vol. 107, p. 142 107, 14 Oct. 2015, ISSN: 0003-6951. DOI: 10.1063/1.4933038. [Online]. Available: https://aip.scitation.org/doi/abs/10.1063/1.4933038.

[205] S. Hua and W. Zhang, "Anisotropy of 2pa, 3pa, and kerr effect in nonpolar zno," *Optics Letters, Vol. 46, Issue 16, pp. 4065-4068*, vol. 46, pp. 4065–4068, 16 Aug. 2021, ISSN: 1539-4794. DOI: 10.1364/OL.432882. [Online]. Available: https://www.osapublishing.org/ol/abstract.cfm?uri=ol-46-16-4065.

[206] B. T. Diroll, M. S. Kirschner, P. Guo, and R. D. Schaller, "Optical and physical probing of thermal processes in semiconductor and plasmonic nanocrystals," *Annual Review of Physical Chemistry*, vol. 70, pp. 353–377, 1 2019, ISSN: 0066-426X. DOI: 10.1146/annurev-physchem-042018-052639.

[207] P. Maity, T. Debnath, and H. N. Ghosh, "Ultrafast charge carrier delocalization in cdse/cds quasi-type ii and cds/cdse inverted type i core–shell: A structural analysis through carrier-quenching study," *The Journal of Physical Chemistry C*, vol. 119, pp. 26 202–26 211, 46 Nov. 2015, ISSN: 1932-7447. DOI: 10.1021/acs.jpcc.5b08913. [Online]. Available: https://pubs.acs.org/doi/10.1021/acs.jpcc.5b08913.

[208] E. D. Goodwin, D. B. Straus, E. A. Gaulding, C. B. Murray, and C. R. Kagan, "The effects of inorganic surface treatments on photogenerated carrier mobility and lifetime in pbse quantum dot thin films," *Chemical Physics*, vol. 471, pp. 81–88, Jun. 2016, ISSN: 03010104. DOI: 10.1016/j.chemphys.2015.07.031. [Online]. Available: https://www.sciencedirect.com/science/article/pii/S0301010415002220.

[209] S. Shokhovets, L. Spieß, and G. Gobsch, "Spectroscopic ellipsometry of wurtzite zno and gan: Examination of a special case," *Journal of Applied Physics*, vol. 107, p. 023 509, 2 Jan. 2010, ISSN: 0021-8979. DOI: 10.1063/1.3285485. [Online]. Available: http://aip.scitation.org/doi/10.1063/1.3285485.

[210] R. A. Negres, J. M. Hales, A. Kobyakov, D. J. Hagan, and E. W. V. Stryland, "Experiment and analysis of two-photon absorption spectroscopy using a white-light continuum probe," *IEEE Journal of Quantum Electronics*, vol. 38, pp. 1205–1216, 9 Sep. 2002, ISSN: 00189197. DOI: 10.1109/JQE.2002.802448.

[211] L. C. Zhang, G. Yang, K. Wang, *et al.*, "Highly ordered zno nanohole arrays: Fabrication and enhanced two-photon absorption," *Optics Communications*, vol. 291, pp. 395–399, Mar. 2013, ISSN: 0030-4018. DOI: 10.1016/J.OPTCOM.2012.11.032.

[212] S. Mani, J. I. Jang, and J. B. Ketterson, "Highly efficient nonresonant two-photon absorption in zno pellets," *Applied Physics Letters*, vol. 93, p. 041 902, 4 Jul. 2008, ISSN: 0003-6951. DOI: 10.1063/1.2965107. [Online]. Available: https://aip.scitation.org/doi/abs/10.1063/1.2965107.

[213] C. Zhang, F. Zhang, T. Xia, *et al.*, "Low-threshold two-photon pumped ZnO nanowire lasers," *Optics Express*, vol. 17, no. 10, p. 7893, May 2009, ISSN: 1094-4087. DOI: 10.1364/oe.17.007893. [Online]. Available: https://www.osapublishing.org/abstract.cfm?uri=oe-17-10-7893.

[214] A. P. Roth, J. B. Webb, and D. F. Williams, "Absorption edge shift in zno thin films at high carrier densities," *Solid State Communications*, vol. 39, pp. 1269–1271, 12 Sep. 1981, ISSN: 0038-1098. DOI: 10.1016/0038-1098(81)90224-6.

[215] K. Sokolowski-Tinten and D. von der Linde, "Generation of dense electron-hole plasmas in silicon," *Physical Review B*, vol. 61, p. 2643, 4 Jan. 2000. DOI: 10.1103/PhysRevB.61.2643. [Online]. Available: https://journals.aps.org/prb/abstract/10.1103/PhysRevB.61.2643.

[216] M. Law, L. E. Greene, J. C. Johnson, R. Saykally, and P. Yang, "Nanowire dye-sensitized solar cells," *Nature Materials 2005 4:6*, vol. 4, pp. 455–459, 6 May 2005, ISSN: 1476-4660. DOI: 10.1038/nmat1387. [Online]. Available: https://www.nature.com/articles/nmat1387.

[217] I. M. Catalano, A. Cingolani, and M. Lepore, "Two-photon absorption spectra of direct and indirect materials: Zno and agcl," *Physical Review B*, vol. 33, p. 7270, 10 May 1986, ISSN: 01631829. DOI: 10.1103/PhysRevB.33.7270. [Online]. Available: https://journals.aps.org/prb/abstract/10.1103/PhysRevB.33.7270.

[218] C. Bauer, G. Boschloo, E. Mukhtar, and A. Hagfeldt, "Ultrafast relaxation dynamics of charge carriers relaxation in zno nanocrystalline thin films," *Chemical Physics Letters*, vol. 387, pp. 176–181, 1-3 Mar. 2004, ISSN: 0009-2614. DOI: 10.1016/J.CPLETT.2004.01.106.

[219] K. Virkki, E. Tervola, M. Ince, T. Torres, and N. V. Tkachenko, "Comparison of electron injection and recombination on TiO_2 nanoparticles and zno nanorods photosensitized by phthalocyanine," *Royal Society Open Science*, vol. 5, 7 Jul. 2018, ISSN: 20545703. DOI: 10.1098/rsos.180323. [Online]. Available: http://dx.doi.org/10.1098/rsos.180323.

[220] K. R. Siefermann, C. D. Pemmaraju, S. Neppl, *et al.*, "Atomic-scale perspective of ultrafast charge transfer at a dye–semiconductor interface," *Journal of Physical Chemistry Letters*, vol. 5, pp. 2753–2759, 15 Aug. 2014. DOI: 10.1021/JZ501264X. [Online]. Available: https://pubs.acs.org/doi/full/10.1021/jz501264x.

[221] S. Lian, J. A. Christensen, M. S. Kodaimati, C. R. Rogers, M. R. Wasielewski, and E. A. Weiss, "Oxidation of a molecule by the biexcitonic state of a cds quantum dot," *Journal of Physical Chemistry C*, vol. 123, pp. 5923–5930, 10 Mar. 2019, ISSN: 19327455. DOI: 10.1021/ACS.JPCC.9B00210. [Online]. Available: https://pubs.acs.org/doi/full/10.1021/acs.jpcc.9b00210.

[222] H. Zhu, Y. Yang, K. Hyeon-Deuk, *et al.*, "Auger-Assisted Electron Transfer from Photoexcited Semiconductor Quantum Dots," *Nano Letters*, vol. 14, no. 3, pp. 1263–1269, Mar. 2014, ISSN: 1530-6984. DOI: 10.1021/nl4041687. [Online]. Available: http://pubs.acs.org/doi/10.1021/nl4041687.

[223] H. J. Yun, T. Paik, M. E. Edley, J. B. Baxter, and C. B. Murray, "Enhanced charge transfer kinetics of cdse quantum dot-sensitized solar cell by inorganic ligand exchange treatments," *ACS Applied Materials and Interfaces*, vol. 6, pp. 3721–3728, 5 Mar. 2014, ISSN: 19448252. DOI: 10.1021/AM500026A. [Online]. Available: https://pubs.acs.org/doi/abs/10.1021/am500026a.

[224] J. K. Utterback, R. P. Cline, K. E. Shulenberger, J. D. Eaves, and G. Dukovic, "The motion of trapped holes on nanocrystal surfaces," *The Journal of Physical Chemistry Letters*, vol. 11, pp. 9876–9885, 22 Nov. 2020, ISSN: 19487185. DOI: 10.1021/ACS.JPCLETT.0C02618. [Online]. Available: https://pubs.acs.org/doi/full/10.1021/acs.jpclett.0c02618.

[225] J. K. Utterback, A. N. Grennell, M. B. Wilker, O. M. Pearce, J. D. Eaves, and G. Dukovic, "Observation of trapped-hole diffusion on the surfaces of cds nanorods," *Nature Chemistry*, vol. 8, pp. 1061–1066, 11 Jul. 2016, ISSN: 1755-4330. DOI: 10.1038/nchem.2566. [Online]. Available: http://www.nature.com/doifinder/10.1038/nchem.2566.

[226] E. A. Dalchiele, C. J. Pereyra, D. Ariosa, *et al.*, "Scattering of light by zno nanorod arrays," *Optics Letters, Vol. 46, Issue 10, pp. 2360-2363*, vol. 46, pp. 2360–2363, 10 May 2021, ISSN: 1539-4794. DOI: 10.1364/OL.422706. [Online]. Available: https://opg.optica.org/abstract.cfm?uri=ol-46-10-2360.

[227] N. V. Tepliakov, M. Y. Leonov, A. V. Baranov, *et al.*, "Quantum theory of electroabsorption in semiconductor nanocrystals," *Optics Express, Vol. 24, Issue 2, pp. A52-A57*, vol. 24, A52–A57, 2 Jan. 2016, ISSN: 1094-4087. DOI: 10.1364/OE.24.000A52. [Online]. Available: https://opg.optica.org/viewmedia.cfm?uri=oe-24-2-A52&seq=0&html=true.

[228] C. Zhang, Y. Xia, Z. Zhang, *et al.*, "Combination of cation exchange and quantized ostwald ripening for controlling size distribution of lead chalcogenide quantum dots,"

Chemistry of Materials, vol. 29, pp. 3615–3622, 8 Apr. 2017, ISSN: 15205002. DOI: 10.1021/acs.chemmater.7b00411. [Online]. Available: http://pubs.acs.org/doi/10.1021/acs.chemmater.7b00411.

[229] G. Nagamine, T. A. C. Ferreira, D. B. Almeida, *et al.*, "Sample concentration affects optical gain results in colloidal nanomaterials: Circumventing the distortions by below band gap excitation," *ACS Photonics*, vol. 9, pp. 156–162, 1 Jan. 2022, ISSN: 2330-4022. DOI: 10.1021/acsphotonics.1c01293. [Online]. Available: https://pubs.acs.org/doi/10.1021/acsphotonics.1c01293.

[230] A. Furube, R. Katoh, T. Yoshihara, *et al.*, "Ultrafast direct and indirect electron-injection processes in a photoexcited dye-sensitized nanocrystalline zinc oxide film: The importance of exciplex intermediates at the surface," *Journal of Physical Chemistry B*, vol. 108, pp. 12 583–12 592, 33 Aug. 2004, ISSN: 15206106. DOI: 10.1021/JP0487713/. [Online]. Available: https://pubs.acs.org/doi/full/10.1021/jp0487713.

[231] C. Strothkämper, A. Bartelt, P. Sippel, T. Hannappel, R. Schütz, and R. Eichberger, "Delayed electron transfer through interface states in hybrid zno/organic-dye nanostructures," *Journal of Physical Chemistry C*, vol. 117, pp. 17 901–17 908, 35 Sep. 2013, ISSN: 19327447. DOI: 10.1021/JP402042A. [Online]. Available: https://pubs.acs.org/doi/full/10.1021/jp402042a.

[232] P. Kumar and S. K. Pal, "Ultrafast multiexponential electron injection dynamics at a dye and zno qd interface: A combined spectroscopic and first principles study," *Physical Chemistry Chemical Physics*, vol. 18, pp. 29 571–29 581, 42 Oct. 2016, ISSN: 1463-9084. DOI: 10.1039/C6CP04610J. [Online]. Available: https://pubs.rsc.org/en/content/articlehtml/2016/cp/c6cp04610j.

[233] L. Gundlach, R. Ernstorfer, and F. Willig, "Dynamics of photoinduced electron transfer from adsorbed molecules into solids," *Applied Physics A: Materials Science and Processing*, vol. 88, pp. 481–495, 3 Aug. 2007, ISSN: 09478396. DOI: 10.1007/S00339-

007-4054-1/METRICS. [Online]. Available: https://link.springer.com/article/10.1007/s00339-007-4054-1.

[234] A. Furube, R. Katoh, K. Hara, S. Murata, H. Arakawa, and M. Tachiya, "Ultrafast stepwise electron injection from photoexcited ru-complex into nanocrystalline zno film via intermediates at the surface," *Journal of Physical Chemistry B*, vol. 107, pp. 4162–4166, 17 May 2003, ISSN: 10895647. DOI: 10.1021/JP034039C/. [Online]. Available: https://pubs.acs.org/doi/full/10.1021/jp034039c.

[235] M. Borgwardt, M. Wilke, T. Kampen, *et al.*, "Charge transfer dynamics at dye-sensitized zno and tio2 interfaces studied by ultrafast xuv photoelectron spectroscopy," *Scientific Reports 2016 6:1*, vol. 6, pp. 1–7, 1 Apr. 2016, ISSN: 2045-2322. DOI: 10.1038/srep24422. [Online]. Available: https://www.nature.com/articles/srep24422.

[236] A. Namekawa and R. Katoh, "Exciton annihilation in dye-sensitized nanocrystalline semiconductor films," *Chemical Physics Letters*, vol. 659, pp. 154–158, Aug. 2016, ISSN: 00092614. DOI: 10.1016/j.cplett.2016.07.026.

[237] Y. Liang, J. E. Thorne, and B. A. Parkinson, "Controlling the electronic coupling between cdse quantum dots and thiol capping ligands via ph and ligand selection," *Langmuir*, vol. 28, pp. 11 072–11 077, 30 Jul. 2012, ISSN: 07437463. DOI: 10.1021/LA301237P. [Online]. Available: https://pubs.acs.org/doi/full/10.1021/la301237p.

[238] P. Tiwana, P. Docampo, M. B. Johnston, H. J. Snaith, and L. M. Herz, "Electron mobility and injection dynamics in mesoporous zno, sno 2, and tio2 films used in dye-sensitized solar cells," *ACS Nano*, vol. 5, pp. 5158–5166, 6 Jun. 2011, ISSN: 19360851. DOI: 10.1021/NN201243Y/. [Online]. Available: https://pubs.acs.org/doi/full/10.1021/nn201243y.

[239] J. Zhu, F. Fan, R. Chen, H. An, Z. Feng, and C. Li, "Direct imaging of highly anisotropic photogenerated charge separations on different facets of a single bivo ¡sub¿4¡/sub¿

photocatalyst," *Angewandte Chemie International Edition*, vol. 54, pp. 9111–9114, 31 Jul. 2015, ISSN: 14337851. DOI: 10.1002/anie.201504135. [Online]. Available: https://onlinelibrary.wiley.com/doi/10.1002/anie.201504135.

[240] Z. Wang, M. Rafipoor, P. G. Risueño, *et al.*, "Phonon-assisted auger process enables ultrafast charge transfer in cdse quantum dot/organic molecule," *The Journal of Physical Chemistry C*, vol. 123, pp. 17 127–17 135, 28 Jul. 2019, ISSN: 1932-7447. DOI: 10.1021/acs.jpcc.9b03348. [Online]. Available: https://pubs.acs.org/doi/10.1021/acs.jpcc.9b03348.

[241] S. Ghosh, M. Ghosh, P. Kumar, A. S. Sarkar, and S. K. Pal, "Quenching of the excitonic emission of zno quantum dots due to auger-assisted hole transfer to cds quantum dots," *The Journal of Physical Chemistry C*, vol. 120, pp. 27 717–27 723, 48 Dec. 2016, ISSN: 1932-7447. DOI: 10.1021/acs.jpcc.6b11011. [Online]. Available: https://pubs.acs.org/doi/10.1021/acs.jpcc.6b11011.

[242] M. J. Fahimi, D. Fathi, and M. Ansari-Rad, "Accurate analysis of electron transfer from quantum dots to metal oxides in quantum dot sensitized solar cells," *Physica E: Low-dimensional Systems and Nanostructures*, vol. 73, pp. 148–155, Sep. 2015, ISSN: 1386-9477. DOI: 10.1016/J.PHYSE.2015.05.030.

[243] R. Benchamekh, N. A. Gippius, J. Even, *et al.*, "Tight-binding calculations of image-charge effects in colloidal nanoscale platelets of cdse," *Physical Review B - Condensed Matter and Materials Physics*, vol. 89, p. 035 307, 3 Jan. 2014, ISSN: 10980121. DOI: 10.1103/PHYSREVB.89.035307/. [Online]. Available: https://journals.aps.org/prb/abstract/10.1103/PhysRevB.89.035307.

[244] A. L. Asatryan, A. L. Vartanian, A. A. Kirakosyan, and L. A. Vardanyan, "Electric field and image charge effects on impurity-bound polarons in a cds colloidal quantum dot embedded in organic matrices," *Physica B: Condensed Matter*, vol. 503, pp. 70–74, Dec. 2016, ISSN: 0921-4526. DOI: 10.1016/J.PHYSB.2016.09.020.

[245] M. W. Allen, C. H. Swartz, T. H. Myers, T. D. Veal, C. F. McConville, and S. M. Durbin, "Bulk transport measurements in zno: The effect of surface electron layers," *Physical Review B - Condensed Matter and Materials Physics*, vol. 81, p. 075 211, 7 Feb. 2010, ISSN: 10980121. DOI: 10.1103/PHYSREVB.81.075211/. [Online]. Available: https://journals.aps.org/prb/abstract/10.1103/PhysRevB.81.075211.

[246] L. Zhang and J. M. Cole, "Anchoring groups for dye-sensitized solar cells," *ACS Applied Materials and Interfaces*, vol. 7, pp. 3427–3455, 6 Feb. 2015, ISSN: 1944-8244. DOI: 10.1021/am507334m. [Online]. Available: https://pubs.acs.org/doi/10.1021/am507334m.

[247] H. Wei, J.-W. Luo, S.-S. Li, and L.-W. Wang, "Revealing the origin of fast electron transfer in tio2 -based dye-sensitized solar cells," *Journal of the American Chemical Society*, vol. 138, pp. 8165–8174, 26 Jul. 2016, ISSN: 0002-7863. DOI: 10.1021/jacs.6b03524. [Online]. Available: https://pubs.acs.org/doi/10.1021/jacs.6b03524.

[248] M. Hosseini, A. Haghighatzadeh, and B. Mazinani, "Enhanced third-order optical susceptibility in heterogeneous wurtzite zno/anatase TiO_2 core/shell nanostructures via controlled TiO_2 shell thickness," *Optical Materials*, vol. 92, pp. 1–10, Jun. 2019, ISSN: 09253467. DOI: 10.1016/j.optmat.2019.03.042. [Online]. Available: https://linkinghub.elsevier.com/retrieve/pii/S0925346719302137.

[249] F. W. Wise, "Lead salt quantum dots: The limit of strong quantum confinement," *Accounts of Chemical Research*, vol. 33, pp. 773–780, 11 Nov. 2000, ISSN: 0001-4842. DOI: 10.1021/ar970220q. [Online]. Available: https://pubs.acs.org/doi/10.1021/ar970220q.

[250] H. I. Wang, I. Infante, S. ten Brinck, E. Canovas, and M. Bonn, "Efficient Hot Electron Transfer in Quantum Dot Sensitized Mesoporous Oxides at Room Temperature," *Nano Letters*, vol. 18, no. 8, pp. 5111–5115, Aug. 2018, ISSN: 15306992. DOI: 10.1021/

acs.nanolett.8b01981. [Online]. Available: http://pubs.acs.org/doi/10.1021/acs.nanolett.8b01981.

[251] W. A. Tisdale, K. J. Williams, B. A. Timp, D. J. Norris, E. S. Aydil, and X. Y. Zhu, "Hot-electron transfer from semiconductor nanocrystals," *Science*, vol. 328, pp. 1543–1547, 5985 Jun. 2010, ISSN: 0036-8075. DOI: 10.1126/science.1185509. [Online]. Available: https://www.sciencemag.org/lookup/doi/10.1126/science.1185509.

[252] E. Baldini, T. Palmieri, A. Dominguez, P. Ruello, A. Rubio, and M. Chergui, "Phonon-driven selective modulation of exciton oscillator strengths in anatase tio 2 nanoparticles," *Nano Letters*, vol. 18, pp. 5007–5014, 8 Aug. 2018, ISSN: 1530-6984. DOI: 10.1021/acs.nanolett.8b01837. [Online]. Available: https://pubs.acs.org/doi/10.1021/acs.nanolett.8b01837.

[253] D. Pan, N. Zhao, Q. Wang, S. Jiang, X. Ji, and L. An, "Facile synthesis and characterization of luminescent tio2 nanocrystals," *Advanced Materials*, vol. 17, pp. 1991–1995, 16 Aug. 2005, ISSN: 0935-9648. DOI: 10.1002/adma.200500479. [Online]. Available: http://doi.wiley.com/10.1002/adma.200500479.

[254] J. Ouyang, C. Schuurmans, Y. Zhang, *et al.*, "Low-temperature approach to high-yield and reproducible syntheses of high-quality small-sized pbse colloidal nanocrystals for photovoltaic applications," *ACS Applied Materials and Interfaces*, vol. 3, pp. 553–565, 2 Feb. 2011, ISSN: 1944-8244. DOI: 10.1021/am101129m. [Online]. Available: http://pubs.acs.org/doi/10.1021/am101129m.

Appendix A

Direct Excitation and Pseudo Quantum Yields

Knowing the quantum yield during an ultrafast charge injection experiment is usually very difficult to estimate. This meanst hat most charge injection experiments have no way to know how much of the photoexcited carriers make it into optically "bright" states. To estimate the quantum yield (QY) of charge injection, a series of 343 nm pump - UV probe experiments were done. The QY was estimated by assuming that if all the photons absorbed by the QDs resulted in an electron transferred to the ZnO, what bleach amplitude would be expected. The bleach amplitude between direct excitation and sensitized samples was compared using the absorbed photon count as the normalizing factor. The max bleach amplitude from direct excitation was plotted vs. the estimated absorbed photons/cm^2, as shown in figure A.1. The maximum bleach amplitude was reached after <1 ps at 365 nm for all measurements. The QY was estimated by equation A.1:

$$\Phi_{QD} = \frac{B_{ZnO}(\phi)}{2 * \Delta OD_{max}} \tag{A.1}$$

Where $B_{ZnO}(\phi)$ is the fit function shown in figure A.1a, and the factor 2 is due to the carrier-to-absorbed photon ratio, where an absorbed photon creates a single carrier in ZnO from charge injection, compared to the 2 carriers created after direct excitation. ΔOD_{max} is the maximum ZnO bleach amplitude after QD excitation. This assumes that the bleach amplitude in ZnO has equal contributions from holes and electrons. Within the range of fluences used (500 nJ - 6 mJ/cm^2) the bleach amplitude vs. absorbed photon count was

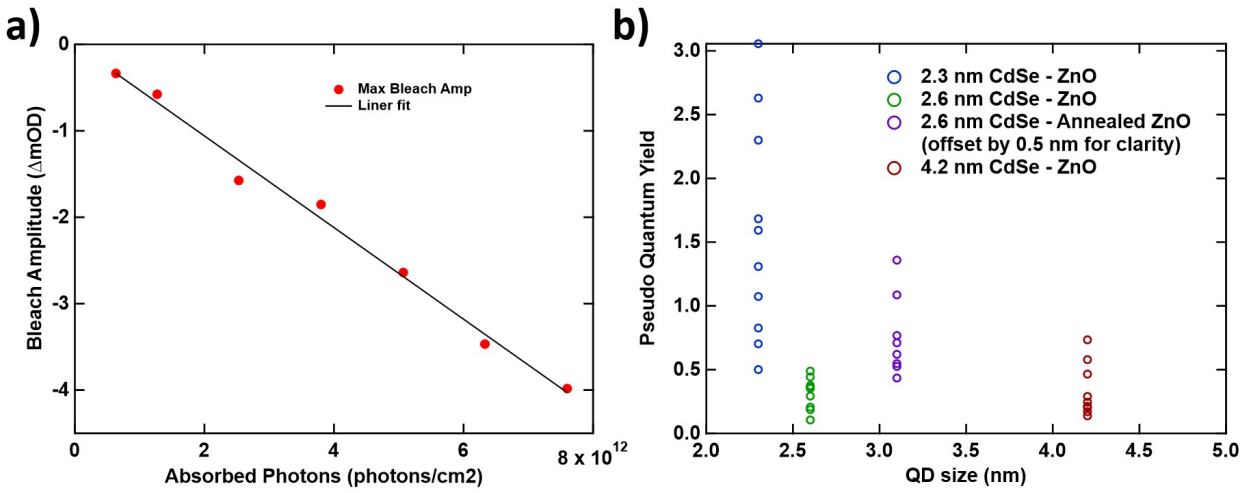

Figure A.1: a) The peak bleach amplitude at 365 nm plotted against the estimated number of absorbed photons (red trace). Also included is the linear fit of this signal (black trace). b) The extracted injection efficiency for each UV spot dataset plotted against the QD size for 2.3 nm sample (blue), 2.6 nm CdSe (green) and with annealed ZnO (purple), and 4.2 nm CdSe (red). The values span a range of values, with the 2.3 nm CdSe - ZnO having the widest variability due to two-photon absorption.

linear, however the kinetic behavior was not strictly linear, with the kinetic decay changing from single exponential decay to multi-exponential decay.

The estimated QY for the UV datasets is shown in figure A.1. The 2.3 nm CdSe sample has a number of factors that affects the estimation of it's QY, including the presence of two-photon absorption. However, the QY from spot to spot varies significantly, and is also high in general. This includes some spots with a QY much greater than 1. The variance could be due to inhomogeneously distributed QDs since the static UV-Vis is used to calculated the excitation density, but this should result in some spots with much lower QY. Two photon absorption in this case would give a constant baseline increase in QY, since it shouldn't vary from one spot to the next, and has the same photon to generated carrier ratio (2 photosn:2 carriers) as charge transfer (1 photon:1 carrier). One proposed mechanism that would explain the more dramatic variation is heterostructure - promoted two photon absorption. This has been shown in the case of TiO_2 coated ZnO where the difference in the refractive index of TiO_2 and ZnO would result in added internal reflection within the ZnO.[248] CdSe has a similar refractive index to TiO_2, and it's nanoscale size could enhance the electric field

magnitude. Since TPA scales with the square of the electric field magnitude this would result in a large enhancement of TPA that would also scale with the population of sensitizing quantum dots. Another consideration is the two-photon absorption due to pump-probe overlap. However, this should also be a constant baseline increase, rather than a factor that varies from spot to spot.

For the 4.2 and 2.6 nm CdSe sensitized ZnO the QY is less than 60 percent, with a mean QY of 40 percent. If the first two kinetic decays are attributed to charge injection, that means that almost 20 percent of injected electrons from both injection pathways are trapped, or undergo back electron transfer. Since back electron transfer is estimated to be greater than the temporal window, it seems likely that trap states are saturated over the 100 ps temporal window. Notably, the annealed ZnO sample has an overall higher QY than either the unannealed 2.6 nm or 4.2 nm CdSe samples. This is consistent with a decreased trap state density in the annealed sample. It's difficult to say whether both charge transfer pathways have the same quantum yield, or different quantum yields. A homogeneous trapping rate across both charge transfer pathways is likely to be the dominant mechanism here since the relative amplitudes of the visible and UV charge injection pathways match. If there was less trapping for one charge injection pathway over another, the expectation is that there would be a mismatch between the relative amplitudes between the UV and visible kinetics.

Appendix B

Synthesis of PbSe - TiO2 Heterostructure

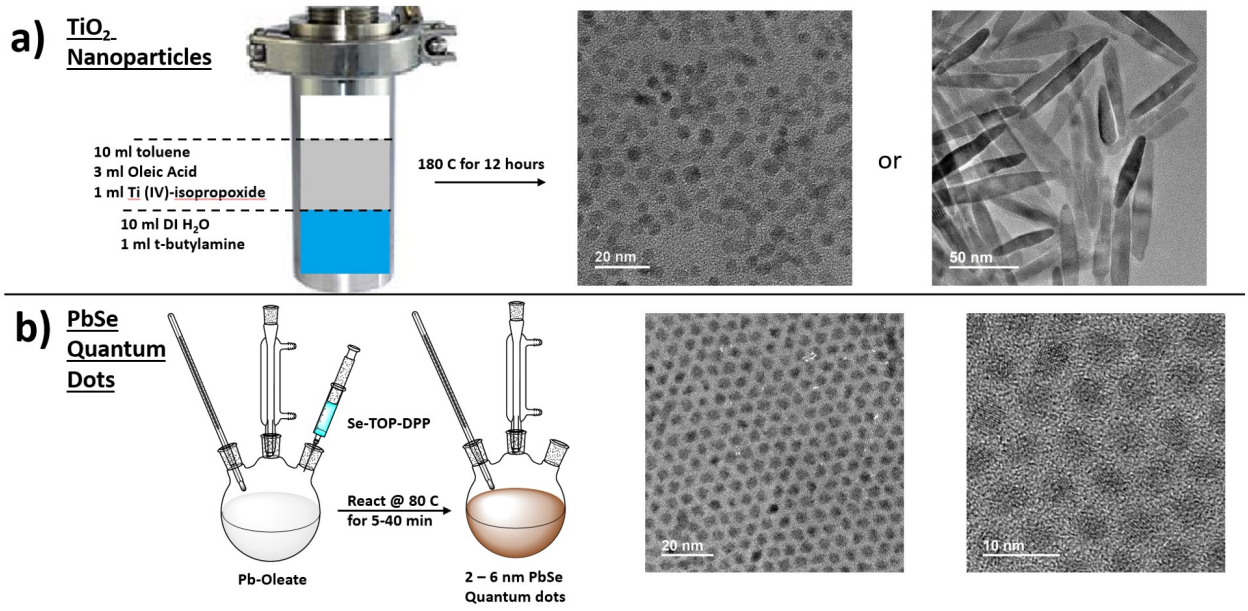

Figure B.1: a) Synthetic pathway for TiO_2 nanoellipsoids employing a biphasic bomb method. The initial biphasic mixture is shown inside the bomb. Reaction proceeds at 180 °C for 12 hours. At right are TEM images of the nanoparticles and nanorods that are grown concurrently. The nanoparticles will be concentrated primarily in the aqueous phase, while the nanorods will be concentrated in the organic phase. b) Synthetic method for the PbSe quantum dots employing a heat-up method. The reaction mixture is combined at low temperatures and heated up to the reaction temperature of 80 °C. The size of quantum dots is controlled by varying the reaction time, producing monodisperse samples between 2 and 6 nm QDs.

This chapter describes the synthesis and ultrafast optical results of a novel PbbSe - TiO_2 heterostructure. PbSe QDs are at the limit of strong confinement due to their very large Bohr exciton radius.[249] PbSe QDs have a large tunable band gap range and exciton wavefunctions

that extend significantly beyond the QD physical dimensions. Hot electron transfer is a process that is thought to give efficient electron transfer on the femtosecond timescale, and which has been seen in PbSe - TiO_2 QDHs before. There's still debate about the timescale and efficiency of this process though.[250], [251] UV - probe OTA can unambiguously assign the timescale of this process by monitoring the band gap dynamics of TiO_2 where charge injection results in Coulombic screening of the a-axis excitonic transition.[90], [252] The bifunctional linker used here, NaDMPS, has been shown to vastly improve the photochemical stability of PbS quantum dots, and the sulfonate group provides a very robust coordination to the TiO_2 surface.[85], [246]

PbSe - TiO_2 QDHs were synthesized as shown in figure B.1. TiO_2 nanostructures were grown with a biphasic mixture, grown in a bomb reaction vessel.[253] In brief, 10 mls of deionized water was added to the reaction vessel, along with 1 ml t-butylamine. 10 mls of toluene was then added, and gently mixed with 3 mls of oleic acid and 1 ml Ti(IV)-isopropoxide. After sealing the vessel, growth took place at 180 °C for 12 hours. After cooling down the resulting biphasic mixture was carefully separated into aqueous and organic components. The organic phase will be milky white and contain the nanoellipsoids, which are be 50 - 200 nm long and $\sim$ 20 nm wide. This phase was washed with methanol 3 times to remove excess oleic acid.

PbSe quantum dots were synthesized with a heat up method.[254] 4 mmols of Pb-oleate was added to 16 mls of octadecene. The mixture was purged with N_2 after heating up to 100 °C, then degassed under vacuum for 60 minutes. 1 mmol of Se was dissolved in 5 mls of trioctylphosphine under an inert atmosphere, followed by addition of 4 mmols of diphenylphosphine. The Pb-oleate solution was cooled to 80 °C, then the Se-DPP-TOP mixture was quickly injected. The reaction mixture is allowed to react for 5 minutes to yield 2.6 nm QDs, 20 minutes for 3 nm QDs, or 40 minutes for 4.3 nm QDs. The reaction is quenched with a cold water bath. The reaction mixture was worked up by precipitating the QDs with $\sim$ 30 mls acetone, then centrifuging at 12 krpm fr 5 minutes. After discarding the

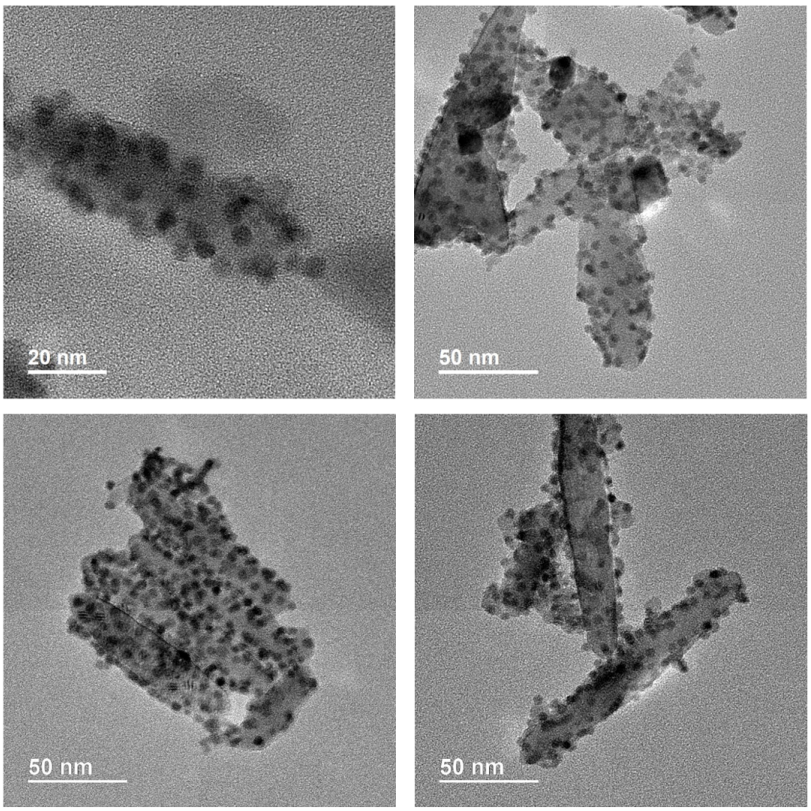

Figure B.2: a) - d) TEM images of conjugated PbSe QDs and TiO_2. The QDs are 5 nm in diameter.

supernatant, the QDs were dissolved in 10 mls toluene. This procedure was repeated up to 3 times more.

The results of a biphasic conjugation procedure are shown in the TEM images displayed in figure B.2. To chemically conjugate the QDs and nanoellipsoids, 5 mls of deionized water was mixed with 1 to 5 mmols of sodium 1,2-dimercaptopropanesulfonate (NaDMPS). A typical reaction employed 100 μmls of PbSe QDs with 1 ml TiO_2 diluted to 5 mls with toluene. The reaction mixture was purged with N_2, and stirred overnight at 45 °C. The resulting solution is washed 3 to 5 times with toluene, and centrifuged at 5 krpm for 10 minutes, then redispersed in 5 ml of 10 mM NaDMPS. The conjugated mixture will have a muddy quality.

Figure B.3 shows example data of OTA on the TiO_2 nanoellipsoids. This sample had significant experimental difficulties. The nanoellipsoids suffered from very high scattering cross-sections creating a turbid solution, which requires long collection times. Photoexcitation

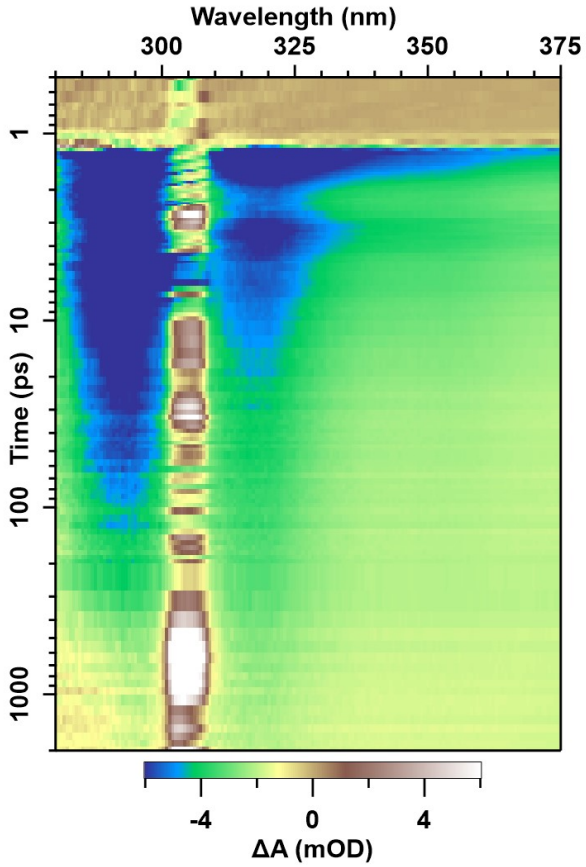

Figure B.3: The 2 dimensional data for UV-probe OTA on TiO_2 heterostructures, after excitation with $40\mu J/cm^2$ of 305 nm.

results in a strong bleach of the c- and a-axis bound excitonic transitions at 292 nm and 319 nm respectively. The a-plane transition also shows a strong oscillation, with a frequency that matches the acoustic phonon in TiO_2.[252] The nanoellipsoids have a large variation in length, but are consistently 20 nm or so in width. Because the 319 nm excitonic transitions is bound in the a-axis and the oscillation is not seen in the c-axis transition at 292 nm, such a coherent oscillation could only be observed if the a-plane was oriented along the minor-axis of the ellipsoids. Charge transfer OTA experiments on the PbSe sensitized QDHs could not be complete due to persistent aggregation of PbSe, which strongly affected the OTA spectra. In addition, the prolonged measurement times lead to oxidation of the PbSe even with the improved stability from DMPS.